

EXPLORATION OF THE COLD CRACKING RISKS AND LIMITS FOR WELDING REPAIR APPLICATIONS OF LOW-ALLOY FERRITIC STEEL NUCLEAR COMPONENTS

A thesis submitted to the University of Manchester for the degree of Doctor of Philosophy in the Faculty of Science and Engineering

2023

Alexandre A. M. PAGET

LIST OF CONTENTS

List of Contents	.2
List of Symbols & Abbreviations	10
Name Abbreviations	10
Technical Abbreviations	11
Units	15
Symbols	17
List of Illustrations2	21
Pictures	21
Figures2	24
List of Diagrams3	31
List of Tables3	37
List of Conventions3	39
System of Units	39
Scaling Convention	39
Crack Identification Convention	40
Abstract	42
Declaration ²	43
Copyright Statement	43
Acknowledgements	44
I General Introduction	46
I.1 Project Background & Motivations	46

I.1.A	The nuclear industry's role in global electricity generation	46
I.1.B	The pressurised water reactor : a recognised technology	46
I.1.C	The maintenance challenges	48
I.1.D	The engineering challenges	51
I.1.E	The technical limits	52
I.1.F	The research & development opportunities	53
I.2	Project Ambitions	54
I.2.A	Aims and objectives	54
I.2.B	Framework	55
I.3	Thesis Structure	55
II Lite	erature Review	57
II.1	Introduction to General Theory	57
II.1.A	Candidate welding processes	57
II.1.	A.1 Arc-welding principles	57
	II.1.A.1.a Shielded metal arc-welding	57
	II.1.A.1.b Gas tungsten arc-welding	58
II.1.	A.2 Examples of typical defects	59
II.1.	A.3 The heat-affected zone	60
	II.1.A.3.a Definition	60
:	II.1.A.3.b Basics of metallic microstructures	61
	II.1.A.3.c Formation of microstructures	63
	II.1.A.3.d Arc-welding & microstructure modifications	
II.1.B	Cold cracking	71
II.1.	B.1 Phenomenon description	71

II.	1.B.2 Th	e failure mechanisms	72
II. I	1.B.3 Th	e causes	74
II.1.0	C Focu	s on the cold cracking factors	75
II.	1.C.1 Co	oupling phenomena	75
II. I	1.C.2 Ki	netics of occurrence	76
II. I	1.C.3 A	critical microstructure	78
	II.1.C.3.a	Identification history	78
	II.1.C.3.b	Microstructure in cold cracking occurrence	79
II.	1.C.4 Hy	drogen embrittlement	83
	II.1.C.4.a	Adsorption, desorption	83
	II.1.C.4.b	Absorption, diffusion, trapping	85
	II.1.C.4.c	Categorisation of the hydrogen content	88
	II.1.C.4.d	Effusion	89
	II.1.C.4.e	Degradation mechanisms	89
	II.1.C.4.f	Observable consequences	94
	II.1.C.4.g	Hydrogen embrittlement in cold cracking	95
II.	1.C.5 Me	echanical loads	99
	II.1.C.5.a	Action stresses	99
	II.1.C.5.b	Reaction stresses	100
	II.1.C.5.c	Residual stresses	103
	II.1.C.5.d	Stress amplifying conditions	
	II.1.C.5.e	Stress attenuating conditions	
		Loading modes in fracture mechanics	
		Stress in cold cracking occurrence	
II.2	State-of-	-the-Art	114

	II.2.A	Preventing cold cracking.	114
	II.2.B	Deeper investigations	117
	II.2.C	Recent research into cold cracking & discussion	119
	II.3	Conclusions Drawn from the Literature Review	124
	II.3.A	Welding test procedures	124
	II.3.B	Modelling & simulation	126
	II.3.C	Small-scale testing	127
I	II Met	thodology and Optimisation	130
	III.1	Foreword	130
	III.2	Materials	130
	III.3	Research Plan	131
	III.4	Welding Conditions & Parameters	132
I	V Stu	dy of the Tekken Welding Test	138
	IV.1	Foreword	138
	IV.2	Methods	138
	IV.2.A	Modelling & simulation	138
	IV.2.B	Material properties	139
	IV.2.	B.1 Base metal	139
	IV.2.	.B.2 Filler metal	141
	IV.3	Qualification Using Dilatometry Testing	141
	IV.3.A	Experiment description	141
	IV.3.B	Modelling & simulation	143
	IV.3.C	Results	143

IV.3.D	Discussion	148
IV.4 Q	pualification Using Jominy Testing	149
IV.4.A	Experimental method	149
IV.4.B	Pyrometer qualification	155
IV.4.C	Modelling & simulation	159
IV.4.D	Adjustment of the thermal solution	160
IV.4.E	Results	162
IV.4.F	Discussion	164
IV.5 T	ekken Modelling	167
IV.5.A	Meshing strategy	167
IV.5.B	Automation of coherent meshing	169
IV.5.C	Boundary & initial conditions	170
IV.5.D	Modelling optimisation	171
IV.5.E	Equivalent heat source	172
IV.6 R	esults	183
IV.7 D	iscussion & Conclusion	187
V Weldin	g Test Benchmarking	190
V.1 F	oreword	190
V.2 T	ekken Method	194
V.2.A	Observations	194
V.2.B	Methods	195
V.2.C	Results & discussion	203
V3 Ir	nplant Method	208

V.3.A	Observations	208
V.3.B	Methods	210
V.3.C	Results & discussion	218
V.4 Co	onclusions	223
V.4.A	Summary	223
V.4.B	Crack detection by acoustic emission	224
V.4.C	Extraction by electrical discharge machining	225
V.4.D	Benchmarking conclusions	225
V.4.E	Recommendations	227
VI Behav	viour Study of the Heat-Affected Zone Exposed to Hydroger	ı228
VI.1 Fo	oreword	228
VI.2 M	[ethods	228
VI.3 Re	eproduction of Typical Heat-Affected Zone Microstructures	229
VI.3.A	Targeted microstructure types	229
VI.3.B	Heat treatment procedures	231
VI.3.C	Metallographic observations	232
VI.3.C	C.1 Optical microscopy	233
VI.3.C	C.2 Electron microscopy	233
VI.3.C	C.3 Hardness measurements	235
VI.3.C	C.4 Conclusions	235
VI.4 H	ydrogen Solubilities	236
VI.4.A	Hydrogen charging.	237

VI.4.C	Hydrogen content distribution	240
VI.5 N	Mechanical Testing	242
VI.5.A	As-quenched	244
VI.5.B	Hydrogen-exposed material	245
VI.5.C	Effect of time since hydrogen charging	250
VI.6 F	Result Analyses & Discussion	252
VI.6.A	Fractography	252
VI.6.2	A.1 Optical microscopy	252
VI.6.2	A.2 Electron microscopy	253
VI.6.B	Evolution of the mechanical properties	258
VI.6.C	Quantification of the ductility loss	261
VI.6.D	Limits of this work	264
VI.7	Conclusions	266
II Gen	eral Conclusion	268
VII.1 S	Summary	268
VII.2 R	Recapitulation of the Main Results and Observations	269
VII.2.A	Outcomes of the Tekken test investigation	269
VII.2.B	Outcomes of the welding test benchmarking	269
VII.2.C	Outcomes of the material study	270
VII.3 A	Answers to the Ambitions of this Project	270
VII.3.A	Deterministic versus probabilistic criteria	270
VII.3.B	Tekken versus historical implant test	271
VII.3.C	Viability of bead tempering methods	271

VII.4	Recommendations for Further Work	272
Bibliogr	raphy	273

Word count : 47 741

LIST OF SYMBOLS & ABBREVIATIONS

NAME ABBREVIATIONS

SI : International System of Units

IEA : International Energy Agency

OECD : Organisation for Economic Co-operation and Development

EDF : Électricité De France

USA : United State of America

UK : United Kingdom

EPRI : Electric Power Research Institute

ASME : American Society of Mechanical Engineers

NBBI : National Board of Boiler and pressure vessel Inspectors

ASN : Autorité de Sûreté Nucléaire

AFCEN : Association Française pour les règles de Conception, de

Construction et de surveillance en Exploitation des chaudières

électro-Nucléaires

R&D : Research and Development

PRISME : Performance, Risque Industriel, Surveillance pour la Maintenance

et l'Exploitation

MaSC : Modelling and Simulation Centre

SAFER : Simulation en Appui à la Fabrication Et aux Réparations

SINDRI : Synergistic utilisation of INformatics and Data centRic Integrity

engineering

LaSIE : Laboratoire des Sciences de l'Ingénieur pour l'Environnement

CNRS : Centre National de la Recherche Scientifique

IS : Institut de Soudure

IIW : International Institute of Welding

ISO : International Organization for Standardization

NeT-TG8 : The European Network on Neutron Techniques Standardisation for

Structural Integrity – Task Group 8

NeT-TG4 : The European Network on Neutron Techniques Standardisation for

Structural Integrity – Task Group 4

NeT-TG6 : The European Network on Neutron Techniques Standardisation for

Structural Integrity – Task Group 6

NNUMAN : New NUclear MANufacturing

MACE : Department of Mechanical, Aerospace and Civil Engineering

ASTM : American Society for Testing and Materials

IRDL : Institut de Recherche Dupuy de Lôme

UBS : Université Bretagne-Sud

TECHNICAL ABBREVIATIONS

N.P.P. : Nuclear Power Plant

L.T.O. : Long-Term Operation

N.S.S.S. : Nuclear Steam Supply System

P.W.R. : Pressurised Water Reactor

L.W.R. : Light Water Reactor

N.I. : Nuclear Island

S.S.Cs. : Structures, Systems and Components

B.N.I. : Balance of Nuclear Island

T.I. : Turbine Island

B.o.P. : Balance of Plant

R.P.V. : Reactor Pressure Vessel

E.P.R. : *initially* European Pressurised Reactor, *then renamed* Evolutionary

Power Reactor

B.M.I. : Bottom-Mounted Instrumentation

A508 Gr. 3 Cl. 1 : SA-508 Grade 3 Class 1

H.A.C.C. : Hydrogen-Assisted Cold Cracking (= delayed cracking = under-

bead cracking = H.I.C.C. = cold cracking)

H.I.C.C. : Hydrogen-Induced Cold Cracking (= delayed cracking = under-

bead cracking = H.A.C.C. = cold cracking)

P.W.H.T. : Post-Weld Heat Treatment

T.B.W. : Temper Bead Welding

H.E. : Hydrogen Embrittlement

F.E.M. : Finite Element Method

H.P.C. : High-Performance Computing

G.T.A.W. : Gas Tungsten Arc-Welding

S.M.A.W. : Shielded Metal Arc-Welding

A.C. : Alternative Current

D.C. : Direct Current

M.M.A. : Manual Metal Arc-welding (= M.M.A.W. = flux shielded arc

welding = stick welding)

M.M.A.W. : Manual Metal Arc-Welding (= M.M.A. = flux shielded arc-

welding = stick welding)

T.I.G. : Tungsten Inert Gas

T.A.G. : Tungsten Active Gas

C.T.W.D. : Contact Tip to Workpiece Distance (= C.T.D.)

C.T.D. : Contact Tube Distance (= C.T.W.D.)

H.A.Z. : Heat-Affected Zone

F.C.C. : Face-Centred Cubic

B.C.C. : Body-Centred Cubic

B.C.T. : Body-Centred Tetragonal

C.C.T. : Continuous Cooling Transformation diagram

T.T.T. : Time-Temperature-Transformation diagram (= I.T.)

I.T. : Isothermal Transformation diagram (= T.T.T.)

P.A.G.S. : Prior Austenite Grain Size

F.H.A.Z. : Fine-grained Heat-Affected Zone (= F.G.H.A.Z.)

F.G.H.A.Z. : Fine-Grained Heat-Affected Zone (= F.H.A.Z.)

C.H.A.Z. : Coarse-grained Heat-Affected Zone (= C.G.H.A.Z.)

C.G.H.A.Z. : Coarse-Grained Heat-Affected Zone (= C.H.A.Z.)

M.V.C. : Micro-Void Coalescence

H.A.C. : Hydrogen-Assisted Cracking

U.T.S. : Ultimate Tensile Strength

T.E. : Temper Embrittlement

T.M.E. : Tempered Martensite Embrittlement

H.C.P. : Hexagonal Close-Packed

H.I.C. : Hydrogen-Induced Cracking

H.E.A.C. : Hydrogen Environment-Assisted Cracking

I.H.A.C. : Internal Hydrogen-Assisted Cracking

H.E.DE. : Hydrogen-Enhanced Decohesion

H.E.L.P. : Hydrogen-Enhanced Localised Plasticity

A.I.D.E. : Absorption-Induced Dislocation Emission

S.A.W. : Submerged-Arc-Welding

F.C.A.W. : Flux-Cored Arc-Welding

G.M.A.W. : Gas Metal Arc-Welding

C.T.E. : Coefficient of Thermal Expansion

TR.I.P. : TRansformation-Induced Plasticity

A.T.T.B. : Ambient Temperature Temper Bead

C.T.S. : Controlled Thermal Severity test

R.C.C. : Rigid Restraint Cracking test

T.C. : ThermoCouple

A.E. : Acoustic Emission

A.V.C. : Arc Voltage Control

E.D.M. : Electrical Discharge Machining

L.V.D.T. : Linear Variable Differential Transformer

E.M. : Electron Microscopy

E.B.S.D. : Electron BackScatter Diffraction

I.C.H.A.Z. : Inter-Critical Heat-Affected Zone

S.E.M. : Scanning Electron Microscope

P.A.U.T. : Phased-Array Ultrasonic Testing

T.O.F.D. : Time-Of-Flight Diffraction

I.Q. : Image Quality

T.D.S. : Thermal Desorption Spectroscopy

Units

pm : picometre

nm : nanometre

μm : micrometre

mm : millimetre

mm² : square millimetre

mm³ : cubic millimetre

TW·h : terawatt-hour

% : percentage

MW : megawatt

° : degree angle

°C : degree Celsius

cm : centimetre

at% : atomic percentage

wt% : weight percentage

°F : degree Fahrenheit

K : kelvin

s : second

min : minute

h : hour

Pa : pascal

MPa : megapascal

cm²/s : diffusion coefficient

ppm : parts-per-million

wppm : weight parts-per-million

atm : standard atmosphere

eV : electron-volt

P----: : ISO grit size designation

rpm : revolutions per minute

mm/s : millimetre per minute

W : watt

J : joule

V : volt

A : ampere

kg_f : kilogram-force

HV : Vickers pyramid number

HVn: HV measured using a test load of $n \text{ kg}_f$

g : gram

g/L : gram per litre

°C/s : degree Celsius per second

K/s : kelvin per second

 $W \cdot m^{-2} \cdot K^{-1}$: watt per square meter per kelvin

wt%/s : weight percentage per second

K/min : kelvin per minute

dB : decibel

SYMBOLS

symbol	description	(unit)
etc.	et cetera	
&	and	
mini	minimum	
max	maximum	
Ø	diameter	
Δ	difference operator	
0D	zero-dimensional space	
1D	one-dimensional space	
2D	two-dimensional space	
3D	three-dimensional space	
Ra	profile roughness parameter	μm
Fe	iron atom	
C	carbon atom	
Н	hydrogen atom	
H^+	hydron	
H_2	dihydrogen (molecular hydrogen)	

H_{ad} adsorbed hydrogen

H_{ad}⁺ adsorbed hydron

H_{ab} absorbed hydrogen

H_{ab}⁺ absorbed hydron

Fe₃C iron carbide compound

Mn manganese atom

Ni nickel atom

Mo molybdenum atom

MnS manganese sulphide compound

P phosphorus atom

Cr chromium atom

V vanadium atom

Cu copper atom

Nb niobium

Ti titanium

Sn tin

H₂O water

OH- hydroxide

e⁻ electron

p⁺ proton

H₃O⁺ hydroxonium

SiC silicon carbide

Al₂O₃ aluminium oxide

NH₄SCN ammonium thiocyanate

16MND5 low-alloy ferritic steel (= 16MnNiMo05)

SFVV3 low-alloy ferritic steel

20MnMoNi55 low-alloy ferritic steel

SA-508 low-alloy ferritic steels

18MND5	low-alloy ferritic steel	
T24	low-alloy ferritic steel	
Alloy 182	nickel-based alloy	
Alloy 600	nickel-based alloy	
Alloy 52M	nickel-based alloy	
AISI 316L	stainless steel	
AISI 304	stainless steel	
AISI 310	stainless steel	
ER70S-3	ferritic steel	
T	temperature	°C or K
γ-Fe	allotropic form γ of iron	
δ-Fe	allotropic form δ of iron	
α-Fe	allotropic form α of iron	
α'-Fe	allotropic form α' of iron	
T_r	temperature where 50 % re-crystallisation occurs in 1 hour	°C or K
T_m	melting temperature	
Ac_1	transformation start temperature from α -Fe to γ -Fe	°C or K
Ac_3	transformation finish temperature from α -Fe to γ -Fe	°C or K
L	liquid form	
t	time	S
T_ℓ	limit temperature	°C or K
t_{ℓ}	limit time	S
σ	stress	MPa
σ_{avg}	average stress	MPa
σ_{xx}	orthogonal normal stress	MPa
σ_{yy}	orthogonal normal stress	MPa
σ_{zz}	orthogonal normal stress	MPa
3	strain	%

3	emissivity	-
K_t	stress concentration factor	-
K	stress intensity factor	-
K	emissivity slope ratio	-
Taust	austenitisation temperature	°C or K
Ar_3	transformation start temperature from γ -Fe to α -Fe	°C or K
Ar_{I}	transformation finish temperature from γ -Fe to α -Fe	°C or K
$M_{\scriptscriptstyle S}$	martensitic (α '-Fe) transformation start temperature	°C or K
M_f	martensitic (α '-Fe) transformation finish temperature	°C or K
Τ	dislocation	
CE	equivalent carbon content	wt%
<i>t</i> _{8/5}	cooling duration from 800 °C to 500 °C	S
CE_{IIW}	equivalent carbon content (IIW's formula)	wt%
CE_{Gra}	equivalent carbon content (Graville's formula)	wt%
GB-α	grain boundary ferrite	
β-Ni	allotropic form β of nickel	
E	Young's modulus	Pa
E	energy	J
A	elongation	%
Φ	heat flux	W
η	efficiency	-
U	voltage	V
I	current intensity	A
v	speed	mm/s
Q	quantity of heat	J
F_3	welded joint form factor	-

LIST OF ILLUSTRATIONS

PICTURES

Picture II-a :	examples of root cold cracks occurring in different configurations and zoomed view of a tiny intergranular cold crack in a heat-affected zone (sources: from public illustrations, literature and experiments carried out during this research project)
Picture II-b :	illustrations of manganese sulphide (notch form) and combination of manganese sulphide (MnS) with calcium aluminates (round shape) inclusions observed within low-alloy steel 18MND5 (polishing : $\frac{1}{4}$ µm – etching : 2 % nital during \approx 30 s)
Picture III-a :	welding of an ISO 3690 mock-up (source : the IS)134
Picture III-b :	analysis of an ISO 3690 sample using metallic mercury (source : the IS)
Picture IV-a :	pushrod dilatometer machine used during the NeT-TG8 and NNUMAN programs (source : [243])
Picture IV-b:	sealed tubular furnace utilised for the Jominy specimen austenitisation
Picture IV-c :	Jominy quenching test setup instrumented with pyrometry
Picture IV-d :	spot-welded micro-thermocouples on a sample representing the upper surface of the Jominy specimen (PASEPMARTY1 sample)
Picture IV-e :	alignment of the arc-welding torch electrode and the pyrometer beam spot with the micro-thermocouple (pyrometer beam spot represented by the laser targeting light feature – PASEPMARTY1 sample)
Picture IV-f:	heating of the calibration sample up to 1 050 ± 50 °C using the robotised tungsten inert gas arc-welding station (PASEPMARTY1 sample) 158
Picture IV-g:	extra 40 mm thick mock-up left over from a previous Tekken campaign

Picture IV-h:	tungsten inert gas welding torch configuration and example of dummy mock-up used to make sure the installation was functioning properly
Picture IV-i :	one of the y-slot dummy mock-ups used to make sure the installation and the weld program were functioning properly
Picture IV-j:	the thermocouple-instrumented mock-up before and after assembly, and after the welding run completion (220406-TEK1-WH-INC-TC specimen)
Picture IV-k:	cross-section comparison of the two buried thermocouples monitoring the same zone (the slot gap does not meet the standard dimensions [191] due to limitations in the manufacturing tolerance when working from two half-blocks)
Picture IV-1 :	cross-section comparison of two buried thermocouple monitoring different zones (the slot gap does not meet the standard dimensions [191] due to limitations in the manufacturing tolerance when working from two half-blocks)
Picture V-a:	raw images used in the macrographs given in Figure V-a and Figure V-b
Picture V-b:	welding and instrumentation setup used to conduct the cold cracking Tekken tests at EDF PRISME (OLDTEK2 preliminary welding test)
Picture V-c :	highlight of the tapered chamfers added to the welding groove (220401-TEK2-WH-INC mock-up)
Picture V-d:	highlight of the support shims used to thermally insulate the mock-up from the welding table (220401-TEK2-WH-INC welding test) 197
Picture V-e :	weld bead deposit into the Tekken groove of the cold cracking test 220325-TEK1-WH-INC
Picture V-f:	extraction by electrical discharge machining of the weldment and sample reference engraving prior to the cutting in "slice" samples

	(220314-TEK1-WH-SS & 220318-TEK2-WH-SS mock-ups)202
Picture V-g :	preliminary adjustment of the welding torch and the trajectory, and a weld bead deposition
Picture V-h :	setup used for the implant test campaign
Picture V-i :	specimen loaded on the testing table and instrumented by acoustic emission sensors
Picture V-j :	extraction of unbroken specimens using an annular cutter (sample contained within the extracted cylinder)
Picture V-k :	sample machining on a lathe to expose a longitudinal cutting plane (the surrounding cylinder has been removed in this case)
Picture V-l :	extraction procedure of broken specimens217
Picture V-m :	cold crack in the heat-affected zone (sample MND3, cutting plane 1/3)
Picture V-n :	cold cracks in the heat-affected zone (sample MND6, cutting planes 1/3 and 3/3)
Picture V-o :	small cold crack in the heat-affected zone (sample MND7, cutting plane 2/3)
Picture V-p :	breakage profiles of both fractured implant specimens222
Picture VI-a :	thermal treatment setup utilised in the 3 rd microstructure tempering (fine-grained tempered)
Picture VI-b :	optical micrographs of the 1 st microstructure representing coarse- grained heat-affected zone (greyscale)
Picture VI-c :	optical micrographs of the 2 nd microstructure representing fine-grained heat-affected zone (right image in greyscale)
Picture VI-d :	electron backscatter diffraction analysis of the 1 st microstructure representing coarse-grained heat-affected zone

Picture VI-e :	electron backscatter diffraction analysis of the 2 nd microstructure
	representing fine-grained heat-affected zone
Picture VI-f :	prior austenite grain reconstruction analyses of the 2 nd microstructure
	representing fine-grained heat-affected zone
Picture VI-g :	hydrogen chemical charging setup and approximate sample/solution
	volume ratio (adapted from [280])
Picture VI-h :	Jobin Yvon Horiba EMGA-621W hydrogen analyser (scale, furnace
	and hydrogen detector)
Picture VI-i :	positioning of a notched specimen on the testing machine
Picture VI-j :	tensile test specimens immersed into jacketed reaction beakers used as
	chemical charging cells
Picture VI-k:	Micrographs showing the effect of hydrogen concentration on the
	development of necking in smooth tensile test specimens
Picture VI-l:	breakage profiles of the coarse-grained microstructure (1st) smooth
	tensile test specimens
Picture VI-m:	breakage profiles of the coarse-grained microstructure (1st) V-notched
	tensile test specimens
Picture VI-n :	breakage profiles of the fine-grained microstructure (2 nd) V-notched
	tensile test specimens (including a case having experienced hydrogen
	egress)
Picture VI-o:	breakage profiles of the tempered fine-grained microstructure (3 rd) V-
	notched tensile test specimen
FIGURES	
Figure – 1 :	terminology proposal for describing cracks in weldments throughout
	this manuscript (adapted from [3]) – illustration A
Figure – 2:	terminology proposal for describing cracks in weldments throughout

	this manuscript (adapted from [3]) – illustration B41
Figure I-a :	general overview of a nuclear power plant using the pressurised water reactor design (adapted from [13]) $ A$: nuclear island; B : nuclear steam supply system & structures, systems and components; C : nuclear steam supply system; D : turbine island; E : balance of plant
Figure I-b:	focused view of a nuclear steam supply system (group C) highlighting the reactor pressure vessel (adapted from [19])49
Figure I-c:	focused view of a reactor pressure vessel (R.P.V.) [22] and the layout details of a bottom-mounted instrumentation (B.M.I.) nozzle (adapted from [23], [24])
Figure I-d:	example of a defect location and machined cavity before cladding with the order of magnitude of the dimensions (undisclosed information) 50
Figure I-e:	detail A of the defect (side view – Figure I-d): step-by-step illustration of the repair process (adapted from [25])
Figure II-a :	schematic illustration of the shielded metal arc-welding technic (adapted from [54]–[56])
Figure II-b :	schematic illustration of the gas tungsten arc-welding technics (adapted from [42], [54]–[56])
Figure II-c :	schematic illustrations of some common arc-welding defects (source : [57])
Figure II-d :	macroscopic illustration of the heat-affected zone typical for a low-alloy steel weld (adapted from [58]–[61])
Figure II-e:	illustrations summarising the definition of metallic microstructure, from a part to the lattices of a grain A and a grain B ; nodes on the boundary are shared between these two grains
Figure II-f:	illustrations summarising the definition of metallic microstructure, from the lattice to the atoms, including two examples of atomic arrangement with their respective patterns (adapted from [63], [64]) –

	A: face-centred cubic; B: body-centred cubic
Figure II-g :	schematic illustration of the carbon solubility within austenite [77], and the resulting two ways of its decomposition into cold phases for standard low-carbon steels (adapted from [64], [79])
Figure II-h :	illustration of an intergranular and a transgranular crack paths [95] 72
Figure II-i :	schematic illustration of the most common crack categories produced by cold cracking (non-exhaustive list; hybridisations are possible; cracks would not be expected to occur in the same weldment; according to the convention used throughout this manuscript) – adapted from [84], [96]
Figure II-j :	illustration summarising the main microstructure characteristics 80
Figure II-k:	schematic representations of sites and traps for hydrogen (atoms illustrated in red) in polycrystalline structures (adapted from [63], [113], [146])
Figure II-l :	schematic illustrations of fracture mechanisms assisted by hydrogen (adapted from [113])
Figure II-m :	schematic examples illustrating hybridisation of fracture mechanisms assisted by hydrogen (hydrogen-enhanced decohesion (H.E.DE.), hydrogen-enhanced localised plasticity (H.E.L.P.), absorption-induced dislocation emission (A.I.D.E.) – adapted from [113])
Figure II-n :	summary example of hydrogen flows during an arc-welding operation (type gas tungsten arc-welding) – adapted from [42], [54]–[56], [171]
Figure II-o:	schematic illustration of the privileged hydrogen distribution depending on the metallurgical synergy during the weld cooling (adapted from [2], [172])
Figure II-p :	plastic zone extension according to the assumption about the medium behaviour (source : [192])
Figure II-q :	the three components partitioning the load at a crack tip (source : [197])

Figure II-r:	highlight of the different characterisation methods for notches and cracks (adapted from [196])
Figure II-s:	schematic illustration highlighting the difference between conventional multi-pass welds and those made with temper bead welding (adapted from [25])
Figure IV-a:	illustration of the modelled 2D slice position within the Tekken test mock-up
Figure IV-b:	schematic drawing of the pushrod dilatometer machine used at during the NeT-TG8 and NNUMAN programs (adapted from [243])142
Figure IV-c :	technical specifications of the Jominy specimen (in accordance with the standard [262] specifications)
Figure IV-d:	schematic illustration of the Jominy test setup and position of the pyrometer focal point on the top surface of the specimen (pyrometer beam spot represented by the laser targeting light feature) – left-hand schematic illustration adapted from [262]
Figure IV-e :	technical details of the cutting plan of the Jominy sample for post-test analyses
Figure IV-f:	schematic illustration of the setup engineered to calibrate the dual- wavelength mode of the pyrometer
Figure IV-g:	summary of the boundary conditions applied to the Jominy model. 160
Figure IV-h:	comparison of the experimental (HV1: test load of 1,00 kg _f) and calculated hardness field of the half-side of the longitudinal cross-section of the Jominy ST specimen, completed with metallographic observations of some locations
Figure IV-i:	comparison of the hardness scans processed on the half-side of the longitudinal cross-section of the Jominy standard (ST), P1, and P2 specimens (HV1: test load of 1,00 kg $_{\rm f}$)

Figure IV-j :	illustrations of the mesh generated for a mock-up thickness of 30 mm
Figure IV-k:	coherence illustration from the 15 mm to the 150 mm meshes with a focus on the weld bead area
Figure IV-l :	schematic illustration of the mesh re-positioning (modified scale) and mechanical boundary conditions
Figure IV-m :	thermocouple placement locations (40 mm Tekken test mock-up) 173
Figure IV-n:	thermocouple positions utilised for the calibration of the equivalent hear source
Figure IV-o :	comparison between the experimental hardness scan (220406-Y sample) and the computational prediction (the slot gap does not meet the standard dimensions [191] due to limitations in the manufacturing tolerance when working from two half-blocks)
Figure IV-p :	macrography of the weld (220406-A1 sample – yellow areas: heat-affected zones; green and blue areas: weld metal; green area specifically the deposited filler metal section – raw image given in Picture IV-I) – the slot gap does not meet the standard dimensions [191] due to limitations in the manufacturing tolerance when working from two half-blocks
Figure IV-q :	residual stresses across weld throat in flat test specimens with different groove types (source : [43], [82])
Figure IV-r :	predicted field of the σ_{xx} orthogonal normal stress occurring in the 45 mm Tekken mock-up after a period of 15 min following the well completion (indicative stress values)
Figure IV-s :	predicted field of the σ_{yy} orthogonal normal stress occurring in the 45 mm Tekken mock-up after a period of 15 min following the well completion (indicative stress values)
Figure IV-t :	predicted field of the σ_{zz} orthogonal normal stress occurring in the 45 mm Tekken mock-up after a period of 15 min following the weld

	completion (indicative stress values)
Figure V-a :	macrography of a Tekken test weld bead produced using the selected welding parameters and nickel-based alloy 52M used as filler metal (220401-B sample – yellow areas: heat-affected zones; green and blue areas: weld metal; green area: specifically the deposited filler metal section – raw image given in Picture V-a)
Figure V-b :	macrography of an implant test weld bead produced using the selected welding parameters (sample from MND8 test – consistent scaling with Figure V-a – yellow area: heat-affected zone; green and blue areas: weld metal; green area: specifically the deposited filler metal section – raw image given in Picture V-a)
Figure V-c :	details of the Hsu-Nielsen Source method used to generate pencil lead breakage at known locations on the mock-up (adapted from [275]) 199
Figure V-d :	examples of the accuracy of the calculated impact locations by the acoustic emission system after the re-calibration at the end of the welding cold cracking test (220325-TEK1-WH-INC specimen; area of interest established following the standard [191] guidance)
Figure V-e :	weld bead cracking generated during the 220323-TEK1-WH-FER test using ferritic steel ER70S-3 as filler metal and the corresponding recorded acoustic emissions
Figure V-f :	example of root cracking found using stainless steel AISI 316L as filler metal and the corresponding recorded acoustic emissions (220318-TEK2-WH-SS test – 220318-B sample)
Figure V-g :	surface root & hot cracking (sample 220401-X) and solidification shrinkage cavity (sample 220401-E) found – in the exclusion zones – using Alloy 52M as filler metal and the corresponding recorded acoustic emissions (220401-TEK2-WH-INC test)
Figure V-h :	cold cracks (sample 220325-X) found – in exclusion zone – using Alloy 52M as filler metal and the corresponding recorded acoustic emissions (220325-TEK1-WH-INC test)

Figure V-i :	multi-pass weld Tekken specimen 220408-TEK1-WH-INC-MULTI (220408-C sample; HV1: test load of 1,00 kg _f)
Figure V-j :	technical schemes of the implant test method and circular V-notch layout (adapted from [49], [240])
Figure V-k:	details of the cutting planes locations (helical V-notch design) – source : [240]
Figure V-l:	experimental hardness scan of the transverse cross-section of the MND8 weld bead (HV1 : test load of 1,00 kg _f)
Figure VI-a :	schematic illustration of the sectioned microstructure locations within the heat-affected zone of a multi-pass weld made using the temper bead welding technique (adapted from [25])
Figure VI-b :	layout of the smooth tensile test specimens
Figure VI-c :	layout of the V-notched tensile test specimens (designed according to the implant test standard [240])
Figure VI-d:	Code_Aster simulation of the local stress distribution (trace of the tensor) in the fillet region of a smooth tensile test specimen loaded to an average stress σ_{avg} of 1 495 MPa (calculated in the gauge section)

LIST OF DIAGRAMS

Diagram II-a :	iron-iron carbide (Fe-Fe ₃ C) equilibrium phase diagram at atmospheric pressure (1 atm) as a function of the carbon concentration and the temperature (adapted from [70]–[72])
Diagram II-b :	schematic example of a typical continuous cooling transformation diagram describing the liquid-solid/solid-solid phase transformations of low-carbon steels as a function of the cooling rate [74], [75] (adapted from [58])
Diagram II-c :	Graville diagram demarking zones of welding difficulty for base metal made of steel [90] (adapted from [89])
Diagram II-d :	the three main physico-chemical factors involved in the cold cracking phenomenon
Diagram II-e :	illustration highlighting the numerous couplings within each pair of factors [48], [101]–[108] including the temperature (an indirect factor) - non-exhaustive list
Diagram II-f :	evolution of temperature versus hydrogen concentration in the weld centre and the heat-affected zone after welding completion (adapted from [109])
Diagram II-g :	evolution of tensile stress, temperature and hydrogen concentrations as a function of time after welding completion (adapted from [116], [117])
Diagram II-h :	examples of overall diffusion coefficients of hydrogen as a function of temperature in iron α-Fe and niobium (body-centred cubic unit cells), nickel (face-centred cubic unit cells), and titanium (hexagonal close-packed (H.C.P.) unit cells) – adapted from [113]
Diagram II-i :	solubility of hydrogen in pure nickel and iron as a function of the allotropic form and the temperature (α -Fe & δ -Fe : body-centred cubic ; β -Ni & γ -Fe : face-centred cubic ; α '-Fe : body-centred tetragonal assumed to be the same as in

	boay-centrea cubic) at 1 atm pressure of H ₂ (adapted from [139], [140])
Diagram II-j :	focus on the overall diffusion coefficients of hydrogen in steels as a function of the temperature and the allotropic form of iron (α -Fe: bodycentred cubic; γ -Fe: face-centred cubic; α '-Fe: body-centred tetragonal – diffusivity in body-centred tetragonal assumed to be the same as in body-centred cubic) – adapted from [98]
Diagram II-k :	classic examples of free and solid-solid phase transformation-induced plasticity (TR.I.P.) dilatometric tests: total strain (thermal + elastic + plastic) versus temperature – <i>bainitic transformations</i> (source: [180], [181])
Diagram II-l :	evolution trend of the mechanical load acting on the weld during and after an arc-welding pass – observed by [200] in massive test mock-ups (adapted from [118])
Diagram IV-a :	heat treatment cycle profiles applied during the dilatometry tests of the NeT-TG8 project [228], [243] and the NNUMAN program [225], [229]
Diagram IV-b :	comparison between the simulated 16MND5 dilatation behaviour and the experimental observations for SA-508 (NNUMAN program [225], [229])
Diagram IV-c :	comparison between the simulated 16MND5 dilatation behaviour and the experimental observations for this modelled steel (NeT-TG8 project [228], [243]) as well as for the SA-508 (NNUMAN program [225], [229])
Diagram IV-d :	comparison between the simulated 16MND5 dilatation behaviour and the experimental observations for this modelled steel (NeT-TG8 project [228], [243]) as well as for the SA-508 (NNUMAN program [225], [229])
Diagram IV-e:	comparison between the simulated 16MND5 dilatation behaviour and the experimental observations for this modelled steel (NeT-TG8 project

	[228], [243]) as well as for the SA-508 (NNUMAN program [225], [229])
Diagram IV-f :	comparison between the simulated 16MND5 dilatation behaviour and the experimental observations for SA-508 (NNUMAN program [225], [229])
Diagram IV-g :	comparison between the simulated 16MND5 dilatation behaviour and the experimental observations for the SA-508 (NNUMAN program [225], [229])
Diagram IV-h :	comparison between the simulated 16MND5 dilatation behaviour and the experimental observations for the SA-508 (NNUMAN program [225], [229])
Diagram IV-i :	diagram representing the thermal treatment cycle applied to the Jominy ST specimen
Diagram IV-j :	calibration of the pyrometer based on the thermocouple measurement (PASEPMARTY1 sample – final adjustment : $K = 1,05$)
Diagram IV-k :	adjustment of the 16MND5 material properties to match the calculated cooling of the Jominy specimen with the experimental measurement (Jominy ST specimen)
Diagram IV-l :	hardness curves for steel grade 16MND5 after Jominy end quench hardenability test (Jominy ST specimen – HV10 and HV1 : test load of 10 kgf and 1,00 kgf, respectively)
Diagram IV-m :	diagrams representing the thermal treatment cycles applied to the Jominy P1 & P2 specimens
Diagram IV-n :	results of the mesh element quality control, the criterion being based on the shape ratio of the quadrangles (size : 30 mm thick)
Diagram IV-o :	temperatures recorded by the thermocouples (TC-SU-3-CL failed when it reached the peak temperature)
Diagram IV-p :	comparison of the experimental thermocouples data with the virtual ones of the Code Aster simulation after the heat source parameter

	calibration using a 40 mm Tekken test mock-up
Diagram IV-q :	benchmarking of the relative impact of the Tekken mock-up thickness on the average stress σ_{avg} experienced by the weld bead perpendicular cross-section (relative stress value)
Diagram IV-r :	average stress σ_{avg} evolution 10 hours after the weld completion for the 15 mm, 30 mm and 50 mm Tekken specimens (relative stress value)
Diagram IV-s :	focus on the thermocouple TC-CO-CL location (Tekken 40 mm) correlation between the drop in the stress increase during the metallurgical changes
Diagram V-a :	mechanisms responsible for acoustic emissions during material deformation and their corresponding typical signal amplitudes (source : [274])
Diagram V-b :	hardness comparison of the heat-affected zones produced using the implant and Tekken test methods
Diagram VI-a :	diagrams representing the thermal treatment cycles applied to produce the 1 st and 2 nd microstructure samples
Diagram VI-b :	diagram representing the thermal treatment cycles applied to produce the 3 rd microstructure samples
Diagram VI-c :	hydrogen charging domain in the coarse- and fine-grained microstructures (1 st and 2 nd)
Diagram VI-d :	hydrogen solubility comparison with the tempered fine-grained microstructure (3 rd), as well as with the previous microstructure investigated at the LaSIE during the research project of Qianqiang [47]. [166]
Diagram VI-e :	hydrogen desorption profile obtained during thermal desorption spectroscopy analysis at a heating rate of 230 K/min of the content distribution in the fine-grained microstructure (2 nd) charged at the maximum concentration

Diagram VI-f :	hydrogen content distributions in the coarse- and fine-grained microstructures (1 st and 2 nd) charged at the maximum concentrations
Diagram VI-g :	engineering stress-strain curves comparing specimens not exposed to hydrogen
Diagram VI-h :	engineering stress-strain curves obtained with the coarse-grained microstructure (1st) smooth tensile test specimens exposed to hydrogen 248
Diagram VI-i :	engineering stress-strain curves obtained with the coarse-grained microstructure (1st) notched tensile test specimens exposed to hydrogen 249
Diagram VI-j :	engineering stress-strain curves obtained with the fine-grained microstructure (2 nd) notched tensile test specimens exposed to hydrogen
Diagram VI-k :	engineering stress-strain curves obtained with the tempered fine- grained microstructure (3 rd) notched tensile test specimens exposed to hydrogen
Diagram VI-l :	engineering stress-strain curves obtained with the coarse-grained microstructure (1st) notched tensile test specimens left to stand for 24 hafter exposure to hydrogen
Diagram VI-m :	engineering stress-strain curves obtained with the coarse-grained microstructure (2 nd) notched tensile test specimens left to stand for 24 h after exposure to hydrogen
Diagram VI-n :	showing the effect of introduced hydrogen content on ultimate tensile strength
Diagram VI-o :	showing the effect of introduced hydrogen content on elongation prior to neck formation
Diagram VI-p :	showing the effect of introduced hydrogen content on reduction in area

Diagram VI-q:	diagram comparing the indices of ductility loss between the smooth and
	notched specimens made of the coarse-grained microstructure (1st)
	proportionally to the increase in hydrogen content
Diagram VI-r :	diagram showing the indices of ductility loss of the coarse- and fine-
	grained microstructure (1st and 2nd) specimens proportionally to the
	increase in hydrogen content
Diagram VI-s :	diagram comparing the ductility loss indices obtained with tempered
	and non-tempered (2 nd and 3 rd) fine-grained microstructure specimens
	under equivalent hydrogen concentration (the non-hydrogen exposed
	specimens of the 2 nd microstructure is used as the baseline for both)
	264
Diagram VI-t :	comparison of the results obtained using the smooth tensile specimens
	with those established by [110]
Diagram VI-u :	comparison of the results obtained using the notched tensile specimens
	with those established by [110]

LIST OF TABLES

Table II-A :	summary of common micro-constituents existing in standard steels and some of their characteristics		
Table II-B :	classification of some metals and alloys as a function of their susceptibility to hydrogen embrittlement (source: [135])		
Table II-C :	summary of the most common sites where hydrogen can transit/nest within polycrystalline structures [110], [136]–[138]		
Table II-D :	suggestive summary of the characteristics of fractures observed in hydrogen-assisted cracking [47], [110], [113], [151], [163], [164] 95		
Table III-A :	chemical composition analyses of the employed metals in this research project: 18MND5 batch n° 3375.15 (considered as being 16MND5) & nickel-based alloy Inconel 52M batch n° NX7208TK – <i>values from the material certificates provided by the suppliers</i>		
Table III-B :	diffusible hydrogen contents measured by the mercury displacement method as prescribed by ISO 3690 [145] (source : [254])		
Table III-C :	welding parameters and conditions selected for this research project		
Table IV-A :	summary of the predicted temperature-strain cycles compared with the experiments conducted on this modelled steel (NeT-TG8 project [228], [243]) as well as on the SA-508 (NNUMAN program [225], [229])		
Table V-A :	highlight of the consequences of variations in the diameter of the used filler wires		
Table V-B :	examples of common stress concentration factor K_t at the root of weld of basic joint geometry (adapted from [44], [207])		
Table V-C :	summary of the 2022 Tekken test campaign results204		
Table V-D :	summary of the 2022 implant test campaign results (only valid		

	specimens are included)				
Table VI-A:	hardness measurements in the bulk of the three produced microstructures following the Vickers method (test load of 1,00 kg _f – 12 indents, removal of the two extremes, averaging)				
Table VI-B:	size measurements of the prior austenite grains in the produced microstructures				
Table VI-C:	inclusion density and size in the as-received steel microstructure 236				
Table VI-D :	summary of the hydrogen concentration levels selected for the tensile testing				
Table VI-E :	summary of tests considered valid for subsequent analysis				

LIST OF CONVENTIONS

SYSTEM OF UNITS

The International System of Units, also known by the international abbreviation SI,

defined in the ISO 80000-1 [1] standard is preferred.

Moreover, as a result of the French-English context of this research project, the French

numbering convention is preferred (numbers after the comma are seen as decimals). For

instance:

• two point five: 2,5

• four million: 4 000 000

• thirteen thousand point thirteen: 13 000,13

SCALING CONVENTION

Since scaling conventions are generally quite subjective, depending on the elements

studied, and varying significantly from one field to another, the following convention is

used throughout this manuscript in the experimental investigations:

Pico –

: up to 1 nm (= atomic scale)

Nano –

: from 1 nm to 750 nm

Micro – : from 750 nm to 750 μ m

Meso – : from 750 μ m to 15 mm

Macro - : from 15 mm

39

CRACK IDENTIFICATION CONVENTION

In the literature, the authors do not fully agree on naming the different cracking defects. Hence, the following convention based on [2], [3] is proposed to ease their identification throughout this manuscript (non-exhaustive list; hybridisations are possible):

L : longitudinal orientation 1 : crater crack

T : transverse orientation (including 2.1 : face crack

chevron) 2.2 : throat crack

O: other (branching, radiating, ...) 3: under-bead crack

4 : lamellar tear

5.1 : root crack

5.2 : root surface crack

w: weld metal 6: toe crack

b.a: base metal – heat-affected zone 7: in-bead crack

b.u : base metal – unaffected zone 8 : weld interface crack

: fusion boundary line vicinity 9 : adjacent crack

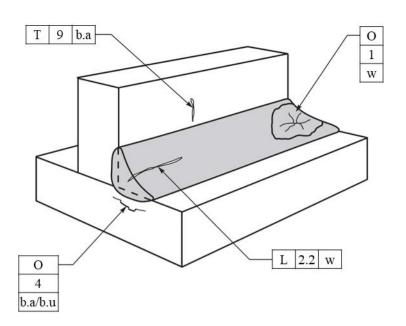
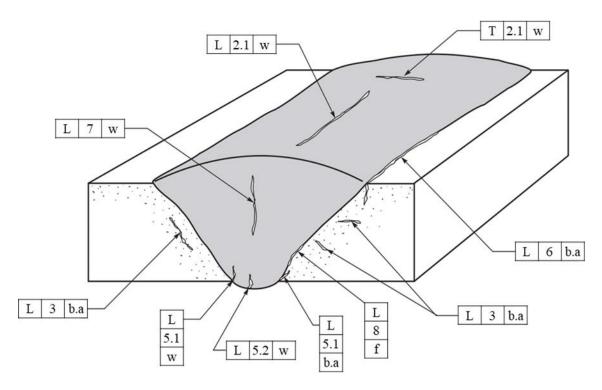


Figure -1: terminology proposal for describing cracks in weldments throughout this manuscript (adapted from [3]) – illustration A



 $\begin{tabular}{ll} Figure-2: & terminology proposal for describing cracks in weldments throughout this manuscript (adapted from [3]) - illustration B \\ \end{tabular}$

ABSTRACT

This project explores the cold cracking risks and limits for welding repair applications in low-alloy ferritic steel nuclear components. This work is part of a series of projects aimed at the codification of these repair applications using bead tempering techniques initiated by the French nuclear industry.

The first part of the project comprised benchmarking of both the Tekken and the historically used implant welding test methods, testing a welding procedure selected to undertake the repairs. An assessment of the viability of this procedure was therefore also established. A computational weld modelling study was first undertaken to size the Tekken test mock-ups and improve understanding of their metallurgical and thermomechanical behaviour. The calibration and qualification of the models required experimental data. These were produced using various instrumented small-scale thermal, metallurgical, mechanical, and chemical tests. An acceptable match between the simulations and experimental results was established. For the welding procedure selected, it was found that the level evolution of the self-restraint conditions reaches a stabilisation above a thickness of 50 mm. Then, the benchmarking of the test methods was carried out experimentally. The Tekken method led to a positive assessment of the proposed repair welding procedure. In contrast, the implant method led to a negative appraisal.

In order to inform the future development of a second, broader model allowing the risk of cold cracking to be predicted using a probabilistic criterion, an experimental study of the behaviour of the heat-affected zone exposed to hydrogen was also conducted. The results demonstrated a net loss of ductility directly attributable to the hydrogen. The hydrogen embrittlement of these microstructures was therefore quantified. Ways of mitigating these material property degradations were also identified, highlighting the benefits offered by the bead tempering techniques.

This work was carried out at the University of Manchester and at the EDF R&D laboratories at Chatou, under the sponsorship of EDF, and involved cross-Channel collaborations with several partners, especially the University of La Rochelle and the Institut de Soudure (the French welding institute).

Alexandre A. M. PAGET ORCiD: 0000-0002-3090-2414

DECLARATION

No portion of the work referred to in the thesis has been submitted in support of an application for another degree or qualification of this or any other university or other institute of learning.

COPYRIGHT STATEMENT

- The author of this thesis (including any appendices and/or schedules to this thesis)
 owns certain copyright or related rights in it (the "Copyright") and they have given
 the University of Manchester certain rights to use such Copyright, including for
 administrative purposes.
- Copies of this thesis, either in full or in extracts and whether in hard or electronic copy, may be made only in accordance with the Copyright, Designs and Patents Act 1988 (as amended) and regulations issued under it or, where appropriate, in accordance with licensing agreements which the University has from time to time. This page must form part of any such copies made.
- The ownership of certain Copyright, patents, designs, trademarks, and other intellectual property (the "Intellectual Property") and any reproductions of copyright works in the thesis, for example graphs and tables ("Reproductions"), which may be described in this thesis, may not be owned by the author, and may be owned by third parties. Such Intellectual Property and Reproductions cannot and must not be made available for use without the prior written permission of the owner(s) of the relevant Intellectual Property and/or Reproductions.
- Further information on the conditions under which disclosure, publication and commercialisation of this thesis, the Copyright and any Intellectual Property and/or Reproductions described in it may take place is available in the University Intellectual Property Policy (see https://documents.manchester.ac.uk/DocuInfo.as
 px?DocID=24420), in any relevant Thesis restriction declarations deposited in the University Library, the University Library's regulations (see https://www.library.manchester.ac.uk/about/regulations/) and in the University's policy on Presentation of Theses.

ACKNOWLEDGEMENTS

First of all, I would like to thank my thesis director, **Prof Michael C. Smith**, for his unfailing supervision throughout these years. His benevolence and kindness were always present during our conversations, unfortunately often remote due to the COVID_19 pandemic. Nonetheless, this allowed us to also descant on the level of snow cover in the alpine massif during lockdown. His experience and foresight have undoubtedly been crucial to the success of this research. I am also extremely grateful to his personal assistant, **Ms Angel Harper**, for her warm welcome when I first arrived at the University of Manchester, and her amazing support throughout these last four years. I would also like to thank my co-supervisor, **Prof John A. Francis**, for his advice and suggestions in the discussion of the findings.

Then, I would like to express my gratitude to the company EDF for having funded this research. I thank my French-English EDF supervisory team, **Dr Vincent Robin**, **Dr Jefri Draup**, **Dr Josselin Delmas**, **Dr Sofiane Hendili**, and **Mr Rafaël Ufarté**, for their great support and their scientific and technical contributions to this work, as well as for having hosted me for more than a year within the PRISME department. Thanks to them, I benefited from the expertise and numerous competencies present at EDF, as well as from the various research facilities.

I would also like to thank **Prof Xavier Feaugas** and **Dr Abdelali Oudriss** for their supervision during my work on the hydrogen embrittlement. I am extremely grateful to them for having hosted me for many months at the University of La Rochelle to carry out these investigations, but also for having provided me with a conducive and friendly working environment after the (very) long months of lockdown, curfew, and remote working. Their teaching and sharing of experience in this specific field of materials science were decisive in the success of this doctoral work.

Also, I thank **Mr Alexis Ferrari** for his numerous tips in welding engineering and for having hosted me during several weeks at the Institut de Soudure to conduct the implant test campaign.

I am grateful to the researchers of the NeT-TG8 and NNUMAN programs, as well as to the IRDL (Université Bretagne Sud), for having shared their experimental data.

Thus, due to the unexpected chain of events resulting from the COVID 19 pandemic,

I had the great opportunity and honour to conduct my research within several scientific laboratories and departments in both England and France. The MaSC and the MTRL of the Department of MACE and EDF Energy R&D (at the University of Manchester), the LaSIE (La Rochelle Université), the PRISME department (EDF R&D Chatou), the Department of Materials (the University of Manchester), and the R&D centre of the Institut de Soudure in Yutz. I would therefore like to extend my warmest thanks to all the staff and students I met there, who have often become very (very) good friends beside whom I have laboured throughout my doctoral years, and, of course, to all the people I met outside of work in these regions and during business trips. Thanks to all of you, I have extraordinary and unforgettable memories that will remain forever associated with this thesis project, especially the first post-COVID social distancing gatherings when pubs were back in business, which will undoubtedly remain forever in the memories (just beside the world war of the face masks) of the rockiest episodes of the 21st century.

I also thank the researchers I met during seminars and conferences for their exchanges and remarks, notably during the SINDRI Conference 2022, IMAT Seggau 2022, Matériaux 2022, and TMS2023.

I am grateful to the Department of Mechanical Engineering (University of Bristol) and the MMC department (EDF R&D Les Renardières) for their last-minute help in sharing their facilities to solve issues with some machine unavailability, and to all the subcontractors involved in this project, especially SEMEFIL Annecy.

I must also thank my family and friends, especially my parents, for their understanding and unfailing support in this last part of my studies. Yes, "it's now time to find a job", as my mother would say.

Finally, I cannot end these acknowledgements without having a particular thought for my cat **Chanel** and my dog **Elka** who have both accompanied me during these last 14 years and whom we sadly had to free from their suffering while writing this manuscript. I wish them a peaceful rest alongside my previous four-legged companions.

I GENERAL INTRODUCTION

I.1 PROJECT BACKGROUND & MOTIVATIONS

I.1.A The nuclear industry's role in global electricity generation

Estimated at 22 848 TW·h in 2019 by the IEA¹ [4], the world's consumption of electricity is constantly increasing. Mainly driven by the economic development of countries outside the OECD², electricity demand is expected to grow faster than any other final energy: about 2 % annually until 2035 [5]. Considering the recent climate challenges, this demand needs to be met by low- and zero-carbon technologies. Nuclear generation produces low-carbon baseload electricity and is, therefore, part of the solution. In June 2022, there were 442 power generation nuclear reactors in service across the world [6] which generated about 12 % of the entire production (2 657 TW·h) [7], plus 67 new reactors under construction. More than one-quarter of the operating reactors are in Europe, and these are one of the oldest fleets.

As one of the world's major electricity operators with 78 operating reactors on several continents [8], the EDF³ group faces some technical challenges in maintaining and modernising its fleet of nuclear power plants (N.P.P.). One of the long-term operation (L.T.O.) challenges consists of qualifying innovative methods and accrediting them with the local regulatory bodies. More precisely, the research presented here focuses on repair techniques for the nuclear steam supply system (N.S.S.S.), the central element of a pressurised water reactor (P.W.R.) – a form of light water reactor (L.W.R.).

I.1.B The pressurised water reactor : a recognised technology

Originally developed in the USA⁴ by Westinghouse, the pressurised water reactor is the most common design within the worldwide fleet: about 65 % of the in-service reactors in 2018 [9]. This is explained by the advantages of this technology in terms of

¹ International Energy Agency

² Organisation for Economic Co-operation and Development

³ Électricité De France

⁴ United States of America

safety, economic efficiency, and technical simplicity. In detail, pressurised water is used to work at high temperatures while keeping the coolant fluid in a liquid form. As a reminder, an illustration of a typical nuclear power plant architecture using this nuclear reactor design is given in **Figure I-a**. The elements forming it are [10]–[12]:

- A steam generator (group A) named "nuclear island" (N.I.), including:
 - Group B: the nuclear steam supply system (group C) surrounded for its control by the structures, systems and components (S.S.Cs.)
 - The rest, called "balance of nuclear island" (B.N.I.), includes for example the emergency diesel generators and the nuclear fuel storage pools
- A unit to convert the energy (group **D**) named "turbine island" (T.I.), including:
 - The turbo-generator system
 - The balance of the turbine island: steam condensers, cooling systems (cooling towers or seawater heat exchangers for instance), secondary pumps, etc.
- The balance of plant (B.o.P.): **installations to inject the produced electricity** (group E) into the electric power system, through a connection with the electric grid

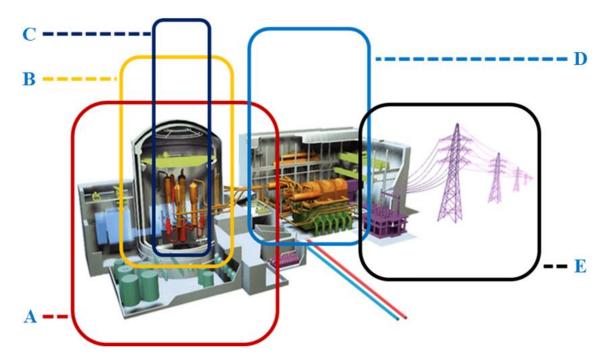


Figure I-a: general overview of a nuclear power plant using the pressurised water reactor design (adapted from [13]) $-\mathbf{A}$: nuclear island; \mathbf{B} : nuclear steam supply system & structures, systems and components; \mathbf{C} : nuclear steam supply system; \mathbf{D} : turbine island; \mathbf{E} : balance of plant

The most recent large pressurised water reactor design is the European Pressurised Reactor (E.P.R.), subsequently renamed Evolutionary Power Reactor. It was developed in France and Germany by Framatome (*ex-Areva*) and Siemens from 1989. It offers a great versatility by accepting various nuclear fuel types and is the most powerful nuclear reactor, with an electricity production capacity of 1 600 MW. A few have recently entered service worldwide, and others are under construction or at the project stage. For instance, Hinkley Point C in the UK⁵ is a twin-reactor E.P.R. project.

I.1.C The maintenance challenges

The reactor pressure vessel (R.P.V.) is the central part of the nuclear steam supply system, and is surrounded by the steam generators, the pressuriser, and the primary pumps (refer to **Figure I-b**). Thermal energy is released by nuclear fission operated in the reactor core, within the reactor pressure vessel – a nuclear chain reaction process. A pressurised heat transfer fluid (light water in the design of a pressurised water reactor) circulates over the reactor core and allows heat transport through individual loops into the steam generators. These components and all the others forming the nuclear steam supply system are exposed to significant thermal and mechanical loads, to neutronic radiation, and to a corrosive environment, among others. Hence, sometimes during the nuclear power plant life cycle, minor material degradation [14]–[17] can occur in very localised zones of the nuclear steam supply system components. As a very high level of structural integrity is expected, these must be promptly repaired to ensure safe operation of the nuclear power plant with minimal impacts on its economic efficiency [18].

⁵ United Kingdom



Figure I-b: focused view of a nuclear steam supply system (group **C**) highlighting the reactor pressure vessel (adapted from [19])

The structural elements we mainly focus on in our research are the bottom-mounted instrumentation (B.M.I.) nozzles of the reactor pressure vessel. They are featured in the design of the major part of EDF's pressurised water reactor fleet. The bottom-mounted instrumentation nozzles are usually interfaced with the reactor pressure vessel by a nickel-based alloy 182 J-groove weld (refer to **Figure I-c**). Although unprecedented in France, this component could need to be partially repaired at some point in the future, following an in-service inspection or in compliance with the maintenance program.

As for the main part of the nuclear steam supply system components, the reactor pressure vessel is made of low-alloy ferritic steel. 16MND5 (for "16MnNiMo05") is the most frequently employed grade to produce the reactor pressure vessel in EDF's pressurised water reactor fleet [20]. It is comparable, for instance, to the steel grades SFVV3, 20MnMoNi55, and SA-508 Grade 3 Class 1 (also abbreviated "A508 Gr. 3 Cl. 1") [15], [21]. It has to be remembered that the description "ferritic steel" does not mean that the metal is constituted of a pure ferritic microstructure. This description is commonly employed to refer to (very) low-carbon steels since, in actual fact, the major proportion of their microstructure is generally made of ferritic grains. Low-carbon steels are also sometimes called "plain-carbon steels" or "mild steels".

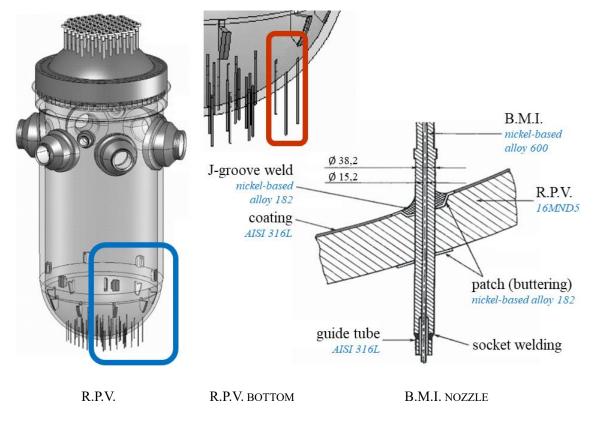


Figure I-c: focused view of a reactor pressure vessel (R.P.V.) [22] and the layout details of a bottom-mounted instrumentation (B.M.I.) nozzle (adapted from [23], [24])

To carry out a bottom-mounted instrumentation nozzle repair, without going into too many details, the nozzle replacement should lead to a fillet weld lying on an Alloy 182 patch that could then need to be repaired if defects are found. This repair would consist of removing the defect, leaving a cavity (refer to **Figure I-d**). This volume would then be re-filled with a multi-pass arc-weld. The final step would be finish machining. A summary is given with **Figure I-e**.

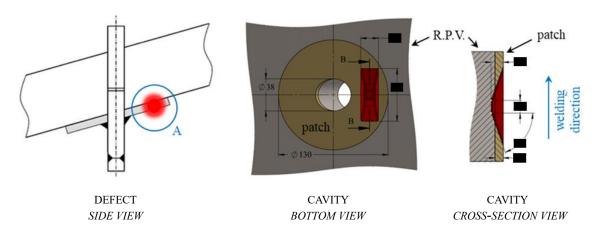


Figure I-d: example of a defect location and machined cavity before cladding with the order of magnitude of the dimensions (undisclosed information)

This process of repair by welding, called "cladding", is well-known and commonly utilised by other conventional industries. At this stage of the investigations, the considered filler metal is the nickel-based alloy 52M. Note that the repair process developed here could also be applied to other locations of the reactor pressure vessel, as well as other nuclear steam supply system components.

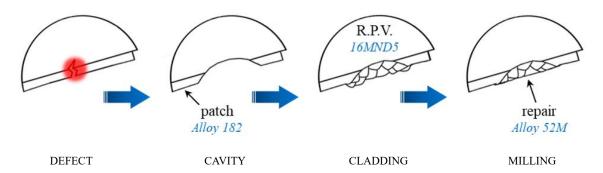


Figure I-e: detail **A** of the defect (side view – **Figure I-d**): step-by-step illustration of the repair process (adapted from [25])

I.1.D The engineering challenges

Any arc-welding process comes with many challenges that must be managed during its execution to ensure adequate quality and efficient results, especially in the nuclear industry. Arc-welding is a multi-physics and chemical process that brings the joined materials to their melting points. Thus, the welded component is exposed to significant thermal gradients, which can lead, among others, to consequent thermo-mechanical stress states and important modifications of the material properties. Furthermore, some additional effects can be highlighted. For instance, considerable chemical interactions can occur, again affecting the material properties to a greater or lesser extent. The problem turns out to be even more complex when the filler metal is different from the base metal (also called "parent metal"). This adds material interface phenomena, such as a dilution of the chemical compositions.

When the combination of these effects has substantial negative consequences, simple deformations of the component are most often observed. However, short- or long-term failure can also occur. Nowadays, the various defects that can be encountered in an arc-welding operation are relatively well-known and classified into different categories [26], [27], such as cracking, shrinkage, porosity, or creep-fatigue (an in-depth list is proposed in section **II.1.A.2**).

I.1.E The technical limits

Although this type of cladding repair can face different potential common defects, our investigations focus only on the risk of cold cracking. This defect type has been identified and studied for several decades. It is also called "delayed cracking", "hydrogen-assisted cold cracking" (H.A.C.C.), "hydrogen-induced cold cracking" (H.I.C.C.), or "under-bead cracking". It occurs in welded joints during cooling, resulting from accumulated mechanical loads and hydrogen in the heat-affected zone (detailed in section **II.1.B**).

In a conventional industrial context, during the fabrication or any repair operation when the component is removable or at least partially accessible, the cold cracking risk is generally suppressed by applying techniques consisting of additional heating(s). The most common are pre-heating, post-heating, and post-weld heat treatment (P.W.H.T.) [28]–[34]. These methods (commonly prescribed and regulated by codes and standards) can also be combined. However, sometimes the component is too large or non-removable (concrete-embedded, for instance) and difficult to access once in-service (due, for example, to other surrounding components or devices). The use of heat treatment can also be limited just by the cost [18]. Consequently, these conventional prevention methods are not always possible [35], [36]. Since it is generally embedded in concrete and is not removable, an in-service reactor pressure vessel falls into this category, with the added problem of radioactivity.

In that respect, advanced welding repair techniques have been developed since the 1960s, initially in Russia and the UK [18], [25], [37]. These are categorised as "bead tempering" or "controlled deposition" methods (refer to section **II.2.A**). They are based on the optimisation of the different bead depositions to partially reproduce the benefits of additional heat treatments thanks to the successive re-heating induced by the welding arc [29], [35], [38]–[40]. The oil and gas industry implemented these innovative methods a few decades ago [25].

In the nuclear industry, a bead tempering technique called "temper bead welding" (T.B.W. – or simply "temper bead") was positively assessed by EPRI⁶ a few years ago [18]. Following this, it has been included in North American regulatory codes [30], [41] edited by the ASME⁷ and the NBBI⁸ [25], [36]. However, not all regulatory codes have

⁶ Electric Power Research Institute

⁷ American Society of Mechanical Engineers

⁸ National Board of Boiler and pressure vessel Inspectors

I.1.F The research & development opportunities

As some of the cold cracking synonyms point out, hydrogen is a key risk factor in this cracking phenomenon [42]–[45], and is supposed to be mitigated by the bead tempering methods. However, considering different hypotheses proposed by industry and accepted by certain regulatory codes across the world, the qualification of these methods generally relies on the assumption of adequate management of the chemical phenomena: in particular, the complete control of potential hydrogen sources. Thus, most of the previous work programmes which permitted these qualifications present some areas for improvement in consideration of the role of hydrogen embrittlement (H.E.) [18] in cases where, despite all the precautions adopted, all possible hydrogen sources would not be suppressed.

This lack of knowledge constitutes a barrier to the qualification of these bead tempering methods by the French regulator ASN⁹ and their codification by the industrial association AFCEN¹⁰, editor of the French regulatory codes [33], [46]. This fact will be considered as the first conservatism throughout this thesis manuscript.

To remove this barrier and authorise deployment of these advanced techniques in France, EDF leads several research and development studies with academic and industrial partners. They cover most phenomena occurring during a welding repair operation and in various fields: residual stresses, metallurgical transformations, thermal phenomena, mechanical properties changes, chemical composition dilution, hydrogen embrittlement, modelling and simulation techniques, etc.

However, EDF did not start from zero. Some of these phenomena have been previously studied for other developments in various welding applications for several decades. The company has built extensive experience in welding testing and simulation with its partners. A previous project on multi-pass welding [47] can be particularly highlighted. It was conducted a few years ago, focusing on the mounting operation of the bottom-mounted instrumentation on not yet in-service reactor pressure vessel, involving different metals. It allowed progress in understanding and predicting the cold cracking risk for this

٠

⁹ Autorité de Sûreté Nucléaire

Association Française pour les règles de Conception, de Construction et de surveillance en Exploitation des matériels des chaudières électro-Nucléaires

application. Nevertheless, the failure criterion researched at that time was binary. This deterministic approach is not wholly appropriate for accurate risk prediction. That will be considered as the second conservatism. A probabilistic criterion could better meet these new expectations.

In addition, it has also been identified as necessary to conduct a deeper examination of the suitability of the historical – and current – welding qualification test approach specified in the French regulatory codes for nuclear applications. Indeed, despite high reliability, this approach has been commonly considered as very severe for several decades [48], [49]. On the other hand, advanced bead tempering methods are more complex and sophisticated than the traditional cladding and normal multi-pass welding processes. Furthermore, the final application targeted is also very specific and unprecedented. Therefore, it can be supposed that this historical qualification approach could be poorly representative of the real conditions. That would result in a too-restrictive evaluation for the viability demonstration of the bead tempering methods [18]. This qualification severity constitutes the third – and last – conservatism.

I.2 PROJECT AMBITIONS

I.2.A Aims and objectives

In summary, this EDF-sponsored current research project presented in this thesis aims to address the following knowledge gap: if all the physical mechanisms behind cold cracking are taken into account, thus including hydrogen embrittlement, is it possible to say whether or not bead tempering methods are worthwhile for repairing in-service reactor pressure vessels? Is it then possible to precisely quantify the risks?

Hence, the objectives to be achieved in order to fulfil this gap can be summarised as:

- To refine the computational prediction abilities and question the appropriateness of probabilistic versus deterministic criteria for cold cracking risk assessment (2nd conservatism)
- To compare different cold cracking tests and explore their relevance for evaluating bead tempering methods (3rd conservatism)
- To take part in the viability demonstration of bead tempering methods for the targeted final application (1st conservatism)

I.2.B Framework

This project was conducted at the University of Manchester. It was supported by EDF through the French team from the PRISME¹¹ department and the UK team based within the MaSC¹², co-founded centre by EDF Energy and the University of Manchester (through the Dalton Nuclear Institute). The research falls within both the SAFER¹³ project and the SINDRI¹⁴ partnership. In addition, certain parts of this research stem from two collaborations with the LaSIE¹⁵ (CNRS¹⁶ – La Rochelle Université) and with the IS¹⁷ (the French welding institute).

The software platform Salome_Meca was used for computational modelling, coupled with the finite element method (F.E.M.) code Code_Aster. Both are developed within partnerships, of which EDF is one of the main actors. The results were then visualised using an integrated version of ParaView. All are under open-source licenses. In addition, EDF's high-performance computing (H.P.C.) facilities (principally the GAÏA cluster) were used to run simulations.

I.3 THESIS STRUCTURE

First, the **literature review** chapter presents the general theory required to understand and study the cold cracking phenomenon. The major physico-chemical phenomena driving it are introduced. Then, a state-of-the-art section introduces common approaches to prevent the cold cracking risk, as well as the latest research on this phenomenon. Finally, the conclusions drawn from the literature review are summarised, and the knowledge gaps are highlighted.

Second, the **methodology and optimisation** chapter details the research methodology adopted to carry out this project. Next, the preliminary work (sub-contracted) to optimise certain welding parameters and its results are presented. Finally, the entire set of welding

¹¹ EDF R&D – département Performance, Risque Industriel, Surveillance pour la Maintenance et l'Exploitation, 78401, Chatou, France

¹² The University of Manchester – MaSC, M13 9PL, Manchester, United Kingdom

¹³ Simulation en Appui à la Fabrication Et aux Réparations

¹⁴ Synergistic utilisation of INformatics and Data centRic Integrity engineering

Laboratoire des Sciences de l'Ingénieur pour l'Environnement – Unité Mixte de Recherche n° 7356, 17042, La Rochelle, France

¹⁶ Centre National de la Recherche Scientifique

¹⁷ Institut de Soudure – centre R&D de Yutz, 57970, Yutz, France

conditions and parameters used throughout this research project is summarised.

After that, the work undertaken during the course of this research project is presented across three chapters :

- The study of the Tekken welding test was of interest to address part of the
 objectives related to the third conservatism. This work reinforced the knowledge
 concerning this type of test mock-up and identified the best dimension to use for
 the experimental benchmarking. The computational prediction abilities have been
 enhanced to meet these objectives.
- The welding test benchmarking chapter presents the experimental comparison of different cold cracking tests and explores their relevance for evaluating bead tempering methods (third conservatism objectives). In addition, these results allowed advances to be made in the pursuit of objectives linked to the first and second conservatisms (respectively, viability demonstration of bead tempering methods, and questioning the appropriateness of probabilistic versus deterministic criteria for cold cracking risk assessment).
- The behaviour study of the heat-affected zone exposed to hydrogen allowed to address part of the objectives related to the first and second conservatisms. These results were of interest to bring additional elements useful for the viability demonstration of bead tempering methods and highlighting the interest in probabilistic criteria. They will also enable the computational prediction abilities to be refined.

It must be noted that this thesis structure presents both computational and experimental results in the same chapter. That reflects the iterative approach employed in this current project between the simulation and experimental means. A detailed discussion and a specific conclusion conclude each of these chapters.

Finally, the **general conclusion** summarises these works' achievements, main outputs, and benefits to the industry.

II LITERATURE REVIEW

II.1 INTRODUCTION TO GENERAL THEORY

II.1.A Candidate welding processes

Two arc-welding processes are currently candidates for multi-pass cladding repairs. The lead candidate is gas tungsten arc-welding (G.T.A.W.), which can be executed either manually or by a welding robot. Shielded metal arc-welding (S.M.A.W.), a strictly manual process, is also being considered.

II.1.A.1 Arc-welding principles

The arc-welding principle is based on raising the temperature by using an electric arc. Its plasma column temperature usually lies between 3 500 °C and 15 500 °C [50]. This heat is used to melt and join the metal. The arc is generated with a power source creating an electrical potential drop, using either alternating or direct current (A.C. or D.C.) [51]. The parts to be welded are connected to one pole, while an electrode is wired to the second pole. The arc is usually initiated by bringing the electrode tip very close to the workpiece. This overrides the resistivity of the air (or shielding gas). Then the electrode is immediately re-positioned to the nominal adequate distance for making the weld. The electrode can either be consumable – the filler metal – or non-consumable, in which case, if a filler metal is required, it will be introduced in the molten pool independently of the electrode.

II.1.A.1.a Shielded metal arc-welding

Shielded metal arc-welding is also known as "manual metal arc-welding" (M.M.A. or M.M.A.W.), "flux shielded arc-welding", or "stick welding". This technique utilises consumable electrodes, which melt to supply the filler metal in the molten pool. The electrode is nowadays made of a flux-coated metal rod. The process was invented in Russia in 1888, using firstly a simple metallic stick [52]. Flux-coated electrodes were developed in the early 1900s. They were initially rather costly, which explains the slow adoption of shielded metal arc-welding before becoming the most common in the

following decades. After melting, the flux protects the molten weld metal from oxidation via a protective atmosphere of gas and and a surface layer of slag. An illustration is given in **Figure II-a**. The slag solidifies during cooling and must be chipped off the weld bead when the cooling is complete. This technique is quite advantageous for basic and short welds because of its simplicity, reliability, and efficiency [53]. In addition, it can be done in any position. The weld quality is highly dependent on the welder's skills, and only a few welding parameters can be adjusted.

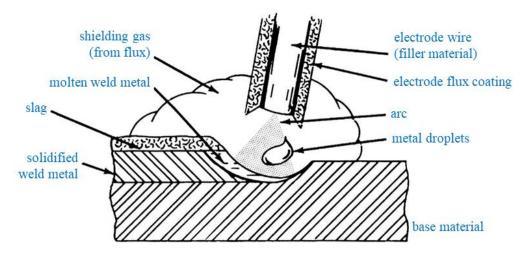


Figure II-a: schematic illustration of the shielded metal arc-welding technic (adapted from [54]– [56])

II.1.A.1.b Gas tungsten arc-welding

The gas tungsten arc-welding technique utilises a non-consumable electrode made from tungsten. It developed slowly in the early 20th century but became suddenly popularised in the 1940s for having solved issues with aluminium welds [51]. This welding process reached maturity in the 1950s, using inert or active shielding gas, with or without a filler metal. This technology is more sophisticated than shielded metal arc-welding since it offers substantially more tuning parameters concerning the protective atmosphere, the welding torch set-up, the electric current shape, the filler metal supply (when applied), etc. Nonetheless, in contrast with the shielded metal arc-welding, it cannot be done in any position. In addition, the welding torch also often requires a cooling system due to its proximity to the arc plasma column. An illustration of gas tungsten arc-welding is given in **Figure II-b**. There are two well-known gas tungsten arc-welding processes: the tungsten inert gas (T.I.G.) and the tungsten active gas (T.A.G.) welding.

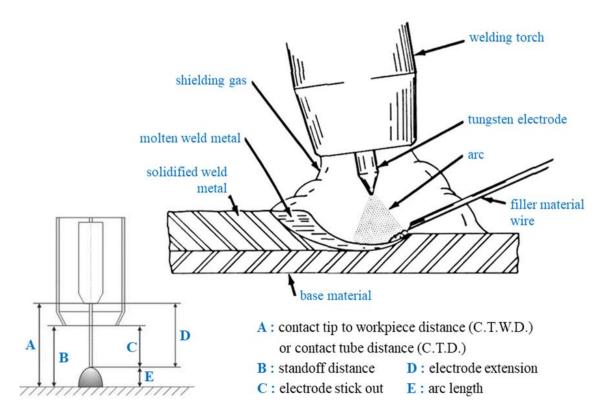


Figure II-b: schematic illustration of the gas tungsten arc-welding technics (adapted from [42], [54]–[56])

II.1.A.2 Examples of typical defects

Some examples of typical short- and long-term defects that are frequently encountered in an arc-welding operation are listed below and illustrated in **Figure II-c** (non-exhaustive list) [26], [27], [57]:

• Short-term:

- Lack of fusion (incompletely fused spots **D**)
- Slag inclusions (typical in shielded metal arc-welding H)
- Contamination of the molten pool (residual grease, oil, ... H)
- Hot cracking (**J**)
- Cold cracking (**J**)
- Weld's topologic defects (undercut (**B**), overlapping (**G**), under-filling (**A**), ...)
- Shrinkage and distortion of the welded assembly/parts
- Porosity (F)
- Solidification shrinkage (cavity)
- Poor penetration (C)
- Spatter (E)
- Excess weld reinforcement (I)

- Lamellar tearing (**J**)
- Burning through (K)

• Long-term:

- Creep-fatigue
- Fatigue cracking
- Stress corrosion cracking (J)

The defect type(s) depend on different factors. For instance, the environment, the metal(s) involved, the welder's skills, the surface preparation, the arc-welding type, the welding parameters, ... Concerning cracks (J), the most common categories are listed according to the convention used throughout this manuscript stated in **Figure – 1** and **Figure – 2** (within the **List of Conventions**).

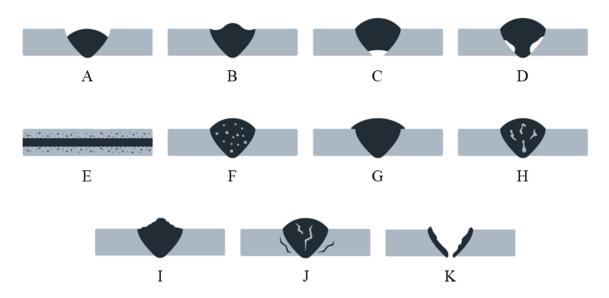


Figure II-c: schematic illustrations of some common arc-welding defects (source: [57])

II.1.A.3 The heat-affected zone

II.1.A.3.a Definition

The area particularly affected during an arc-welding operation, and thus highly sensitive to failures, is commonly called the "heat-affected zone" (H.A.Z.). It is located within the base metal, surrounding the weld metal constituting the bead. Although this area has reduced dimensions, it encompasses significant changes in the material properties caused by the considerable temperatures reached. As shown in **Figure II-d**, the heat-affected zone is usually split into different zones. Their borders are associated with

the peak temperatures encountered during welding, that cause different microstructural changes. This is easily observable, for instance, by hardness measurements or macroscopic observations after surface polishing (often followed by chemical etching).

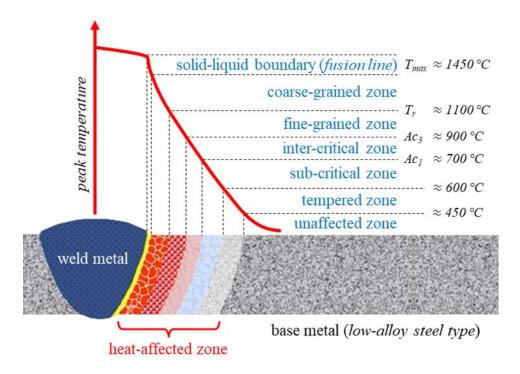


Figure II-d: macroscopic illustration of the heat-affected zone typical for a low-alloy steel weld (adapted from [58]–[61])

II.1.A.3.b Basics of metallic microstructures

The base metals commonly utilised are usually polycrystalline, so consist of multiple individual crystals, called "grains" by metallurgists [62]. The grain size may vary from nanometres to millimetres. Each grain has its own crystallographic orientation. Its atoms follow one or several ordered and specific arrangement patterns formed by repetition of a "unit cell". The latter are themselves repeated by linear translations along the principal directions of the three-dimensional space. These repetitive translations generate the "lattice" of the crystal structure, in other words, the entire grain. The vertices of the unit cells define the nodes of this lattice. The ensemble of grains, separated from each other by frontiers called "grain boundaries", form the so-called "metallic microstructure". This is summarised in **Figure II-e** and **Figure II-f**. Metallurgists define the type of microstructure micro-constituents using several criteria. For instance, in steels, the organisation within the unit cells (based on the various allotropic forms of iron – solid phases such as ferrite and austenite), the proportions of a biphasic mixture (such as pearlite and bainite), the formation of compounds (such as cementite), the detailed

morphology (lower and upper bainite, for instance), ... Furthermore, the various microconstituent types are generally regrouped into two categories depending on the temperature range. The ones encountered at ambient temperature are categorised as "cold" micro-constituents, and the others – always in solid state – existing only at high temperatures as "hot" micro-constituents.

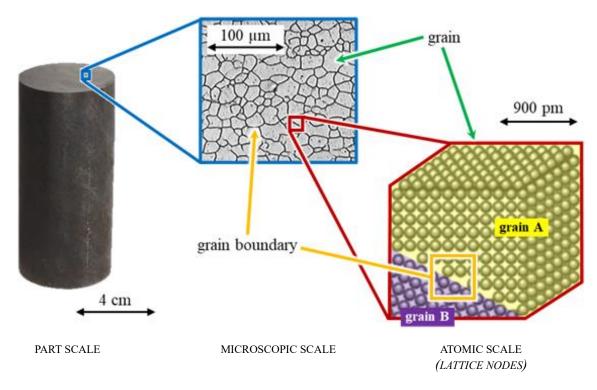


Figure II-e: illustrations summarising the definition of metallic microstructure, from a part to the lattices of a grain A and a grain B; nodes on the boundary are shared between these two grains

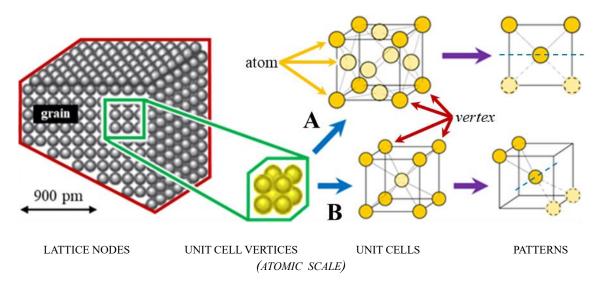


Figure II-f: illustrations summarising the definition of metallic microstructure, from the lattice to the atoms, including two examples of atomic arrangement with their respective patterns (adapted from [63], [64]) – A: face-centred cubic; B: body-centred cubic

II.1.A.3.c Formation of microstructures

The microstructure begins to form as the crystalline melted material cools. It initially consists of a "liquid-solid" phase transformation. From the liquidus temperature, crystals form around randomly dispersed internal sites (commonly called "germination" or "nucleation" steps), following a "solidification front" whose interface propagates from already solidified areas to the remaining liquid ones. These grains "grow" independently from each other throughout the cooling until their edges come into contact. This explains why they "impede" each other during their growth. They have random orientations when the temperature is uniform. Nonetheless, in the case of local heat sources, there are preferential growth orientations which often lead to an anisotropic textured microstructure with aligned grains. Furthermore, during this process, there is generally a redistribution of certain chemical elements, which can thus "segregate" and then may cause crystallisation singularities, such as crystal "dendrites" [65]. The metal is entirely in solid phases at the end of this primary microstructure formation.

Table II-A: summary of common micro-constituents existing in standard steels and some of their characteristics

name	category	stability	chemical composition	arrangement within the unit cells			
MONOPHASIC							
austenite	hot	stable	allotropic form γ of iron (γ-Fe)	face-centred cubic (F.C.C.)			
retained austenite	-	metastable	allotropic form γ of iron (γ-Fe)	face-centred cubic (F.C.C.)			
_	hot	stable	allotropic form δ of iron (δ -Fe)	body-centred cubic (B.C.C.) [66]			
ferrite	cold	stable	allotropic form α of iron (α -Fe)	body-centred cubic (B.C.C.)			
cementite	cold	metastable	iron carbide (Fe ₃ C)	orthorhombic type [67]–[69]			
martensite	cold	metastable	allotropic form α ' of iron (α '-Fe)	body-centred tetragonal (B.C.T.)			
BIPHASIC							
pearlite	cold	mixture	mainly α -Fe + Fe ₃ C	mixture			
bainite	cold	mixture	mainly α -Fe + Fe ₃ C	mixture			

Secondary microstructural transformations occur for various reasons, including changes in temperature and pressure. They are thus "solid-solid" phase transformations. More precisely, a crystalline structure can transform into a different one without passing through a liquid phase.

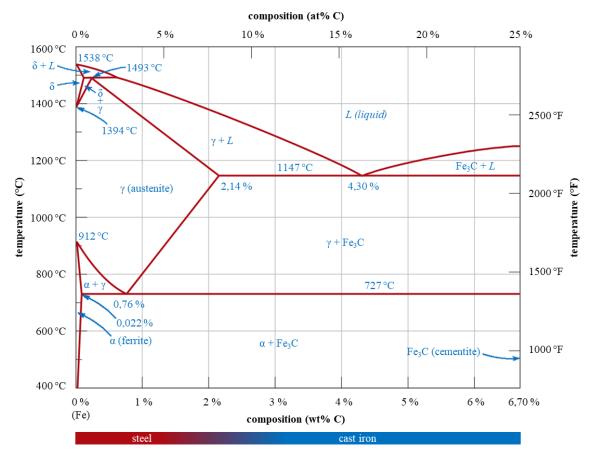


Diagram II-a: iron-iron carbide (Fe-Fe₃C) equilibrium phase diagram at atmospheric pressure (1 atm) as a function of the carbon concentration and the temperature (adapted from [70]–[72])

Therefore, during slow cooling, carbon steels first form the hot micro-constituents and then transform to the cold micro-constituents. Five phases and two biphasic micro-constituents are commonly considered, although exactly what form a steel takes depends upon its thermo-mechanical processing history. **Table II-A** summarises them and gives complementary characteristics, and the different equilibrium phase domains as a function of the carbon concentration are detailed with the iron-iron carbide (Fe-Fe₃C) phase **Diagram II-a**, commonly used for standard steels. Additional phases may be encountered at other pressure ranges, but they will not be present in the case studied. Since they usually result in mixtures of several solid phases, common steels are thus considered to be "polymorphic" [73] and "polyphase" materials. Furthermore, solid-solid phase transformations also induce discontinuous and sudden changes in density, enthalpy, and entropy. However, the magnitude of these changes is generally smaller than during liquid-solid phase transformations.

The initial microstructure of the component is generally obtained during casting. It can be tuned afterwards, for example, by hot working and/or thermal treatments to meet the desired properties. Two common tools are used to guide these options in order to obtain

the desired microstructure and mechanical properties:

- The continuous cooling transformation (C.C.T.) diagram: well adapted to uncontrolled rapid cooling (the most frequent case, including cooling after arcwelding)
- The time-temperature-transformation diagram (T.T.T. also known as "isothermal transformation" (I.T.) diagram): *utilised for usually slower and controlled cooling, such as thermal treatments*

Both are given for specific chemical composition and particular austenitic conditions (the austenite grain size having considerable impacts). They are usually determined experimentally but can also be analytically calculated using appropriate models. A schematic example of a typical continuous cooling transformation diagram for low-carbon steels, such as 16MND5 grade, is given in **Diagram II-b**.

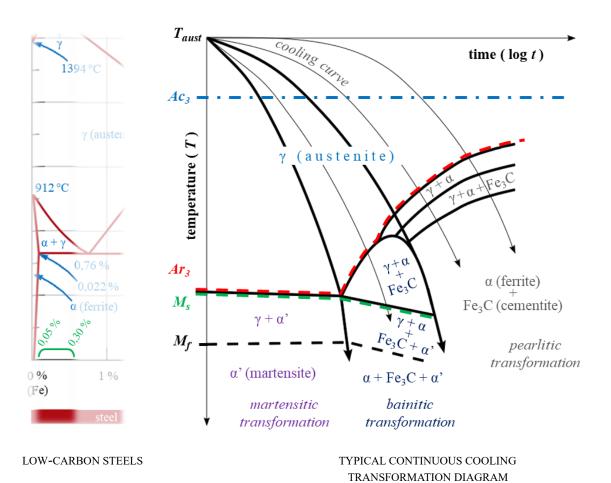


Diagram II-b: schematic example of a typical continuous cooling transformation diagram describing the liquid-solid/solid-solid phase transformations of low-carbon steels as a function of the cooling rate [74], [75] (adapted from [58])

The principal interest in obtaining the targeted micro-constituents, morphology, and grain size, or at least knowing them accurately, lies in the fact that they play a significant role in defining the material properties of a given alloy. Indeed, each micro-constituent has its own characteristics. Concerning standard steels, ferrite is known for having a lower yield strength (also known as "yield point" or "elastic limit") and hardness, and higher ductility, impact toughness and fracture toughness, while it is the opposite for the cementite and martensite. In addition, the crystals' size may also impact the material properties of the metal [76]. It is defined during the germination steps (liquid to solid phases). Therefore, it refers principally to the prior austenite grain size (P.A.G.S.), and sometimes, to some extent, to the prior δ -Fe grain size. For instance, the coarseness of the martensite, which is therefore dependent on the prior austenite grain size, will affect its hardness. In most applications, obtaining a resilient, ductile, and tough metal is preferable.

Concerning the main mechanisms of the austenitic decomposition illustrated in the continuous cooling transformation **Diagram II-b**, they can be summarised as follows:

• Ferritic transformations:

Low-carbon steels contain from 0,05 wt% up to 0,30 wt% of carbon. As shown in the phase **Diagram II-a**, when the carbon concentration exceeds 0,022 wt%, pure ferritic microstructures cannot form. Indeed, even small quantities of carbon atoms – easily dissolved within the large interstitial sites of the austenite face-centred cubic unit cells at this stage [77] – cannot entirely desorb from the material before the formation of ferrite's body-centred cubic unit cells – whose interstitial sites are too small to host the remaining atoms of carbon freely. Consequently, cementite and/or martensite form to "store" them (refer to **Figure II-g**). That is why plain ferritic transformations do not figure in this continuous cooling transformation diagram.

• Pearlitic transformations:

At sufficiently slow cooling rates, diffusion of the solute atoms, such as carbon, can occur over relatively large distances (several inter-atomic distances [78]). This facilitates precipitation and, thus, the formation of cementite compounds. Hence, most of the carbon is absorbed in the cementite, and the remaining iron atoms can form ferrite. Therefore, layers of ferrite and cementite alternate, a typical pearlite microstructure.

• Bainitic transformation:

Under intermediate cooling rates, diffusion of the solute atoms is limited to short distances only. It results thus only disseminated particles of cementite with aggregates of thin platelets, laths, or needles of ferrite, forming the typical microstructure of bainites. However, during the last stages of so-called "bainitic transformations", the formation of bainite often ends up being out-competed by martensite formation.

• Martensitic transformation:

At rapid cooling rates, the diffusion of solute atoms is significantly disrupted. Therefore, it is often referenced as a "diffusionless transformation" – and thus without the formation of precipitates. Consequently, cementite compounds cannot form. The carbon atoms remain thus trapped within the newly created iron unit cells. Instead of being body-centred cubic type (α -Fe), the latter "expands" in highly strained body-centred tetragonal type (α '-Fe). Generally, this induces shear stresses within the lattice of the crystals (acting inside the material, categorised as "internal stresses"), and generates numerous defects between them – principally "dislocations" (often symbolised \bot in schematic representations). The processes applied to deliberately produce martensite are commonly termed "quenching".

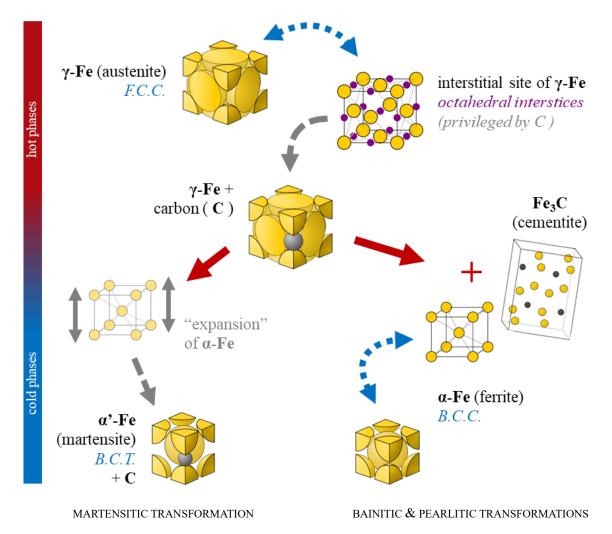


Figure II-g: schematic illustration of the carbon solubility within austenite [77], and the resulting two ways of its decomposition into cold phases for standard low-carbon steels (adapted from [64], [79])

In addition to the carbon concentration and the cooling rate, the rest of the metal's chemical composition can also have a key role [80], even in tiny quantities. Certain alloying elements can facilitate the formation of martensite, such as boron, for instance. Therefore, it is necessary to establish a method to easily quantify the ease of martensite formation for a given steel. Since martensite is the main hard micro-constituent within standard steels, metallurgists have introduced the notion of "hardenability". It is usually expressed through the "carbon equivalent" value [81] (noted CE). Since the iron-carbon system is better understood than any other iron-alloy system, the concept is to convert the percentage of the main other alloying elements to an equivalent percentage of carbon. In some ways, this conversion weighs the impact of a certain range of other elements regarding the reference element [82] (here, the carbon). Hence, the higher the CE value, the better the hardenability. The original formula (II-1) to calculate CE was defined by Dearden and O'Neill [83] in about 1940. Thereafter, several other formulas were proposed to adapt different cases.

[83]
$$CE = C + \frac{P}{2} + \frac{Mn}{6} + \frac{Mo}{4} + \frac{Cr + V}{5} + \frac{Ni}{15}$$
 (II-1)

Lastly, it has also been reported that other factors may also encourage martensitic transformations. For example, inclusions (that promote the nucleation of intergranular ferrites) or large austenitic grain sizes increase the hardenability.

II.1.A.3.d Arc-welding & microstructure modifications

As in thermal treatments, metal microstructures are modified by the heat generated by arc-welding and subsequent cooling. Solid-liquid-solid(-solid) phase transformations occur in the molten area, forming the "weld metal" zone, while in the base metal, only solid-solid phase transformations occur. Nevertheless, base metals are generally more impacted than filler metals. Indeed, filler metals are usually chosen specifically for the arc-welding conditions and the application case, with material properties that can thus accommodate the consequences well. In contrast, base metals are generally selected for material properties that are most suitable for the targeted end use of the component. Therefore, that is why the heat-affected zone is often the most weakened.

The thermal cycle encountered by the material during an arc-welding operation is principally defined by the following [59], [84]:

- *The level of thermal diffusivity*: Dependent on the thermal conductivity, density and specific heat capacity of the matter. These values are temperature-influenced.
- *The initial temperature of the base material*: The lower this temperature, the higher the cooling rate. The initial temperature is often raised by pre-heating.
- The linear heat input generated by the electric arc: The lower the linear heat input, the less the temperature surrounding the weld is heightened. The cooling rate is therefore increased. The heat input per unit of length Q_{linear} [J/mm] is calculated by multiplying the linear arc energy E_{linear} [J/mm] by a thermal efficiency factor [85] (noted η). The latter varies depending on the welding process used. According to standard EN 1011-2 [86], this is 0,8 for the shielded metal arc welding and 0,6 for the tungsten inert gas process. This is summarised in formulas (II-2) and (II-3), where U is the welding voltage [V], I the welding current intensity [A], and v the welding torch travel speed [mm/s].

- *The base material thickness*: The more massive the part, the greater the conduction phenomenon removing heat from the heat-affected zone. The cooling rate is therefore increased again.
 - The peak temperature value and related holding duration: These significantly influence "austenitisation" phenomena, particularly grain growth within the heat-affected zone. The higher the temperature and the longer the duration, the coarser the prior austenite grain size. This explains why austenite grains are bigger close to the "fusion boundary" (the frontier line between the weld metal forming the bead and the base metal) and finer in the remote heat-affected zone ("fine prior austenite grain size" and "coarse prior austenite grain size" are thus frequently employed terms, leading to the terminology "fine-grained heat-affected zone" (F.H.A.Z. or F.G.H.A.Z.)).

[86]
$$E_{linear} = U \times \frac{I}{v}$$
 (II-2)

[86]
$$Q_{linear} = \eta \cdot E_{linear}$$
 (II-3)

From the welders' point of view, the decisive cooling interval in the heat-affected zone's microstructure definition is usually considered from 800 °C to 500 °C [87] (occasionally from 700 °C to 300 °C). Therefore, they often refer to the $t_{8/5}$ duration (for "time from 800 °C to 500 °C") to reflect the cooling rate over the heat-affected zone following the weld completion. The standard EN 1011-2 [86] describes different $t_{8/5}$ formulas depending on the weldment configuration. In addition, they have also transposed the metallurgists' notion of hardenability: they prefer to use its opposite, which they call "weldability". Hence, it reflects the risk of forming a hard and brittle microstructure in the heat-affected zone of the weld. In standard low-carbon steels, it nearly always reflects a transformation into a mixture of bainite and martensite. Therefore, the higher the CE value, the poorer the weldability. To simplify and standardise the CE calculation by welders, the IIW¹⁸ proposed in the 1960s a specific version (symbolised CE_{IIW} , refer to formula (II-4)) which is now incorporated into most the standards and codes [88].

[88]
$$CE_{IIW} = C + \frac{Mn}{6} + \frac{Cr + Mo + V}{5} + \frac{Ni + Cu}{15}$$
 (II-4)

¹⁸ International Institute of Welding

[89]
$$CE_{Gra} = C + \frac{Mn + Si}{6} + \frac{Cr + Mo + V}{5} + \frac{Ni + Cu}{15}$$
 (II-5)

A couple of years after, Graville [90] introduced an additional post-processing method of the equivalent carbon content value [82], [91]. His approach compares the CE value to the carbon content percentage alone. To do so, he defined the **Diagram II-c** with several zones indicating different degrees of weldability. Hence, he also proposed his own version of the CE formula, noted CE_{Gra} (formula (II-5)).

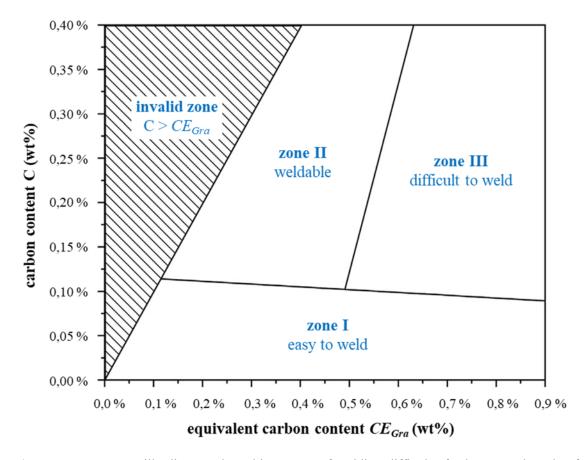


Diagram II-c: Graville diagram demarking zones of welding difficulty for base metal made of steel [90] (adapted from [89])

II.1.B Cold cracking

II.1.B.1 Phenomenon description

Cold cracking. is a common arc-welding defect. It occurs at relatively low temperatures, during the final cooling of the weldment to ambient temperature, the start threshold being about 200 °C [92], thus within solid phases. Depending on the component size, the material properties, the welding parameters used, the potential additional operations (pre-heating, for example), and the environmental conditions (for instance,

ambient temperature, season, inside/outside, draught(s), ...), etc., up to 48 hours can be necessary to complete the final cooling [42], [93], [94]. Therefore, in practice, cold cracking can happen from a few seconds after the weld completion and can arise until the weldment reaches ambient temperature, potentially several days [87]. Cold cracks generally do not have oxidised surfaces, confirming that they form at low temperatures [84].

II.1.B.2 The failure mechanisms

Cold cracking is considered as a local fracture of the weldment. It occurs under different fracture modes (illustrated in **Figure II-h**):

- Intergranular fracture especially with low-alloy and high-carbon steels (cracks following the grain boundaries)
- Transgranular fracture especially with carbon-manganese (C-Mn) steels (cracks crossing the grains)
- Or a mixture of both

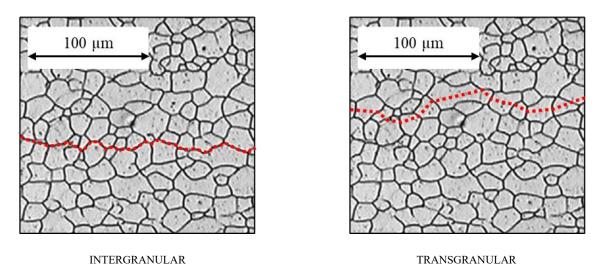


Figure II-h: illustration of an intergranular and a transgranular crack paths [95]

It generally initiates in the heat-affected zone (parent metal), and may extend into the bead (weld metal). However, sometimes, it also initiates directly in the weld metal [84]. The location depends on the material properties and chemical compositions. Moreover, it can occur in ferritic steels despite their high ductility. The crack itself generally does not branch, being essentially planar, and following a "jagged" path. When cold cracking

occurs in the heat-affected zone, the crack is normally oriented parallel to the fusion boundary. The most common crack categories associated with cold cracking are shown in **Figure II-i**, based on the convention used throughout this manuscript stated in the **List of Conventions**, and some snapshots of root cold cracks are given as examples in **Picture II-a**.

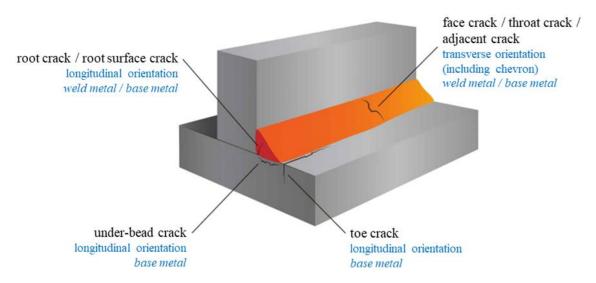
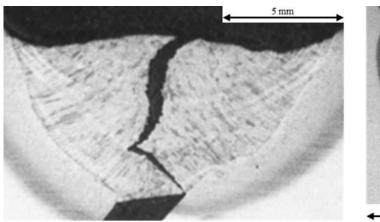


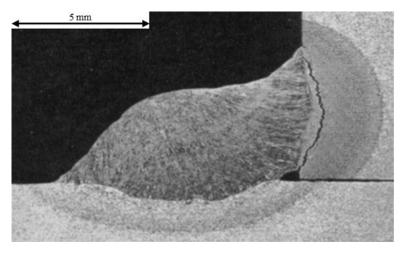
Figure II-i: schematic illustration of the most common crack categories produced by cold cracking (non-exhaustive list; hybridisations are possible; cracks would not be expected to occur in the same weldment; according to the convention used throughout this manuscript) – adapted from [84], [96]

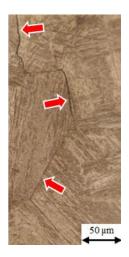


5 mm

IN WELD METAL

FROM HEAT-AFFECTED ZONE TO WELD METAL [97]





IN HEAT-AFFECTED ZONE

MAGNIFIED VIEW

Picture II-a: examples of root cold cracks occurring in different configurations and zoomed view of a tiny intergranular cold crack in a heat-affected zone (sources: from public illustrations, literature and experiments carried out during this research project)

II.1.B.3 The causes

Three main factors are behind the occurrence of cold cracking. It is a combination of the material properties, the loading, and the chemical perturbations acting on the weld. The importance of each factor depends on the proportion of the other two. More precisely, as shown in **Diagram II-d**, this is expressed by the following [42], [45], [91], [98]:

- Formation of low-ductility microstructure(s)
- Presence of a certain content of hydrogen
- Application or generation of consequent mechanical loads (tensile stresses)

Since an hydrogen embrittlement phenomenon involves in this cracking defect, the

cold cracking is thus included in the family of hydrogen-assisted cracking (H.A.C.) [99]–[101].

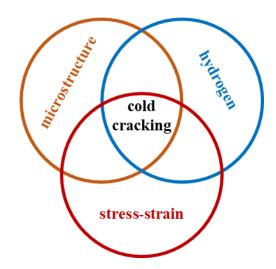


Diagram II-d: the three main physico-chemical factors involved in the cold cracking phenomenon

II.1.C Focus on the cold cracking factors

II.1.C.1 Coupling phenomena

Before going into further details, it is essential to highlight the coupling occurring between the factors. Indeed, as shown in **Diagram II-e**, a number of couplings interact within each pair of factors (including temperature, which is an indirect cold cracking factor). This seriously complicates study of the cold cracking phenomenon since it is difficult to properly isolate a factor to investigate its impact. That is why the prediction and control of this defect type remains a challenging task. Some of these couplings will be discussed below. In addition, although it is an indirect factor, it is should be remembered that most of the material properties are temperature-dependent.

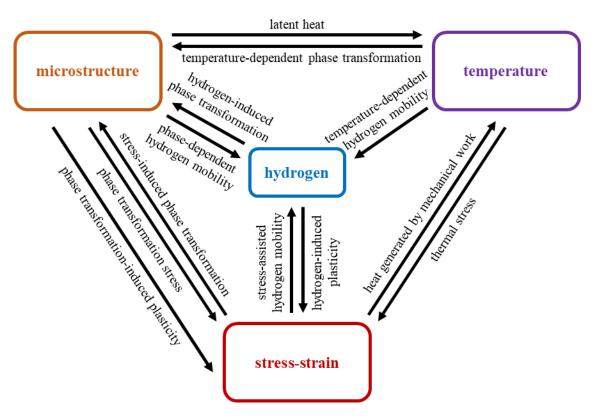


Diagram II-e: illustration highlighting the numerous couplings within each pair of factors [48], [101]–[108] including the temperature (an indirect factor) – *non-exhaustive list*

II.1.C.2 Kinetics of occurrence

The order of occurrence of the three factors following an arc-welding operation has been studied and discussed in the literature, and not only by research focussed upon cold cracking.

It should first be remembered that the peak temperature is reached during the passage of the welding torch, in the area below the electric arc producing metal fusion. Cooling begins quasi-instantly after rapid solidification and crystallisation of the molten weld metal. Since distances are relatively short within the weld zone, diffusion of heat and subsequent cooling occur quasi-simultaneously and evenly at any location. Hence, this explains why the weldment usually entirely returns to a temperature of a few hundred degrees Celsius, typically about 500-300 °C, shortly after the weld torch passage. after this a decrease in the cooling rates is generally observed. The final microstructure of the weldment is set by the whole thermal cycle, particularly the high-rate cooling experienced in weld bead and heat-affected zone. In the base metal, these modifications generally result in a ductility drop within the heat-affected zone, in other words, in transformation into brittle microstructures.

The highest hydrogen concentration is reached more or less concurrently with the peak temperature [109]. However, hydrogen is principally located within the bead (weld metal) at this stage. This emphasises that primary hydrogen absorption is a local phenomenon, occurring in the molten weld metal. After this, hydrogen mobility is complex. Depending on the conditions, it can be a mixture of atomic and/or molecular diffusion (including its transfer from the solidified weld metal to the base metal), trapping, transport, recombination, and effusion [47], [99], [110]–[113]. These phenomena can locally occur at different times and rates. This explains why the dynamics of hydrogen mobility are not uniform within the different areas of the weld, and can evolve significantly over time following the primary absorption. Therefore, discontinuous distributions of hydrogen from the primary source location may result. An example of these dynamics is given in Diagram II-f [109]. The hydrogen concentration also being a source of embrittlement in metallic microstructures [114], [115] (hydrogen embrittlement), double embrittlement of certain weld areas may then be observed.

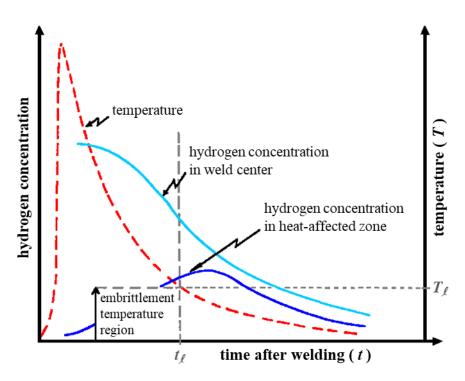


Diagram II-f: evolution of temperature versus hydrogen concentration in the weld centre and the heat-affected zone after welding completion (adapted from [109])

Tensile stresses within the weldment normally develop in the later stages of cooling, below about 300 °C [116]–[118]. **Diagram II-g** illustrates this. The rise in tensile stress can be delayed, depending upon when final cooling takes place, and this is influenced by component size, welding process parameters and pass sequencing, material properties, and operations such as pre-heating.

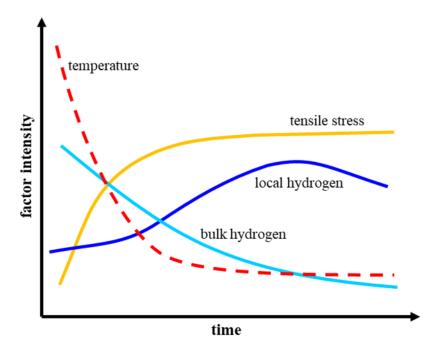


Diagram II-g: evolution of tensile stress, temperature and hydrogen concentrations as a function of time after welding completion (adapted from [116], [117])

Hence, we observe:

- Microstructural changes largely occur prior to the final tensile stress increase
- Depending on the base/filler metal combination, the hydrogen embrittlement can
 overlap either the microstructure changes or the tensile stress increase or both;
 some general observations:
 - The microstructure modifications are usually the first to occur from the heat-affected zone point of view [109], [116]–[118]
 - In the weld metal, the hydrogen peak concentration can occur simultaneously (or even prior) to the microstructure changes [109]

II.1.C.3 A critical microstructure

II.1.C.3.a Identification history

Although hydrogen and mechanical loading factors were quickly identified as driving the cold cracking phenomenon, the importance of the microstructure type as such was only generally recognised in the 1980-90s. Indeed, although it was rapidly understood that a third influencing factor was necessary to explain the occurrence of cold cracks, researchers still needed to agree on what to use. Hence, several assumptions based on

material mechanical parameters were proposed [119], [120], such as the hardness, the elastic limit, the ultimate tensile strength (U.T.S.), the toughness, ...

However, over the years, it has been concluded that using material mechanical parameters to define this third factor is inappropriate since they can vary significantly between the various metals in which cold cracking can be encountered. Therefore, they cannot be universal [100]. Finally, it has emerged that the microstructure in its entirety that should be used to express this remaining factor [120]–[122]. This includes, among other aspects, the crystalline lattice structure and the grain size. It is thus a relatively universal criterion. Paradoxically, as shown previously in **II.1.C.2**, despite being the last to be identified, the susceptible microstructure is the first feature to be established.

II.1.C.3.b Microstructure in cold cracking occurrence

Both weld and base metal microstructures are important. However, as stated previously (II.1.A.3.d), filler metals can be tailored to ensure the weld metal is more resistant to cold cracking. Thus, filler metals made of nickel-based alloys and stainless steels, commonly used in some reactor pressure vessel welds, are well known to be generally resistant to cold cracking. However, even when these fillers are used, the base material is still low-alloy steel, so its susceptibility must be carefully assessed. Indeed, it was empirically concluded in [119] that low alloy steels are susceptible to forming microstructures sensitive to the occurrence of cold cracks when their equivalent carbon content *CE* exceeds about 0,43 wt%. The carbon equivalent of 16MND5 is about 0,586 wt% when calculated according to the formula (II-4). Thus, it must be considered relatively susceptible to this type of defect in the presence of hydrogen.

Given that the equivalent carbon content is an indicator of hardenability, it is suggested that hard micro-constituents contribute to making the microstructure susceptible (refer to **Figure II-j**). Moreover, this steel is classified as difficult to weld by the *CE* analysis method proposed by Graville [90] (zone III of **Diagram II-c**). However, other microstructural characteristics must be considered to quantify the importance of this factor. Examples include:

• Any crack propagation in polycrystalline materials is generally significantly inhibited when evolving within fine-grained microstructures (**Figure II-j**). This is explained by the fact that the crack needs to change direction more frequently [123],

representing an additional energy dissipation. This crack propagation resistance is usually expressed with the fracture toughness parameter. This partly explain why cold cracks generally originate and evolve mainly in coarse-grained regions [84], such as the heat-affected zone area close to the fusion boundary.

- It has been established that grain boundary ferrites (symbolised GB-α) also contribute to the weakening of the microstructure [124]. Indeed, [125] experimentally observed that plastic deformation accumulates and initiates microcracks within the ferrites on the prior austenite grain boundaries.
- Due to complicated couplings, strain can also embrittle low-carbon steel microstructures. For instance, a phenomenon known as "strain-ageing" can occurs when certain conditions are met. This is explained by the diffusion of interstitial solute atoms, such as carbon and nitrogen, to dislocations [126], [127].

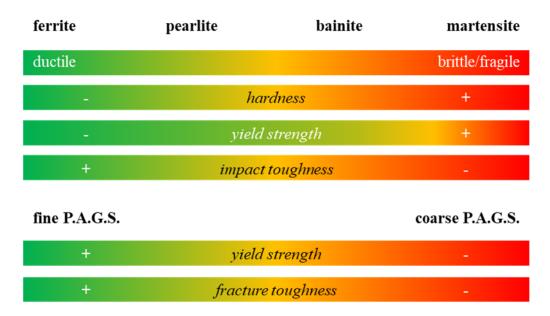


Figure II-j: illustration summarising the main microstructure characteristics

In the case of multi-pass welding, the successive re-heating of the weld-affected microstructures by the next runs generally induce beneficial effects on the microstructure. Indeed, they may reproduce specific mechanisms of common types of thermal treatment. Some of them can be highlighted, for instance:

• *Recovery* (moderate temperatures):

Going into an advanced description of the plasticity phenomenon, it represents the storage by grains of deformation energy by creating dislocations in their crystalline structure, which is then reflected by permanent deformations. It is these defects that

the thermal treatment of "recovery" repairs by making them spontaneously mobile. Indeed, this allows them to eliminate themselves as well as the associated internal stresses, either by moving to a free-surface of the material, or by moving to a grain boundary, or by aligning and forming a "tilt boundary" – which reflects a low misorientation grain boundary [127], sort of sub-boundary. These mechanisms do not induce further distortions of the material or modification of the grain size and shape (no austenitisation). Therefore, the affected portion of the heat-affected zone can lower its hardness and regain ductility.

• **Tempering** (moderate temperatures):

During the beginning of the tempering of quenched microstructures, the carbon atoms can migrate and start to precipitate into crystallographic defects (such as dislocations). Consequently, martensite – which is metastable – is decomposed into ferrite and transition carbides [127], [128]. In addition, depending on the chemical composition of the steel, particularly the carbon content, some of the austenite does not transform into martensite during the quenching, even at temperatures below the martensitic transformation finish threshold (M_f) . This constitutes so-called "retained austenite". Hence, in parallel to the martensite decomposition, part of this retained austenite converts into a sort of bainite, containing also transition carbides in place of the usual and stable cementite. Finally, after a combination of sufficient temperature and length of time, the tempering completes with the precipitation of the generated transition carbides into cementite [127]. As in the recovery, there is no change of the grain size and shape (no austenitisation). Therefore, the part of the heat-affected zone undergoing tempering effects can – again – reduce its hardness and regain ductility. However, there are two important points to note about tempering:

- All the martensite would completely convert if the tempering is carried out for too long and/or at an excessive temperature.
- Sometimes, at some point in the progression of the expected beneficial mechanisms of tempering, abnormal embrittlement phenomena can be observed during a small and specific temperature interval [127]:
 - Indeed, some impurities such as phosphorus, tin, arsenic and antimony can segregate/migrate to prior austenite grain boundaries and then initiate weak spots within the polycrystalline structure [129], [130]. This is called "temper

embrittlement" (T.E.) or "two-step embrittlement" (reversible).

- A second phenomenon known either as the "tempered martensite embrittlement" (T.M.E.), "one-step embrittlement", or "350 °C / 500 °F embrittlement" can be observed (irreversible). This degradation mechanism is thought to result from several mechanisms proposed throughout the scientific community, including retained austenite decomposition to ferrite and cementite, cementite coarsening, and the mechanical-induced transformation of retained austenite into martensite [128], [131], [132].

• Annealing (significant temperatures):

This is a three-stage process [127], including recovery as the first step during the temperature rise. After that, when a certain critical temperature is reached, the grains start to reform. This activation temperature varies with both the chemical composition and the initial microstructural conditions (principally initial grain size and their strain level), but it is always above the austenitisation temperature (T_{aust}). This second stage is known as re-crystallisation (assimilated as a re-austenitisation in the case of low-alloy steels). Hence, new grains will nucleate, essentially from the grain boundaries [78], free of any strain, grow, and thus replace the initial grains. In a certain manner, the microstructure would return to a state of equilibrium. This second stage completes once the annealing has been held for a sufficient time (depending mainly on the temperature and the initial grain size [78]). The ratio between holding duration and temperature is commonly quantified with the recrystallisation temperature (T_r), which corresponds to 50 % re-crystallisation in 1 hour [127]. T_r is generally between 0,3 and 0,6 melting temperature T_m (depending again on the chemical composition and the initial conditions). After these two first stages, the controlled cooling could be started, avoiding excessive grain growth, and driving subsequent solid-solid phase transformations. The metal would significantly recover its ductility and lower hardness. Nevertheless, if the annealing is continued for a while, it can enter the third stage, where the grains would continue to grow and become coarser, at the expense of some other recrystallised grains in their neighbourhood. However, this stage would re-deteriorate the mechanical properties of the metal, such as its toughness. Usually, the part of the heat-affected zone subject to annealing effects only encounters the two first stages. It can generally refine its prior austenite grain size [76], reduce its hardness and regain ductility.

In addition, these beneficial effects on the microstructure and mechanical properties are coupled with other mitigations, such as reduction in hydrogen embrittlement. and the relief of residual stresses. This will be described in the specific sections **II.1.C.4.e** and **II.1.C.5.e**. However, successive re-heating can also induce detrimental effects. For instance, a well-known phenomenon named "quench-ageing" can be observed at low reheat temperatures [133], and could lower the ductility of a part of the heat-affected zone. This phenomenon can be explained by a few different mechanisms [134]. The transformation of a part of the cementite into unstable carbides and the precipitation of nitrides are among the most known [126].

II.1.C.4 Hydrogen embrittlement

The changes induced by hydrogen exposure were identified early in iron and steels, during the second half of the 19th century [115]. It is usually observed that hydrogen can lead to more or less significant deterioration of metals. This is related to the hydrogen embrittlement phenomena. Depending on their degree of sensibility to hydrogen embrittlement, **Table II-B** proposes a ranking of some common types of metals and alloys.

Table II-B: classification of some metals and alloys as a function of their susceptibility to hydrogen embrittlement (source: [135])

susceptibility ranking	material examples	
high	high-strength steels at high-yield strength	
	high-strength nickel steels	
	medium-strength and low-strength steels	
	iron-silicon monocrystals	
	cobalt alloys	
low	stainless steels (such as AISI 310 or AISI 304)	
negligible or non-existent	copper alloys	
	stabilised stainless steels	
	aluminium alloys	
	molybdenum	

II.1.C.4.a Adsorption, desorption

Hydrogen can be present in the vicinity of metal surfaces in either gaseous or liquid

states. Hydrogen alone is unstable in its atomic form (H) at normal pressure and temperature. Therefore, it is always associated with (an)other atom(s), forming molecules. However, only atomic hydrogen can be dissolved into the crystalline structures of metals. Hence chemical reactions must occur to liberate the hydrogen atoms.

In the "pure" gaseous form, the hydrogen atoms are available only in pairs, commonly termed molecular hydrogen or dihydrogen (H_2) or diatomic hydrogen. In that case, as described by formula ($\mathbf{H-6}$) (Tafel's reaction), H_2 is first dissociated and adsorbed at the surface into its atomic form (H_{ad}).

[136]
$$H_2 \rightleftharpoons 2 H_{ad}$$
 (II-6)

Additionally, hydrogen can also be available within vapours of various substances. An evident example is the neutral water molecule H₂O in gaseous form. Hence, H₂O molecules can be reduced according to Volmer's reaction described by formula (II-7) into H_{ad} atoms and hydroxide ions OH⁻ (forming basic solutions).

[110]
$$H_2O + e^- \rightarrow OH^- + H_{ad}$$
 (II-7)

In liquid forms, the hydrogen may be available for adsorption, for instance, within aqueous acidic electrolytes (such as hydroxonium ions, symbolised H₃O⁺ or simply H⁺), or obviously within neutral liquid water, H₂O. In the case of the latter, the same Volmer's reaction given in (II-7) applies. Concerning H₃O⁺, another Volmer's reaction occurs (refer to formula (II-8)), reducing it into H₂O and H_{ad}. Subsequently, the produced H₂O can also be reduced as described before.

[110]
$$H_3O^+ + e^- \rightarrow H_2O + H_{ad}$$
 (II-8)

Nevertheless, in general at this stage, the adsorbed atomic hydrogen tries first to recombine with (an)other atom(s), either by reverse Tafel's reaction (formula (II-6)) or by Heyrovsky's reactions (some examples given in formula (II-9) and formula (II-10)), and then desorb from the metal's surface.

[110]
$$H_{ad} + H_3 O^+ + e^- \rightarrow H_2 + H_2 O$$
 (II-9)

[110]
$$H_{ad} + H_2O + e^- \rightarrow H_2 + OH^-$$
 (II-10)

II.1.C.4.b Absorption, diffusion, trapping

The recombination process can be inhibited, allowing the adsorbed atomic hydrogen would be preferentially absorbed into the bulk metal to recover stability.

[110]
$$H_{ad} \to H_{ab}^+ + e^-$$
 (II-11)

Hydrogen is the smallest atom known. Thanks to this low atomic radius $(5,3\cdot10^{-2} \text{ nm})$, the adsorbed hydrogen atom (H_{ad}) can easily penetrate the crystalline structure a metal [117] (absorption process). To do so, it releases an electron e^- – it results thus a surplus proton p^+ in the absorbed atomic hydrogen [106], which is temporarily under an ionic form (H_{ab}⁺) – and then bound with another atom of the metal (refer to formula (II-11)). The capacity of hydrogen absorption by a given material is only limited by solubility.

Table II-C: summary of the most common sites where hydrogen can transit/nest within polycrystalline structures [110], [136]–[138]

geometry	orientation	scale	content form	examples
0D	point	lattice	absorbed atom	vacancies, interstices
1D	linear	lattice	absorbed atom	dislocations
2D	planar	microstructure	atom/molecule reservoi	r grain boundaries, twin boundaries
3D	volumetric	microstructure	molecule reservoir	micro-voids, pores, micro-cracks, precipitates

Afterwards, the absorbed hydrogen atoms (H_{ab}) diffuse deeper into the bulk material. They can even be transported, especially by mobile dislocations. Generally, a certain part of the hydrogen content is trapped during the diffusion process.

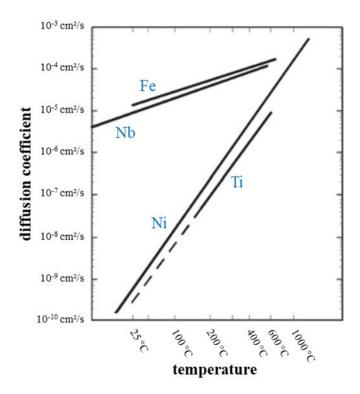


Diagram II-h: examples of overall diffusion coefficients of hydrogen as a function of temperature in iron α -Fe and niobium (body-centred cubic unit cells), nickel (face-centred cubic unit cells), and titanium (hexagonal close-packed (H.C.P.) unit cells) – adapted from [113]

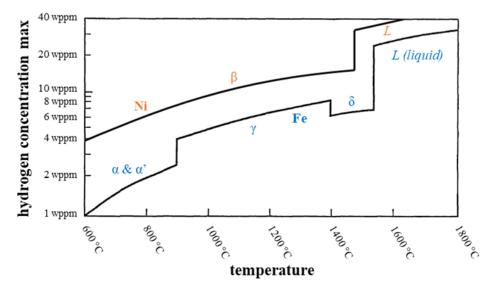


Diagram II-i: solubility of hydrogen in pure nickel and iron as a function of the allotropic form and the temperature (α-Fe & δ-Fe: body-centred cubic; β-Ni & γ-Fe: face-centred cubic; α'-Fe: body-centred tetragonal – solubility in body-centred tetragonal assumed to be the same as in body-centred cubic) at 1 atm pressure of H₂ (adapted from [139], [140])

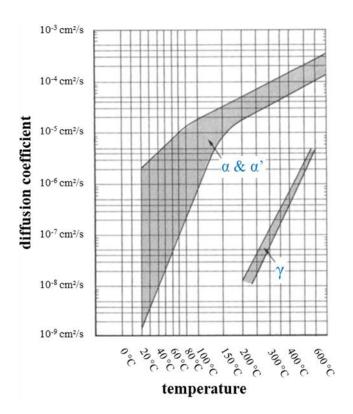


Diagram II-j: focus on the overall diffusion coefficients of hydrogen in steels as a function of the temperature and the allotropic form of iron (α-Fe: body-centred cubic; γ-Fe: face-centred cubic; α'-Fe: body-centred tetragonal – diffusivity in body-centred tetragonal assumed to be the same as in body-centred cubic) – adapted from [98]

The overall solubility and the trapping ability are closely interrelated and partly driven by the same factors. They are furthermore significantly amplified by singularities and defects, such as those presented in **Table II-C** and **Figure II-k**. This may also be promoted by other factors, for instance:

- Mechanical loads and deformations [101], [107], [108], [141] (especially tensile stresses)
- The inclusions [43]: "reservoir" effect and stress concentrations (detailed in the corresponding section **II.1.C.5.d**)
- Temperature [113], [136], [142]–[145]: the higher the temperature, the higher the mobility and diffusion of hydrogen atoms; the variations of some hydrogen diffusion coefficients as a function of temperature are presented in **Diagram II-h** and **Diagram II-j**; on the other hand, significantly low temperature may lock it, freezing the atoms' displacement
- The types of atomic arrangement of the unit cells [136], [139]: indeed, the hydrogen solubility is strongly influenced by the allotropic form of iron (solid phases), each

offering different arrangements and number of interstitial sites in the lattice formed – this is illustrated in **Diagram II-i** and **Diagram II-j**

• Grain boundary ferrites [47], [125]: encourage the opening of micro-cracks under tensile stresses

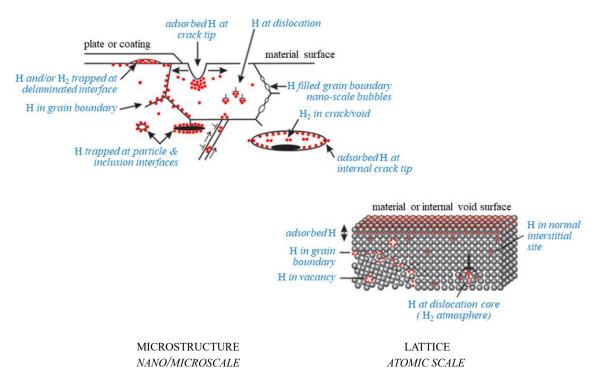


Figure II-k: schematic representations of sites and traps for hydrogen (atoms illustrated in red) in polycrystalline structures (adapted from [63], [113], [146])

II.1.C.4.c Categorisation of the hydrogen content

As suggested above, the absorbed atomic hydrogen content is distributed between mobile and trapped quantities. The hydrogen present in the microstructure under diatomic form or within any other molecules is almost exclusively mobile from an atomistic point of view and thereby not considered here.

At the atomic scale, even mobile hydrogen atoms are actually "jumping" from one – weak – trap to another. Therefore, to jump, H_{ab} atoms need a certain amount of energy. This activation energy allows absorbed atomic hydrogen to be classified into the three categories presented below [137], [138], [147]:

• The diffusible hydrogen content (mobile): weak traps with negligible effect on the H atom diffusion [110], [112] – activation energy: about 0,10-0,26 eV

- The reversibly trapped hydrogen content: activation energy: about 0,20-0,40 eV [112]
- The irreversibly trapped hydrogen content: represents the H_{ab} atoms permanently trapped (only high temperatures close to T_m can "liberate" this quantity [148]); once the saturation of these irreversible traps is reached, they do not affect the hydrogen diffusion process anymore [110], [112] activation energy: about 0,45-0,62 eV

II.1.C.4.d Effusion

However, during their diffusion within the bulk metal, a part of the diffusible hydrogen atoms moves in the direction of the metal surface (effusion process). In a way, this is the opposite phenomenon to the absorption process. Once the surface is reached, these previously absorbed hydrogen atoms return to the stage of adsorbed atoms. To do so, the inverse reaction described above in formula (II-11) occurs. This time, the H_{ab} transfers one e⁻ to a metal's atom. Hence, once again, the re-adsorbed hydrogen atom is temporarily under an ionic form H_{ad}⁺ (refer to formula (II-12)). After that, as described previously at the adsorption stages II.1.C.4.a, these re-adsorbed hydrogen atoms seek again to recombine with (an)other atom(s), and then desorb from the metal's surface.

[110]
$$H_{ab} \to H_{ad}^+ + e^-$$
 (II-12)

II.1.C.4.e Degradation mechanisms

First of all, it is important to remember the difference between the various terminologies relating to hydrogen-induced degradation. Indeed, as recently noted by Martin and Sofronis [149], there is often confusion of usage between the hydrogen-induced cracking (H.I.C.) and hydrogen embrittlement terms. Hydrogen-induced cracking is cracking without any applied mechanical load, whose only driving force for propagation is the molecular pressure caused by the hydrogen at the crack tip [150]. In contrast, hydrogen embrittlement describes a decrease in the triggering threshold energy for defect formation in materials following hydrogen exposure. This leads to a loss of ductility [151]. Hence, the best ways to refer to cracking where hydrogen and stress are conjointly involved are, for instance: hydrogen-assisted cracking, hydrogen-enhanced cracking, hydrogen environment-assisted cracking (H.E.A.C.), or internal hydrogen-

assisted cracking (I.H.A.C.). Back into the welding field, it explains why using the term "hydrogen-induced cold cracking", another appellation for "cold cracking" presented previously, can be contentious. Indeed, as previously mentioned, the stress state is one of the decisive factors in a cold cracking phenomenon. Therefore, the research presented throughout this manuscript will only focus on the hydrogen embrittlement phenomena.

Although the embrittlement of metals by hydrogen was identified almost 150 years ago, the exact degradation mechanisms involved in cracking are still subjects of debate within the scientific community [110], [112]. Several mechanisms have been proposed to interpret and describe the effects observed in metals following hydrogen exposure. Nevertheless, it is commonly recognised that only atomic hydrogen is responsible for the degradation. The various interpretations are generally made of combinations of recurring stages following absorption. Some are given as examples [111], [152]:

- Hydrogen diffusion
- Tensile stresses hydrogen-assisted cracking is generally associated with mode I loading [153] (detailed in the corresponding section **II.1.C.5.f**)
- The role of hydrogen in various phenomena, such as:
 - Formation of brittle micro-constituents
 - Precipitation phenomena
 - Modification of chemical bonds
- Dislocation emission and egress
- Hydrogen trapping
- The pressure induced by atomic or molecular hydrogen
- Movement of vacancies
- The hydrogen transport to:
 - Crack tips
 - Dislocations
 - Interstices
 - Vacancies
 - ...
- The hydrogen effects on dislocation mobility
- The transport of hydrogen by mobile dislocations mobility promoted by stressstrain

- The hydrogen concentration at particle-matrix interfaces
- etc.

To date, only a few interpretations enjoy consensus support through the scientific community [99], [113], [154], [155]. Some of them are listed below (certain are also illustrated in **Figure II-I**):

• Hydride formation and fracture:

Established by [156] in the late 1960s – This assumes the formation and fracture of hydrides at crack tips. However, it can only occur under conditions where hydrogen has sufficient time to diffuse ahead of crack tips, and only at temperatures where the hydride phase would be stable and sufficiently brittle [113].

Typical resulting fracture feature (suggestive) : cleavage-like (mainly facets)

• Hydrogen-enhanced decohesion (H.E.DE. – decohesion model):

Established by [114] in the 1960s and reinforced by [157] over the 1970s – Based on the interaction of hydrogen and iron electrons, which leads to a decrease in the cohesive atomic forces.

Typical resulting fracture features (suggestive): brittle intergranular or transgranular (mainly facets)

• Hydrogen-induced phase transformation [158]:

One of the concepts of this mechanism is based on the succession of these two events [103]:

- *Hydrogen-promoted creation of equilibrium vacancies*
- Vacancy-stimulated solid-solid phase transformations (change into more brittle micro-constituents)

• Hydrogen-enhanced localised plasticity (H.E.L.P. – plasticity theory):

Established by [105] in the 1970s and reinforced by [159] over the 1990s – Based on a decrease in the repulsive interactions between dislocations and obstacles due to the evolution of hydrogen concentration. Since the hydrogen concentration is highly localised, it is thus also the case for the evolution of plasticity.

Typical resulting fracture feature (suggestive): mainly slip-bands and/or dimples

• High hydrogen pressure bubble or void [160]:

This mechanism is related to the precipitation of H atoms followed by their

recombination into H_2 , generating thus a high pressure in the metal microstructure matrix. It can occur when the conditions of absorption and diffusion are unstable [155].

• Absorption-induced dislocation emission (A.I.D.E.):

Established by [161] in the 1980s – This theory is more complex than the hydrogen-enhanced decohesion and hydrogen-enhanced localised plasticity interpretations. It explains hydrogen degradation by nucleation and movement of dislocations into the material. It supposes that the hydrogen must first be absorbed near crack tips before inducing any degradation.

Typical resulting fracture features (suggestive): intergranular or transgranular, cleavage-like (mainly dimples)

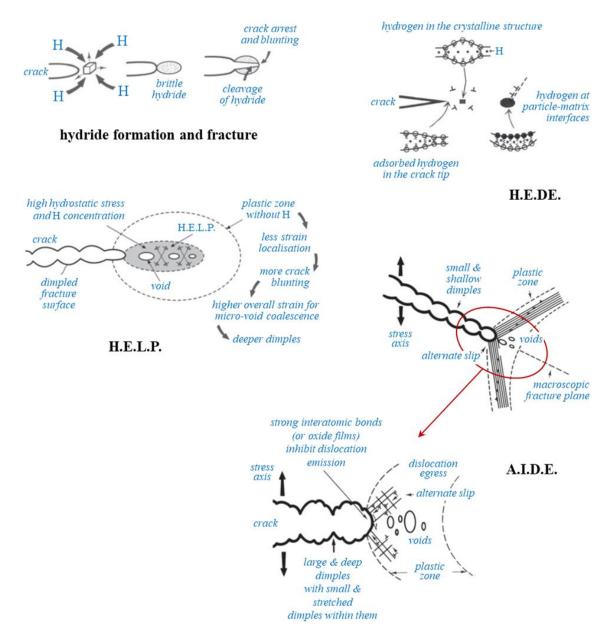


Figure II-1: schematic illustrations of fracture mechanisms assisted by hydrogen (adapted from [113])

Although much evidence, mostly experimental, has been established for each mechanism [113], none is universal and can adequately describe the full range of the role of hydrogen. In addition, it has also been pointed out that these different mechanisms can also occur conjointly (examples shown in **Figure II-m**). Consequently, controversies persist over the definition of characteristics that would permit the distinction of which mechanism effectively occurs in each given situation. Nevertheless, it has been observed that their predominance can be correlated with various factors, such as the material properties and microstructure characteristics, the surrounding conditions, the intensity of the stress state, the hydrogen concentration, ... The hydrogen-enhanced decohesion, hydrogen-enhanced localised plasticity, and absorption-induced dislocation emission are currently the three most dominant mechanisms recognised within the scientific

community [47], [110], [111], [162].

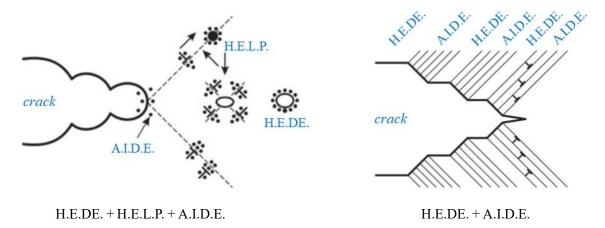


Figure II-m: schematic examples illustrating hybridisation of fracture mechanisms assisted by hydrogen (hydrogen-enhanced decohesion (H.E.DE.), hydrogen-enhanced localised plasticity (H.E.L.P.), absorption-induced dislocation emission (A.I.D.E.) – adapted from [113])

In conclusion, considering these various hypotheses on the hydrogen degradation mechanisms, it can be postulated that its action generally resides in :

- Promoting the emergence of brittle micro-constituents
- Assisting in the propagation of defects such as cracks this can therefore be also assimilated to a loss of ductility

In addition, mobile hydrogen is commonly considered to be more detrimental than immobile content [112]. Therefore, reversibly trapped hydrogen is in turn more damaging than irreversibly trapped content.

II.1.C.4.f Observable consequences

The loss of ductility induced by hydrogen embrittlement affects the fracture mode. Consequently, variations in fracture surface topography can be used to estimate the hydrogen level present during cracking. A summary of the fracture modes observed in hydrogen-assisted cracking is given in **Table II-D**.

Table II-D: suggestive summary of the characteristics of fractures observed in hydrogen-assisted cracking [47], [110], [113], [151], [163], [164]

fracture morphology	fracture mode		typical feature(s)	H level
micro-void coalescence	ductile	transgranular	deep dimples	negligible
micro-void coalescence or cleavage-like or quasi-cleavage	ductile-brittle	transgranular	shallow dimples & few rough rupture facets	low
cleavage-like or quasi- cleavage	ductile-brittle	transgranular	rough fracture facets around inclusions surrounded by shallow dimples	medium
cleavage	brittle	transgranular	rough fracture facets and very shallow dimples along the grain boundaries	high
decohesion	brittle	intergranular	smooth fracture facets along grain boundaries	very high

II.1.C.4.g Hydrogen embrittlement in cold cracking

The determining role of the hydrogen embrittlement factor in cold cracking phenomenon was established around 1940 [45]. Hydrogen embrittlement may amplify loss of ductility in the weld and heat-affected zone already initiated by the formation of brittle micro-constituents during the cooling [165], [166]. First, it must be explained how hydrogen can be present in the vicinity of the weld pool and penetrate the shielding gas or slag.

There are many potential sources of hydrogen, liquid, solid or gaseous. A non-exhaustive summary is given below:

- Moisture (H₂O) in the coating of manual metal arc-welding electrodes, in the flux used in submerged-arc-welding (S.A.W.), or in flux-cored wires used in so-called flux-cored arc-welding (F.C.A.W.) [42], [84], [98], [167]:
 - Air moisture captured by the flux or the electrode coating (hygroscopic behaviour)
 - Insufficient bake-out before use
 - Hydrogenous compound(s) in the coating or flux
- H₂ deliberately added to the shielding gas mixture used in gas metal arc-welding (G.M.A.W.) or gas tungsten arc-welding [168] (H₂ promotes weld penetration, increases the welding process efficiency, may reduce the superficial oxidation, etc.)
 prohibited for multi-pass welding and certain types of metals (non-austenitic

stainless steels, steels with high hardenability, etc.)

- Hydrogen present in the metal before welding [98]:
 - Remaining from the casting process (especially in thick components)
 - Following service at high temperature and high hydrogen partial pressure
 - From corrosion processes, especially in acidic environments
- Humid environmental conditions (H₂O) and insufficient covering of the shielding atmosphere
- Leakage from the cooling system of the welding torch
- Insufficient surface cleaning or contamination of the electrodes or flux or wires [98], [169]:
 - Oil or grease
 - Water (condensation for instance)
 - Dust and dirt
 - Rust (hydrated iron oxide)
 - Paint and coating
 - Cleaning and degreasing fluids

It has been demonstrated that the high temperatures in the arc plasma are sufficient to produce the dissociation of dihydrogen, as well as any other molecule containing H atoms, into atomic or ionic hydrogen [170] (illustrated in **Figure II-n**). Hence, a certain amount may be adsorbed and absorbed by the metal, principally dissolved into the molten weld pool since liquid phases offer the greatest solubilities (refer to **Diagram II-i**). The concentration of dissolved hydrogen from dihydrogen gas can be described with Sieverts' law [170]. According to this, the concentration of hydrogen at equilibrium is proportional to the temperature and the partial pressure of diatomic hydrogen.

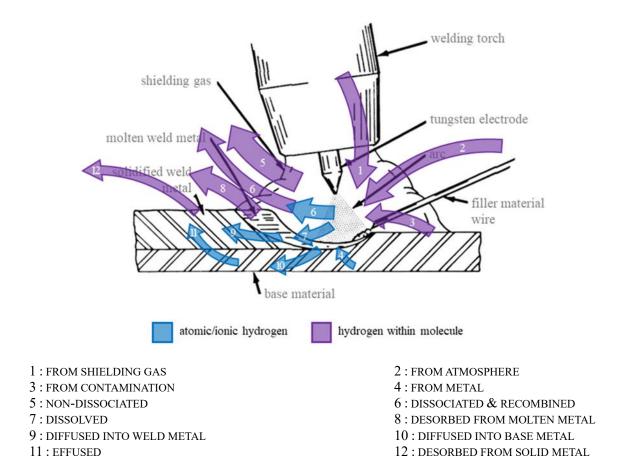


Figure II-n: summary example of hydrogen flows during an arc-welding operation (type gas tungsten arc-welding) – adapted from [42], [54]–[56], [171]

At this point, the diffusion process begins. However, a large part of the hydrogen dissipates during solidification, either by conventional effusion and desorption as described previously (II.1.C.4.d), or by recombination into H₂ directly in the molten weld metal, leading to the formation of "blowholes". If enough hydrogen remains after solidification, the weld metal becomes supersaturated [91], and the diffusion – and effusion – processes are amplified. If certain conditions are met, hydrogen can cross the fusion boundary into the heat-affected zone, and subsequently into the rest of the base metal. The resulting repartition of the hydrogen will be crucial in predicting the area where cold cracks are most likely to occur. In the general case of steels, it is commonly stated that [2], [91], [172] (illustrated in Figure II-o):

• If the base metal heat-affected zone completes its transformation into cold microconstituent(s) before the weld metal ($Ar_{l \ weld \ metal} < Ar_{l \ heat-affected \ zone}$), hydrogen will not diffuse much towards the base metal heat-affected zone because cold phases have a lower solubility than the austenite (hot phase) and will thus "reject" it – refer to **Diagram II-i**. Consequently, hydrogen will remain mainly in the weld metal at the end of the solid-solid phase transformations.

• Conversely, if the base metal heat-affected zone remains austenitic longer than the weld metal $(Ar_{l weld metal} > Ar_{l heat-affected zone})$, as the latter cools, it will "reject" the hydrogen, which can, this time, diffuse into the austenitic base metal heat-affected zone. Consequently, hydrogen will be mainly within the heat-affected zone (base metal) at the end of the solid-solid phase transformations.

Once the steel has transformed into cold micro-constituent(s), the hydrogen embrittlement phenomena begin to operate, and cold cracking may occur, involving some of the degradation mechanisms presented above (II.1.C.4.e).

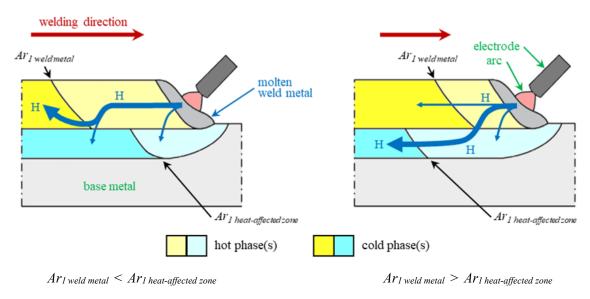


Figure II-o: schematic illustration of the privileged hydrogen distribution depending on the metallurgical synergy during the weld cooling (adapted from [2], [172])

In this project, the base metal is made of ferritic steel while the filler metal is a nickel-based alloy. As suggested in **Diagram II-i**, since an arc-welding operation is generally executed under atmospheric pressure conditions, the nickel does not undergo any solid-solid phase transformations and remains in its stable phase β-Ni (face-centred cubic) following the liquid-solid phase transformation. Thus, in this case, metallurgical changes have a limited effect on the hydrogen distribution. The solubility of hydrogen is higher in nickel than in iron (refer to **Diagram II-i**). Moreover, its diffusion coefficient in nickel decreases rapidly with cooling, reaching a low value (refer to **Diagram II-h**). Considering these two points, hydrogen is unlikely to diffuse much into the base metal heat-affected zone. The selected nickel-based alloy (52M) is known to be relatively resistant to hydrogen embrittlement and is unlikely to form brittle micro-constituent, so the risk of cold cracking is considered here to be quite limited. Nevertheless, as suggested in the

introduction (I.1.C), even small risks must be considered and investigated in a field of application such as the nuclear industry.

II.1.C.5 Mechanical loads

Before detailing the role of the mechanical loads involved in cold cracking, the main types of stresses will be introduced. This review will focus only on crystalline materials as some definitions may slightly differ for amorphous materials.

In general, stress is defined as an average force acting over a given area, and is closely tied to strain. Stresses may be divided into two categories: action and reaction stresses, depending upon whether they can contribute to plastic collapse of a structure [29], [111], [173], [174]. Weld residual stresses are reaction in nature. Nevertheless, residual stresses will be identified as a third category throughout this manuscript to facilitate comprehension and discussion.

II.1.C.5.a Action stresses

Action stresses are considered as resulting directly from the external excitation of a given system. They are necessary to satisfy the laws of static equilibrium. In the usual case, since the involved solicitations are quantifiable, the corresponding stresses are thus easily predictable. A non-exhaustive list of some common examples is given below:

• Static load and pre-load:

- Force and moment generated during :
 - Service: induced by the weight of fluid carried out into a pipe, wind force onto a surface, ...
 - Operations of fabrication, manufacturing, repairing, etc.: typically induced by clamping, lifting, ...
- Pressure: caused by under-pressure fluid carried out into a pipe, submarine pressure, ...

• Gravity:

The gravity-induced loads are principally generated by the own component or structure weight.

II.1.C.5.b Reaction stresses

Reaction stresses are considered as resulting indirectly from any excitation of a given system. Therefore, the corresponding stresses can be tough to estimate and predict, particularly when complex phenomena are involved as coupling, among others. Some examples are given below (non-exhaustive list):

• Dynamic load:

The dynamic loads are principally due to forces and moments generated during service (necessary to satisfy the laws of dynamic equilibrium): for instance, induced by elements in linear or rotary movement.

• Thermal stress or thermo-mechanical load:

For various reasons, components can be exposed to temperature changes. These changes intrinsically induce density modifications of materials. We are focusing here only on the exposure of solids to high temperatures (global or local). Significant heat sources can be commonly generated either during:

- The operations of fabrication, manufacturing, repairing, etc.: *typically induced* when machining, welding by fusion, grinding, ...; usually local
- The service : *for instance, when carrying/storing cold or hot fluid* ; mostly global (whole component)

Most materials expand when they are exposed to heat. This thermal strain can be easily calculated, especially when the material is considered homogenous and has an isotropic coefficient of thermal expansion (C.T.E.). If the material is constrained, this strain generates thus thermal stress due to size incompatibility [174] (expansion or depression) versus stiffness. This constraint effect can operate at any scale, within a component itself (constrained by thermally unaffected zones: *local internal stress*) or an assembly of several components (whole parts constrained to

each other). The usual causes are, for instance:

- Heterogeneous temperature field with significant gradients within the component [111]; the stress intensity depends strongly on the overall stiffness
- Over-constrained assembly of several components and expansion in opposite directions
- Heterogeneous or anisotropic coefficient of thermal expansion which can lead to an expansion mismatch, especially when:
 - A component (or a group of components) is made of different materials, each
 of which may have different coefficient of thermal expansion: typical in
 welding when the base metal is different from the filler metal
 - More than one solid phase is present within the same material, each also having a specific coefficient of thermal expansion [175]: typical in welding within the base metal (heat-affected zone versus unaffected zone)

This thermal stress amount can be deduced using adequate constitutive behaviour laws for the given material (and under a given solid phase if applicable). The "standard" thermal stress is considered throughout this manuscript as not exceeding the yield strength of the material. Therefore, it is supposed to dissipate with temperature homogenisation since the original material density is recovered. When the thermal stress exceeds the elastic limit, it may cause residual stresses. This case will therefore be attached to the specific section.

• Solid-solid phase transformation stresses:

As previously mentioned (II.1.A.3.c), each solid phase in a steel has a characteristic density at a given temperature, driven by its lattice structure (Figure II-f and Figure II-g). Therefore, changes in microstructure often cause volume changes, which can be classically observed with dilatometry or Satoh [176] testing (Diagram II-k). Just like thermal dilation, this volume change generates strain, and if the material is constrained, the transformation strain induces stress [102]. In most cases, a component cannot deform to accommodate this strain. It may thus be considered as a form of internal stress [175]. The residual quenching stress is a typical example [177]. Sometimes, the stress can dissipate if, for example, the material returns to its

original phase distribution, additional stress-relieving treatments are realised (for instance, annealing), or if other action constraints acting on the component are released. However, due to various parallel couplings and phenomena, a solid-solid phase transformation strain is rarely completely recovered in an industrial application such as an arc-welding operation. Consequently, this type of transformation nearly always ends up leading to residual stress phenomena. This case will be thus considered in the specific section.

• *Other causes* – for instance :

- Elastic properties mismatch
- Chemical incompatibilities
- Swelling mismatch during irradiation with neutrons [178]
- Magnetic repulsion
- Electrostatic repulsion
- Compressibility mismatch during pressure changes [179]

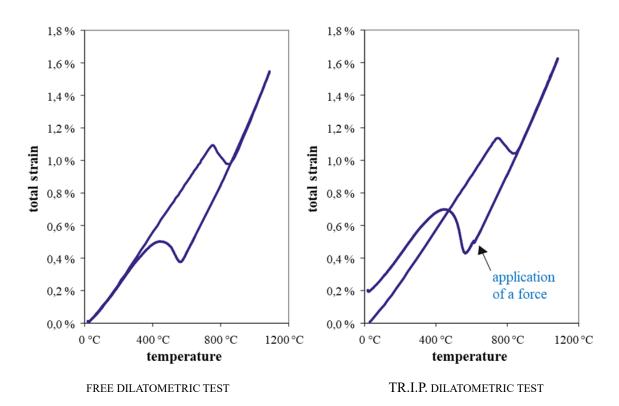


Diagram II-k: classic examples of free and solid-solid phase transformation-induced plasticity (TR.I.P.) dilatometric tests: total strain (thermal + elastic + plastic) versus temperature – *baintic transformations* (source: [180], [181])

II.1.C.5.c Residual stresses

Residual stresses are those which remain in a given system after the cessation of any external action [182], [183]. It mostly results from the incapacity of the material to return to a fully unconstrained state [29]. It is a long-term stress, which subsists in equilibrium with its surroundings within the material. In some particular situations, it can be deliberately introduced to enhance material properties, for example, for producing toughened glass [184]. It can by generated by different phenomena. Some are given below as examples (non-exhaustive list):

• A local plastic deformation of the material

Permanent and non-reversible deformations of the material – induced for instance by :

• Load exceeding the elastic limit:

This load has produced a strain misfit between different parts of the component/structure that cannot be accommodated elastically (and therefore reversibly). Local plastic deformation has then taken place. Consequently, when this load is removed, the material still has internal misfits, which must be accommodated by, at best, an elastic strain distribution which results in stresses that self-equilibrate of any plane within the component/structure, or a combination of further plastic flow and a final elastic field. It has to be noted that the elastic limit value is highly temperature-dependent and varies between materials. This threshold can be reached by (given with some examples):

- action stress: possibly caused by an excessive weight load; this may be
 deliberate: in a rolling or shot peening processes
- reaction stress : an excessive thermal stress
- combination of several action and/or reaction stresses [175], [185]

• Complex physico-chemical phenomena like, for instance, certain couplings:

Solid-solid phase transformation-induced plasticity (TR.I.P.) phenomenon [104], which generally implies a solid-solid phase transformation in the material combined with the application of an external mechanical load, even inferior to the macroscopic yield strength of the material [180], [186] (refer to the illustration given in **Diagram II-k**)

- Hydrogen-induced plasticity: hydrogen-enhanced localised plasticity phenomenon [105], [106], [113], [159], [187] (a mechanism of hydrogen embrittlement, refer to the corresponding section **II.1.C.4.e**)
- Persisting reaction stresses, or not fully relieved: for instance, stress resulting from solid-solid phase transformations, persisting chemical incompatibilities inducing stress, ...

Particularly, as mentioned previously, solid-solid phase transformations nearly always generate residual stresses. If no mitigating operation has been undertaken, their intensity may remain significant and even approach the rupture limit value in the case of fragile material (or micro-constituent).

• Material shrinkage during liquid-solid phase transformation

After a local melting of a material, *such as after an arc-welding operation*, large temperature gradients are generally involved. Hence, a differential cooling may take place [29]. During the solidification, certain areas solidify faster than others. Shrinkage can therefore occur. This material contraction may, in turn, induce deformations. When dealing with a massive part, *such as a thick section of pipe*, the self-restraint intensity is usually very high. Hence, the unaffected zones of the material cannot deform to accommodate the deformations due to contraction. A significant amount of residual stress can thus result despite complete temperature homogenisation. Mostly in tensile stress, especially within the weld near region.

Residual stresses are classified into different categories depending on the length scale over which they operate [183]. This facilitates the study of these phenomena and eases the choices of appropriate actions to control their impact. Three categories are commonly used:

• Type I: macroscopic scale: equilibrate over large distances, can be the size of the whole component/structure

Also named "macro-residual stress" or "long-range residual stress". It is considered as a "continuum mechanics" stress, which may occur within any crystalline material. The stress state generated by a quenching operation or produced by shot or laser peening are great examples of macro-residual stresses.

• Type II: microscopic scale: equilibrate over the dimension of a certain number of crystals

Also called "intergranular residual stress", it concerns principally polycrystalline materials. It has to be noted that this stress is nearly always present, even at low levels [183]. This is explained by the fact that each grain is oriented differently from its neighbours. Considering that a crystal has a more or less anisotropic behaviour, thus, each oriented grain shows slight differences in its material properties [174]. This stress amount can be exacerbated after having undergone thermal stresses. In addition, polyphase materials are intrinsically even more exposed. This type II stress also typically occurs following microstructure modifications since residual solid-solid phase transformation stresses may persist.

• Type III: atomic scale: equilibrate over the crystal structure within several atomic distances of the grain

Also named "sub-micro residual stress", it may occur within any crystalline material. Its occurrence can result of:

- Crystallographic defects : dislocations or vacancies, for example
- Alloying elements: atoms inserted between or replacing the original ones of the unit cell: for instance, carbon atoms within iron unit cells to form steels
- Embrittling elements: atoms inserted between the ones of the unit cell: the hydrogen embrittlement phenomenon is a good example

II.1.C.5.d Stress amplifying conditions

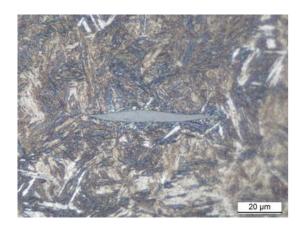
The impact of applied loads can often be increased by local features of the component or microstructure. Two common sources of local load amplification are :

- Geometric singularities and topologic imperfections
 - Chamfers and fillets, typically when they are too small
 - Welding grooves: incorrect face preparation as well as root bevel and gap [125]
 (especially affecting stresses transverse to the welding direction [111])
 - Notches
 - Holes
 - Undercuts

Cavities

• Coarse inclusions within metallic microstructure matrix

This form microscopic circular or elliptic holes, or notches (especially following rolling and forging operations); some illustrations are given in **Picture II-b**. It is well known that they are likely to be the origin of cleavage cracks because of the significant local stress concentration involved [120]. This explained by the fact that they are stiffer/stronger than the matrix, and consequently, not going to deform at the same rate.





NOTCH SHAPE

CIRCULAR HOLE SHAPE

Picture II-b: illustrations of manganese sulphide (notch form) and combination of manganese sulphide (MnS) with calcium aluminates (round shape) inclusions observed within low-alloy steel 18MND5 (*polishing*: $\frac{1}{4} \mu m - etching$: 2 % nital during $\approx 30 \text{ s}$)

Local load amplification is quantified using the stress concentration factor K_t [188], which is the ratio between the nominal stress, $\sigma_{nominal}$, and peak stress, $\sigma_{local\ max}$, on a cross section containing the concentrating feature, see equation (II-13). Analytical formulae defining K_t exist for a number of geometrical features. It can also be estimated using numerical methods, such as finite element method.

$$K_t = \frac{\sigma_{local\ max}}{\sigma_{nominal}} \tag{II-13}$$

II.1.C.5.e Stress attenuating conditions

A number of deformation mechanisms may act to attenuate the stress level. These are all based on the conversion of elastic strains into inelastic strains [127]. Residual stresses are a consequence of plasticity-induced strain misfits, and may be beneficial or detrimental depending upon their distribution (see **II.1.C.5.c**). Generally speaking,

inelastic deformation acts to mitigate stresses [174], even residual stresses when further plasticity arises later after their occurrence. Plasticity represents the ability of a solid material to undergo permanent and non-reversible deformation, which supersedes the material's elastic behaviour. Hence, since stress is a response to an elastic strain, a permanent change would "fix"/"freeze" the latter. Inherently, the stress will thus disappear. A permanent deformation can be due to various causes. Some situations are given below as examples:

• Permanent mechanical deformation

- As can be observed with most of the tensile curves, especially of low-carbon steels, when a deformation reaches the elastic limit, it causes itself plasticity. Thus, it diminishes the increasing rate of the further stress it induces. Sometimes, it even reduces it during a short interval between the "upper" and "lower yield point". This way of transiting from the elastic to the plastic domain is called "strain-hardening" or "work-hardening". It may be voluntarily reached to modify the material properties, of which the increase of the elastic limit for instance, thanks to cold- or hot-metalworking operations.
- In the case where a first elastic strain constrains a material, such as in residual stresses, if a second one is applied punctually, their sum can thus induce permanent deformations. Hence, after the second load removal, the final stress intensity would be lower than initially.

However, it must be remembered that plastic deformations may also lower the material ductility and raise its hardness, which can be undesired.

• Creep

Long-term phenomena can contribute to alleviating – to a certain extent – some of the global stress amount. The creep, also known as "cold flow", is a good example [189]. It generally results from a constant mechanical load, such as gravity, and is considered to cause delayed irreversible deformation (in other words, not instantaneous). In a certain manner, the material ends up accommodating this load with time. The bending of a beam or a shelf after several years is a good illustration. A particularity of the creep is that it can also occur for stress levels that are still below the yield strength of the material. Furthermore, significant temperatures generally promote and accelerate creep.

• Heating or re-heating

Heating most materials may mitigate the overall stress level thanks to various heatactivated, or at least heat-accelerated, mechanisms. Some examples are proposed below:

- Concerning crystalline material, certain phenomena affecting their microstructure can also induce plasticity, for instance :
 - The re-crystallisation can be here particularly highlighted. Indeed, as shown precedingly, a sufficient temperature can encourage the grains to reform. Hence, new "strain-free" crystals will nucleate, grow, and can thus replace those elastically and plastically deformed (return to a state of equilibrium). This is particularly researched during the thermal treatment of annealing.
 - The solid-solid phase transformation-induced plasticity coupling effect, to a certain extent (previously introduced).
- As mentioned above, creep phenomena can be significantly accelerated. They
 nearly always occur at some point in most thermal treatments.
- The yield stress may drop below the local residual stress owing to temperature increase. This would then refer to the case previously mentioned above: when the deformation reaches the elastic limit, it causes itself plasticity, which mitigates the stress level.

These phenomena are commonly observed – and well received – in the case of multi-pass arc-welding since many re-heating of the material at significant temperatures are induced over the runs.

• Other causes

Other phenomena can induce plastic deformations. For instance, one of the couplings precedingly mentioned with the hydrogen factor can be cited : the hydrogen-induced plasticity phenomenon.

II.1.C.5.f Loading modes in fracture mechanics

Fracture mechanics, first introduced in the early 1920s by [190], is essential for describing the propagation of cold cracks and quantifying the risk of structural failure.

Fracture mechanics concepts are used widely in order to ensure the structural integrity of welds. It is widely recognised that metallic materials always contain defects caused by the fabrication processes and service exposure, arc-welding being no exception. This presents a dilemma: What is the maximum size for acceptable discontinuities or defects (assuming that they are crack-like), and at what point does the density of sub-critical defects become excessive? Fracture mechanics has the ability to address these questions. The critical size of a cold crack given in the ISO¹⁹ standard [191] is an excellent example of its application. According to this testing method standard, a cold crack is deemed present above a length of 500 μ m.

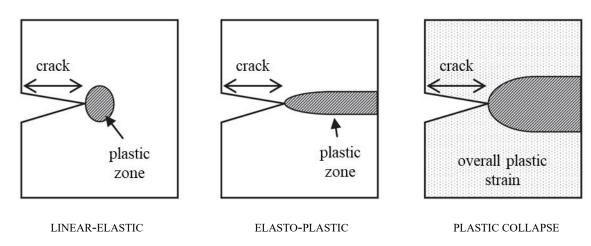


Figure II-p: plastic zone extension according to the assumption about the medium behaviour (source: [192])

For accompanying the further developments present throughout this manuscript, it is particularly essential to bear in mind the two following statements:

• Inelastic deformations are always present around the crack front [193]: the assumption of a linear elastic medium is then highly unrealistic [194] – indeed, under this assumption, local stresses around geometric singularities are estimated using stress concentration factor K_t , which assimilate cracks as notches with a radius tending towards zero: that would predict infinite stresses at the crack tip, which is not realistic; therefore, concerning cracks, the local stress state around the crack tip must be estimated using stress intensity factor K [193], [195], [196] (refer to **Figure II-r**) – the crack front is thus a plastic zone, as shown in **Figure II-p**

109

¹⁹ International Organization for Standardization

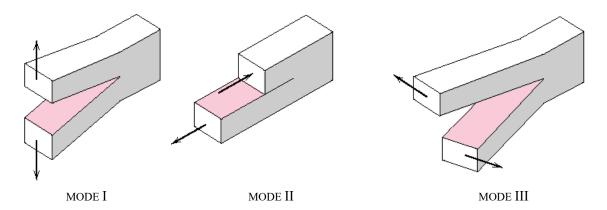
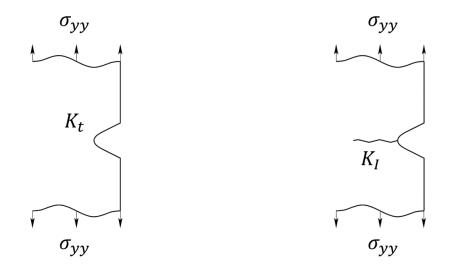


Figure II-q: the three components partitioning the load at a crack tip (source: [197])

- As illustrated in **Figure II-q**, the load at a crack tip is considered by the theory as being a combination of three independent components called "modes":
 - Mode I: opening mode tensile stress normal to the crack plane (as shown in Figure II-r)
 - *Mode II*: sliding mode shear stress acting parallel to the crack plane and perpendicular to the crack front
 - Mode III: tearing mode shear stress acting parallel to the crack plane and parallel to the crack front

(Each mode having a specific definition of the stress intensity factor [193] : K_I , K_{III} , K_{III})



 ${\tt NOTCH: STRESS\ CONCENTRATION\ FACTOR} \qquad \qquad {\tt CRACK\ (MODE\ I): STRESS\ INTENSITY\ FACTOR}$

Figure II-r: highlight of the different characterisation methods for notches and cracks (adapted from [196])

II.1.C.5.g Stress in cold cracking occurrence

Previously, it was shown that the rapid cooling generates brittle microstructures. These are then embrittled again by hydrogen embrittlement phenomena. However, even though this medium is doubly embrittled, a cold cracking failure would not occur without a fatal mechanical load. This load being composed of various stresses, of which the main ones were presented above, this section will thus detail the role of the implicated ones. Though, not all stresses are detrimental concerning cracking phenomena. Indeed, compressive stress state even prevents crack initiation or propagation. They tend to "close" the eventual cracks. On the other hand, tensile stresses tend to "open" them and, thus, encourage their initiation and propagation.

Concerning relatively massive components made of standard steels – *stainless steels excluded* – , constituting thus the base metal, the principal sources of loads following an arc-welding run are generally :

• The thermal stress-strain: induced by the intense heat input generated for the metal melting

Usually inducing compressive stress (reaction), its impact is, however, limited since it occurs principally when the metals are molten and/or at high temperatures, having poor mechanical resistance. Therefore, it can easily deform to accommodate the deformations and does not thus take any stress [173]. Moreover, it dissipates rapidly due to the cooling occurring shortly after the weld run completion. Its beneficial effect is thus negligible in the cold cracking phenomenon . More broadly, it is marginal in any ulterior defect or failure.

• The residual stresses: as shown precedingly, several causes can be involved; some induce a compressive load while others are tensile

Overall, this one is nearly always carefully considered because it can cumulate with the action stresses commonly applied in service, which were validated during the design dimensioning. This can thus lead to failures at levels lower than those at which the failure would occur under the effect of action stresses alone [182], [184]. Many examples of incidents with more or less serious damage exist in any industry. Their amount following an arc-weld can be of the order of the initial material's elastic limit [29]. Consequently, they can be strongly decisive, for instance, in the stress corrosion cracking [198] or the cold cracking defects. Two of them can be

particularly highlighted:

• The solid-solid phase transformation stress-strain: induced by the cooling following the metal solidification

As demonstrated with dilatometry tests (refer to **Diagram II-k**), its dilation intensity is not negligible [199]. It is thus usually also compressive stress (initially reaction). Therefore, this is considered to have a significant positive impact on preventing cold cracks. It does quasi-not dissipate after the cooling completion, which is why it is considered here among the residual stresses. In complement, it was though demonstrated that, despite its impact being considerable for single-pass welds, it attenuates in multi-pass welds due to the repetition of the thermal cycles (repetitive tempering effect and stress relieving). Consequently, its impact prevails only in the final run of a multi-pass pass weld [111].

• Liquid-solid phase transformation material shrinkage:

Nevertheless, the residual stresses overall amount nearly always results in tensile stress following the welding run. This is due predominantly, and by far, to the metal shrinkage during liquid-solid phase transformation. Moreover, its intensity increases as the weld cools down. Then, it stabilises at its maximum level. Because of the welded parts massiveness, the restraint intensity level is generally significant.

Moreover, except for creep and any other long-term phenomena, all the presented stress amplifying and attenuating phenomena may also play a role within the mechanical load involved in the cold crack occurrence.

Over the 1960s, a Japanese research group [200] indirectly monitored the overall load acting on a weld by instrumenting the flanks of massive welding test mock-ups. The mock-up flanks were slightly deformed despite being remote from the weld area [118]. Hence, the evolution trend of the global stress state following an arc-welding run was qualitatively estimated. An example of the typical curve trend obtained is shown in the time-dependent **Diagram II-I**. Hence, it was established that despite some compressive stresses, the stress level induced by the material shrinkage is greater and makes the overall residual stress state in tension.

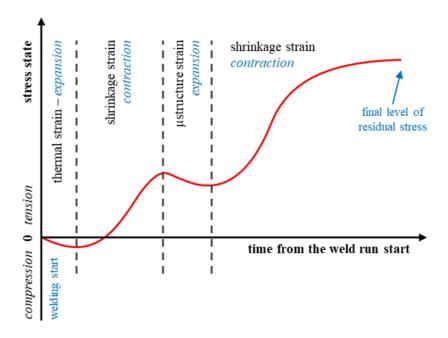


Diagram II-1: evolution trend of the mechanical load acting on the weld during and after an arcwelding pass – observed by [200] in massive test mock-ups (adapted from [118])

In conclusion, such a residual stress state creates favourable conditions for crack opening and propagation up to critical sizes. Indeed, the *load mode I* described by the fracture mechanic theory is therefore expected to occur on any potential defect. Besides its propensity to factorise cracking, it is also recognised as a catalyst in hydrogen mobility [107] and hydrogen embrittlement phenomena [153]. Consequently, this plenty justifies its decisive role of cold cracking factor. Furthermore, since cold cracking is a time-limited cracking phenomenon, it can be assimilated from this point of view as a monotone loading.

In addition, some researchers have also investigated the main orientations of this mechanical load. In particularly, they highlighted direction changes between single- and multi-pass weld [111]. They concluded that in the case of single-pass weld, the tension load is predominantly transversal to the welding direction. On the other hand, in multi-pass weld, over the repetitive runs, this tensile stress ends up by following a longitudinal orientation. Considering that the loading mode I is predominant in cracking direction [195], [197], this suggest thus that longitudinal cold cracking most likely occurs within single-pass weld, or at least during the first runs of a multi-pass weld, while during the last runs and after the weld completion transverse cold cracking is most likely expected.

II.2 STATE-OF-THE-ART

II.2.A Preventing cold cracking

To commence this section, an example of a logical workflow to prevent the risk of cold cracking is proposed. In general, susceptibility to this type of defect is estimated on the basis of:

- Knowledge of the materials
- The experience of welders and engineers
- Simple empirical tools for weldability assessment such as those presented previously (mainly analytical or graphical methods **II.1.A.3.d**):
 - A limit value of carbon equivalent CE (such as the one established by [119])
 - Graville's diagram [90]

Hence, if it is known or found that at least one of the alloys is potentially sensitive, a first set of basic prevention methods can be applied. These aim to reduce at least one of the three factors of the cold cracking. phenomenon. For example:

- *Substitution with steels containing less carbon.* This principally reduces the impact of the microstructure factor, reducing the hardenability.
- Application of additional heating(s): This may mitigate each of the three factors [28], [29], [31], [201]. It is the measure commonly mandated by most design and regulatory codes such as [30], [33]. Optimised parameters of these additional heatings can be established empirically using analytical or graphical methods. For instance, [202], [203] both propose methods to estimate the temperature to apply during the additional heating.
- Optimisation of the welding parameters [123], [204]–[206]: The weld process parameters can also influence each of the three factors. For instance, [42] demonstrated that a right combination of parameters permits to reduce the diffusible hydrogen content within the weld deposit. Moreover, increasing the heat input may reduce the formation of brittle micro-constituents (thanks to lower cooling rates), and therefore mitigate the risk of cold cracking in the heat-affected zone [84]. However, the diffusion distance for the hydrogen to effuse from the weld bead increases as the heat input goes up. Consequently, the risk of cold cracking in the

weld metal is therefore increased.

- *The joint geometry of the weld*: The design of the joint or groove influences the stress state factor, principally by modifying the stress concentration factor [207].
- The use of additional device(s): For instance, [208] highlighted the interest of using run-on/run-off plates on both sides of the weld. They allow to start and end the weld without forming defects associated with the start and stop regions where 3D cooling transients, constraint, and stresses occur.
- *The realisation of additional welding run(s)*: Supplementary weld beads on both sides [209] (similar principle with run-on/run-off plates).
- The type of electrodes, flux or shielding gas: The quantity of atomic/ionic hydrogen generated in the arc is influenced by the electrode type or the shielding gas used. For instance:
 - Basic electrodes usually introduce less hydrogen into the molten weld metal than rutile or cellulosic electrodes [84]; indeed, the coating of this electrode type produces basic slag, which offers a higher water capacity [167], and thereby reduces the generation of hydrogen from H₂O molecule dissociation by the electric arc (refer to section **II.1.C.4.g**)
 - [42], [167] both suggest that a higher oxidation potential of the shielding gas or flux may reduce the generation of hydrogen. The addition of fluoride-containing compounds in the flux can have a similar effect
 - Specific ingredients added to the flux formulation can react with atomic/ionic hydrogen to form insoluble hydrogen-containing products in the molten weld metal [167]
- The utilisation of bead tempering methods in multi-pass welds: These principally reduce the impact of the microstructure factor, tempering brittle micro-constituents and increasing their toughness [18], [29], [35], [210], [211]. The most known being the temper bead welding (refer to Figure II-s), the half-bead technique, the alternate temper bead, and the cold repair (also known as "ambient temperature temper bead" A.T.T.B.) [25], [34], [36], [211], [212]. In brief, bead tempering methods consist of depositing a tempering layer first, whose heat-affected zone (within the base

metal) is then tempered by the subsequent filling layers. Nevertheless, some still include one or more additional light heating(s).

• The utilisation of innovative arc-welding solutions: Among others:

- [213] suggested that the double-sided double arc-welding technique may allow the reduction or elimination of pre-heating thanks to the increased heat input
- [214] suggested that using hybrid laser-arc-welding may reduce the amount of diffusible hydrogen

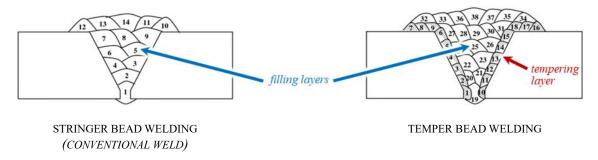


Figure II-s: schematic illustration highlighting the difference between conventional multi-pass welds and those made with temper bead welding (adapted from [25])

Nevertheless, in the case of sensitive applications, the prevention measure(s) undertaken must be qualified for the welding configuration to be executed. To do so, the simplest way is to carry out specific welding tests assessing the risk of cold cracking, such as those described by the ISO standard [87] (detailed in the following section **II.3.A**):

- The controlled thermal severity (C.T.S.) test
- The Tekken test
- The Lehigh test
- The implant test

However, sometimes these tests are not conclusive and do not permit the development of a viable welding procedure. It may also turn out that none of the standard tests reproduce the proposed application faithfully enough. This may lead to misinterpretations, either too favourable or too severe. Therefore, further investigations may be warranted. They should permit better understanding and control of the phenomena involved and therefore better assess the risk of cold cracking for a given application.

II.2.B Deeper investigations

When deeper investigations are required, they may be based upon:

More sophisticated and/or instrumented welding tests (not necessarily those included in standards):

Among many other examples, the modified implant tests developed by [121] or the rigid restraint cracking (R.C.C.) test used by [199] can be cited. According to the literature, about 200 test procedures are used to investigate the cold cracking phenomenon [82], [93], [97], [215]–[218]. Depending on their characteristics, they can permit assessment of the base material, the filler material, or both. In addition, they can be separated into two main categories: external restraint and self-restraint tests. However, it remains difficult to control each cold cracking factor separately. For instance, altering the base material thickness can influence both the cooling rates and, thereby, the microstructure changes occurring in the heat-affected zone, and the level of hydrogen retained in the weld [84].

• Development of new methods of instrumentation or measurement :

For instance, innovative techniques of residual stress measurement [219], hydrogen content diffusing under the weld bead [220], ...

• Small-scale testing:

- Metallurgical tests, such as the Jominy test (also called "Jominy end-quench test" – invented by [221], [222])
- Analysis of chemical phenomena, for instance, the ISO 3690 [145] test used to determine the hydrogen content in weld metal
- Mechanical testing, such as tensile or Charpy impact testing
- Thermo-mechanical behaviour characterisations, for instance, using the "hot disk" test method [223]
- Computational simulations to investigate particular phenomena, such as hydrogen transport [224], hydrogen embrittlement [105], metallurgical transformation [225], [226]

• Welding modelling:

Numerical models can be used to reproduce specific details of a given application. In addition, data from small scale testing can be utilised to feed and validate these models, allowing therefore a great degree of fidelity. After simulating the thermal phenomena experienced by the material, calculations to predict the residual stresses, the metallurgical modifications, the deformations, or even the chemical phenomena can be run. Nevertheless, numerical models are not necessarily cheaper than experimental approaches. Indeed, modelling a problem can be very time-consuming requiring significant researcher time and computing resource. The supporting small-scale experimental testing also incurs costs and time.

Different approaches can be combined. For instance, it is common practice to feed numerical modelling with experimental results from characterisation of material properties. Overall validation of a computational simulation chain by comparison with an instrumented experimental welding test is also a widespread practice.

The results obtained from such investigations can be exploited in many different ways. Some common examples are proposed below:

- To establish empirical baselines:
 - Failure criteria, deterministic or probabilistic, for instance :
 - Advanced analytic formulas, such as the equations proposed by [202] to estimate a critical stress, or by [111] to calculate a critical content of hydrogen
 - Advanced graphical tools [109], [203], [227]
 - Limit values, such as the critical carbon equivalent percentages presented previously [119]
- To propose reliable computational simulation chains including couplings that can be used to study complex configurations [47], [174], [228], [229]

Finally, these investigations and their outcomes can make it possible to demonstrate either:

- The existence of suitable combination(s) of welding parameters and eventual preventive measure(s) to propose a viable welding procedure ensuring welds free of cold cracks in the specific case studied
- The impossibility of ensuring defect-free welds in the specific case studied

II.2.C Recent research into cold cracking & discussion

Several recent studies about the cold cracking phenomenon can be found in the literature, following either experimental or computational approaches or sometimes a combination of both. Most works looking at the whole welding process conducted their investigations focusing on a welding test [38], [48], [230]–[232], nearly always one of those described by the ISO standard [87]. In addition, they often undertook some more basic small-scale testing, such as the analysis of the hydrogen content in the weld metal [38], [47], [89], [233], mechanical testing [47], [111], [234], studies on the impacts induced by microstructure changes [111], [234], or stress level measurements [111], [118].

Research focusing on only one of the factors involved in cold cracking may also be of great interest. For instance, the investigations on the hydrogen embrittlement phenomena conducted by [101], [110], [112], [165], [171], on the microstructure modifications and/or its impact on the material properties made by [78], [225], [226], [235], [236], and on the residual stresses induced by welding processes realised by [219], [225], [228] have provided results and conclusions that contribute to the understanding of the cold cracking phenomenon.

Nevertheless, a reduced selection of recent work closest to the topic explored by this new research project and dealing with the same or similar base metal are particularly relevant.

The review conducted by [36] at EDF and the IS in the early 2010s suggested the feasibility of certain bead tempering methods to solve challenges encountered within the French nuclear power plant fleet (using the same candidate filler metal as in this project). They also recommended post-heating at a temperature of 60 °C. They concluded that computational simulations would assist in the definition of optimal welding parameters and, more broadly, develop the knowledge and skills required before their inclusion in regulatory codes. In parallel, experimental investigations sub-contracted by EDF to the IS [237] confirmed the potential of innovative welding techniques through implant test campaigns. The implant test was used because it is the only one included in the French regulatory code to date for such repair processes. Nevertheless, the investigations highlighted the risk of conservatism induced by the severity of this test method.

Then, as implemented by [238] a few decades ago, a group of researchers [40], [48],

[232], [239] developed new computational weld models with the specific goal of predicting the risk of cold cracking, using a probabilistic approach. They also focused on the implant test, partly due to its regulatory position, and partly because it allows varying the different parameters independently [239]. Hence, depending on the conditions applied, it can produce both cracking and non-cracking cases, which facilitates the calibration and validation steps of the computational models before using them on any real weld configurations [40], [232]. In conclusion they suggested several recommendations to facilitate acceptance of bead tempering methods:

- They pointed out that prediction of the metallurgical transformation kinetics defining the obtained microstructures is essential to study the cold cracking phenomenon. The microstructure influences the material properties, so the reliability of the subsequent mechanical and chemical computations depends on the quality of the metallurgical predictions. However, they recognised that the computational solutions then available were still too limited in this area to ensure a reliable estimation of the risk of cold cracking [239].
- They highlighted that the conclusions drawn from implant test campaigns are often too conservative and consequently not representative of the conditions of real multipass welding applications [48]. This testing method conservatism was also pointed out later by Consonni [18]. Furthermore, implant testing might not be suitable for investigating dissimilar metal welding, due to differences in mechanical properties between the materials involved. Nevertheless, Da Silva and Haouas [237] observed in their experiments that using the smallest implant diameter prescribed by the ISO standard [240] seemed to solve this problem.
- Hence, they suggested that future investigations should use other testing methods or simple mock-up weldments closer to the final application. Once again, the review of [18] converged to the same conclusions, proposing, in addition, the option of using a modified version of the implant test. Nevertheless, the resistance to cold cracking of the low-alloy ferritic steel and the welding processes used in the nuclear industry are among the reasons for their selection. Therefore, intentionally unfavourable conditions should be used to generate cold cracks within a test mock-up [40], [232]. For instance, they suggested low arc energy, conditions promoting hydrogen absorption, and any singularities in the mock-up design that could cause a stress concentration.

• Finally, they also concluded that further small-scale testing would be welcome to improve the reliability of the numerical models, especially in probabilistic approaches [40], [232].

The conclusions drawn from the previous project of Qianqiang [47] conducted at EDF, previously highlighted in the introduction chapter (I.1.F), are of particular interest. Indeed, the topics examined during this investigation are close those of this new research project. However, the filler metal used was stainless steel, not Alloy 52M, and using additional heating(s) was not an impossible option since the final application was a manufacturing operation. It was rather a matter of process optimisation. Qianqiang developed a Code_Aster module modelling hydrogen diffusion and trapping, and then built a complete computational 3D simulation chain, including couplings, to predict the occurrence of cold cracks. A deterministic criterion was used, based on the results obtained from several characterisation experiments. To that end, the following small-scale tests were used:

- A mechanical testing campaign was conducted at the LaSIE by [166] to evaluate the level of hydrogen embrittlement using flat tensile test specimens, and establish thus baselines to feed his failure criterion
- ISO 3690 [145] tests to quantify the diffusible hydrogen in the weld metal were conducted at the IS to feed his simulation
- The results found by [241] with thermo-mechanical testing was exploited to verify the reliability of the computational models ("hot disk" test method)

Then, he calibrated and validated his numerical model with several Tekken welding tests, of which some were thermally instrumented by thermocouples (T.C. – also known as a "thermo-electrical thermometer"). An acoustic emission (A.E.) system was also used on each welding test to aid the detection of cold cracks during the test, prior to post-test destructive analysis of the mock-ups. Moreover, observations of the fracture surfaces were conducted to verify their consistency with the hydrogen embrittlement characterisation experiments. The output of this project is quite consistent and permits significant progress in the prediction of the risk of cold cracking. Qianqiang also recommended additional modelling development, particularly by using a ductile-brittle fracture model instead of a simple brittle model and by modelling crack propagation in addition to the initiation. Beyond this, some points requiring further investigations can be added:

- Calibration and validation of the hydrogen diffusion model through instrumented test mock-ups and/or additional characterisation experiments. Indeed, although existing laws and models were used, the input values utilised (such as permeation and diffusion coefficients, among others) were obtained from investigations conducted several decades ago [242] and not necessarily on the same metal microstructure.
- Evaluation of the relevance of both the Tekken test itself and the selected Tekken mock-up design parameters to the proposed plant repair.
- Direct comparison of the Tekken and implant tests.
- A single microstructure was used to characterise hydrogen embrittlement using mechanical testing. The chosen micro-constituent distribution and prior austenite grain size are not representative of a typical coarse-grained heat-affected zone produced following an arc-weld, which is the region most susceptible to cold cracking.
- There is a discussion among the EDF researchers of the relevance of the cold cracking results produced during the Tekken testing campaign as problems related to dilution phenomena (from the filler metal to the heat-affected zone) have been raised.
- The plant application is a multi-pass weld, so it might be interesting to investigate
 the impact of deposition of subsequent welding beads, which is supposed to be
 beneficial. Qianqiang only studied deposition of a single weld bead.
- Further calibration and validation of the computational prediction of microstructure.

In the paper published by Consonni and Verdon [34], the stresses generated during a cladding repair using the ambient temperature temper bead technique and the same candidate filler metal (Alloy 52M) were calculated using simulation. An experimental implant test campaign was then conducted. Following the execution of a single welding pass – representative of the first bead deposition – and without pre-heating, they found that cold cracks may occur within the heat-affected zone under loading representing the residual stress levels predicted. They identified a minimum pre-heating temperature of 75 °C to prevent cold cracking, concurring thus with the conclusions of [36]. However,

they highlighted two limitations in their study:

- The number of implant tests conducted was insufficient to confirm a non-failure condition at this pre-heating temperature
- The loading of the implant specimens at the predicted overall residual stresses generated during the real welding application may be overly conservative since a single deposited weld bead might not generate the same residual stress level

During his research project [110], Rhode focused on two cold cracking factors: microstructure and hydrogen embrittlement. He also investigated the impact of microstructure on hydrogen diffusion kinetics. These investigations were conducted on both on 16MND5 and T24 low-alloy steels. Rhode performed mechanical tests using both notched and smooth cylindrical tensile test specimens, with supporting characterisation, such as permeation tests or analyses of the hydrogen content. Most of the investigations used samples having uniform microstructure. Important conclusions were:

- The notched tensile test specimens were unable to distinguish the ductility of different microstructures. The reason seems to be that the stress concentration in the notch root outweighs the influence of microstructure.
- The hydrogen solubility is higher within the heat-affected zone than in unaffected base metal. However, the diffusion coefficient is highest in the unaffected base metal (at room temperature).
- The micro-constituent distribution within the heat-affected zone microstructure seems to have a limited influence on the hydrogen trapping phenomena.
 Nevertheless, the investigations of hydrogen embrittlement in each particular weld microstructure are of interest.
- The ISO standard method [145] to analyse the hydrogen content is limited for advanced characterisations. Other methods seem to be more advantageous as they may permit the extraction of additional data.
- Couplings between microstructure and mechanical properties, and between microstructure, hydrogen diffusion and hydrogen embrittlement, should be more widely implemented into numerical simulations of arc-welding processes to enhance prediction of the overall degradation in material properties.

 Additional experimental characterisations should be undertaken to verify the transferability of these results to multi-phased microstructures representing the whole heat-affected zone.

Finally, recent work carried out by EDF with several partners has characterised the mechanical behaviour of the candidate filler metal [228], [243] (using Chaboche's elastovisco-plastic model [244]) and has implemented tools for generating continuous cooling transformation diagrams as a function of the steel chemical composition [226], [245]–[247]. These developments have been implemented in the numerical simulation suite developed by EDF.

II.3 CONCLUSIONS DRAWN FROM THE LITERATURE REVIEW

II.3.A Welding test procedures

Experimental welding tests appear essential in the global study of the cold cracking phenomenon. Since the mechanisms involved are not fully understood and/or modelled, analytic and computational studies are not sufficient.

Many researchers have highlighted the severity of assessments conducted using the implant test (developed by Granjon at the IS in the 1960s). They also note that a certain number of tests are required to avoid any misinterpretation. The ISO standard [240] specifies that three tests are necessary to validate a non-cracking condition — but that a single test is sufficient to confirm a cracking condition. This repeatability requirement may significantly increase the size of the testing campaign and must be anticipated during the design of experiments. Nevertheless, this test procedure presents some advantages:

- The stress state applied is independent of the welding conditions to be investigated (it is an externally loaded test). Thus, it is easy to obtain both cracking and non-cracking conditions, which can both guide an implant test campaign and help to calibrate a numerical model of the implant test.
- The implant test is relatively straightforward and minimises material consumption.
 The post-test destructive analysis procedure is also quite rapid.
- It is the only test currently recognised by the French regulatory authority.

In addition, despite difficulties that might be encountered in the assessment of dissimilar metal welds using the implant method, it should be suitable for the pair of metals considered here by using the smallest diameter, which is Ø 6 mm. However, considering the size and tolerance requirements for the notch given by the standard [240], specimen manufacture likely requires experienced operators.

Beyond the regulatory code guidelines, there is no universal consensus on the best cold cracking test method. Moreover, the relevance of the implant test procedure to the specific component and repair procedure considered here can be questioned. The thickness of the implant test specimen does not exceed 20 mm, whereas the reactor pressure vessel shell usually varies between 200 mm and 300 mm [17], [248]. This opens the door to the exploration of other test methods which could be more appropriate to the application. Developing a modified implant test could be pertinent. Nevertheless, other existing tests should be assessed first, especially those proposed in standards.

First, looking at the specific mock-ups developed during parallel research projects led by EDF in relation to the welding repair case studied here, the NeT-TG8²⁰ program mock-up [228], [243] can be mentioned. It consists of a massive block specimen with a groove in which five weld beads are deposited. This multi-pass test aims to reproduce closely the conditions of the welding repair, particularly the self-induced stress state and the metal microstructures produced by the effects of successive weld thermal cycles. However, it is not clear that the stress level generated would be sufficient to meet the unfavourable conditions required for cold crack occurrence.

Looking at the other standard test methods, two monolithic mock-ups have been proposed and may be relevant here: the Lehigh and the Tekken test devices. The first was conceived and developed by [249] in 1946, the latter by the Technical Research Institute of the Japanese National Railways also in the mid-20th century. Both are plane-slotted specimens, usually made of the assembly of two half-sides joined together by multi-pass welding. Their slots have a specific shape that produces a certain stress concentration [82], [97], [215], [216] (self-restraint tests). They are derived from a whole category of mock-ups whose slots are centred or sometimes offset towards the edges and for which various existing geometries enable adjustment of the stress concentration factor [250], [251]. To modify the self-restraint intensity, and thus the stress level generated, the mock-up thickness can be adjusted from a thin plate of a few millimetres to a block of several

The European Network on Neutron Techniques Standardisation for Structural Integrity – Task Group 8

centimetres [173]. The standard Lehigh and the Tekken have, respectively, a centred U-joint and a centred oblique y-slot. These types of tests require good repeatability in the case of non-cracking to confirm this result. The Tekken is the easiest to machine and has already been used at the EDF welding laboratory [47]. It thus appears to be the best choice.

The dimensions of any Tekken mock-ups should be optimised prior to their manufacture using computational simulations. These require calibration, for which thermocouple arrays are a proven technique. Several researchers have placed their thermocouples into narrow, deep holes close to the fusion boundary [47], [252]. This enables them to estimate the heat source shape precisely. However, concerning the needs in the investigation of the cold cracking phenomenon, evaluating the overall evolution of the temperature gradient by measuring surface temperature appears sufficient. Indeed, it was demonstrated during the NeT-TG4²¹ and NeT-TG6²² programs that appropriately designed surface mounted thermocouple arrays can be sufficient for this purpose. Therefore, additional surface temperature measuring techniques could be considered, such as pyrometry. Acoustic emission techniques may be also of interest to assist the analysis of the welded mock-ups by identifying the time and location of cracking during the tests themselves.

Finally, according to the logic given by the theory, the most critical weld deposited is the first one [34] since the base metal is at ambient temperature and no re-heating effect has yet occurred. Consequently, experiments should first focus on single-bead welds.

II.3.B Modelling & simulation

Welding simulation is likely to become increasingly important in predicting the risk of cold cracking defects in complex weldments. Indeed, it could facilitate risk assessment with a finer margin of error than experimental test methods, while reducing time and cost. Moreover, it has a proven track record in predicting several of the phenomena that drive the occurrence of cold cracks.

As suggested before, considering the real needs in the investigation of the cold cracking phenomenon, the number of various calculations to run, and the numerous

The European Network on Neutron Techniques Standardisation for Structural Integrity – Task Group 4
 The European Network on Neutron Techniques Standardisation for Structural Integrity – Task Group 6

assumptions and simplifications that would likely be required, it appears unnecessary to resort to overly sophisticated models of each mechanism involved in cold cracking, but rather to adopt a consistent and relevant set of simulations. In addition, 2D models may be sufficient to calibrate and validate a first approach. However, following the industrial expectations and the suggestions given in the literature, probabilistic approaches seem to be the most pertinent in risk prediction.

Nevertheless, modelling retains some limitations. These can result from incomplete models and/or non-pertinent input data. First, the ability to accurately predict microstructure development must be assessed, as this factor strongly influences the stress-strain response and the hydrogen sensitivity, the two other causes leading to cold crack occurrence. Second, the module modelling hydrogen diffusion and trapping developed by [47] offers promise. However, it requires a number of input parameters whose relevance to the actual microstructure of the base metal investigated can be questioned. Moreover, as this chemical calculation is the last to be run and coupled with the previous thermal, metallurgical, and mechanical predictions, it must be kept in mind that the quality of its results is highly dependent on their prior accuracy. Consequently, many experiments could be necessary to calibrate and validate the hydrogen module.

On the other hand, both thermal and mechanical models for welding simulation have been developed over several decades, benefiting from numerous experimental characterisations that ensure confidence in the required input data [253] and the simulation procedures, and provide validation of the thermo-mechanical predictions. The inclusion of metallurgical prediction in the analysis pipeline is less well developed, so requires more extensive validation.

II.3.C Small-scale testing

Finally, as is almost always the case, small-scale material testing appears to be of primary importance in the investigation of the cold cracking phenomenon. This covers two main interests:

It allows a single mechanism or process to be isolated and studied. This facilitates
the understanding of complex phenomena, and allows the development of relevant
models.

• Important material properties can be identified and measured, allowing the implementation of mechanistic models in computational simulations.

The set of characterisations envisaged in this research project is detailed in the following chapters. Nevertheless, a few conclusions drawn from the existing literature can be stated beforehand.

First, it has been noted that the experimental and numerical results of the Jominy end quench test are often "viewed" in different ways. Experimentalists typically look at one or two line(s) in the sub-surface region of the bar, while computational simulation developers visualise the entire longitudinal cross section of the bar, which nevertheless seems to return radially homogeneous results. This raises the question of whether the simulation agrees with the actual measurements made. However, this problem can be avoided with a little more sample preparation allowing experimental assessment of the entire longitudinal cross-section.

Second, mechanical testing campaigns appear inescapable to investigate hydrogen embrittlement phenomena, especially for building reference observations to feed computational models. Therefore, some key points can be underlined:

- Tensile testing is the most used method in previous work. Other methods could be relevant, such as toughness tests which assess the material resistance to crack propagation and/or its ability to absorb energy by plastically deforming without fracturing. Nevertheless, Charpy impact testing is not relevant, since it investigates energy absorption by rapid deformation, which is not the case with the cold cracking phenomenon. Tensile tests, on the other hand, present two substantial advantages:
 - The implant welding test is based on this mechanical testing method, so the two tests offer a higher degree of transferability and comparison
 - Mechanical behaviour laws and models are generally calibrated using stressstrain data derived using tensile tests
- V-notched specimens have been argued as poorly suited to evaluating the impact of
 microstructure. However, both smooth and notched specimens are commonly used
 to study hydrogen embrittlement, since they investigate different aspects of the
 mechanical load.

- The candidate microstructures, however produced, must be representative of the heat-affected zone ones.
- Although their use can be argued to be conservative, using specimens with uniform
 microstructures is important to avoid variations due to microstructural gradients.
 Clearly specimens containing realistic microstructural gradients could also be used
 to provide supplementary data.

III METHODOLOGY AND OPTIMISATION

III.1 FOREWORD

The conclusions presented previously enable the establishment of the research plan and the simplifying assumptions for this project.

First of all, despite the candidate bead tempering technique being the temper bead welding, it has been considered throughout this project that it would be the cold repair technique. In contrast to the temper bead welding which includes light pre-heating and post-weld heat treatment, the cold repair does not require any additional heating [25], [211]. This allows the research to be simplified, and maintains a safety margin with respect to the conclusions since the cold repair is more demanding than the temper bead welding method. The welding consumables, weld process parameters and configuration are developed in the last section.

III.2 MATERIALS

The low-alloy ferritic steel employed as the base metal in the experiments was from the 18MND5 material batch n° 3375.1, whose chemical composition diverged slightly from specification, allowing it to be treated as a 16MND5 for research purposes. It was produced by Creusot-Loire Industries (France). Its chemical composition is presented in **Table III-A**. Its carbon equivalent is about 0,622 wt% when calculated according to the formula (II-4), which is slightly higher than standard 16MND5 (≈ 0,586 wt%). The nickel-based alloy utilised as filler metal wire was Inconel 52M (heat/batch n° NX7208TK) supplied by Special Metals Corporation (USA). Its chemical composition is given in **Table III-A**. These are the same batch and heat/lot of materials used in the NeT-TG8 program.

Table III-A: chemical composition analyses of the employed metals in this research project: 18MND5 batch n° 3375.15 (considered as being 16MND5) & nickel-based alloy Inconel 52M batch n° NX7208TK – values from the material certificates provided by the suppliers

BASE METAL											
considered designation	С	Si	Mn	Ni	Cr N	10	P	S	Cu	V	Al
16MND5 rolled quenched tempered	0,181	0,216	1,53	0,625 (0,202 0,	479	0,0063	0,0029	0,111	≤ 0,005	0,022
FILLER METAL											
commercial designation	С	Si	Mn	Ni	Cr	Mo	P	S	Cu	Со	Al
Inconel 52M (coiled wire)	0,017	0,12	0,72	59,36	30,05	0,01	0,004	0,001	0,03	0,006	0,11
	Nb + Ta	. Fe	Al +	<i>Ti</i> Ti	В		Zr	other			
	0,83	8,49	0,34	4 0,23	3 0,00	1 :	≤ 0,01	≤ 0,50			

It must be noted that the base metal batch employed has been prepared by the supplier like those employed in nuclear steam supply system components manufacturing. This includes, among others, quenching and tempering thermal treatments, and particularly rolling operations. Consequently, particular attention has been paid to the anisotropy of the material, always selecting the same orientation with respect to the rolling direction for specimen extraction, and as it would be in the case of real components.

III.3 RESEARCH PLAN

Two principal areas were first established to address the project expectations:

First, it appeared of interest to conduct benchmarking of the implant and Tekken cold cracking test methods. This allowed examination of the third conservatism concerning the relevance of the implant test, the historical method and the only one recognised by the French regulatory codes [33], [46] for assessing welding procedures used for repair purposes. These results also brought new key findings for discussing the first conservatism relative to the viability of such repair methods using bead tempering. Finally, they were also useful for initiating the thinking on the second conservatism,

questioning the pertinence of a deterministic failure criterion, versus a probabilistic approach, for estimating the risk, either experimentally or by computational analyses.

Second, investigating the behaviour of the welding heat-affected zone exposed to hydrogen, a key factor driving the cold cracking phenomenon, is also important for advancing knowledge of the extent of the hydrogen embrittlement phenomenon in this steel placed in critical conditions of microstructure and mechanical loading. These results have contributed to the progression of the discussion of the first and second conservatisms.

However, there was also a lack of knowledge regarding the stress levels generated in the Tekken mock-ups. Addressing this appeared to be of crucial importance for the discussion of the third conservatism, but also to enable a consistent comparative assessment with the implant test method. Therefore, a modelling study of this test specimen was conducted. The need for small-scale testing to provide input data and qualify a reliable numerical simulation chain was also identified and addressed.

Finally, for the reasons previously mentioned in the literature review conclusions **II.3.B**, the development of hydrogen diffusion modelling was not extended during the course of this project in view of the lack of reliable input data required to enhance, calibrate and validate the prediction abilities of such a model, and the significant number of additional experiments needed to address this. Nevertheless, it would be of interest to aid the discussion of the first conservatism.

III.4 WELDING CONDITIONS & PARAMETERS

The welding processes and parameters used throughout this project were selected during previous studies led by EDF and its partners. The tungsten inert gas processes were preferred. The parameters were developed in order to enable the implementation of bead tempering methods. However, some possible variation remained in the following parameters:

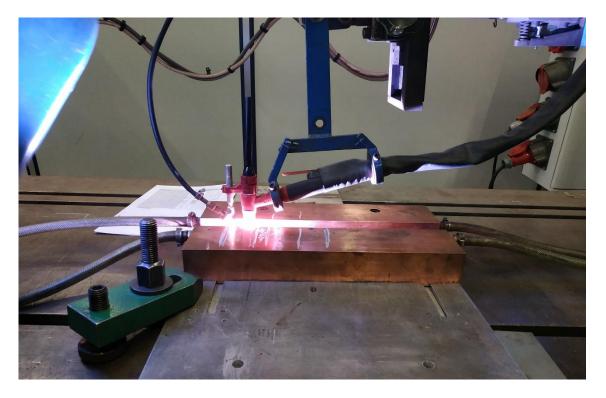
- Current intensity
- Voltage
- Welding torch travel speed
- Filler wire feeding speed

The ranges of some of these were refined during the NeT-TG8 program [228], [243] to optimise the quality of the weld bead deposit.

On the other hand, [40], [232] recommend that intentionally unfavourable conditions should be imposed to allow formation of cold cracks within this class of low-alloy ferritic steels.

Furthermore, the exact content of hydrogen that could be found in the shielding welding atmosphere during such a repair – in real conditions within the containment building of the nuclear steam supply system – was not known at this stage. Consequently, it was decided to focus our investigations in the worst degraded conditions to ensure sufficient safety margins. It was therefore hypothesised that using a shielding gas containing a certain amount of hydrogen to artificially reproduce the hydrogen sources could be of interest.

Therefore, considering the remaining tolerances in the parameters, the values that lead to the maximum hydrogen content in the weld metal were sought. Due to the skills required and hazards associated with the experimental method described by ISO 3690 standard [145] (metallic mercury, mercury vapours, and very low-temperature liquids (-78 °C to -196 °C)), this initial small-scale campaign was entirely sub-contracted by EDF to the IS welding laboratory of Yutz. The IS has produced a complete technical report [254] describing this testing campaign. **Picture III-a** and **Picture III-b** show some stages of these experiments. These results are summarised in **Table III-B**.



Picture III-a: welding of an ISO 3690 mock-up (source: the IS)



Picture III-b: analysis of an ISO 3690 sample using metallic mercury (source : the IS)

The maximum hydrogen concentration introduced into the weld metal during these tests was 0.73 ± 0.06 wppm using the set of parameters H. The latter were retained for the next stages of this project. However, as the cross-sectional area of the weld bead was too small to weld the cold cracking test mock-ups correctly, the filler wire feeding speed was thus changed to 3.0 m/min. In addition, the IS estimated the hydrogen contents present in the Alloy 52M wire to be 8.98 wppm using katharometry analysis method (also known as "gas analysis by thermal conductivity measurement"). Such a concentration is considered high compared to usual levels in filler metals commonly employed.

Table III-B: diffusible hydrogen contents measured by the mercury displacement method as prescribed by ISO 3690 [145] (source: [254])

test reference	H ₂ content in shielding gas	current intensity [A]	voltage [V]	welding torch travel speed [cm/min]	filler wire feeding speed [m/min]	linear energy [kJ/cm]	deposited metal section [mm²]	diffusible H in weld metal [wppm]
B1	0 %	240	13,2	12	1,5	15,84	5,27	0,0
B2	0 %	240	12,3	12	1,5	14,76	10,71	0,0
В3	0 %	240	12,3	12	1,5	14,76	9,21	0,0
D1	2 %	180	11,0	6	2,0	9,90	22,41	0,0
D2	2 %	180	11,2	6	2,0	10,08	24,62	0,0
D3	2 %	180	11,3	6	2,0	10,17	22,52	0,0
E1	2 %	240	14,3	12	1,5	17,16	9,39	0,0
E2	2 %	240	14,2	12	1,5	17,04	8,29	0,0
E3	2 %	240	14,5	12	1,5	17,40	8,29	0,0
F1	5 %	220	13,4	9	1,8	14,74	12,60	0,0
F2	5 %	220	13,6	9	1,8	14,96	13,73	0,0
F3	5 %	220	13,5	9	1,8	14,85	13,50	0,0
G1	5 %	180	13,4	6	2,0	12,06	24,97	0,0
G2	5 %	181	13,4	6	2,0	12,13	27,65	0,6
G3	5 %	179	13,4	6	2,0	11,99	24,62	0,0
H1	5 %	238	15,6	12	1,5	18,56	7,73	0,7
H2	5 %	240	15,6	12	1,5	18,72	8,51	0,7
Н3	5 %	239	15,6	12	1,5	18,64	8,30	0,8
I1	5 %	220	13,5	9	1,8	14,85	15,08	0,6
I2	5 %	220	13,5	9	1,8	14,85	13,72	0,3
I3	5 %	220	13,5	9	1,8	14,85	12,01	0,5

0 % : Air Liquide Arcal PRIME (99,998 % Ar) – **2** % : Linde Varigon 2 (98 % Ar + 2 % H_2) – **5** % : Linde Varigon 5 (95 % Ar + 5 % H_2)

Hence, the final welding conditions and parameters selected are detailed in **Table III-C**. In addition, [36] suggested that tilting the welding torch may impact the penetration depth and thereby the risk of lack of fusion. Consequently, it was decided to maintain the torch in a vertical position throughout the welding tests to prevent any inconsistency in the results.

Table III-C: welding parameters and conditions selected for this research project

parameter	value
shielding gas	Linde Varigon 5 (5 % H ₂ + 95 % Ar)
gas flow rate	$11.0 \pm 0.3 \text{ l/min}$
welding torch travel speed	0,12 m/min
nominal current intensity low	$240\pm1~A$
nominal current intensity high	$240 \pm 1 \text{ A}$
pulsing frequency	0 Hz (direct current)
time high	N/A
time low	N/A
start current intensity	$20\pm1~A$
final current intensity	$30 \pm 1 \text{ A}$
filler wire feeding speed	3,0 m/min
contact-tip to workpiece distance	$30{,}75 \pm 0{,}50 \text{ mm}$
standoff distance	$21,25 \pm 0,35 \text{ mm}$
electrode stick out	$15,00 \pm 0,1 \text{ mm}$
electrode extension	$24,50 \pm 0,25 \text{ mm}$
arc length (from groove bottom)	$6,25 \pm 0,25 \text{ mm}$
filler metal wire-electrode distance	$2,50 \pm 0,25 \text{ mm}$
gas cup internal diameter	Ø $11,25 \pm 0,10 \text{ mm}$
filler metal wire diameter	Ø 0,9 mm
start of pre-gas (purge before arc on)	n-5,00 s
arc on	n-0,20 s
start of current ramp up	n s
end of current ramp up	n+0,95 s
start of filler wire feeding	n+2,40 s
start of torch moving	n+3,20 s
arc polarity	electrode [-]
end of torch moving	N-2,65 s
end of filler wire feeding	N-0,20 s
start of current ramp down	N s
end of current ramp down	N+4,40 s
arc off	N+4,45 s
post-gas (shielding after arc off)	N+4,45+15 s
electrode	tungsten – 2 % lanthanum

electrode angle 30°

arc voltage control feature (A.V.C.) enabled

voltage $15,60 \pm 0,75 \text{ V}$

welding process type tungsten inert gas (T.I.G.)

linear energy 18,720 kJ/cm

average power 3,744 kW

IV STUDY OF THE TEKKEN WELDING TEST

IV.1 FOREWORD

Prior to manufacture of the Tekken specimens used in the next welding test benchmarking chapter, a series of computational studies was conducted to investigate the generated self-restraint intensity (published paper: [255]). The residual stress level applied to the weld increases with the mock-up thickness, at the expense of higher material consumption. It was decided to aim at maximum residual stress state in order to generate the highest risk of cold cracking. The optimal dimensions were therefore sought. To feed the simulation, a mock-up left over from the precedent campaign carried out by [47] was used for a thermally instrumented welding test (using nickel-based alloy 52M as filler metal). In addition, several small-scale characterisations were conducted to adjust and/or qualify the simulation calculation sequence. The outputs of this chapter were of interest to address part of the objectives related to the third conservatism (exploring the Tekken test relevance for evaluating bead tempering methods).

IV.2 METHODS

IV.2.A Modelling & simulation

A 2D thermo-metallo-mechanical finite element model was constructed. This idealisation ensures a good ratio between the calculation duration and sufficient accuracy of the results. The model represents a mid-length transverse cross-section of a Tekken mock-up, as shown in **Figure IV-a** (ISO 17642-2 [191] standard design). This ignores the perturbations at the welding start and stop positions at the bead extremities. Models were generated and run for a full range of different mock-up thicknesses (15 mm to 150 mm), allowing rapid identification of the stress state level for each Tekken size for the base and filler metals and welding parameters previously defined (refer to **III.4** and **Table III-C**).

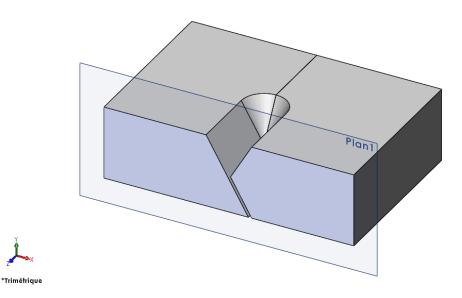


Figure IV-a: illustration of the modelled 2D slice position within the Tekken test mock-up

The simulation followed this sequence order: thermal, metallurgical, and finally, mechanical calculations. A full metallo-mechanical coupling was used. The thermal calculation obviously drives all subsequent calculations, but this is not considered as a coupling as such. On the other hand, liquid-solid and solid-solid phase transformations can significantly impact thermal kinetics, especially due to the latent heat effects. As is commonly practised, this is also not treated as a coupling as such, but it is reflected in the thermal property tables used as input data.

IV.2.B Material properties

IV.2.B.1 Base metal

The material properties used in the simulation of the 16MND5 steel were principally sourced from the compilations made at EDF [223], [253], [256], [257]. In order to reliably reproduce the actual mechanical properties of this metal batch after quenching-tempering-rolling operations, the initial distribution of micro-constituents was assumed to be a mixture made of 61 % ferrite and 39 % bainite (which may not reflect the real microstructure composition).

To address the computational welding simulation's specific needs, the used mechanical model combined a classical plastic behaviour modelling the low-temperature cases (when viscous effects are still negligible) and a visco-plastic behaviour hardenable at high temperatures [258]–[260]. It also covered strain-hardening recovery mechanisms and metallo-mechanical coupling. The latter included the solid-solid phase transformation-

induced plasticity phenomenon as well as a definition (based on a mixing law) of the thermo-elastic and visco-plastic behaviours as a function of the proportions of the micro-constituents. Furthermore, the strain-hardening was described in a non-linear way. To that end, for each micro-constituent and each temperature interval, a set of isotropic strain-hardening curves as a function of the cumulative plastic strain was provided as input data, thus describing parametric surfaces. Consequently, the reliability of the mechanical calculations depends closely on the quality of the metallurgical predictions. However, it must be noted that the thermo-elastic law only considers two sets of volume and coefficient of thermal expansion parameters for the unit cells: one for the cold micro-constituents and a second for the hot micro-constituents [261].

In order to refine the microstructure prediction abilities used for the particular chemical composition of this steel batch, a specific continuous cooling transformation diagram was calculated using a tool recently developed at the MaSC, based on Li's model [226], [245]–[247]. However, a preliminary estimation of the austenitisation temperature and prior austenite grain size range that could be typically encountered in the gas tungsten arcwelding process was necessary. Considering the observations of [226], a range from 3 μ m to 130 μ m was adopted. Hence, the average value (66 μ m) and the commonly considered temperature of welding molten pools (1 450 °C [58]–[60]) were utilised to run this continuous cooling transformation diagram calculation. It was directly returned under a format readable by the Code Aster solver.

During simulation, the feature enabling this solver to adapt its interpretation of the continuous cooling transformation diagram as function of the calculated grain size was activated. Nevertheless, the reliability of the prior austenite grain size prediction was questioned due to the lack of information on the source of the input parameters provided by the Code_Aster documentation for the 16MND5 steel [256]. Moreover, although the model used is proven, it has since been extended by [226]. Indeed, it was proposed to move from a single linear model to the combination of two successive ones, switching from one to the other at a certain temperature threshold.

Therefore, assessing the relevance of this newly built input dataset was first necessary. This was done using the small-scale characterisation experiments:

• Simulation of the dilatometry testing campaigns performed during parallel studies : assessment of the thermo-metallo-mechanical predictions.

• Realisation of a standard Jominy test ISO 642 [262] : assessment of the thermometallurgical predictions.

IV.2.B.2 Filler metal

The considered material properties of the nickel-based alloy 52M were sourced from the supplier certificate and the recent characterisations and compilations made by EDF and its partners. A metallurgical calculation was not required for this filler metal. It was thus neutralised using artificial values. The behaviour law employed is based on Chaboche's elasto-visco-plastic model [244], whose parameters were refined during the NeT-TG8 program [228], [243]. Considering that the cold cracking susceptibility of the weld metal did not require to be studied and that parallel projects have enabled its behaviour to be extensively described, it did not appear necessary to process further verifications.

IV.3 QUALIFICATION USING DILATOMETRY TESTING

Dilatometry is a small-scale test method of interest in assessing the reliability of material datasets utilised in welding simulations. It allows investigation at the same time of both conventional thermal expansion behaviour and solid-solid phase transformation. It is also commonly employed to establish continuous cooling transformation diagrams experimentally.

IV.3.A Experiment description

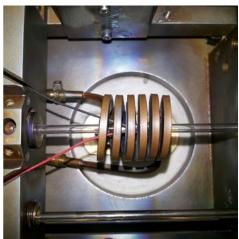
A dilatometer measures the change of length of a cylindrical specimen as a function of temperature. A range of temperature cycles relevant to weld fusion zone and heat-affected zone conditions have been explored as part of the NeT-TG8 and NNUMAN²³ programs [225], [228], [229], [243] in order to establish the continuous cooling transformation behaviour of two low-alloy pressure vessel steels. The profiles of the heat treatment cycles applied are given in **Diagram IV-a**. NeT-TG8 investigated the same batch of 16MND5 steel batch used in this project, while NNUMAN examined A508 Gr. 3 Cl. 1 steel. The used SA-508's carbon equivalent is about 0,603 wt% when calculated

141

²³ New Nuclear Manufacturing

according to the formula (II-4), which is slightly less than the used 16MND5 (≈ 0.622 wt%). The sample sizes were Ø 4 mm \times 10 mm long, and the used test machine was a Bähr-Thermoanalyse DIL-805. Pictures and a schematic illustration of the free dilatometry machine are given in **Picture IV-a** and **Figure IV-b**. The specimen is heated by an induction coil, which also serves as a cooling nozzle by spraying an inert gas flow (helium). The temperature is monitored using a thermocouple spot-welded onto the sample surface (S-type : 0 °C to 1 700 °C). The push-rod displacement is recorded using a linear variable differential transformer (L.V.D.T.).





SEALED CHAMBER

SAMPLE AND HEATING COIL

Picture IV-a: pushrod dilatometer machine used during the NeT-TG8 and NNUMAN programs (source: [243])

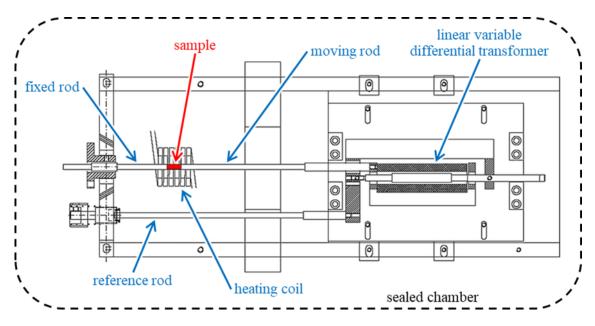


Figure IV-b: schematic drawing of the pushrod dilatometer machine used at during the NeT-TG8 and NNUMAN programs (adapted from [243])

IV.3.B Modelling & simulation

The 2D axisymmetric modelling of the dilatometry test specimen (half-rod) during this current research project used a mesh of 125 linear quadratic elements of about 400 μ m \times 400 μ m. The tests themselves were modelled using first an imposed temperature history that reproduced the induction heating and any high temperature dwell, and then the cooling phase in which heat loss from the sample to the helium gas via forced convection and radiation were explicitly modelled, with a heat transfer coefficient of 90 W·m⁻²·K⁻¹ [263], [264], and an emissivity coefficient ε = 0,07 [265]. The nodes of one half-rod end were considered as embedded along the longitudinal direction, and the nodes of the half-rod axis of symmetry as fixed along the transverse direction. The displacement was therefore followed using the nodes on the other half-rod end. Some adjustments were made to improve the correspondence of the prediction with the experimental results. Especially the volume ratio coefficient used by the Code_Aster solver to predict the solid-solid phase transformation strain between cold and hot micro-constituents (the only two densities considered by Code_Aster).

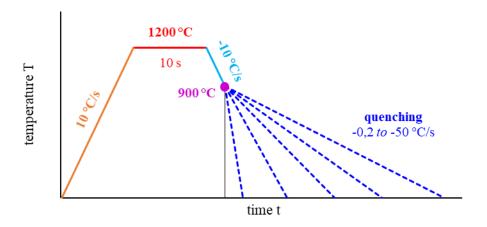


Diagram IV-a: heat treatment cycle profiles applied during the dilatometry tests of the NeT-TG8 project [228], [243] and the NNUMAN program [225], [229]

IV.3.C Results

The predicted temperature-strain cycles (calculated during this current project) compared with the experiments (conduced during the dilatometry tests of the NeT-TG8 project [228], [243] and the NNUMAN program [225], [229]) are presented in the following diagrams. The different cooling rates investigated are summarised in **Table IV-A**, including the micro-constituent distribution expected according to the observations previously done by [225].

Table IV-A: summary of the predicted temperature-strain cycles compared with the experiments conducted on this modelled steel (NeT-TG8 project [228], [243]) as well as on the SA-508 (NNUMAN program [225], [229])

cooling rate	diagram	micro-constituent distribution expected [225]
-50 °C/s	Diagram IV-b	\geq 95 % of martensite + retained austenite
-20 °C/s	Diagram IV-c	\geq 95 % of martensite + retained austenite
-10 °C/s	Diagram IV-d	≈ 80 % of martensite + 15 % of bainite + retained austenite
-5 °C/s	Diagram IV-e	≈ 60 % of bainite + 35 % of martensite + retained austenite
-2 °C/s	Diagram IV-f	\geq 95 % of bainite + retained austenite
-1 °C/s	Diagram IV-g	\geq 90 % of bainite + retained austenite
-0,2 °C/s	Diagram IV-h	\geq 90 % of bainite + retained austenite

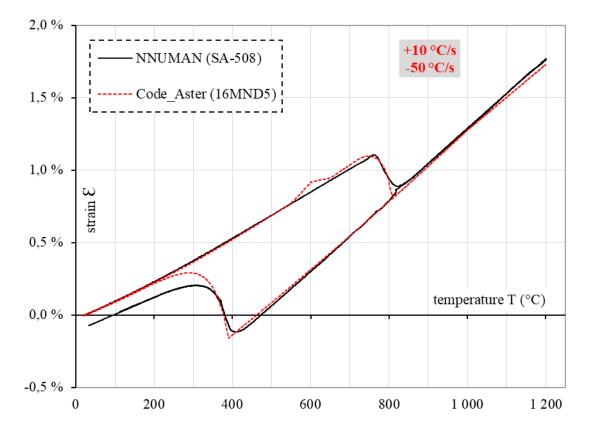


Diagram IV-b: comparison between the simulated 16MND5 dilatation behaviour and the experimental observations for SA-508 (NNUMAN program [225], [229])

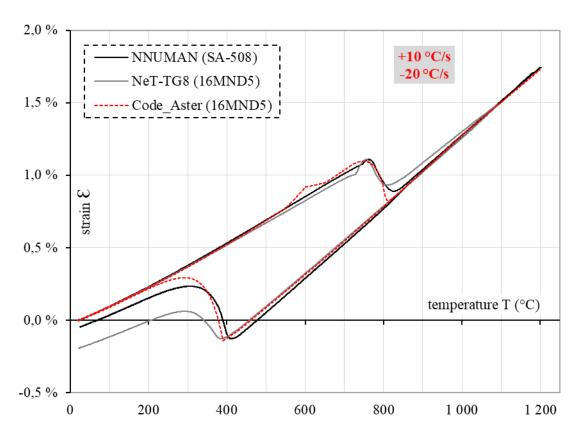


Diagram IV-c: comparison between the simulated 16MND5 dilatation behaviour and the experimental observations for this modelled steel (NeT-TG8 project [228], [243]) as well as for the SA-508 (NNUMAN program [225], [229])

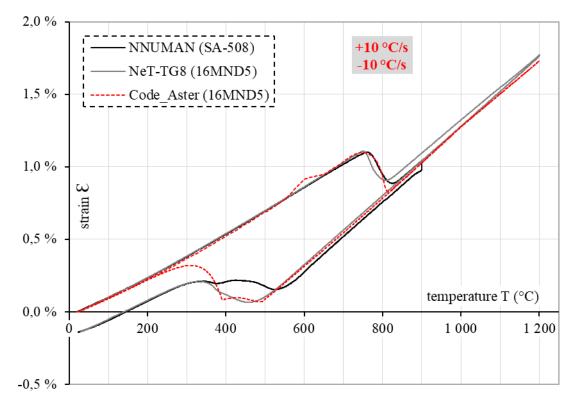


Diagram IV-d: comparison between the simulated 16MND5 dilatation behaviour and the experimental observations for this modelled steel (NeT-TG8 project [228], [243]) as well as for the SA-508 (NNUMAN program [225], [229])

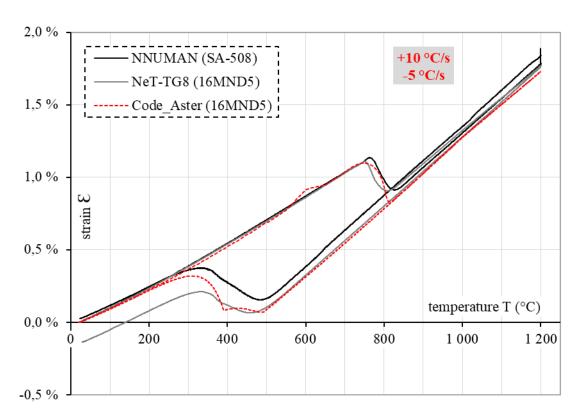


Diagram IV-e: comparison between the simulated 16MND5 dilatation behaviour and the experimental observations for this modelled steel (NeT-TG8 project [228], [243]) as well as for the SA-508 (NNUMAN program [225], [229])

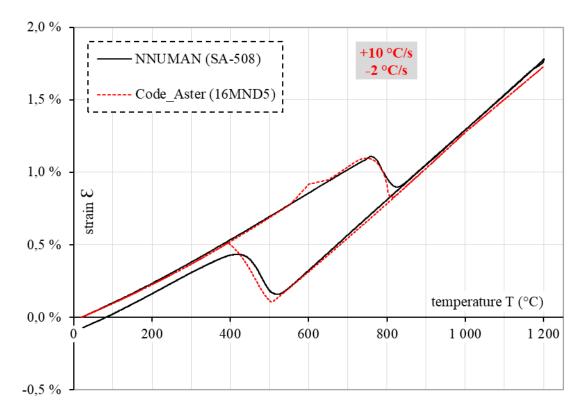


Diagram IV-f: comparison between the simulated 16MND5 dilatation behaviour and the experimental observations for SA-508 (NNUMAN program [225], [229])

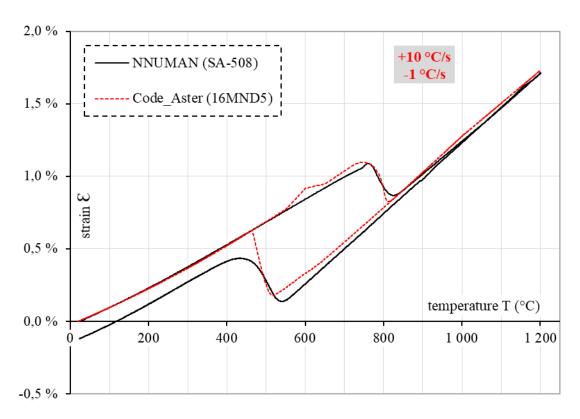


Diagram IV-g: comparison between the simulated 16MND5 dilatation behaviour and the experimental observations for the SA-508 (NNUMAN program [225], [229])

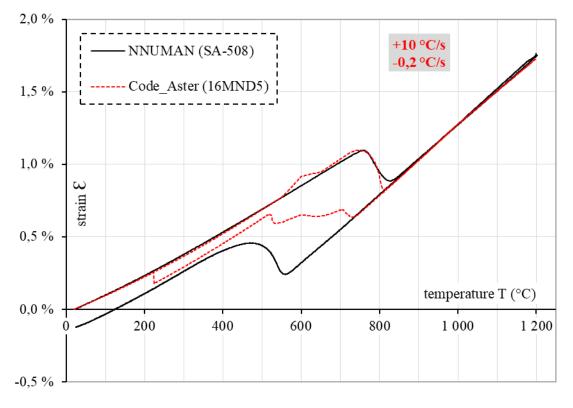


Diagram IV-h: comparison between the simulated 16MND5 dilatation behaviour and the experimental observations for the SA-508 (NNUMAN program [225], [229])

Despite some discrepancies, the dilatometry curves of 16MND5 and SA-508 agree relatively well. In the -50 °C/s and -20 °C/s cooling rates (**Diagram IV-b** and **Diagram IV-c**, respectively), it is evident that the transformations are likely to be predominantly martensitic (occurring at ≈ 400 °C). However, in any case, the 16MND5 seems to have a slightly lower transformation temperature (≈ 20 °C) than SA-508. The simulated curves of the 16MND5 agree pretty well with the experimental ones provided by the NeT-TG8 project [228], [243] and the NNUMAN program [225], [229], being generally closer to the 16MND5 results. Nevertheless, the prediction seems unstable and unrealistic regarding the slowest cooling rate (-0,2 °C/s, **Diagram IV-h**).

IV.3.D Discussion

Considering the deviation between the two experimental studies, the reliability of the micro-constituent distribution prediction was considered as being rather good for cooling rates faster or equal to -1 °C/s. This concerns, thereby, principally the martensitic and bainitic transformations. However, for slower cooling rates, the calculation was unstable and different from the experimental observations, predicting a proportion of ferrite. This may likely be caused by the limit of the continuous cooling transformation diagram calculation and/or solver interpolation issues and/or errored grain size prediction.

The simulation of the austenitic transformation was quite accurate. However, no explanation was found regarding the little, recurrent, and unexpected sudden expansion observed during the heating, near 600 °C.

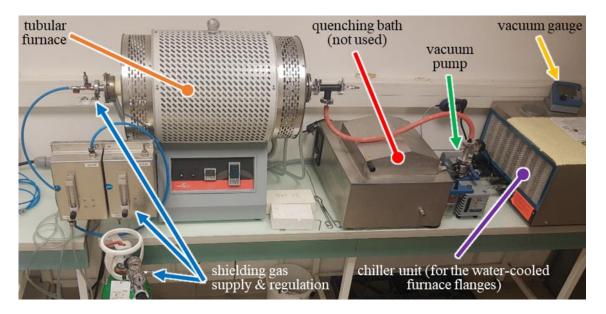
Nevertheless, the reliability of the model predictions was considered sufficient to use Code_Aster to estimate the expansion caused by metallurgical transformations in the heat-affected zone, as the expected cooling rates were faster than -1 °C/s.

IV.4 QUALIFICATION USING JOMINY TESTING

The Jominy test [221], [222], also known as "end quench hardenability test", is commonly used to assess the hardenability of a given steel. One single test allows the investigation of a wide range of cooling rates (approximately from 270 K/s to 0,7 K/s [266]). That is why it is a useful experiment to complete this assessment of the used material dataset reliability, mainly in terms of prediction of micro-constituent distributions over a large cooling rate range.

IV.4.A Experimental method

This quench test was executed following the ISO 642 standard [262] at La Rochelle Université (LaSIE) and post-test examination was conducted at the University of Manchester. The specimen was first machined by turning. To be consistent with the other experiments, the Jominy bar was extracted along the rolling direction of the 16MND5 block. As recommended by the standard, the bottom end surface – on which the cooling water jet would be applied – was smoothed (down to Ra 0,8 µm) in order to ensure good heat transfer. The specimen was then uniformly heated from ambient temperature under a protective atmosphere to prevent surface oxidation. Which could affect heat transfer efficiency. This was done using a laboratory tube furnace ThermConcept ROS 75/700/12-3. After purging the ambient air twice with a vacuum pump, a constant shielding gas flow of argon was applied through the tube, and the heating started. This setup is shown in **Picture IV-b**. A hook was screwed on the top side of the bar to facilitate handling. A low heat dissipation impact induced by this feature was assumed. The Jominy specimen technical drawing is given in **Figure IV-c** (in accordance with the standard [262] requirements).



Picture IV-b: sealed tubular furnace utilised for the Jominy specimen austenitisation

It was decided to focus this experiment on the coarse-grained heat-affected zone close to the fusion boundary, because this is the most critical microstructure with respect to the risk of cold cracking. Considering the typical temperature of a molten metal pool generated during an arc-welding operation ($\approx 1\,450\,^{\circ}\text{C}$), the austenitisation of the Jominy specimen was processed at $1\,200\,^{\circ}\text{C}$, the maximum temperature attainable by this furnace. As required by the standard, the bar was held at this temperature for 30 minutes to ensure homogeneous austenitisation.

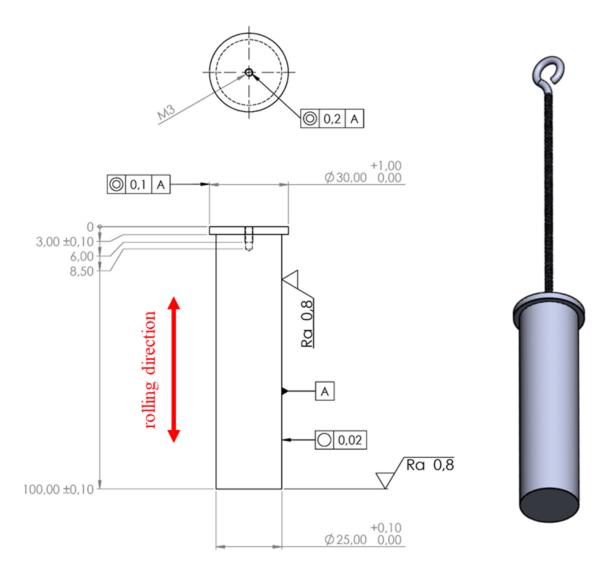


Figure IV-c: technical specifications of the Jominy specimen (in accordance with the standard [262] specifications)

Once the holding duration was completed, the specimen was extracted from the furnace chamber, positioned onto the Jominy test bench in less than 5 seconds, and then cooled down from the bottom end face by a controlled water jet (refer to **Figure IV-d**). Tap water was used as cooling fluid (18,5 \pm 2 °C). Therefore, various cooling rates were experienced along the Jominy bar, enabling a wide scan in a single test. The thermal cycle is summarised in **Diagram IV-i**.

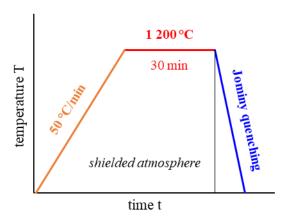


Diagram IV-i: diagram representing the thermal treatment cycle applied to the Jominy ST specimen

In addition, a setup was engineered to monitor the temperature transient occurring during the Jominy quenching in order to calibrate the computational simulation of the test. The sealed chamber of the furnace did not allow passage for thermocouple wires, and the short transfer time between furnace and quenching rig made the presence of wires problematic. A digital pyrometer offering easy mounting on a setup thanks to a portable head with a fibre optic link was available at the EDF PRISME welding laboratory. Its temperature measurement range is 350-1 300 °C. This option was thus explored and appeared to be relevant. This device was supplied by Advanced Energy Industries (*ex-LumaSense Technologies*), model IMPAC IGAR 12-LO MB 13. It measures using a two-colour principle (also known as "bi-chromatic") in which two adjacent wavelengths – 1,28 μ m and 1,65 μ m – are used to calculate the temperature using the ratio principle. This technique offers two significant advantages compared with a standard single-colour pyrometer:

- The temperature measurement is independent of the emissivity ε of the object over a wide range of temperature
- It eliminates several factors that degrade the accuracy of a conventional singlecolour instrument, such as dust in the field of view, dirty viewing windows or lenses, surface roughness, and oxidation.

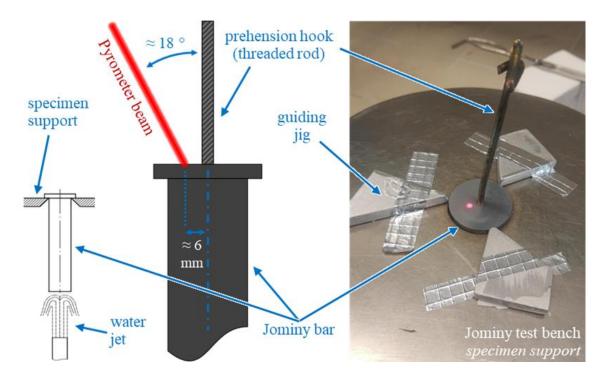
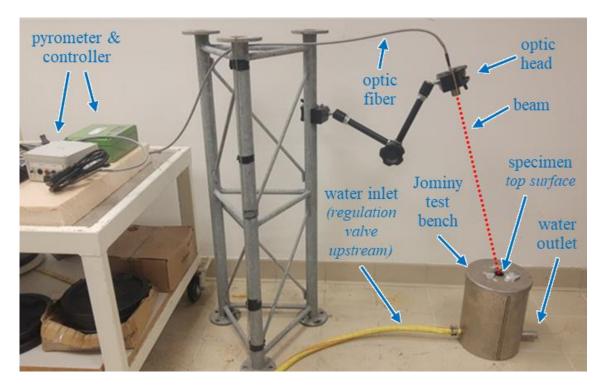


Figure IV-d: schematic illustration of the Jominy test setup and position of the pyrometer focal point on the top surface of the specimen (pyrometer beam spot represented by the laser targeting light feature) – left-hand schematic illustration adapted from [262]

It was necessary first to establish the calibration reliability of this dual-wavelength mode. This preliminary step is described in the next section **IV.4.B**. Then, the focal point of the pyrometer beam – spot size Ø 2,7 mm; 60 cm from the front of the lens of the optic head – was positioned using the laser targeting light feature on the top surface of the bar when placed on the Jominy test bench. The beam spot was placed a few millimetres distance from the bar centre with an incidence angle of $18 \pm 2^{\circ}$ to allow sufficient working space for handling and positioning the hot sample from the furnace to the test stand (refer to **Figure IV-d**). Three additional jig guides were added to the Jominy test bench to compensate for the backlash, thereby ensuring precise specimen positioning with respect to the pyrometer beam spot. The complete instrumented Jominy test rig setup is shown in **Picture IV-c**.



Picture IV-c: Jominy quenching test setup instrumented with pyrometry

After quenching, the specimen was prepared for metallurgical analysis. First, the specimen was cut into three longitudinal "slices" using electrical discharge machining (E.D.M.), see Figure IV-e (Ra 0,4 μm). The surfaces were then wet ground down to P1200 grade using silicon carbide (SiC) papers (grinding parameters : 150-300 rpm) then polished down to 1/4 µm grade using polycrystalline diamond solutions (polishing parameters: 150 rpm). The surface preparation consumables were supplied by MetPrep, SIA Abrasives Industries or Spectrographic. Hardness measurements were made using an EMCO-TEST DuraScan 80 G5 machine (Vickers method). The ISO standard [262] prescribes a single line of measurement of the outer sub-surface on two sides of the specimen using a test load of 30 kg_f. However, this machine was limited to 10 kg_f. This maximum load was thus used to process standard measurements on one side only (plane 1). In addition, three measurement lines were also realised parallel to the standard line (thereby also on plane 1) with a minimum increment of 0,25 mm and using a test load of 1,00 kg_f to be consistent with the hardness measures realised during other projects, such as the NeT-TG8 program [228], [243]. Furthermore, the half-side of the longitudinal cross-section of the bar (plane 2) was mapped with minimum intervals of 0,50 mm to enable consistent comparisons with computed simulation (test load of 1,00 kg_f). Finally, the prior austenite grain size of the quenched microstructure (longitudinal cross-section – plane 2) was optically measured using observations made with a digital microscope Keyence VHX-5000 after chemical etching using 2 % nital reagent for 30 seconds.

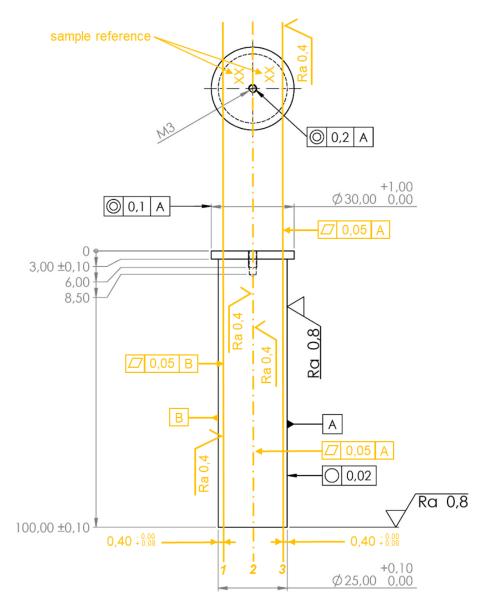


Figure IV-e: technical details of the cutting plan of the Jominy sample for post-test analyses

IV.4.B Pyrometer qualification

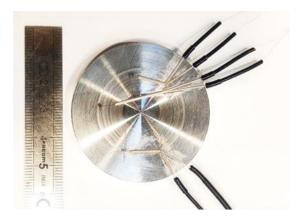
Calibration of the pyrometry measurements was first undertaken at EDF PRISME prior to processing the Jominy test at the LaSIE. Adjustments were possible by tuning the emissivity slope ratio K (refer to (IV-1)).

$$K = \frac{\varepsilon_{wavelength 1}}{\varepsilon_{wavelength 2}}$$
 (IV-1)

To that end, a sample reproducing the top surface of the Jominy bar was machined by turning. Three K-type micro-thermocouples (chromel-alumel ; \emptyset 65 μ m wires; thermocouple size $\approx \emptyset$ 250 μ m; -180 °C to 1 200 °C operating range) were spot-welded onto one side (refer to **Picture IV-d**). The advantage of a micrometre-sized thermocouple

is that it offers a low thermal inertia thanks to its small volume, which allows thereby highly dynamic monitoring of temperature changes, at the expense of more difficult fabrication and welding. In addition, again thanks to their small size, they enable very localised measurements, which is of interest when significant thermal gradients occur.







Picture IV-d: spot-welded micro-thermocouples on a sample representing the upper surface of the Jominy specimen (PASEPMARTY1 sample)

The sample and the pyrometer optic head were then positioned in order to reproduce the Jominy test conditions: a distance of 60 cm from the front of the lens to the sample, and an incidence angle of $18 \pm 2^{\circ}$ (refer to **Figure IV-f**). The pyrometer beam spot was focused and centred onto one of the thermocouples (refer to **Picture IV-e**). Only one thermocouple was used at a time. When one failed, another was then used. A sufficient distance was respected between the thermocouple and the ceramic wire sheaths to minimise the measurement perturbations (refer to **Picture IV-d**). The microthermocouple wires were assumed sufficiently thin to be neglected.

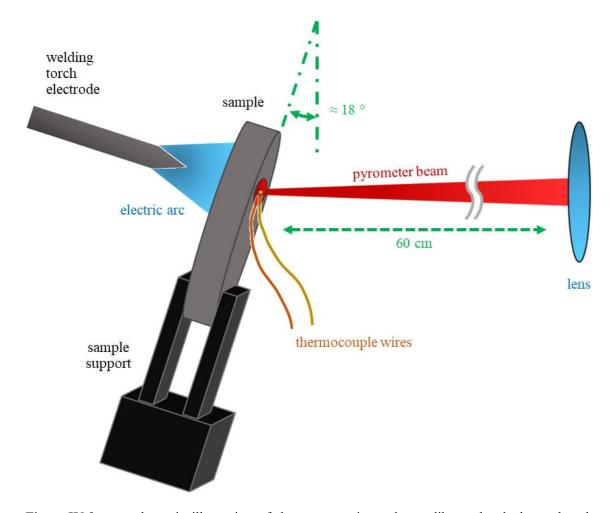
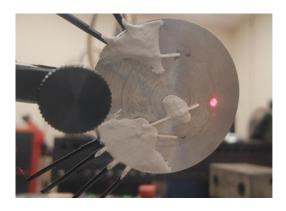


Figure IV-f: schematic illustration of the setup engineered to calibrate the dual-wavelength mode of the pyrometer

The sample was then heated from the back face using an electric arc – approximately aligned with the thermocouple and the pyrometer beam spot (refer to **Picture IV-e**) – generated with the robotised tungsten inert gas welding station Valk Welding VWPR QE Extern²⁴ (refer to **Picture IV-f**). The signal from the thermocouple was recorded using a thermocouple input module National Instruments NI 9213 (mounted on a cDAQ 9174 chassis) and connected to the computer using the acquisition software LabVIEW SignalExpress. The pyrometer was connected to the computer using the software Advanced Energy Industries InfraWin 5.0.1.41.C (control and signal acquisition).

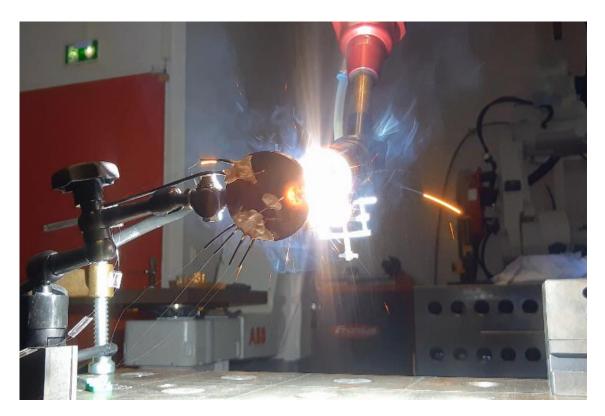
²⁴ Composed of a VWPR-TIG I welding torch, a WGIII-E1400 robot system (Panasonic TA-1400 model), a torch water cooling system, and a control software (laboratory computer)





Picture IV-e: alignment of the arc-welding torch electrode and the pyrometer beam spot with the micro-thermocouple (pyrometer beam spot represented by the laser targeting light feature – PASEPMARTY1 sample)

Therefore, the pyrometer was calibrated using the thermocouple values as baselines. The thermocouple measurement system was calibrated by the manufacturer. It was thus considered reliable. Each thermocouple tolerated five to ten tests before failing. Approximately 25 runs were necessary to adjust the emissivity slope ratio K between the two pyrometer wavelengths. The final K adjustment was re-tested twice to establish the repeatability, which was very satisfactory. The obtained calibration is shown in **Diagram IV-j**. The signals of both measurement systems were almost perfectly matched, proving the qualification and reliability of the pyrometer setup to monitor Jominy specimen cooling under this configuration.



Picture IV-f: heating of the calibration sample up to 1050 ± 50 °C using the robotised tungsten inert gas arc-welding station (PASEPMARTY1 sample)

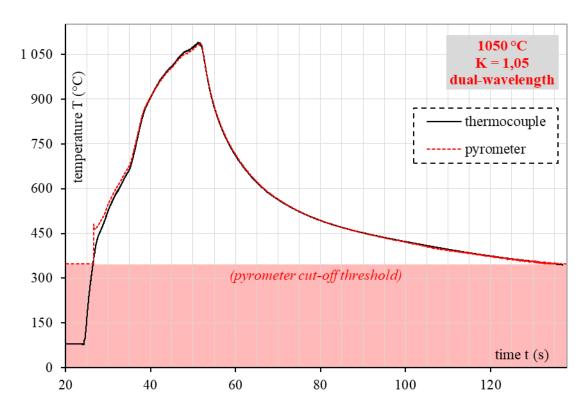


Diagram IV-j: calibration of the pyrometer based on the thermocouple measurement (PASEPMARTY1 sample – final adjustment: K = 1,05)

IV.4.C Modelling & simulation

A 2D axisymmetric model of the Jominy specimen was constructed using 5 000 linear quadrilateral elements of size about 500 μ m × 500 μ m. The imposed temperature history comprised first heating by forced convection, reproducing the shielding gas flow in the furnace, with a surface heat transfer coefficient of 90 W·m⁻²·K⁻¹ [263], [264]), then followed by a second general heat exchange reproducing the loss during the transfer and quenching. Considering the presumed air circulation generated by the sample moving and then by the water jet flow in the closed test rig "box", the forced convection exchange coefficient was kept. The radiation loss was also included (ground or machined steel surfaces : $\varepsilon = 0.50$ [265]). The water jet cooling was simulated by imposing a boiling/liquid heat transfer on the bottom end of the bar : 6 500 W·m⁻²·K⁻¹ [263]. The sequence of the applied boundary conditions is summarised in **Figure IV-g**.

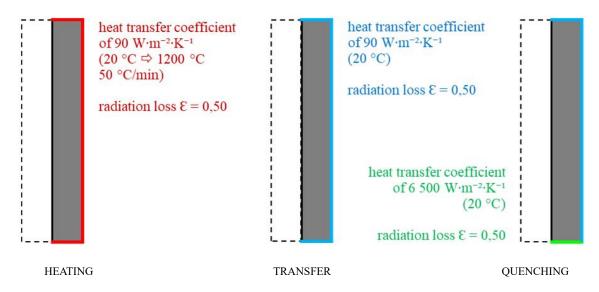


Figure IV-g: summary of the boundary conditions applied to the Jominy model

The initial micro-constituent distribution has been kept at 61 % of ferrite & 39 % of bainite (refer to IV.2.B.1). As the specimen is fully austenitised here, it was not considered necessary to reflect the actual initial microstructure. The hardness values of some of the micro-constituents were adjusted using experimental data for coarse-grained microstructures, obtained from dilatometry and Jominy tests, and during the behaviour study of the heat-affected zone exposed to hydrogen (section VI.3.C.3), as follows:

- -2 °C/s ⇒ nearly pure bainitic microstructure [225] ⇒ 290 HV
- From -20 °C/s ⇒ nearly pure martensitic microstructure [225] ⇒ 450 HV

IV.4.D Adjustment of the thermal solution

The initial simulation of the cooling kinetics of the upper surface of the specimen did not agree with the experimental measurement made using the pyrometer (refer to **Diagram IV-k**). The imposed thermal boundary conditions were considered realistic, with heat loss dominated by the water jet. Moderate variations in the heat transfer coefficient representing the water jet produced only minor changes in the metal temperature history.

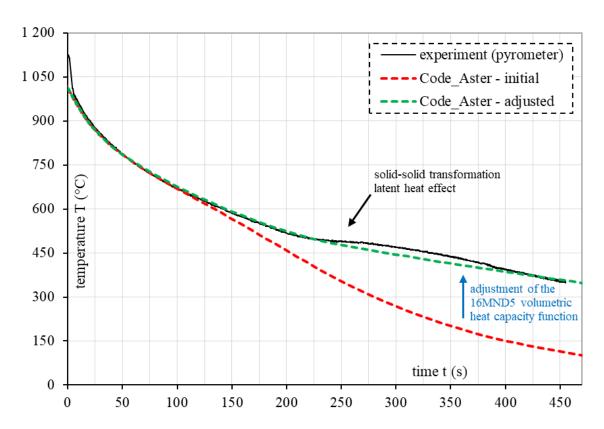


Diagram IV-k: adjustment of the 16MND5 material properties to match the calculated cooling of the Jominy specimen with the experimental measurement (Jominy ST specimen)

Moreover, an inflexion of the experimental curve is observed when the divergence with the initial simulation curve becomes more pronounced (refer to **Diagram IV-k**). A similar inflexion of the temperature curve was also observed by [266] during their Jominy experiments instrumented with thermocouples at several locations along the bar. A detailed examination of this inflexion shows that it occurred at about 500 °C. The cooling rate measured from 800 °C onwards was approximately -2 °C/s. This corresponds to the temperature at which the bainitic transformation began, as observed previously in the dilatometry test reproducing this cooling rate (refer to **Diagram IV-f**).

Consequently, the gap between the experiment and simulation was assumed to be due to approximations in the estimation of the solid-solid phase transformation latent heat of this steel. The volumetric heat capacity function was thus adjusted to fit the modelling with the experiment (refer to **Diagram IV-k**). Once the temperature calculation of the top surface was correct, the entire cooling kinetic prediction of the Jominy bar was considered reliable since the cooling operates from the bottom to the top. Hence, the reliability of the following comparison in terms of micro-constituent distribution was improved.

IV.4.E Results

The hardness field was calculated from the predicted microstructure of the Jominy bar following a mixing law proportional to the percentage of each micro-constituent. It must be noted that the prior austenite grain size did not feature in the prediction of hardness. It was then compared with the experimental mapping (refer to Figure IV-h). The simulation predicted a quasi-uniform distribution along the radial direction of the bar, while the experiment showed variations. Indeed, it highlighted a central region harder than the outer periphery at the bottom end of the bar. On the other hand, a "layer effect" was observed in the upper area, following the rolling direction of this steel batch. The prior austenite grain size was measured at several locations. A size of $\approx 130 \pm 30 \,\mu m$ was evaluated within the outer regions, and $\approx 175 \pm 50 \, \mu m$ in the inner areas. However, since these measurements were made using optical microscopy, they could overestimate the real grain sizes. Electron microscopy (E.M.) would allow more reliable estimations, specifically using electron backscatter diffraction (E.B.S.D.) analyses. Nevertheless, this order of magnitude of the prior austenite grain sizes is consistent with the measurement processed using electron microscopy on smaller samples having been exposed to the same thermal cycle during the material study chapter, section VI.3.C.

In addition, the line measurements of the outer sub-surface hardness are plotted in **Diagram IV-I**. The calculated hardness plot is also included. No major difference was found in terms of general trend between the measures made using the test load of 10 kg_f and 1,00 kg_f. However, the lightest test load measurements highlighted considerable deviations at some areas along the test bar.

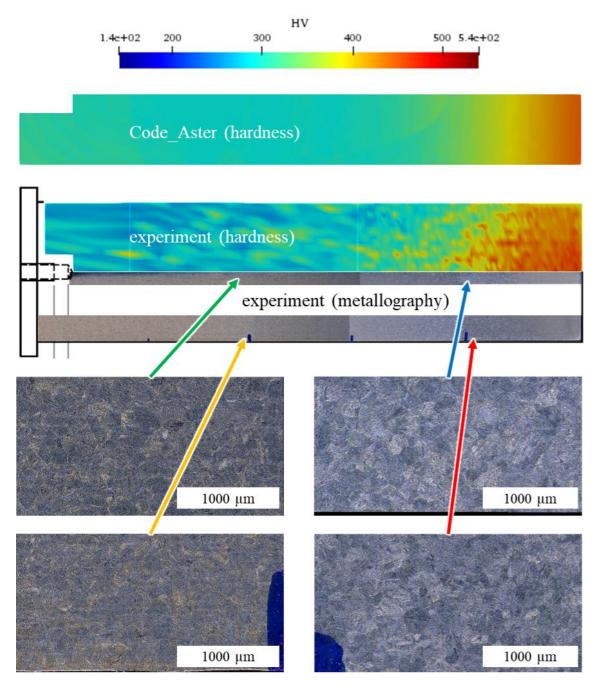


Figure IV-h: comparison of the experimental (HV1: test load of 1,00 kg $_{\rm f}$) and calculated hardness field of the half-side of the longitudinal cross-section of the Jominy ST specimen, completed with metallographic observations of some locations

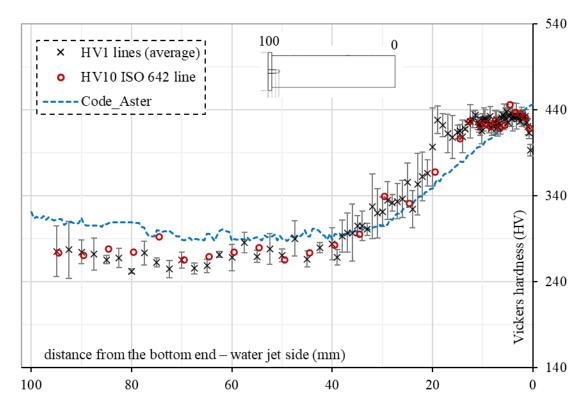


Diagram IV-1: hardness curves for steel grade 16MND5 after Jominy end quench hardenability test (Jominy ST specimen – HV10 and HV1: test load of 10 kg_f and 1,00 kg_f, respectively)

IV.4.F Discussion

The largest discrepancy between the simulation and experiment was observed at the ends of the bar (refer to **Diagram IV-I**). However, regarding the bottom face where the water jet was applied, this observation is not supported by the 2D mapping, which showed a good prediction of the general trend (refer to **Figure IV-h**). The deviation at the top face of the bar, was unexpected, as the cooling rates had been corrected during the calibration step presented previously (section **IV.4.D**). Moreover, the dilatometry test to model comparison already given in **Diagram IV-f** suggests that the predictive accuracy of the model should be good in this cooling range. Thus, this could be explained by overly approximative modelling assumptions or imprecise interpolations made by the solver. Nevertheless, this was a small-scale issue that was not considered to be a major potential cause of inaccuracy in the heat-affected zone predictions for arc-welds.

The most interesting observation was maybe from the experimental hardness mapping shown in **Figure IV-h**. At the bottom end of the bar, the central region appeared to be more hardenable than the outer periphery. It has been observed by [267] that the cooling rates do not diverge much between the central and outer regions at any location along the

bar during a standard Jominy test. Consequently, this hardness variation cannot be caused by faster cooling. In contrast, slight variations in the prior austenite grain size were observed between the inner and outer zones. Following the austenitisation operated during the sample heating, it seems that the austenite grains have grown larger in the central than in the peripheral zone of the Jominy bar. This may explain the higher degree of hardenability in this area. However, residual quenching stresses could also have occurred and interfered with the penetration of the hardness test machine's indentor, inducing inconsistent hardness measures along the radial direction. Finally, decarburisation of the peripheral region during specimen heating could also have occurred. This last hypothesis is perhaps unlikely as the heating operation was conducted under a shielding atmosphere.

However, it can be argued that standard Jominy testing does not reproduce the rapid thermal cycles experienced during a welding operation. Indeed, holding the specimen at 1 200 °C for so long (30 min) could lead to extensive grain growth. Consequently, the grain sizes could no longer be representative of weld microstructures. Thus, two non-standard Jominy tests were processed, aiming to get closer to welding thermal cycles. Only the holding duration was modified during the first one (referenced as "P1"). The simulation showed that only \approx 210 s were sufficient to reach a uniform temperature of 1 200 °C within the Jominy bar. Regarding the second one (referenced as "P2"), the austenitisation temperature was also reduced. As explained in detail in the **behaviour study of the heat-affected zone exposed to hydrogen**, a temperature of 870 °C was selected in order to get closer to the thermal cycles experienced in the remote heat-affected zone. The simulation showed that a holding time of \approx 800 s is required to uniformise the temperature within the bar at this lower austenitisation temperature. The P1 and P2 thermal cycles are summarised in **Diagram IV-m**.

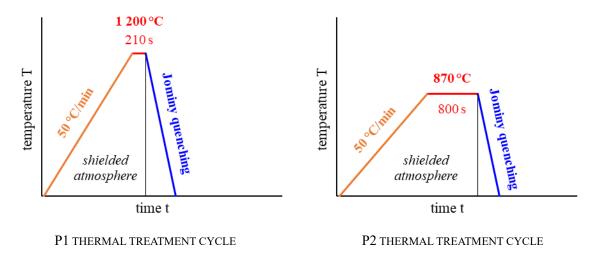


Diagram IV-m: diagrams representing the thermal treatment cycles applied to the Jominy P1 & P2 specimens

The hardness scans given in **Figure IV-i** did not show a significant difference between the standard "ST" and P1 Jominy tests, except for a reduction in the difference in hardenability between the central and outer peripherical regions. However, the scan of the P2 specimen suggested an incomplete austenetisation (disparate hardness peaks of 597 HV). This last test was thus invalided for any comparison.

The "layer effect" parallel to the longitudinal axis of the Jominy bars observed in the upper area was likely to result from the manufacturing steps during the production of this steel batch. This could be due to, for instance, the rolling operations, the thermal treatments, or simply non-uniformity in chemical composition in the ingot post-casting.

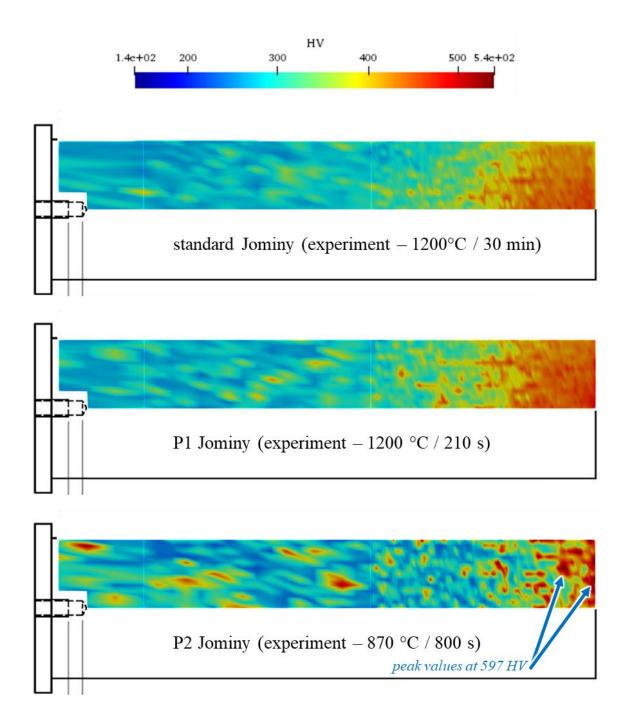


Figure IV-i: comparison of the hardness scans processed on the half-side of the longitudinal cross-section of the Jominy standard (ST), P1, and P2 specimens (HV1: test load of $1,00~kg_f$)

IV.5 TEKKEN MODELLING

IV.5.A Meshing strategy

As presented previously in **Figure IV-a**, only slices representing the mid-length transverse cross-section of the Tekken mock-ups were modelled in 2D. The meshes were built of linear quadratic elements (4 977 for the 30 mm specimen). Particular attention

was paid to the element refinement and quality in the critical areas surrounding the weld bead. The element size adopted in these locations was about $250 \, \mu m$, gradually increasing in the remote areas that were expected to be relatively unaffected. The weld bead thickness was estimated at 4,5 mm since no experimental tests had been carried out at that time.

The sketching and meshing operations were fully executed using Python command script instructions for Salome_Meca. To aid computation, the slices were subdivided into different zones constituting the global geometry and then concatenated. Some illustrations of the mesh modelling of the 30 mm thick mock-up are given in **Figure IV-j**.

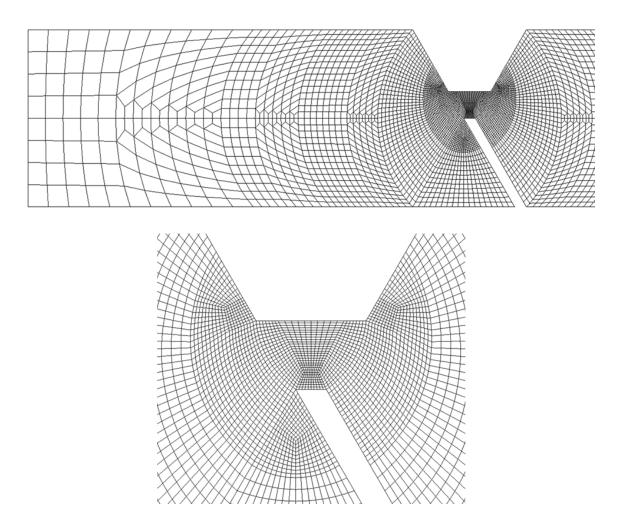
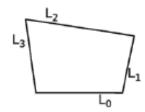


Figure IV-j: illustrations of the mesh generated for a mock-up thickness of 30 mm

The global element quality assessment has shown that 82 % of the elements have an aspect ratio inferior to 1,50, which was considered acceptable for this study (refer to **Diagram IV-n**). In particular, elements within the heat-affected zone and fusion zone all have relatively good aspect ratios despite the geometry singularities. The method utilised for calculating this ratio is given with formulas (IV-2)-(IV-3)-(IV-4) [268]. Note that a

perfect square would have a ratio equal to 1,00.



[268]
$$\operatorname{area} = \frac{1}{2} \| \overrightarrow{L_0} \times \overrightarrow{L_1} \| + \frac{1}{2} \| \overrightarrow{L_3} \times \overrightarrow{L_2} \|$$
 (IV-2)

[268]
$$L_{max} = max(L_0, L_1, L_2, L_3)$$
 (IV-3)

[268] element aspect ratio =
$$\frac{L_{max}(L_0 + L_1 + L_2 + L_3)}{4 \cdot \text{aera}}$$
 (IV-4)

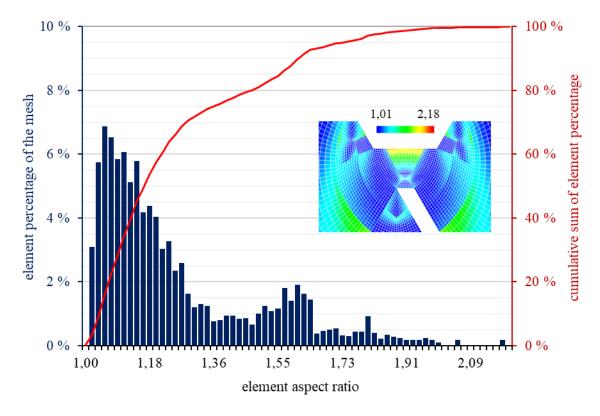


Diagram IV-n: results of the mesh element quality control, the criterion being based on the shape ratio of the quadrangles (size: 30 mm thick)

IV.5.B Automation of coherent meshing

Given the wide range of Tekken model thicknesses to be studied, a sampling of representative thicknesses was selected: every 5 mm from 15 mm to 50 mm thick, then every 10 mm from 50 mm to 100 mm, and a final thickness of 150 mm. This resulted in

a total of 14 Tekken tests to simulate.

The meshing command script was coded to automatically adjust the element sizes when necessary to ensure suitable junctions at the refinement zone frontiers. The element size of the critical area mentioned previously was however imposed. In addition, the biggest element size (at the mock-up edges) was set at 3 mm for mock-ups under 25 mm thick, and then at 4 mm for other dimensions.

This algorithmic automation permitted the Tekken mock-up meshes to be produced with constant and coherent characteristics to minimise the risk of mesh differences confusing the results. **Figure IV-k** illustrates this for two extreme sizes, 15 mm and 150 mm thick.

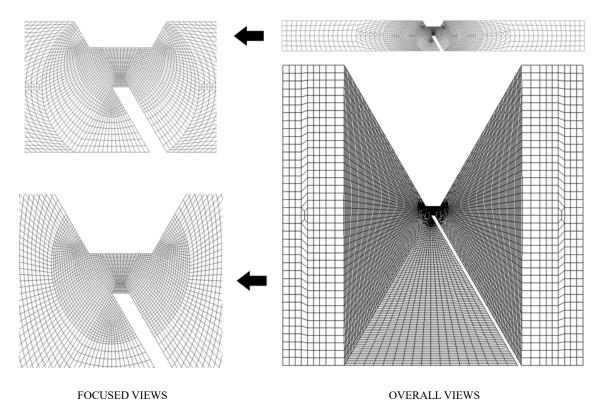


Figure IV-k: coherence illustration from the 15 mm to the 150 mm meshes with a focus on the weld bead area

IV.5.C Boundary & initial conditions

Conventional convective heat exchange and radiation loss were considered in the thermal calculation. The value of the exchange coefficient with ambient air was set at $15 \text{ W}\cdot\text{m}^{-2}\cdot\text{K}^{-1}$, which is slightly superior to natural convection [263], [264] to include the shielding gas flow effect. The emissivity coefficient was assumed at $\varepsilon = 0.50$ as the

average value for ground or machined steel surfaces [265]. The previously adjusted hardness values for some of the base metal (16MND5 steel) micro-constituents were used. However, since the initial micro-constituent distribution of the 16MND5 steel was set to 61 % ferrite & 39 % bainite for reproducing its actual mechanical behaviour (as explained in IV.2.B.1), the hardness of the "ferrite" micro-constituent was altered to make the overall hardness of this mixture coincide with the real value measured in the 16MND5 steel "as provided" during the behaviour study of the heat-affected zone exposed to hydrogen (215 HV – refer to section VI.3.C.3). The hardness of the Alloy 52M filler metal was set at 185 HV as experimentally measured during the NeT-TG8 program [243]. In the mechanical calculation, the nodes of the two slice extremities were considered fully embedded to reproduce the Tekken mock-up stiffness (refer to Figure IV-I).

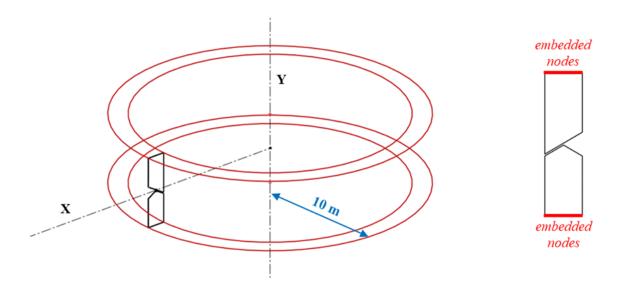


Figure IV-1: schematic illustration of the mesh re-positioning (modified scale) and mechanical boundary conditions

IV.5.D Modelling optimisation

The selected modelling type was axisymmetric about the Y-axis [269]. This approach allows more realistic out-of-plane constraint than mathematical plane strain, and aids mechanical solution convergence in Code_Aster, according to the developer team. However, the Tekken test specimens are not axisymmetric. Therefore, the modelled mock-up has been rotated by 90°, and placed at 10 meters from the Y-axis to give an effectively infinite radius and tackle the non-axisymmetry of this test device. The impact of this large radius was successfully examined by a quick comparison with one meter shorter and one meter longer radii: the results were not affected. **Figure IV-I** summarises this re-positioning.

IV.5.E Equivalent heat source

The heat input induced by the electric arc of the welding torch was reproduced through a uniform heat flux Φ imposed on every element in the weld metal which varied with time. This was simply composed of two stages: a heating phase, as described in equation (IV-5), and a cooling phase, as described in equation (IV-6).

$$\Phi_{heating} = \frac{Q_{max}}{\Delta t_1 \times t}$$
 (IV-5)

$$\Phi_{heating} = \frac{Q_{max}}{\Delta t_2 \times (t - (\Delta t_1 + \Delta t_2))}$$
 (IV-6)



Picture IV-g: extra 40 mm thick mock-up left over from a previous Tekken campaign

For calibrating the parameters of this modelled heat source, an instrumented Tekken test was performed at EDF PRISME using the welding parameters selected previously (refer to III.4). To that end, an extra 40 mm thick mock-up left over from a previous Tekken campaign carried out by [47] was used for the thermally-instrumented welding test. This specimen was made from a different 16MND5 steel batch and to a slightly smaller width. These small differences were judging unlikely to affect the heat source calibration. At this time, this specimen was specially machined in two parts to facilitate its instrumentation (shown in **Picture IV-g**). Far-field and near-field K-type microthermocouples were placed at 12 different locations, both buried in drilled holes and

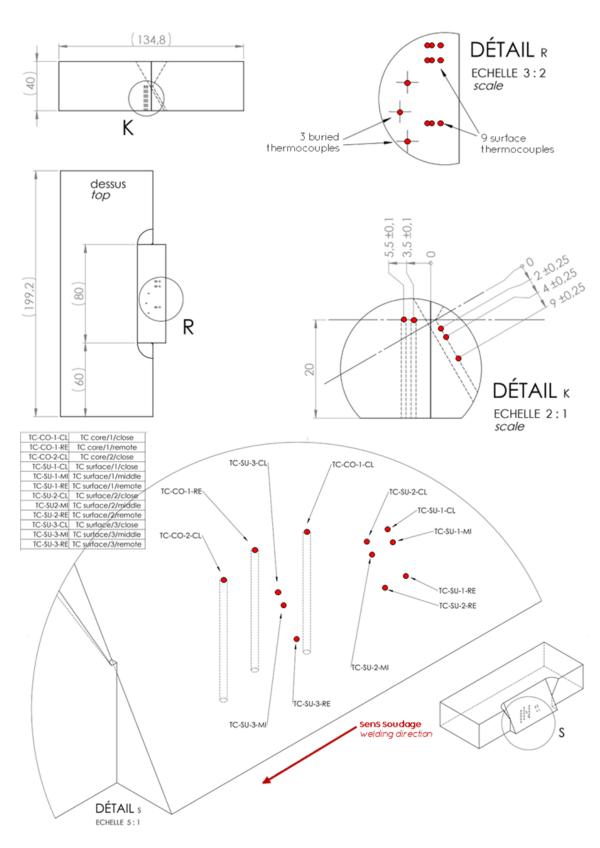


Figure IV-m: thermocouple placement locations (40 mm Tekken test mock-up)

Some thermocouple locations were doubled or tripled to determine repeatability. The surface thermocouples were covered with ceramic paste to protect them from any potential perturbation caused by radiation from the electric arc or convective exchanges (refer to **Picture IV-j**). Then, the two parts were aligned and assembled with several tack welds. It must be noted that the slot gap did not meet the standard dimensions [191] due to limitations in the manufacturing tolerance when working from two half-blocks. The Tekken test device was then placed on special supports (visible in **Picture IV-j**) to insulate the specimen from the welding table thermally. The edge of these support shims in contact with the mock-up is V-shaped to minimise heat transfer. The selected welding parameters and conditions imposed to maintain the welding torch in a vertical position (reasons previously explained in section **III.4**). Standard J-pipes – the element guiding the filler metal wire into the weld pool – were not suitable because of the reduced space due to the Tekken groove design. The groove extremities were thus chamfered, but this was not sufficient. Consequently, a specific J-pipe was designed to tackle this issue (shown in **Picture IV-h**).





Picture IV-h: tungsten inert gas welding torch configuration and example of dummy mock-up used to make sure the installation was functioning properly





Picture IV-i: one of the y-slot dummy mock-ups used to make sure the installation and the weld program were functioning properly

Welding VWPR QE Extern previously introduced (IV.4.B). Dummy specimens (shown in Picture IV-i) representing the y-slot of the Tekken test mock-up were used to make sure the selected methodology and parameters were functioning properly. In addition, two old mock-ups were used as ultimate verifications. The same thermocouple acquisition system supplied by National Instruments and the LabVIEW software were used. Thermocouple recording was also checked using a heat gun before proceeding with the instrumented test. The recorded temperature curves are plotted in Diagram IV-o. The thermocouple "TC-SU-3-CL" failed when it reached the peak temperature, probably because it was caught in the weld pool. A considerable deviation was observed between the two buried thermocouples measuring a doubled position (TC-CO-CL), whereas the measurements made with the surface thermocouples showed good repeatability between the tripled positions.



Picture IV-j: the thermocouple-instrumented mock-up before and after assembly, and after the welding run completion (220406-TEK1-WH-INC-TC specimen)

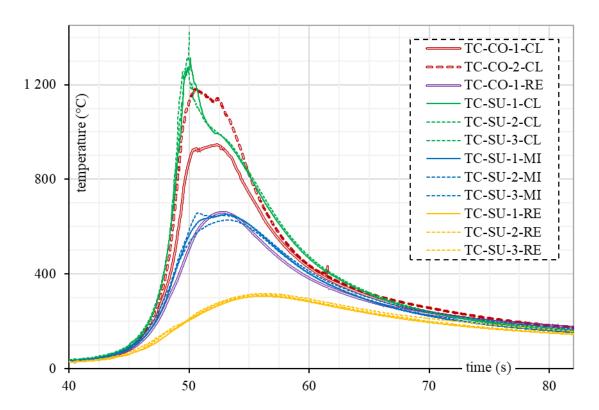


Diagram IV-o: temperatures recorded by the thermocouples (TC-SU-3-CL failed when it reached the peak temperature)

The records from only three far-field thermocouple positions were preferred for heat source calibration because they are not unduly sensitive to the simplified form of the heat source. They are detailed in **Figure IV-n**. The three corresponding thermal cycle curves from the experiment were generated by first synchronising the time axis, and then averaging when doubled or tripled. A wide range of heat source parameter combinations was simulated using a design of experiment matrix. Then, the set providing the most suitable match in terms of peak temperatures and cooling rates was selected. Hence, the identified parameters used in equations (**IV-5**)-(**IV-6**) were $Q_{max} = 18,0 \text{ J}$, $\Delta t_1 = 6,0 \text{ s}$, and $\Delta t_2 = 8,6 \text{ s}$.

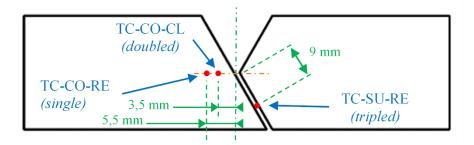


Figure IV-n: thermocouple positions utilised for the calibration of the equivalent heat source

The heating phase has been considered as having a limited impact for the needs of this study. The heat capacity function of the base metal has been again slightly adjusted to

correct lags caused by latent heat effects. The comparison between the experimental data and the obtained simulation results with the calibrated heat source is presented in **Diagram IV-p**.

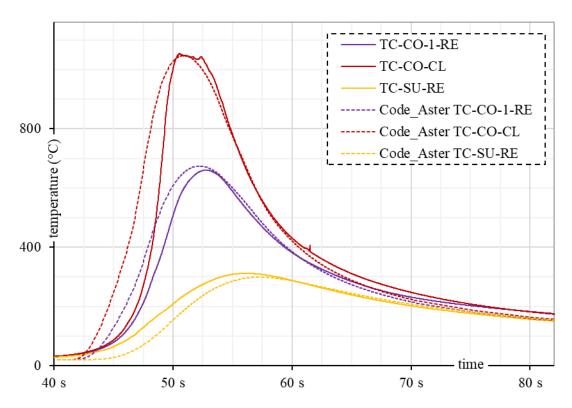
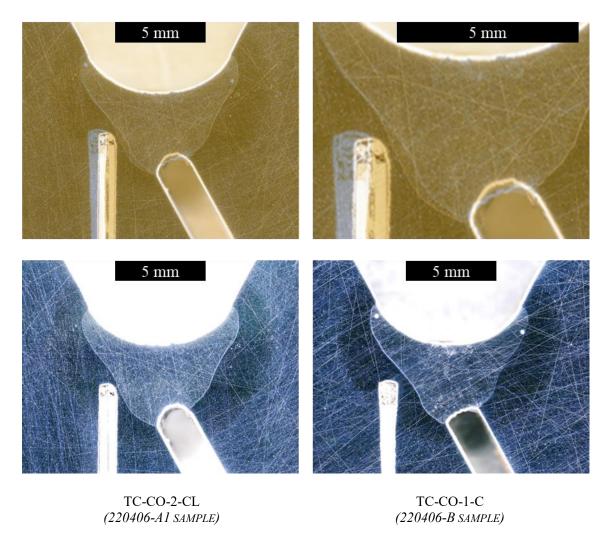


Diagram IV-p: comparison of the experimental thermocouples data with the virtual ones of the Code_Aster simulation after the heat source parameter calibration using a 40 mm Tekken test mock-up

The area of interest of this instrumented mock-up was extracted by electrical discharge machining. After that, the sample was sliced by wet precision cutting, and then wet ground and polished following the same procedure as for the Jominy half-bar (IV.4.A). The cutting planes passed through (or close to) the positions of the thermocouples. It was observed that the distance from the fusion boundary to buried thermocouples can vary by several tenths of a millimetre despite careful preparation and test execution (refer to Picture IV-k). This explains the poor repeatability of this measurement. This distance variation was caused by the fluctuation in the shape of the molten metal pool during the weld run and the precision error during the hole/well drilling.



Picture IV-k: cross-section comparison of the two buried thermocouples monitoring the same zone (the slot gap does not meet the standard dimensions [191] due to limitations in the manufacturing tolerance when working from two half-blocks)

Then, the hardness field of one of the cross-sections was scanned with a load of $1,00 \text{ kg}_f$ and a minimum pitch of 0,25 mm in the heat-affected zone where significant gradients were expected. The measured hardness distribution is compared with the prediction made using the calibrated heat source in **Figure IV-o**. Although the height of the weld bead was assumed to be greater in the meshes modelling the Tekken specimens, the shape and cross-sectional area of weld metal were close to reality. In contrast, the calculated heat-affected zone dimensions showed some differences from the experiment. This is likely due to the simplifications assumed in the shape of the equivalent heat source and to inaccurate reproduction of the delay in the austenitisation that occurs at high heating rates, shifting the Ac_1 and Ac_3 values used by the model to calculate the metallurgical transformations.

Regarding the heat-affected zone microstructure, although the simulation did not reproduce the hardness gradient towards the base metal observed experimentally between

the inter-critical heat-affected zone (I.C.H.A.Z.) boundaries (which are controlled again by Ac_1 and Ac_3), possibly explained by the variation in prior austenite grain size, this prediction is not however wrong. Indeed, once again, the prior austenite grain size did not feature in the prediction of hardness. The experimental hardness scan showed that most of the heat-affected zone is above 400 HV. This suggests a quasi-fully martensitic heat-affected zone.

This is also suggested by the common engineering method used by welders based on the $t_{8/5}$ time interval and described by the standard EN 1011-2 [86]. This duration is estimated to be 3,98 s using (II-2), (II-3), and (IV-7) dedicated to 3D heat conductions in massive parts (initial specimen temperature $T_0 = 20 \,^{\circ}\text{C}$; welded joint form factor $F_3 = 0.67$ [86]). This result suggests thus a theoretical cooling rate of -75 °C/s within the overall heat-affected zone.

[86]
$$t_{8/5} = (6700 - 5 \cdot T_0) \times \frac{Q_{linear}}{1000} \times \left(\frac{1}{500 - T_0} - \frac{1}{800 - T_0}\right) \times F_3 \qquad \text{(IV-7)}$$

This estimation is in line with the 2D thermal solution calculated by the simulation, which predicted a cooling rate of -62,8 °C/s within the inter-critical heat-affected zone from 800 °C to 500 °C.

As seen previously (IV.3.C), according to the analyses (refer to Table IV-A) and dilatometry testing (refer to Diagram IV-b) conducted during the NNUMAN program on SA-508 steel [225], [229], such rapid rates lead to nearly pure martensitic microstructure. The microstructure type predicted by the simulation is thus reliable.

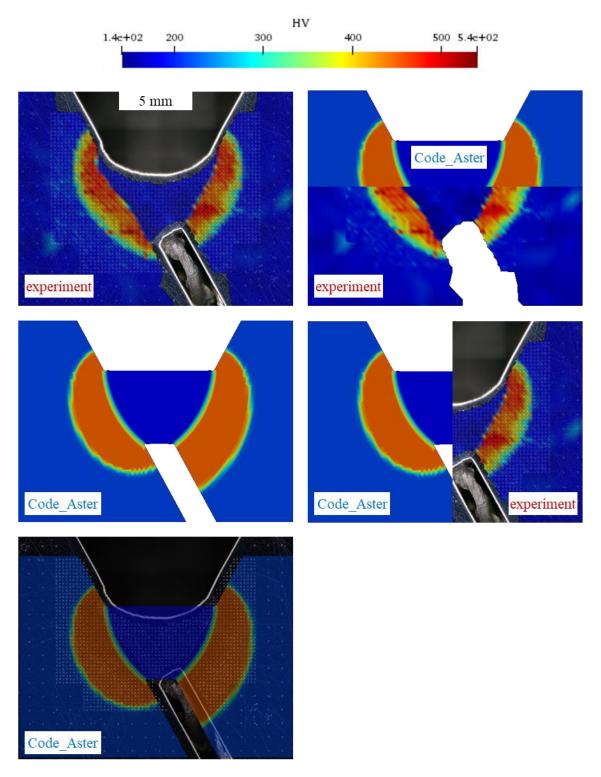


Figure IV-o: comparison between the experimental hardness scan (220406-Y sample) and the computational prediction (the slot gap does not meet the standard dimensions [191] due to limitations in the manufacturing tolerance when working from two half-blocks)

Nevertheless, considering the final needs of this study comparing the stress state levels generated as a function of the mock-up thickness, these moderate discrepancies between simulation and experiment were not considered liable to give rise to results that could lead to significant misinterpretations at the mechanical calculation stage. At least, the

prediction error would be reproduced on each simulated specimen, which would not unduly affect this relative benchmarking.

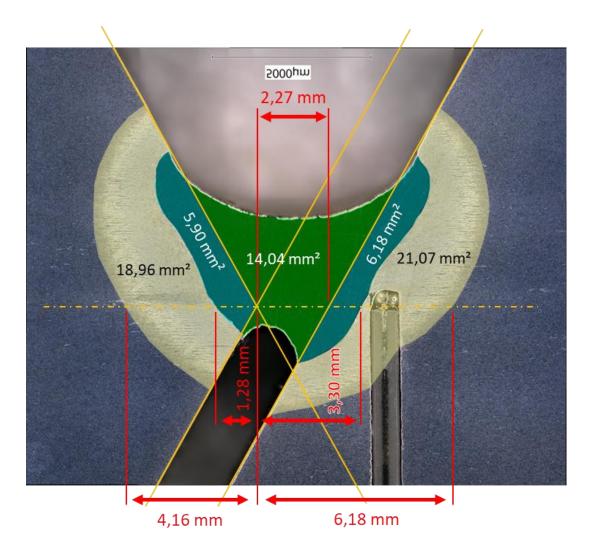
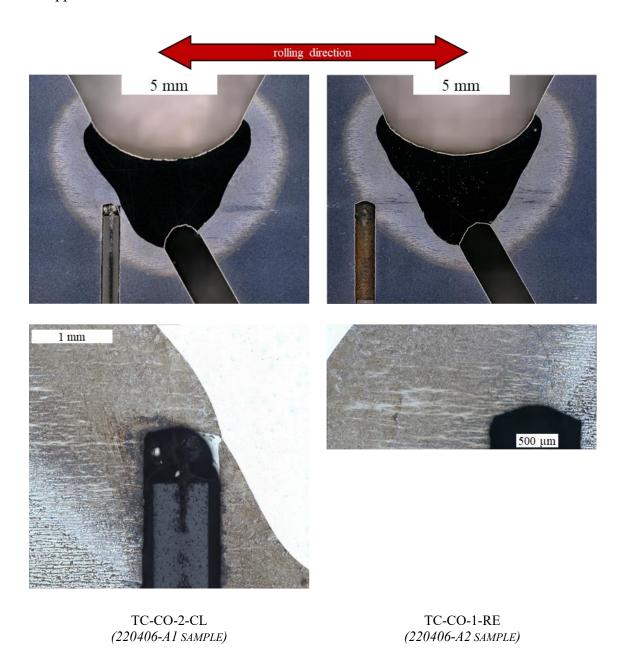


Figure IV-p: macrography of the weld (220406-A1 sample – yellow areas: heat-affected zones; green and blue areas: weld metal; green area: specifically the deposited filler metal section – raw image given in **Picture IV-I**) – the slot gap does not meet the standard dimensions [191] due to limitations in the manufacturing tolerance when working from two half-blocks

Several additional cross-sections were polished and etched following the same procedure, to reveal the fusion boundary and the heat-affected zone microstructure. The macrography of the weld is given in **Figure IV-p** (measurements made using the software Mesurim Pro V3.4). The prior austenite grain size measured in the region close to the fusion boundary varies from 120 μ m to 300 μ m (**Picture IV-I**). However, once again, since these measurements were made using optical microscopy, they could overestimate the real grain sizes.

Finally, although there is a certain degree of uncertainty about how suitable this calibration would be for other mock-up thicknesses (particularly concerning thermal

inertia), which also have slight meshing differences, these parameters were assumed to be applicable at all thicknesses.



Picture IV-1: cross-section comparison of two buried thermocouple monitoring different zones (the slot gap does not meet the standard dimensions [191] due to limitations in the manufacturing tolerance when working from two half-blocks)

IV.6 RESULTS

Once the thermal model was calibrated, the 2D thermo-metallo-mechanical simulation was run on each mesh. According to [43], mainly a uniform normal stress is experienced by bead deposited in an oblique y-slot (refer to **Figure IV-q**). Considering this, the temporal evolution of the nodal loads [270] on the restrained faces (as shown in **Figure**

IV-I) was extracted and used to estimate the average normal stress σ_{avg} occurring on the weld bead cross-section. This last value was then utilised as the benchmark criterion for studying the effect of thickness. This comparison is presented in **Diagram IV-q** at a focused time scale. **Diagram IV-r** shows an observation over a period of 10 hours for the 15 mm, 30 mm and 50 mm specimens. The same trends can be seen in these predictions as suggested in the bibliography by [118], [200], who describes each different region of the curves in **Diagram II-I**.

In addition, the predicted fields of the σ_{xx} , σ_{yy} , and σ_{zz} orthogonal normal stresses are given in **Figure IV-r**, **Figure IV-s**, and **Figure IV-t** for the 45 mm Tekken mock-up after a period of 15 min following the weld completion. However, it must be reminded that these values are only indicative and were not thoroughly verified. Nonetheless, these illustrations highlight the stress concentration that peaks in the root region of the weld.

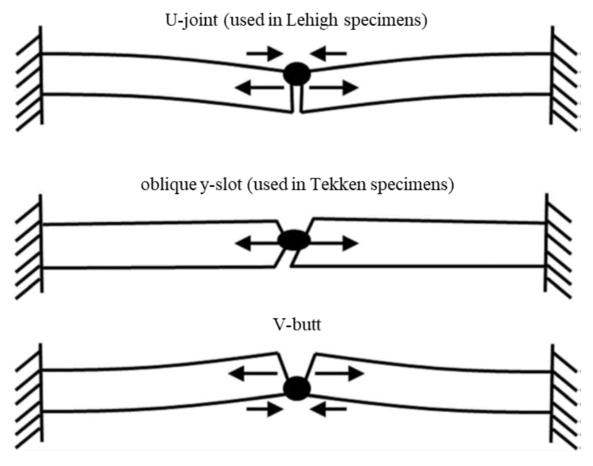


Figure IV-q: residual stresses across weld throat in flat test specimens with different groove types (source: [43], [82])

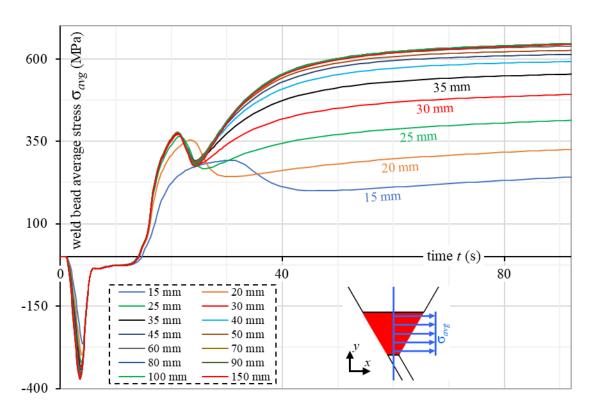


Diagram IV-q: benchmarking of the relative impact of the Tekken mock-up thickness on the average stress σ_{avg} experienced by the weld bead perpendicular cross-section (relative stress value)

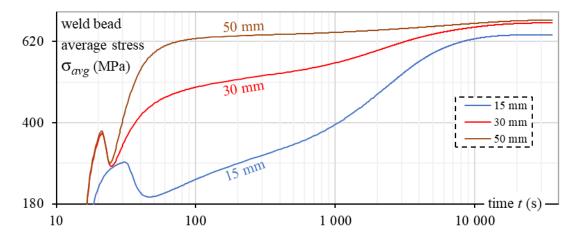


Diagram IV-r: average stress σ_{avg} evolution 10 hours after the weld completion for the 15 mm, 30 mm and 50 mm Tekken specimens (relative stress value)

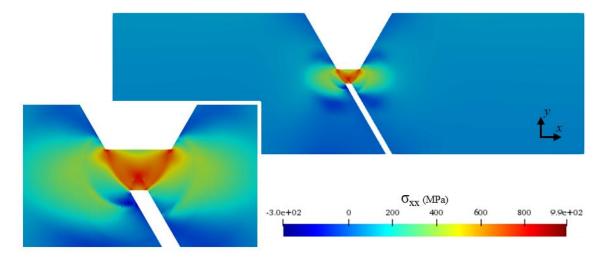


Figure IV-r: predicted field of the σ_{xx} orthogonal normal stress occurring in the 45 mm Tekken mock-up after a period of 15 min following the weld completion (indicative stress values)

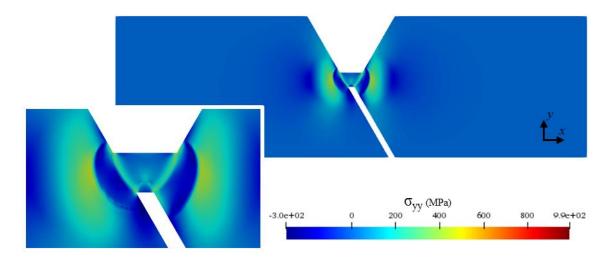


Figure IV-s: predicted field of the σ_{yy} orthogonal normal stress occurring in the 45 mm Tekken mock-up after a period of 15 min following the weld completion (indicative stress values)

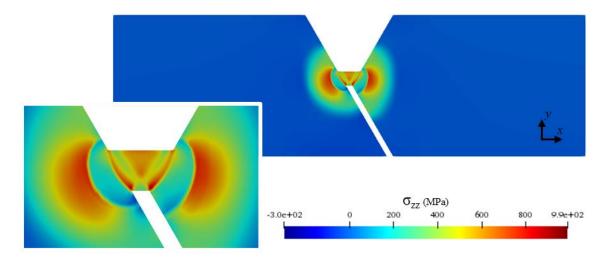


Figure IV-t : predicted field of the σ_{zz} orthogonal normal stress occurring in the 45 mm Tekken mock-up after a period of 15 min following the weld completion (indicative stress values)

IV.7 DISCUSSION & CONCLUSION

A numerical study enriched by experimental analyses was conducted to develop understanding of the Tekken welding test. The finite element model was used to investigate the effect of mock-up thickness on the self-restraint conditions. The thickness is often considered as the major parameter for driving the stress state self-generated in this test device [82], [215], [216], [271]. Nevertheless, there was a lack of precise information on this impact. This study has permitted to propose a qualitative estimation through a first approach in 2D. A complete benchmarking of the different thicknesses was established, focusing on the level of the average normal stress experienced by the weld bead.

The results show a compressive stress state during the filler metal deposition and the beginning of the cooling. This is in line with the experimental observations by indirect measurement conducted by [118] using similar y-slit crack test specimens. However, this must be treated with caution: the simulation approach considers the weld metal elements already in place before their simulated deposition, without a deactivation or mitigating feature for their thermo-mechanical characteristics. Considering that the weld metal is molten at this stage, the magnitude of this first part of the mechanical results cannot be considered as entirely correct. Only the results after complete metal solidification can be exploited here. According to the experimental and computational results produced, it can be estimated that the weld metal is fully solidified approximately five seconds after the passage of the welding torch. At that stage, the stress state is more or less equal to zero.

Following this, rapid growth of the tensile stress is observed, until a sudden drop. The divergences for the smallest thicknesses start at the end of this first stress increase. The drop observed results from metallurgical changes from hot to cold micro-constituents, as seen previously with the dilatometry testing. This aspect has been studied in detail by [199], who measured a similar drop in magnitude during their welding test. This is mainly caused by the atomic re-arrangement occurring within the unit cells during solid-solid phase transformations, as well as differences in the thermo-mechanical properties of the different micro-constituents. This correlation is shown in **Diagram IV-s** with a 40 mm Tekken mock-up by focusing on the local changes surrounding the closest thermocouple to the fusion boundary (TC-CO-CL).

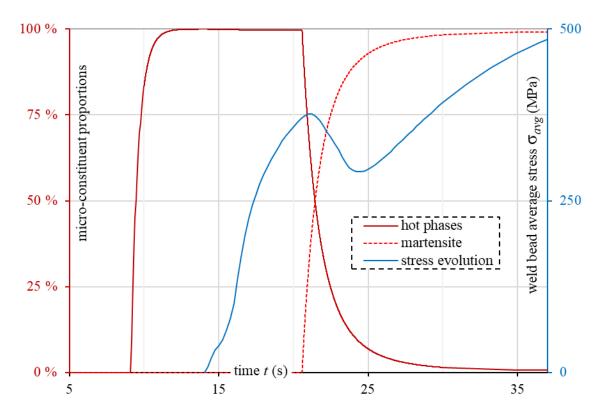


Diagram IV-s: focus on the thermocouple TC-CO-CL location (Tekken 40 mm): correlation between the drop in the stress increase during the metallurgical changes

After solid-solid phase transformations are complete, the tensile stress increase resumes. The increasing rate is rather moderated in the thinnest specimen thicknesses due to their lower mass, which reduces the cooling rate. From this point onwards, there is a net effect of the thickness. The maximum achievable self-restraint condition is reached above a thickness of 50 mm, it can take more than 10 hours to experience the final residual stress level. Moreover, it was found that this stabilisation phenomenon is insensitive to variations of the material and equivalent heat source parameters made during the model calibration steps, which raised confidence in these findings.

Thanks to this study and the established benchmarking, it has been possible to conclude that for the remainder of this research project, a thickness approaching 50 mm would provide the best compromise for quickly maximising the stress state using this metal combination with these specific welding parameters.

Finally, this study has also permitted to identify several elements that would require further development:

 Quantitively speaking, the convergence to a maximum stress state of about 650 MPa may seem plausible. Nevertheless, this would require additional verifications before any conclusion on the absolute values of the residual stress experienced.

- An extensive tensile testing campaign under different temperature intervals and for several microstructure types of this base metal would be of interest to finely adjust its material properties and calibrate the model.
- Improvements of the meshing strategy are now possible using the weld macrography realised at the end of this project. This would allow modelling of the actual weld bead shape, the y-slot dimensions, fusion boundaries, and heat-affected zone limits.
- The equivalent heat source could also be improved by modelling its shape accurately and refining its parameters using the measured isotherm boundaries.
- The calculation duration could be optimised by applying simpler material behaviour models to regions outside the heat-affected zone.
- Prior austenite grain size is an important variable, as the prediction of the microconstituent proportions within the heat-affected zone is highly dependent on this
 parameter. This only had an impact in the smallest thicknesses, since heat
 dissipation there was insufficient to lead to fully martensitic heat-affected zones.
 However, a lack of experimental data and model development makes optimisation
 of this part of the solver difficult.
- Finally, a transposition to a 3D model would be of interest to validate a part of the assumptions made for these 2D simulations.

V.1 FOREWORD

This chapter compares the conclusions drawn from the Tekken and implant test methods relating to the viability of the welding procedure proposed to carry out the specific repairs presented previously, with respect to the risk of cold cracking. Hence, it explores their relevance for evaluating bead tempering methods (third conservatism objectives). In addition, the produced results allowed advances to be made in the pursuit of objectives linked to the first and second conservatisms (respectively, viability demonstration of bead tempering methods, and questioning the appropriateness of probabilistic versus deterministic criteria for cold cracking risk assessment).

As with the heat source calibration of the numerical Tekken model, the Tekken cold cracking tests were carried out during the second part of this current research project at the EDF PRISME welding laboratory. Metallurgical samples were prepared and analysed at the University of Manchester (Department of Materials and Department of MACE²⁵). The implant test campaign and the subsequent analyses were carried out during a secondment of a few weeks at the IS welding laboratory of Yutz. The IS has produced a complete technical report [272] describing this testing campaign.

Both test campaigns, followed requirements of the ISO standards [87], [191], [240]. Only the first bead of a multi-pass weld repair was studied here because it is the at the highest risk of cold cracking [34]. Both tests were therefore single-bead type. Particular attention was paid to the environmental conditions during testing, through measurements of ambient temperature and humidity made using a Rotronic H1-20D data logger. The Tekken testing was performed during spring, while the implant testing was carried out during summer, when heat waves were experienced. Consequently, instead of being $\approx 22 \pm 3$ °C, the ambient temperature – and thereby the initial temperature of the specimens – during the implant campaign was $\approx 29 \pm 3$ °C.

-

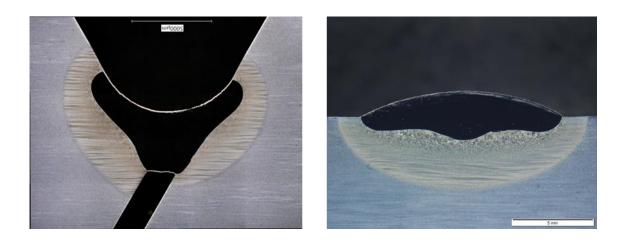
²⁵ Department of Mechanical, Aerospace and Civil Engineering

Table V-A: highlight of the consequences of variations in the diameter of the used filler wires

parameter	value				
Al	Alloy 52M				
filler metal wire diameter	Ø 0,9 mm				
filler metal depositing rate	15 896,250 mm³/m of torch travel				
theorical deposited metal section	15,90 mm ²				
AISI 316	AISI 316L & ER70S-3				
filler metal wire diameter	Ø 1,0 mm				
filler metal depositing rate	19 624,215 mm³/m of torch travel				
theorical deposited metal section	19,62 mm ²				

As previously mentioned, the same welding parameters and welding configuration were applied for both test types. Nevertheless, for some reasons detailed in the next section, two other filler metals were also used for comparison purposes. It must be noted that their wire diameter was slightly thicker than that of the Alloy 52M one (Ø 1,0 mm versus Ø 0,9 mm). The impacts of this variation are summarised in **Table V-A**.

Differences in specimen design and ambient temperature led to slower cooling rates in the implant tests. Using formulas (II-2)-(II-3)-(IV-7), in the Tekken mock-ups $t_{8/5}$ was 4,00 s ($F_3 = 0.67$ [86]), inducing cooling rates of the order of -75 °C/s, while in the implant tests $t_{8/5}$ was 6,08 s ($F_3 = 1.00$ [86]). This corresponds to a cooling rate of the order of -50 °C/s. Fortunately, this cooling rate still leads to almost pure martensite in the heat-affected zone. The configurations of the Tekken implant weld beads are compared in **Figure V-a** and **Figure V-b** with consistent picture scaling and key dimensions and cross-sectional areas evaluated using a Keyence VHX-5000 digital microscope and the software Mesurim Pro V3.4 (raw images given in **Picture V-a**). It can be seen that similar cross-sectional areas of both weld metal and heat-affected zone were measured in the two configurations.



SAMPLE FROM MND8 TEST

Picture V-a: raw images used in the macrographs given in Figure V-a and Figure V-b

220401-B SAMPLE

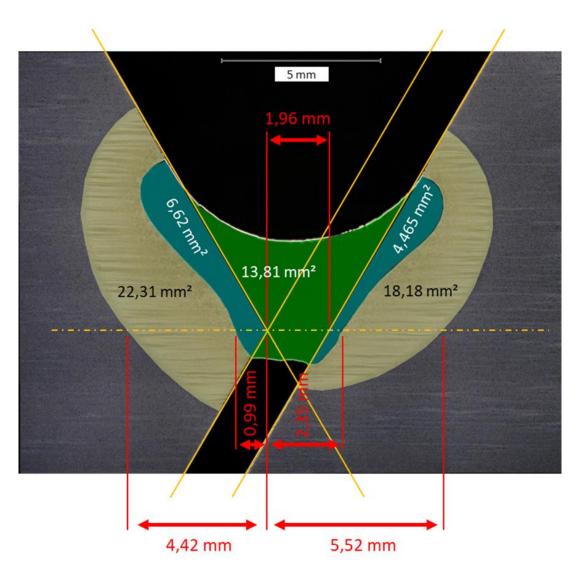


Figure V-a: macrography of a Tekken test weld bead produced using the selected welding parameters and nickel-based alloy 52M used as filler metal (220401-B sample – yellow areas: *heat-affected zones*; green and blue areas: *weld metal*; green area: *specifically the deposited filler metal section* – raw image given in **Picture V-a**)

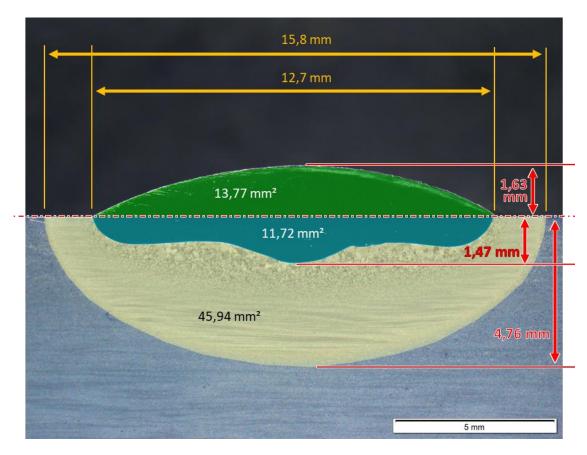


Figure V-b: macrography of an implant test weld bead produced using the selected welding parameters (sample from MND8 test – *consistent scaling with Figure V-a* – yellow area: *heat-affected zone*; green and blue areas: *weld metal*; green area: *specifically the deposited filler metal section* – raw image given in **Picture V-a**)

Cracking releases energy in the form of transient elastic waves, so each test mock-up was instrumented with an acoustic emission detection system to attempt to quickly assess the outcome of the test in advance of destructive analysis, and to record the time of initiation of any possible cracks. This system (Vallen Systeme AMSY-6) consists of several sensors (VS160-NS) operating in an array. It is managed with a computer using the software Vallen Control Panel (R2015.0430.6 release). The sensors were held in place on the mock-ups by magnetic holders. Silicone grease was used as a coupling agent to ensure good transmission of waves. The acoustic emission data also enabled optimised positioning of the Tekken specimen cutting planes, such that they were placed in regions where acoustic activity suggestive of defect occurrence was located from the time lag between the wave arrival at each sensor. To calibrate the acoustic emission location module, pencil leads were broken at selected locations. The parameters were then adjusted to match the true locations (ASTM²⁶ E976 standard method [273]). However, as the specimen was not a simple infinite plate, wave propagation was not in a homogeneous medium, so perfect location accuracy was not possible. An intergranular crack emits a

²⁶ American Society for Testing and Materials

signal of an amplitude about 65 dB when it occurs [274] (some examples of acoustic emission sources are given in **Diagram V-a**). Nevertheless, detecting such a signal does not necessarily mean a cold crack has formed.

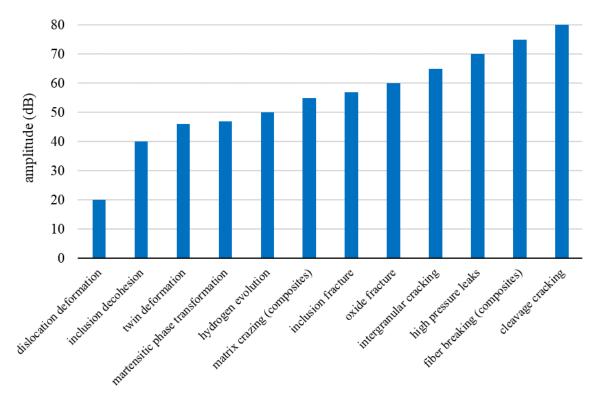


Diagram V-a: mechanisms responsible for acoustic emissions during material deformation and their corresponding typical signal amplitudes (source: [274])

V.2 TEKKEN METHOD

V.2.A Observations

- According to [207], the stress concentration factor K_t generated at the root of the weld by an oblique y-slot design varies from 3,5 for non-tilted bead lower side (forming a 120° angle) to 4,7 for highly tilted bead lower side (angle reduced to 100°). These estimates were made using 30 mm thick mock-ups with flat weld root surfaces. From these observations, **Table V-B** adapted from [44] with additional cases illustrates the variation of K_t with some different slot/joint layouts.
- According to the standard [191], a cold crack is deemed present if it exceeds 500 μm in a Tekken specimen.
- The standard [191] defines two ways of depositing the weld bead depending on

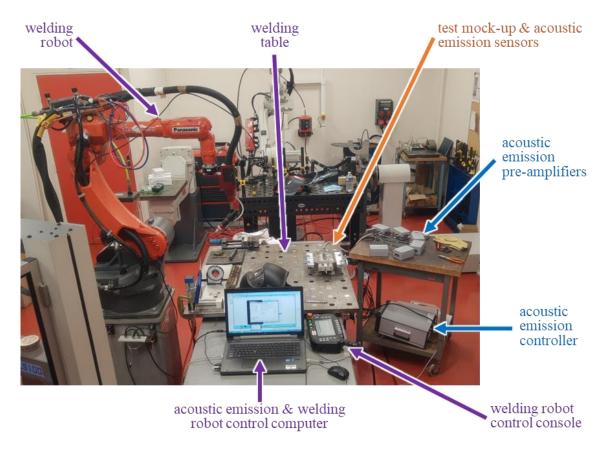
whether an automated or manual method is used. When welding manually, the weld starts and ends beyond the groove. In the case of automated welding, the weld starts and ends directly in the groove, without reaching the ends.

Table V-B: examples of common stress concentration factor K_t at the root of weld of basic joint geometry (adapted from [44], [207])

groove type	illustration	K_t	groove type	illustration	K_t
oblique y (lower side non-tilted)	51 30 120°	3,5	single bevel-2	5 <u>T</u> 30	5,4
oblique y (lower side slightly tilted)	51 30 114°	4,0	single bevel-3	30 5 1 h/4 n	6,9
oblique y (lower side highly tilted)	51 30 100°	4,7	single bevel-4	30 5 h/4 h	3,5
double Vee	5 1 30 60°×60°	3,7	symmetric Y	5 30	4,2
single bevel-1	5T 30	5,8			

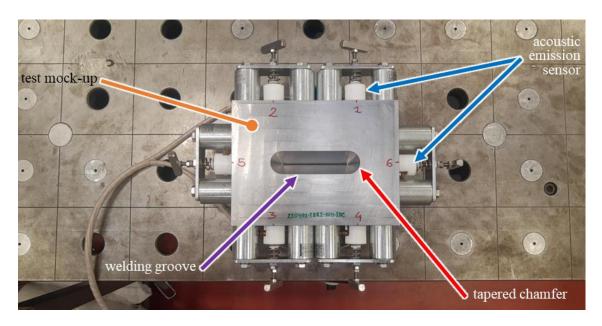
V.2.B Methods

Changing the thickness of a Tekken specimen allows control of the intensity of the self-restraint condition. The modelling of the previous chapter suggests that the best compromise between restraint and bulk would be a thickness of 50 mm. However, after considering the available dimensions of base metal blocks in the stock of the EDF PRISME welding laboratory, a thickness of 44 mm was used.



Picture V-b: welding and instrumentation setup used to conduct the cold cracking Tekken tests at EDF PRISME (OLDTEK2 preliminary welding test)

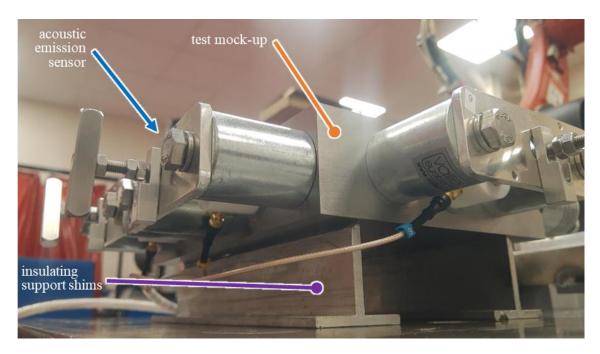
In contrast with the usual standard practice [191], instead of working from two half-blocks, the mock-ups were made of a single plate whose y-slot was machined by electrical discharge machining. Thus, any risk of misinterpretation resulting from the presence and impact of "anchor welds" was avoided (sort of multi-pass tack welds prescribed by the ISO standard [191]). Note that fabrication by welding will generate residual stresses, and thereby could affect the self-restraint conditions. Fabrication by assembling also makes it more difficult to respect the size tolerances specified by the standard.



Picture V-c: highlight of the tapered chamfers added to the welding groove (220401-TEK2-WH-INC mock-up)

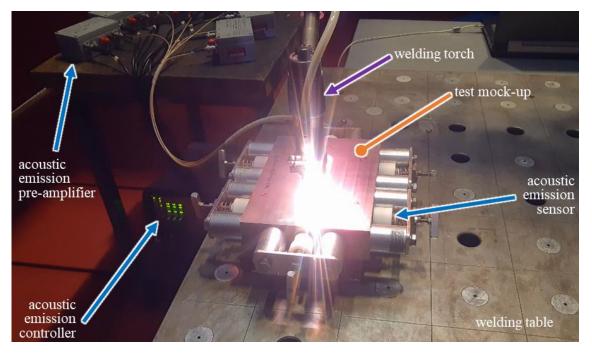
Particular attention was paid to the orientation of the slot with respect to the rolling direction of this batch of steel. It was chosen to orient the weld bead transverse to the rolling direction.

It should be noted that tapered chamfers were inserted at the ends of the slot groove in order to leave sufficient space for welding torch access (shown in **Picture V-c**). This is a slight deviation from the standard. Also, as mentioned in the section describing the selection of welding parameters, the vertical orientation of the torch was kept fixed.



Picture V-d: highlight of the support shims used to thermally insulate the mock-up from the welding table (220401-TEK2-WH-INC welding test)

The cold cracking tests were conducted using the same facilities as the Tekken test instrumented by thermocouples (using the robotic tungsten inert gas welding station Valk Welding VWPR QE Extern shown in **Picture V-b**). The insulating support shims were retained to allow unrestrained deformation (refer to **Picture V-d**). Since an automated welding process was employed, care was taken to leave a gap between the ends of the weld bead and the edges of the slot as required by the standard in this case. Note that the standard excludes the bead ends from cold-cracking evaluation, since these undergo complex 3D deformation associated with the arc state and stop transients, and they have a higher propensity for any type of defect. **Picture V-e** shows the weld deposit into the Tekken groove of one of the mock-ups. The duration of the welding run was about 45 s (this does not include the pre-gas, post-gas, and robot displacements).



Picture V-e: weld bead deposit into the Tekken groove of the cold cracking test 220325-TEK1-WH-INC

The initial welding tests were performed on specimens which were expected to crack, to verify the acoustic emission system's capabilities and to produce typical examples of cracking. The acoustic emission system was re-calibrated at the end of each test (after the 48-hour delay), because the presence of the weld bead was required to reproduce realistic elastic wave propagation. The Hsu-Nielsen Source method was used to generate impacts at known locations (refer to **Figure V-c**). This simply consists of breaking pencil leads on the sample surface. The acoustic parameters were then adjusted to make the calculated locations match the actual impact positions as closely as possible, as shown in **Figure V-d**.

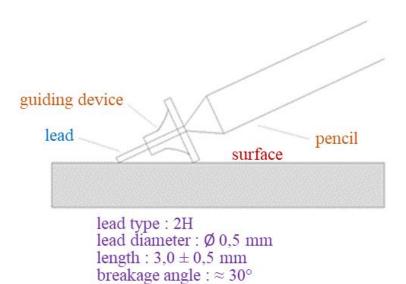


Figure V-c : details of the Hsu-Nielsen Source method used to generate pencil lead breakage at known locations on the mock-up (adapted from [275])

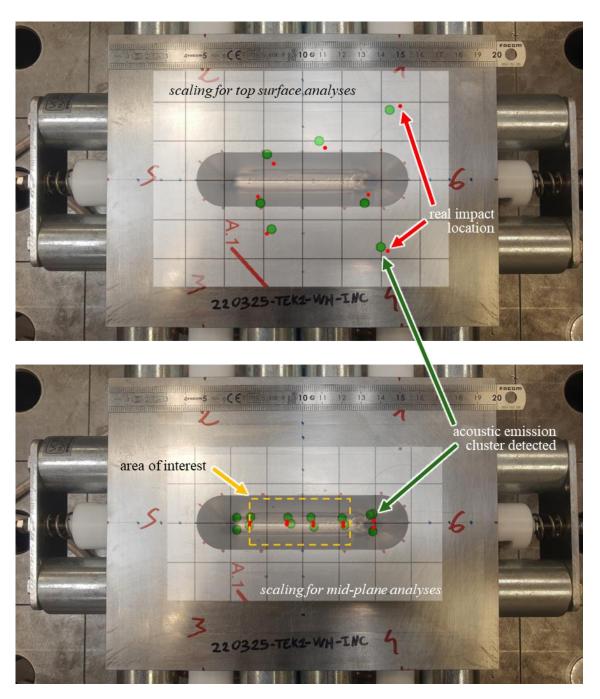


Figure V-d: examples of the accuracy of the calculated impact locations by the acoustic emission system after the re-calibration at the end of the welding cold cracking test (220325-TEK1-WH-INC specimen; area of interest established following the standard [191] guidance)

A first test using the ferritic steel ER70S-3 as filler metal was carried out to undertake the calibration. It is important to note that using a shielding gas doped in hydrogen is normally strongly prohibited when using this type of filler metal. However, here, this allowed cold cracking to be generated reliably. Cracking occurred almost instantaneously a few minutes after the completion of the weld, along the entire length of the bead, from the surface (refer to **Figure V-e**). It was therefore observable by eye, without requiring destructive examination. The acoustic emission system recorded this crack's formation

and propagation.

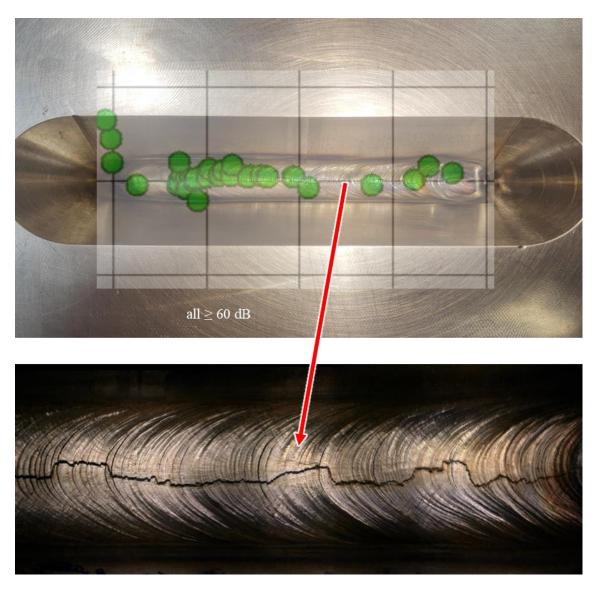
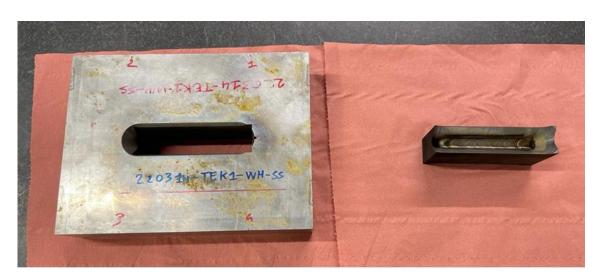


Figure V-e: weld bead cracking generated during the 220323-TEK1-WH-FER test using ferritic steel ER70S-3 as filler metal and the corresponding recorded acoustic emissions

After that, tests using AISI 316L stainless steel filler wire were conducted to attempt to reproduce the cracking results reported by [47] during the previous Tekken campaign at EDF PRISME. It must be noted that the wire feeder failed during the first of these three tests (220314-TEK1-WH-SS specimen), at the beginning of the weld bead deposit. This run was then restarted, and this test completed. During these three tests, a few clusters of acoustic activity were found, but no visible surface defects except for some longitudinally oriented cracks and/or crater cracks within the exclusion zones at the bead ends.

Finally, tests using the nickel-based alloy 52M filler wire were carried out to meet the objectives of this campaign. In addition, an extra mock-up was welded with 19 beads to explore the effect of multi-pass welding. No attempt was made to follow bead tempering

principles, in order to generate "worst case" conditions again. The stringer bead welding deposit method [25] was applied. It must be noted that the wire feeder failed during this extra test, at the beginning of the second bead deposit. This run was then restarted, and the multi-pass weld continued. Relatively low acoustic activity was recorded during any of these tests. Again, no major surface defects were observed other than longitudinally oriented cracks and/or crater cracks in the exclusion zones.







Picture V-f: extraction by electrical discharge machining of the weldment and sample reference engraving prior to the cutting in "slice" samples (220314-TEK1-WH-SS & 220318-TEK2-WH-SS mock-ups)

All weldments except the initial ferritic filler specimen were monitored using acoustic emission for a minimum of 48 hours after completion of welding, before ceasing

monitoring and removing the weldment from the welding table. Most tests were welded on Friday evenings to take advantage of the silence of the weekend within the welding laboratory. After testing was complete, selected Tekken specimens were then cut by electrical discharge machining into several "slice" samples (refer to **Picture V-f**), which were wet ground, polished and chemically etched following the same procedure as for the Jominy half-bar to reveal the microstructure (**IV.4.A**) and thus facilitate the search for possible cracks. Each sample was engraved with its reference. The observations were processed at the University of Manchester and at the EDF MMC metallographic laboratory, using digital microscopes Keyence VHX-5000 and VHX-7000, and optical microscopes Leica DM 2500 M and DMi 8.

As shown in **Picture V-f**, the number of cutting planes (6 to 7) realised for each specimen is higher than the one foreseen by the standard (5) [191]. Although they were positioned based on the acoustic emission results, attention was paid not to exceed the distance between each plane specified in the standard. It should be noted that only a few of them are presented as examples in this manuscript. In addition, any observed defects have been listed and documented. However, since this study focuses on cold cracking, the others will not be developed extensively here.

V.2.C Results & discussion

The results of the post-test investigations are summarised in **Table V-C**. It was noted that it is not easy to produce weld root surfaces that are always of the same inclination. Moreover, they may not always be perfectly flat, even along the same bead. They were frequently concave, and sometimes convex. This may have considerably affected the stress concentration factor, K_t , even at different points along the same groove.

Table V-C: summary of the 2022 Tekken test campaign results

	during welding				
test designation	relative humidity	ambient temperature	filler metal	result (zone of interest)	
220323-TEK1-WH-FER	24,0 %	23,4 °C	ER70S-3	weld metal breakage	
220314-TEK1-WH-SS	32,1 %	22,1 °C	AISI 316L	weld metal root cracking	
220318-TEK2-WH-SS	23,4 %	22,6 °C	AISI 316L	weld metal root cracking	
220321-TEK3-WH-SS	31,3 %	22,4 °C	AISI 316L	weld metal root cracking	
220325-TEK1-WH-INC	26,6 %	23,9 °C	Alloy 52M	passed	
220401-TEK2-WH-INC	30,6 %	19,0 °C	Alloy 52M	passed	
220408-TEK1-WH-INC-MULTI	34,9 %	21,8 °C	Alloy 52M multi-passes	passed	

It was not possible to reproduce the cold cracking results found by [47] using AISI 316L wire with our slightly different welding parameters, but with a similar linear welding energy. A possible explanation is the occurrence of root (or surface root) cracks in the weld metal in both interest and exclusion zones (an example is shown in Figure V-f – 220318-B sample). These are presumably hot cracking. The risk of hot cracking peaks before that of cold cracking during cooling. Consequently, these root cracks have probably reduced the overall stress in the weld, in particular the phenomenon - specifically sought with this test method - of local stress concentration in the heataffected zone of the root region. These root crack occurrences could be explained by the difference in the welding parameters and the chemical composition of the filler wire used in this new campaign. Indeed, in the previous one, a stainless steel AISI 316L-Si was used. Silicon doping has the advantage of improving the wettability of the molten metal bath. However, this type of stainless steel is not qualified by the regulatory code [33] - which only authorises certified AISI 316L wire. The latter was the only one stocked in the laboratory during this new campaign and was therefore the one used. Other than cold cracking of the heat-affected zone or root cracking, a few additional defects were observed in the molten metal in both interest and exclusion zones (mainly solidification shrinkage and/or – presumably – hot cracking again).

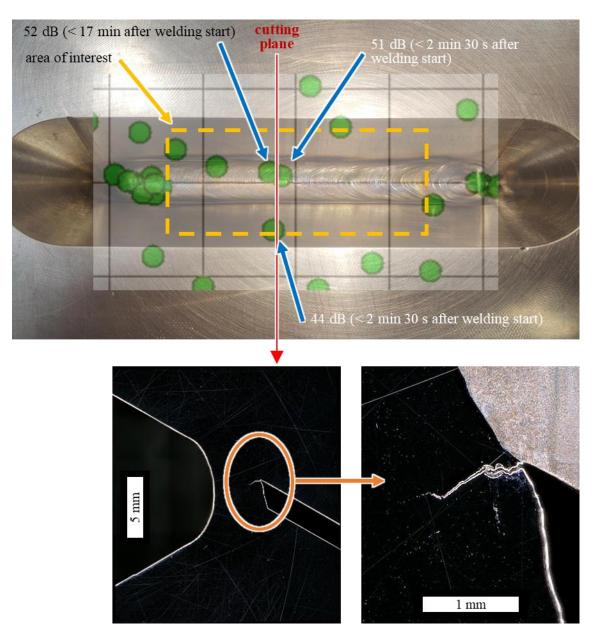


Figure V-f: example of root cracking found using stainless steel AISI 316L as filler metal and the corresponding recorded acoustic emissions (220318-TEK2-WH-SS test – 220318-B sample)

Concerning the tests conducted using the nickel-based alloy 52M wire, no defects, or at least no defects that could significantly modify the stress state, were found in the regions of interest. Only minor defects due to inclusions in the base metal could be observed there. However, in the start region (exclusion zone) of the first of these two mock-ups, in addition to a surface root cracking, hot cracks – again, probably – of considerable length were found in a dilution band region between the base and weld metal (shown in **Figure V-g** – cutting plane 220401-X). For one of these, in view of its proximity to the base metal grains, it could have been hybridised with some cold cracking. In the stop region (exclusion zone), a considerable cavity likely caused by solidification shrinkage was observed (cutting plane 220401-E). In the start region of the second mock-

up, a cold crack of a significant extent was found in the heat-affected zone (refer to **Figure V-h** - 220325-X). Nevertheless, the fact that these hot and cold cracks did not propagate outside the exclusion zones suggests that they were initiated by the transitional effects inherent to the welding onset (regions experiencing a triaxial stress concentration). Furthermore, the conclusions regarding the multi-pass test are identical, but with slightly more minor defects in the weld metal of the zone of interest (likewise, solidification shrinkage and - presumably - hot cracking).

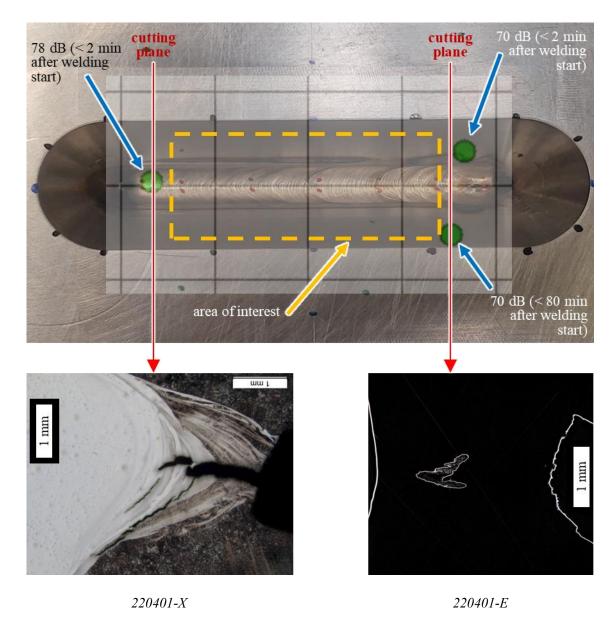


Figure V-g: surface root & hot cracking (sample 220401-X) and solidification shrinkage cavity (sample 220401-E) found – in the exclusion zones – using Alloy 52M as filler metal and the corresponding recorded acoustic emissions (220401-TEK2-WH-INC test)

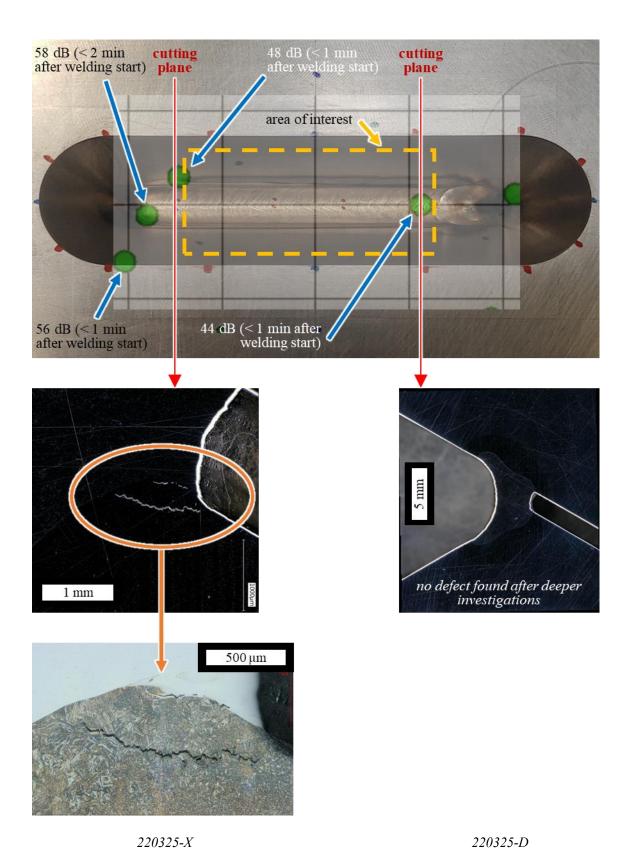


Figure V-h: cold cracks (sample 220325-X) found – in exclusion zone – using Alloy 52M as filler metal and the corresponding recorded acoustic emissions (220325-TEK1-WH-INC test)

Thus, the Tekken testing campaign indicates that, this welding procedure will not cause cold cracking in the context of the envisaged repairs, despite the severely degraded conditions imposed by the presence of hydrogen in the shielding gas and the total absence of additional heating of the mock-ups.

Finally, a portion of the heat-affected zone of the multi-pass Tekken mock-up was mapped by hardness scanning using the same equipment as the Jominy half-bar (refer to section **IV.4.A**). The illustration of the obtained hardness field is given in **Figure V-i**. Measurements were done using a load of 1,00 kg_f and a pitch of 0,50 mm.

HV

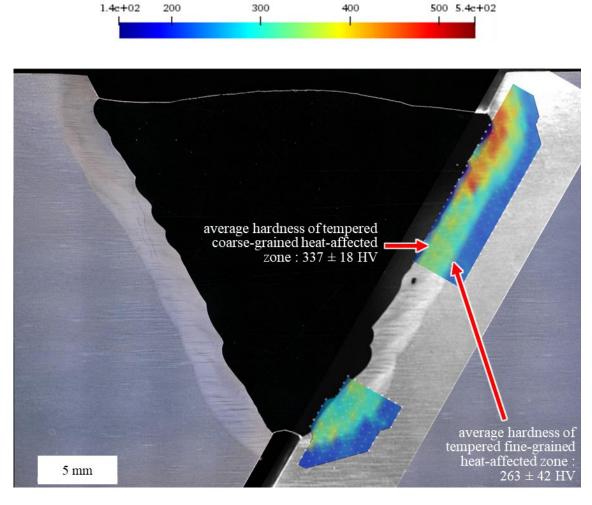


Figure V-i: partial experimental hardness scan of the heat-affected zone of the multi-pass weld Tekken specimen 220408-TEK1-WH-INC-MULTI (220408-C sample; HV1: test load of 1,00 kg_f)

V.3 IMPLANT METHOD

V.3.A Observations

• The implant specimen's V-notch is used to create a geometric singularity. According to the calculation method proposed by [188], the K_t coefficient generated by such a

notch design (given in **Figure V-j**) is 4,08. Two notch designs are proposed by the standard [240]:

- Helical design: makes the positioning of the notch in the heat-affected zone obvious [49]
- Circular design : *the easiest to machine*
- There are differences in national practice for defining the threshold for cold cracking. According to [49], the most appropriate criterion for welded joints is the onset of cracking, not fracture of the specimen. Consequently, the failure criterion adopted in this study is the occurrence of cracking, regardless of its length.
- The standard [240] does not allow manual deposit of the weld bead for this testing method.

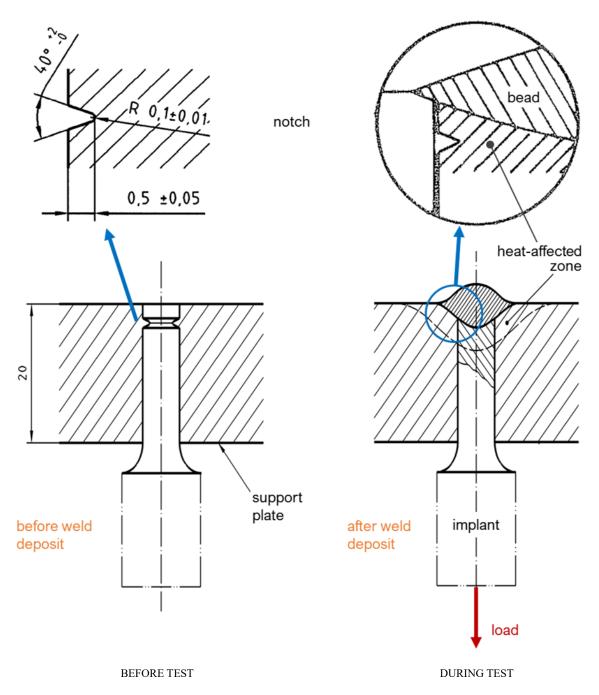


Figure V-j: technical schemes of the implant test method and circular V-notch layout (adapted from [49], [240])

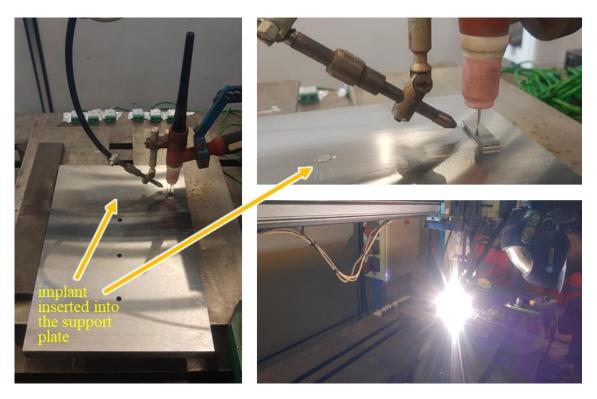
V.3.B Methods

The implant test specimens were turned to a diameter of \emptyset 6 mm (the smallest diameter defined by the standard). Furthermore, it was decided to use the circular notch design. All the implant specimens were extracted parallel to the rolling direction in order to orient the tensile loading in the same way as for the Tekken specimens and thus prevent inconsistencies in the results caused by possible anisotropy in the material properties. Each implant was engraved with its reference. The notches were machined with a tight

tolerance, thus assuring constant K_t values. Continuity of the mechanical properties was not required for the support plates (made from the same 16MND5 batch), so the orientation with respect to the rolling direction was not controlled. Each plate had four holes and could therefore be used for four tests.

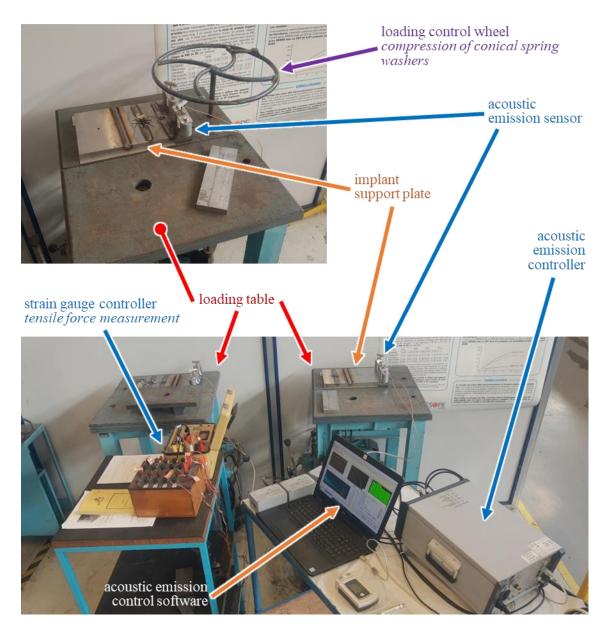
Weld beads were deposited at IS using automated TIG welding. The welding equipment comprised a SAF MECACYCLE S welding manipulator, a Fronius MagicWave 4000 power supply, a Tiger Process TP1002 manual wire feeder, and a TG18 standard tungsten inert gas water-cooled welding torch. In contrast to the robotic installation at EDF PRISME, this automated welding station does not have an arc voltage control feature (A.V.C.). The voltage was thus regulated manually using the height adjustment vernier of the welding torch while monitoring the voltage with a calibrated clamp multimeter (Metrix Electronics MX 675). This measuring device was also used for current intensity adjustment.

The top of the implant must be aligned with the support plate surface. The position of the notch was adjusted by reducing the length of the implant specimen (by machining) before positioning the specimen in one of the holes of the plate. Several preliminary adjustment tests on a simple base metal plate were conducted in order to estimate the length to be removed so that the notches would be in the coarse-grained heat-affected zone (as shown in **Figure V-j**), as close as possible to the fusion line, where the conditions for cold cracking are most favourable.

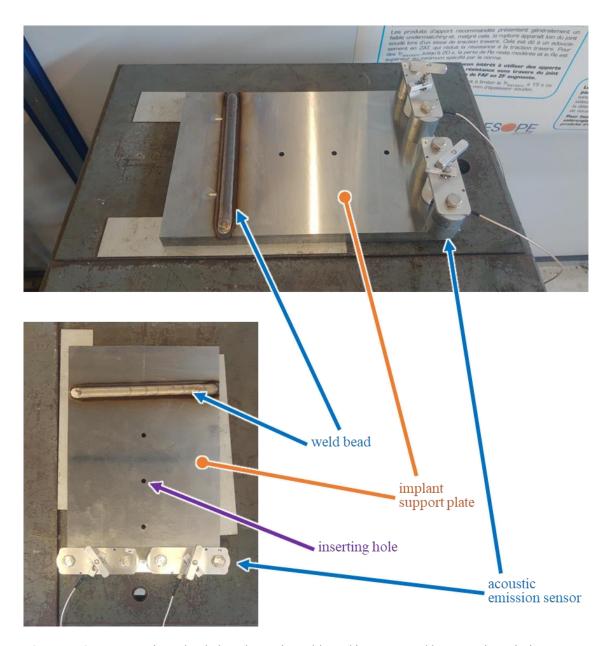


Picture V-g: preliminary adjustment of the welding torch and the trajectory, and a weld bead deposition

A weld bead was then deposited following a linear path passing over the centre of the implant (refer to **Picture V-g**). The weld bead was started and stopped at sufficient distances from the implant to be ensure it responded to steady state welding conditions. Immediately after welding completion, the assembly was transferred to the tensile loading bench (shown in **Picture V-h** and **Picture V-i**), and the load was progressively applied to the implant's bottom end in less than one minute once the temperature had fallen to between 150 °C and 100 °C, measured with a thermocouple probe fixed to the surface of the implant specimen. Since the loading of the specimen is independent from the thermomechanical phenomena, thermal insulation with the welding and testing tables is useless here. In addition, it was not necessary to attempt to locate the possible cracks for this test method, so there was no need to calibrate the acoustic system location module.



Picture V-h: setup used for the implant test campaign



Picture V-i: specimen loaded on the testing table and instrumented by acoustic emission sensors

In contrast to the Tekken test method, the level of the applied stress state is controlled. The tensile stress value is calculated at the net section at the root of the notch. The tensile force is calculated from the loading bar deformation of the test machine measured by strain gauges.

Several stress levels were applied for a minimum period of 16 hours (except if breakage occurs), starting from a high value and lowering in 50 MPa increments to a load that did not lead to a cracking condition and, as prescribed by the ISO standard, was repeatable at least three times (a cracking condition did not require repetition). This allowed to identify the 50 MPa interval where the critical stress lies.

Once this interval was identified, tests with light pre-heating of 50 °C loaded to the

upper interval limit (cracking condition) were performed to investigate its impact. It must be noted that the $t_{8/5}$ time is affected by pre-heating to this temperature, although it increases only slightly from 6,08 s to 6,44 s. This still leads to cooling rates of the order of -50 °C/s, and thereby to martensitic heat-affected zones.

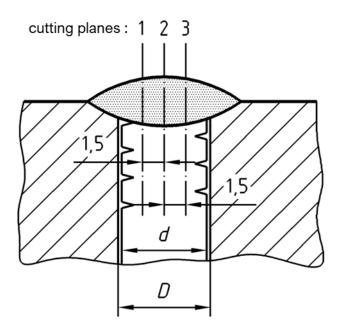
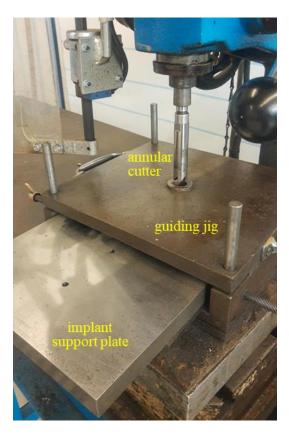


Figure V-k: details of the cutting planes locations (helical V-notch design) – source : [240]

Unbroken specimens were sectioned and examined after completion of testing. A cylinder comprising the implant and the surrounding weld and base metal region was first extracted by grinding, band saw cutting, milling (refer to Picture V-j), and dry disc cutting. The welding direction was first engraved on the upper side of the cylinder. It was then resin mounted and machined on a lathe to expose a first longitudinal cutting plane with respect to the weld bead (refer to Picture V-k). The sample surfaces were then wet ground using silicon carbide (SiC) papers and polished down to 1 µm grade using polycrystalline diamond solutions. They were finally etched using 10 % nital reagent for a few seconds. The position of the notch with respect to the weld metal was first measured using a stereo microscope Olympus SZX9. In some cases, molten weld metal infiltrated the gap between the implant and the plate, and thus reached the notch and filled it. However, this was not considered a cause of non-conformity because experience suggests that it does not affect the stress concentration experienced by the notch region. If the test was deemed valid, an optical microscope Olympus IC70 and a digital microscope Keyence VHX-5000 were used to search for possible cold cracks. Each sample was then re-machined to allow the second, and then the third plane to be examined following the same procedure (refer to Figure V-k).



Picture V-j: extraction of unbroken specimens using an annular cutter (sample contained within the extracted cylinder)



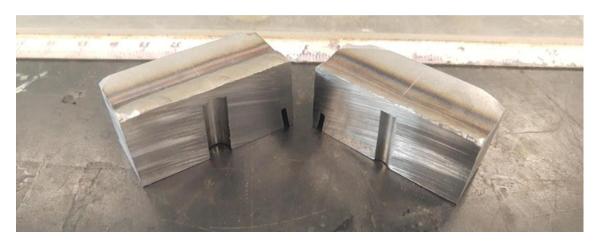


Picture V-k: sample machining on a lathe to expose a longitudinal cutting plane (the surrounding cylinder has been removed in this case)

In the case of broken implants, as shown in **Picture V-l**, the surrounding region was extracted as a rectangular block by dry disc cutting. This block was then cut in half using wet precision cutting. Following the same surface preparation procedure, this longitudinal cross-sectional plane was analysed to verify the position of the notch with respect to the weld metal before confirming the test validity.

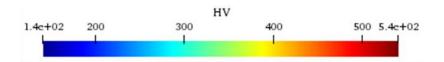






Picture V-1: extraction procedure of broken specimens

In addition, a transverse cross-section of the weld bead was extracted by wet band saw cutting and analysed at the University of Manchester by hardness scanning using the same equipment as the Jominy half-bar (IV.4.A). The hardness distribution is given in **Figure** V-I. Measurements were performed using a load of 1,00 kg_f and a minimum pitch of 0,50 mm in areas experiencing strong gradients, such as the heat-affected zone.



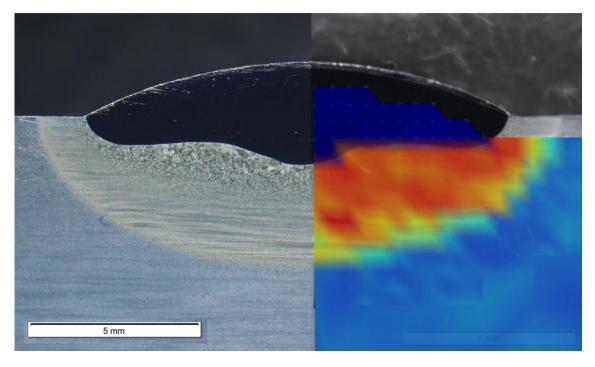
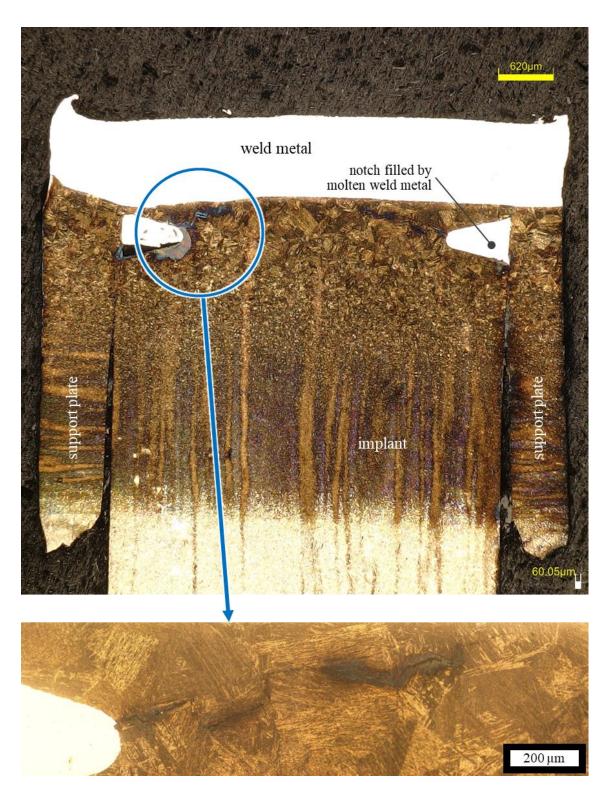


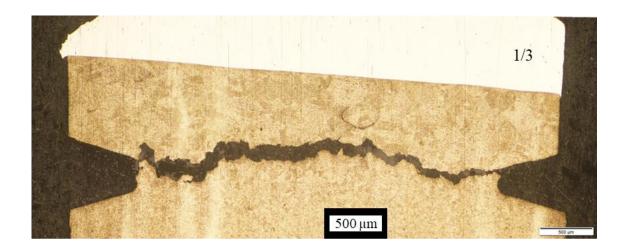
Figure V-1: experimental hardness scan of the transverse cross-section of the MND8 weld bead $(HV1: test load of 1,00 kg_f)$

V.3.C Results & discussion

The first implant test was invalidated because the notch was fused in the weld pool. However, it allowed final adjustment of the notch placement. The remaining tests conducted without pre-heat identified the critical stress for cold cracking to be between 350 MPa and 400 MPa. Some examples of cracked specimens are given in **Picture V-m**, **Picture V-n**, and **Picture V-o**.



Picture V-m: cold crack in the heat-affected zone (sample MND3, cutting plane 1/3)





Picture V-n: cold cracks in the heat-affected zone (sample MND6, cutting planes 1/3 and 3/3)



Picture V-o: small cold crack in the heat-affected zone (sample MND7, cutting plane 2/3)

The first 50 °C pre-heated test was found to be crack-free (load of 400 MPa). However, the second test led to a total breakage after a loading time of about 15 hours (the noise caused by the breakage was heard by a technician present at the time). It was therefore concluded that this pre-heating temperature does not significantly affect the critical stress

value, at the 50 MPa interval used for testing. This finding is slightly more limiting than the one found in the previous 2011 campaign [237] using the welding parameters of the time (no cracking condition at 400 MPa).

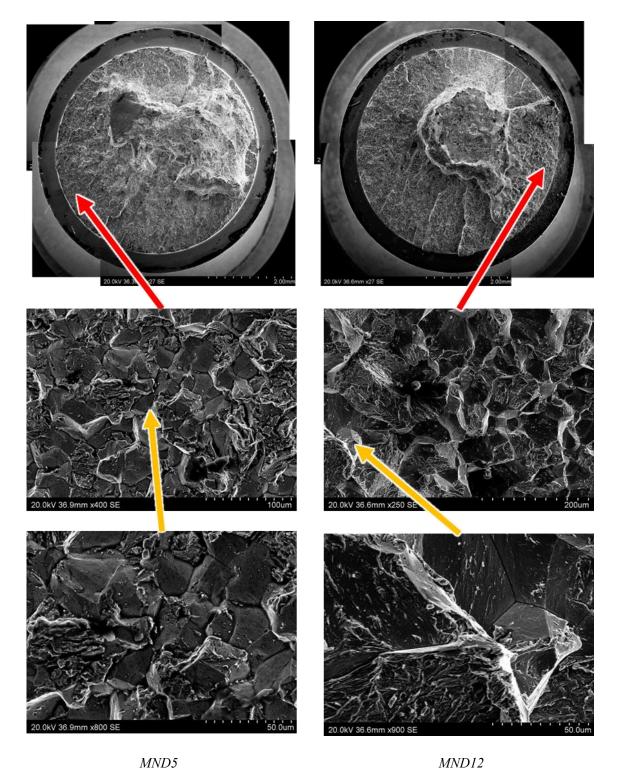
Table V-D: summary of the 2022 implant test campaign results (only valid specimens are included)

testdesignation	during welding		pre-heating		
	relative humidity	ambient temperature	temperature	load	result
MND2	30,6 %	31,8 °C	N/A	400 MPa	no crack
MND3	29,8 %	31,7 °C	N/A	500 MPa	crack
MND4	49,9 %	27,6 °C	N/A	450 MPa	crack
MND5	32,3 %	28,9 °C	N/A	400 MPa	breakage
MND6	32,3 %	28,9 °C	50 °C	450 MPa	crack
MND7	35,8 %	28,5 °C	N/A	400 MPa	crack
MND8	35,8 %	28,5 °C	N/A	350 MPa	no crack
MND9	56,0 %	25,8 °C	N/A	350 MPa	no crack
MND10	56,0 %	25,8 °C	N/A	350 MPa	no crack
MND11	37,6 %	26,9 °C	50 °C	400 MPa	no crack
MND12	37,6 %	26,9 °C	50 °C	400 MPa	breakage

11 valid implant tests were carried out with nickel-based alloy 52M filler metal. Details of the results of each of the 11 tests are given in **Table V-D**. In order to qualify a welding procedure with respect to the risk of cold cracking with the implant method, it is commonly considered that the failure stress should be of the order of the material yield strength [276] (no prescription is given in the standard). The yield strength of 16MND5 is estimated to be 480 ± 65 MPa [17]. Thus, the results of this implant test campaign, imply that this welding procedure is not qualified against the risk of cold cracking under the severely degraded conditions imposed by the presence of hydrogen in the shielding gas, even with the imposition of a light pre-heating of 50 °C.

Electron microscopy of the MND5 and MND12 specimen breakage surfaces was undertaken at the University of Manchester using a scanning electron microscope (S.E.M.) Hitachi S-3400N. Some observations are shown in **Picture V-p**. These observations to identify the type of fracture mode were focused on the areas having experienced the highest stress levels, as these are likely to be where the cracks were initiated. This is thus the area under the notch root. A mix of brittle transgranular (quasi-

cleavage topography) and brittle intergranular (decohesion) regimes was observed for both samples.



Picture V-p: breakage profiles of both fractured implant specimens

V.4 CONCLUSIONS

V.4.A Summary

Two different welding cold cracking test campaigns were conducted under severely degraded imposed conditions in the context of this project. First, significant stress concentrations were involved. Such severity is not common in "real" welds. This is particularly true in the case of the repair studied here, where care will be taken to remove any geometric singularity. But, as noted by [119], severe testing methods ensure margins against the occurrence of unexpected defects or errors that cannot be anticipated. Second, a significant hydrogen content was added to the shielding gas.

In an industrial context with an engineering approach, it may be relevant to determine the exact conditions of the studied repair case in terms of moisture within the containment building of the nuclear steam supply system and get closer to it. A more faithful reproduction of other factors would also be relevant. These might include the ambient temperature, the actual surface conditions of the components, and the preparation before welding (for example, the baking of welding consumables or the orientation of the welding torch).

Regarding the Tekken method, it is not considered realistic to consider the start and stop process transient regions, where the already intentionally degraded conditions are obviously amplified by 3D cooling transients, constraint, and stresses.

The difference in environmental conditions inherent in the timing of these test campaigns imposed moister conditions to the implant tests. Nevertheless, in view of the severe hydrogen doping imposed on the shielding gas, the influence of ambient humidity is considered negligible here.

As shown in **Diagram V-b**, hardness measurements of samples from both test methods showed the consistency of their heat-affected zones. This suggests that the metallurgical conditions are close enough. Furthermore, there is little doubt about the chemical consistency in terms of hydrogen content. Consequently, it is likely that only the mechanical factor is responsible for the differences in the conclusions drawn from these two test methods.

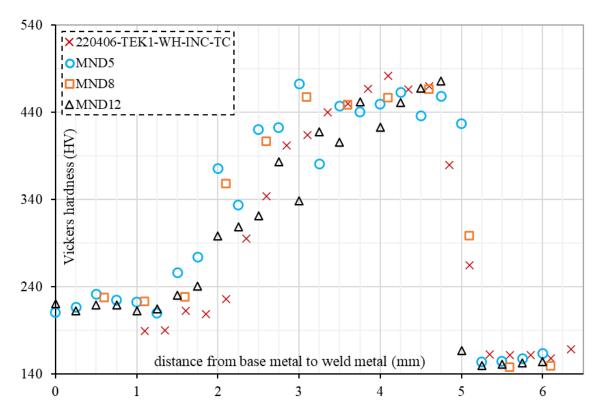


Diagram V-b: hardness comparison of the heat-affected zones produced using the implant and Tekken test methods

V.4.B Crack detection by acoustic emission

Concerning the detection of defects such as cold cracks using an acoustic emission system, the conclusions of this new study are in line with those of [277]. It appears that only defects of significant size or specimen fracture can be detected without ambiguity. The smaller defects were not always identified. This is mainly because their lower signal is diluted within the normal acoustic emissions induced by the establishment of the stress state generated by thermo-mechanical phenomena. In contrast, detected clusters of acoustic emissions did not always correspond to the formation and location of defects.

Nevertheless, the six sensor array, deployed in both the Tekken campaign of [47] and this study, has shown significant gains. This has made it possible to eliminate most of the parasitic emissions occurring outside the area of interest. During the implant campaign, due to the reduced working area and the limitations imposed by the size of the support plates, it was not possible to operate more than two sensors, although this would have been of interest.

Furthermore, as suggested by [277], a deeper exploration by specialists of the possibilities offered by this equipment would probably contribute to the development of

this detection method for cold cracks. [277] cited, for instance, the potential of high frequencies and the energetic evaluation of signals. The exploitation, if possible, of the acoustic emission generated by the progression of hydrogen (≈ 50 dB [274]) could also be of interest.

Finally, other promising techniques for in-process inspection exist and could be of interest for the live detection of cold cracking. For instance, the phased-array ultrasonic testing (P.A.U.T.) and time-of-flight diffraction (T.O.F.D.) methods can be highlighted [24], [278].

V.4.C Extraction by electrical discharge machining

Electrical discharge machining was chosen for slicing the Tekken test mock-ups into several samples. This is not the technique commonly used. It was chosen for the following:

- It increases the cutting precision without significantly extending the machining time.
- The gain in quality of the machined surface reduces the sample preparation time.
- The high level of surface flatness and parallelism greatly facilitates the surface preparation steps.
- There is a low risk of modifying the as-welded microstructure, inducing any machining residual stresses, or complexifying the detection of any defect by crack "clogging".
- Only a few microns of the sub-surface might be affected, which are easily removed during the sample preparation.

V.4.D Benchmarking conclusions

During the benchmarking of these two test methods, it was noted that each method has advantages and disadvantages. It is still difficult to tell which method is better.

As [271] pointed out, it is not easy to produce weld root surfaces in a Tekken specimen

that are always flat. Moreover, they may not always be uniform, even along the same bead. However, it must be noted that the more tilted the root surface, the higher the stress concentration factor (3,5 to 4,7 [207]), which prevents overly optimistic misinterpretation. In addition, it was found that the Tekken configuration is susceptible to other defects that interfere with the study of cold cracking, such as root or surface root cracking (probably hot crack type) and weld metal solidification shrinkage. Indeed, these most probably modify the levels of local stress concentration sought with this test method. The standard does not specify what to do in these cases, although it is presumed that the test cannot be considered valid if this occurs within the area of interest. Nevertheless, the Tekken test method is probably more realistic because of the self-restraint phenomenon, which corresponds to the "real" conditions at a weld. Furthermore, this weld configuration takes into account the effects of the mechanical behaviour of the weld metal on the magnitude of the residual stress generated. This eliminates additional assumptions concerning the mechanical load factor. The self-constraint has been set to its maximum level in this study. Finally, the Tekken test campaign has the advantage of being binary, with a simple pass or fail outcome.

Regarding the implant, it is not always easy to position the notch correctly, close to the fusion boundary, or at least consistently from one test to the next due to variation in the molten weld pool. A helical notch design can solve this problem [49], at the expense of more complex machining. In the current study, even correct machining of the circular notch proved difficult to achieve. In contrast, the welding and post-test analyses of the implant test are easier and faster. In addition, the effects of start and stop process transients are eliminated. Nonetheless, the pass/fail criterion of this method is ambiguous. The standard does not provide a defined approach. However, the common practice of considering that the maximum admissible stress should equal the elastic limit of the tested base metal [276] seems realistic since, once exceeded, plasticity will occur, limiting the increase in mechanical load experienced by the weld. But this assumption is maybe one of the reasons for the severity of this configuration since the mechanical behaviour of the weld metal is possibly less impactful here. Indeed, considering that the elastic limit of the Alloy 52M is lower than that of 16MND5 steel, it could be argued that the earlier yielding of the weld metal mitigates more residual stresses in a real case than in this test.

In conclusion, contradictory results were obtained from two different single-bead test methods prescribed by the same standard [87], [191], [240] for the qualification of the same welding procedure :

- Not admissible according to the implant method using the common yield strength condition
- Admissible according to the Tekken method where the self-restraint condition was set to its maximum

V.4.E Recommendations

For further development of cold-cracking benchmarking, it is suggested to estimate quantitatively what is the actual local stress experienced in the heat-affected zone in each of these two test mock-ups, by modelling and simulation and/or by experimental approaches.

Then, it would be of interest to compare these stress levels with those generated in the case of the investigated plant repair to assess the comparative severity of the test methods.

Subsequently, it may be of interest to explore the possibilities offered by implant specimens with a different notch design generating more realistic K_t , or Tekken mockups with a longer weld groove and/or using run-on and run-off inserts in the groove end sections to tackle the start and stop process transient problems in these regions.

VI BEHAVIOUR STUDY OF THE HEAT-AFFECTED ZONE EXPOSED TO HYDROGEN

VI.1 FOREWORD

This chapter presents a study of hydrogen embrittlement in low-alloy ferritic steel 16MND5. This work was carried out in France during a secondment of several months spent with LaSIE's researchers at La Rochelle Université. This laboratory specialises in research addressing the durability and protection of materials under environmental attack. One of its research groups focuses on the study of interactions between hydrogen, metallurgy, and stress state. The work performed at La Rochelle aimed to understand the influence of hydrogen on the mechanical properties of weld heat-affected zone microstructures. It allowed to address part of the objectives related to the first and second conservatisms (respectively, viability demonstration of bead tempering methods, and highlighting the interest in probabilistic criteria). Two experimental campaigns were run, in 2019 and 2021, each examining a specific area of the heat-affected zone.

VI.2 METHODS

Two primary microstructures were selected, representing fine- and coarse-grained heat-affected zone locations. A third microstructure, representing tempered heat-affected zone material, was also defined. These microstructures were observed and characterised using a number of techniques. The steel batch used was the same as all previous experiments conducted during this project.

Hydrogen solubility in the two first microstructures was then determined. Samples were charged in hydrogen for increasing durations and their content was then measured.

Uniaxial tensile tests were then performed using cylindrical specimens charged with hydrogen to specific concentrations. Both smooth and V-notched specimens were tested. The dimensions of each specimen were measured individually before testing. Tensile tests using as-quenched specimens (without subsequent hydrogen charging) were also performed to establish the baseline stress-strain response of each microstructure. The V-notch was designed following the specifications of the implant test standard [240] to maximise the transferability of the findings to implant test behaviour.

The impact of effusion and desorption kinetics was also investigated. The hydrogen content of each tensile test specimen was measured post-fracture. Subsequently, fractographic observations were made to measure the reduction of area (necking) and to characterise the fracture mode. Finally, the experimental data were analysed to quantify the loss of ductility in each microstructure for both stress states and to allow critical evaluation.

VI.3 REPRODUCTION OF TYPICAL HEAT-AFFECTED ZONE MICROSTRUCTURES

VI.3.A Targeted microstructure types

As discussed above, both the penetration of hydrogen and its consequences in a given steel depend strongly on the microstructure. The heat-affected zone microstructure is highly heterogeneous, so it is likely that the extent of hydrogen-induced embrittlement will be different in different regions of the heat-affected zone region, even assuming a uniform concentration of hydrogen. It is thus necessary to assess a range of possible heat-affected zone microstructures.

Thus, considering a single weld bead deposit, let's start first by reminding in what does the heat-affected zone microstructure vary. It can be summarised by the following:

- The heat-affected zone microstructure varies radially with respect to the heat source, which could be considered here as being the molten weld pool.
 Consequently, the whole heat-affected zone microstructure evolution can be observed along a single segment.
- The usual main changes along this segment are described below, from the fusion boundary towards the unaffected area:
 - From a large to a small prior austenite grain size due to the decrease in the maximum temperature reached
 - From hard to softer microstructures due to the combination of longer cooling times (in other words, lower cooling rates) and smaller prior austenite grain sizes, typically from martensitic to bainitic types

Thus, two types of microstructures should be considered in this study, the first representing the coarse-grained heat-affected zone close to the fusion boundary (1st region pointed out in **Figure VI-a**), and the second representing the fine-grained heat-affected zone (2nd region pointed out in **Figure VI-a**). This corresponds to a prior austenite grain size range from 3 μ m to 130 μ m, as stated in the section **IV.2.B.1**. A series of trials were performed at LaSIE to establish heating and holding conditions that result in a 130 μ m austenite grain size. A parallel project run by EDF at the IRDL²⁷ (CNRS – UBS²⁸) had already established a reliable heat treatment to achieve an austenite grain size of 15 μ m, so this size was adopted as the fine-grained condition.

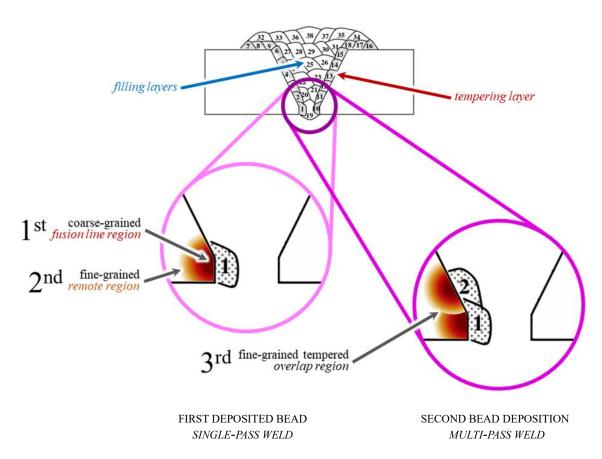


Figure VI-a: schematic illustration of the sectioned microstructure locations within the heat-affected zone of a multi-pass weld made using the temper bead welding technique (adapted from [25])

It was decided to simplify the test matrix by using samples containing only a single and monophasic micro-constituent. Both the coarse- and fine-grained heat-affected zone samples were thus quenched to achieve fully martensitic structures, since martensite is the most brittle heat-affected zone micro-constituent. This is a conservative

230

²⁷ Institut de Recherche Dupuy de Lôme – Unité Mixte de Recherche n° 6027, 56321, Lorient, France

²⁸ Université Bretagne-Sud

simplification.

VI.3.B Heat treatment procedures

The selected microstructures were produced by specific austenisation and quenching thermal treatments, using a laboratory chamber furnace (Carbolite Gero CWF 1200) and a 20 °C water bath. The two thermal treatments are summarised in **Diagram VI-a**. Water quenching allows high cooling rates of about -100 °C/s, which, according to [225], ensures almost fully martensitic microstructures regardless of the austenite grain size.

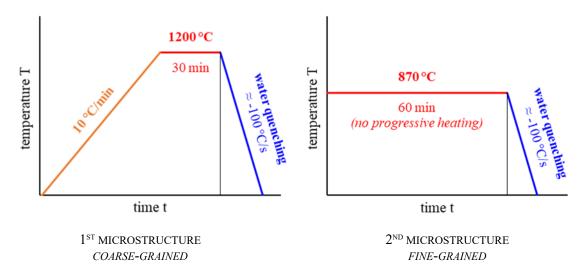


Diagram VI-a: diagrams representing the thermal treatment cycles applied to produce the 1st and 2nd microstructure samples

In a multi-pass weld, the heat-affected zone created by a given bead is "tempered" by the thermal cycle induced by the subsequent adjacent weld run (refer to **Figure VI-a**). Hence, it was decided to briefly explore the hydrogen-induced loss of ductility in tempered microstructures. To that end, a number of fine-grained heat-affected zone microstructure samples were tempered to represent the 3rd region pointed out in **Figure VI-a**. The parameters of the tempering thermal treatment were defined by the IRDL's researchers. The whole thermal cycle applied to these 3rd microstructure samples is summarised in **Diagram VI-b**. Because the tempering procedure is almost 24 h in duration, the samples were heat treated under a protective atmosphere to prevent decarburisation due to excessive oxidation, using a laboratory tube furnace ThermConcept ROS 75/700/12-3. After purging the ambient air twice with a vacuum pump, a constant flow of shielding gas (argon) was applied through the tube, and the thermal treatment started. This setup is shown in **Picture VI-a**.

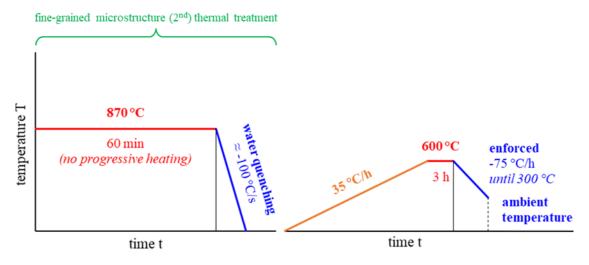
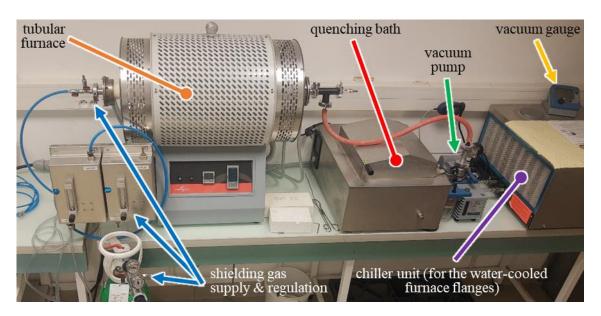


Diagram VI-b: diagram representing the thermal treatment cycles applied to produce the 3rd microstructure samples



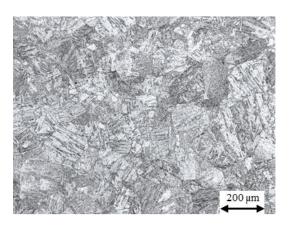
Picture VI-a: thermal treatment setup utilised in the 3rd microstructure tempering (fine-grained tempered)

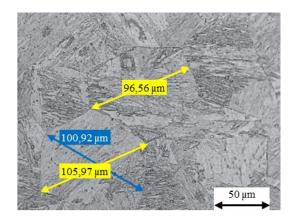
VI.3.C Metallographic observations

Metallographic analyses were carried out at different scales on the produced coarseand fine-grained microstructures (1st and 2nd) to confirm that the thermal treatment parameters produced the expected microstructures. To that end, samples were extracted by wet precision cutting (≥ 1 mm sub-surface was discarded to exclude any edge effect) using an aluminium oxide Al₂O₃ cut-off wheel (cutting parameters : 3~000~rpm~&~0,025-0,070~mm/s). The surfaces were then wet ground down to P4000 grade using silicon carbide (SiC) papers (grinding parameters : 150-300~rpm) then polished down to ½ µm grade using polycrystalline diamond solutions (polishing parameters : 150~rpm). The consumables were supplied by Presi or Struers.

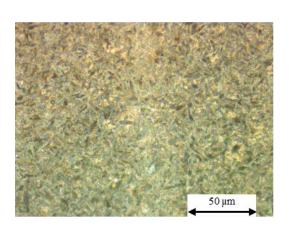
VI.3.C.1 Optical microscopy

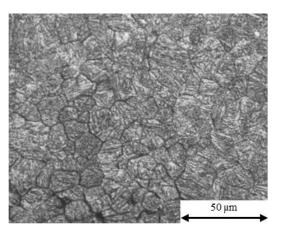
The microstructures were first investigated using optical microscopy. The polished surfaces were chemically etched using Kalling's and 2 % nital reagents for 5 minutes and 30-45 seconds, respectively. They were then observed using a Leica DM6000 M microscope. Pictures of these observations at different magnifications are shown in **Picture VI-b** (coarse-grained – 1^{st} microstructure) and **Picture VI-c** (fine-grained – 2^{nd} microstructure).





Picture VI-b: optical micrographs of the 1st microstructure representing coarse-grained heat-affected zone (greyscale)



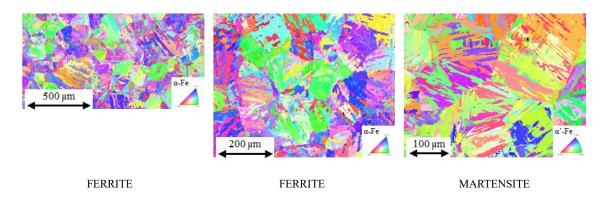


Picture VI-c: optical micrographs of the 2nd microstructure representing fine-grained heat-affected zone (right image in greyscale)

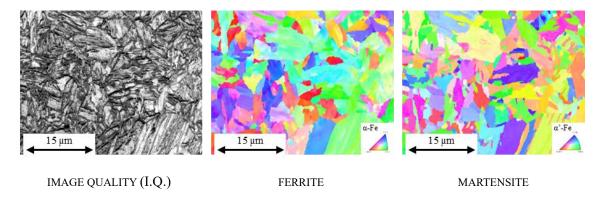
VI.3.C.2 Electron microscopy

Observations were continued using scanning electron microscopy. Surface preparation was completed by electropolishing for 30 s using an electrolyte solution made of picric acid diluted with methanol. Once the samples were placed into the scanning electron microscope (utilised equipment: Philips FEI Quanta 200 FEG/ESEM), E.B.S.D. analyses

were processed and post-processed using the software EDAX TSL OIM Analysis v5. This technique allows, among other things, identification of grain orientations, grain structures, and micro-constituents. Pictures of these observations are shown in **Picture VI-d** (coarse-grained – 1st microstructure) and **Picture VI-e** (fine-grained – 2nd microstructure).

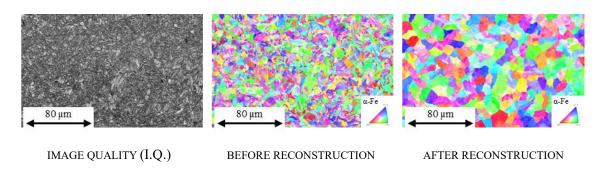


Picture VI-d: electron backscatter diffraction analysis of the 1st microstructure representing coarse-grained heat-affected zone



Picture VI-e: electron backscatter diffraction analysis of the 2nd microstructure representing finegrained heat-affected zone

In addition, prior austenite grain reconstruction analyses was carried out on the finegrained microstructure to aid the prior austenite grain size measurements (**Picture VI-f**).



Picture VI-f: prior austenite grain reconstruction analyses of the 2nd microstructure representing fine-grained heat-affected zone

VI.3.C.3 Hardness measurements

Finally, these observations were completed by Vickers hardness measurements of each of the produced microstructures. The initial hardness of the supplied material was also evaluated. The measurements were made using a Qness Q10 M micro-hardness tester on samples wet ground down to grade \geq P2400 (12 indents, removal of the two extremes, averaging). A test load of 1,00 kg_f was chosen to ensure consistency with previous work on the chosen steel, such as the NeT-TG8 program [228], [243]. The results are summarised in **Table VI-A**.

Table VI-A: hardness measurements in the bulk of the three produced microstructures following the Vickers method (test load of $1,00 \, \mathrm{kg_f} - 12$ indents, removal of the two extremes, averaging)

microstructure	type	hardness	standard deviation
initial as-provided	rolled - quenched - tempered	215 HV1	16 HV1
1 st	coarse-grained	445 HV1	14 HV1
$2^{\rm nd}$	fine-grained	491 HV1	8 HV1
3^{rd}	fine-grained & tempered	280 HV1	7 HV1

In addition, the residual anisotropy caused by the rolling operations was found to have no impact on the consistency of hardness from one orientation to another. This was verified for each of the produced microstructures, as well as for the initial microstructure.

VI.3.C.4 Conclusions

The optical and electron microscopy allowed the evaluation of the prior austenite grain size for the produced microstructures. The measured values are presented in **Table VI-B**. These results were entirely satisfying with respect to the objectives, with a relatively small spread. Moreover, the microscopy also revealed large proportion of martensite in both microstructures by identification of its characteristic structures.

Table VI-B: size measurements of the prior austenite grains in the produced microstructures

Microstructure	type	prior austenite grain size	standard deviation
1 st	coarse-grained	130 µm	30 μm
2^{nd}	fine-grained	12 μm	3 μm

Secondly, the hardness measurements indicated values above 445 HV for the asquenched microstructures (1^{st} and 2^{nd}). For steels with this carbon content, values above 430 HV after quenching tend to indicate almost wholly martensitic microstructures [279]. Therefore, it was concluded that these quenching conditions were reliable for producing martensitic samples. A significant decrease in hardness was observed in the tempered microstructure (3^{rd}), confirming the relevance of this thermal treatment parameters (263 ± 42 HV measured in the tempered remote heat-affected zone of the welding test 220408-TEK1-WH-INC-MULTI – sample 220408-C (**Figure V-i**)). Furthermore, the low standard deviations indicate good homogeneity within each generated microstructure.

Finally, the metallographic observations also gave the opportunity to evaluate the inclusion density in the as-received microstructure of the steel used during this project. This was assessed in both transverse and longitudinal planes with respect to the rolling direction. In addition, the average inclusion size was calculated. These results are presented in **Table VI-C**.

Table VI-C: inclusion density and size in the as-received steel microstructure

	orientation to the rolling direction	value	standard deviation
average size	-	8,68 µm	3,89 µm
density	longitudinal	25,60 inclusions per mm ²	11,61 inclusions per mm²
	transverse	24,15 inclusions per mm ²	9,69 inclusions per mm²

The residual anisotropy caused by the rolling operations was found to also have no impact on the inclusion distribution. Nevertheless, all of the tensile test specimens were extracted with an orientation parallel to the rolling direction.

VI.4 HYDROGEN SOLUBILITIES

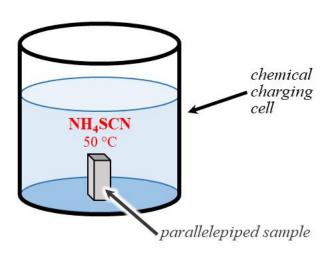
Once the procedures for producing coarse- and fine-grained microstructures (1^{st} and 2^{nd}) were established, their hydrogen solubility was investigated. To that end, $4 \times 4 \times 10 \text{ mm}^3$ parallelepiped samples were extracted with the same previously described procedure, followed by surface preparation consisting of mechanical grinding down to P2400 grade, ethanol-cleaning, and drying using dry air. The specific volume of these samples allows a weight of 1,0 g to be approached, which is best suited to ensure optimal analysis of the hydrogen content with the LaSIE's procedure.

VI.4.A Hydrogen charging

The hydrogen charging procedures commonly used are based on Volmer's kinetics. The most commonly used method is electro-chemical charging [110], [112]. However, during the investigations related to the previous project of Qianqiang [47], LaSIE's researchers noticed that hydrogen contents charged with this technique for this type of steel with martensitic microstructures were poorly reproducible [166]. Moreover, the charging durations were quite long, taking several days to reach the maximum concentration. Consequently, a chemical charging procedure was chosen for this project.

This method consists of simply immersing the samples in a bath of ammonium thiocyanate (NH₄SCN). This solution is prepared by dissolving solid NH₄SCN into liquid water (purified by a Merck Millipore Milli-Q system) at a concentration of 250 g/L (saturation level). The chemical cell must be filled with sufficient solution to ensure a pseudo-infinite hydrogen content available to be absorbed by the samples. The hydrogen charging setup is shown in **Picture VI-g**. Each solution is used only once. The cell is heated to 50 °C, which promotes chemical reactions, and thereby the hydrogen sorption phenomena (adsorption and absorption). The longer the charging duration, the higher the hydrogen concentration in the sample, with a limit at the solubility threshold.





DOUBLE CHARGING CELL SETUP

CHEMICAL CHARGING CELL DETAILS

Picture VI-g: hydrogen chemical charging setup and approximate sample/solution volume ratio (adapted from [280])

The samples were charged for various durations to study the whole hydrogen charging domains of the coarse- and fine-grained microstructures (1st and 2nd). This was not investigated in the tempered fine-grained microstructure (3rd). Only the hydrogen

concentration after charging for the duration associated with the maximum level in the 2^{nd} microstructure was evaluated for this 3^{rd} microstructure. Each test was repeated once or twice to assess reproducibility.

VI.4.B Hydrogen maximum content identification

Once the hydrogen charging was completed, samples were water-rinsed twice and mechanically wet ground again with grade P2400 SiC paper to remove any possible residual corrosion product. They were then acetone-cleaned and weighed.

Each sample was analysed using thermal desorption spectroscopy (T.D.S.) to measure the hydrogen concentration. The equipment used was a Horiba EMGA-621W hydrogen analyser by gas-katharometry (shown in **Picture VI-h**). The sample transfer time from the charging cell to the hydrogen analyser was about five minutes. It must be noted that this results in a slight loss of diffusible hydrogen. The loss was quantified by [147], who evaluated it as about 7 % of the initially charged concentration. Once placed into the sealed furnace of the analyser, the chambers and tubing of this system are bled, and tin (Sn) flux is added to the sample in the crucible. Then, the sample is directly heated to a temperature of 2 000 °C (it melts, so this is a destructive analysis). This temperature releases all the hydrogen, both mobile and immobile.



Picture VI-h: Jobin Yvon Horiba EMGA-621W hydrogen analyser (scale, furnace, and hydrogen detector)

The thermal desorption spectrum obtained is then post-processed to calculate the overall hydrogen content. The results showing the evolution of the hydrogen

concentration as a function of charging time for the coarse- and fine-grained microstructures are presented in **Diagram VI-c** (1st and 2nd). The maximum hydrogen levels were reached in 6 h and 16 h and were $1,28 \pm 0,14$ wppm and $1,47 \pm 0,08$ wppm, respectively. It must be noted that the subsequent slight decrease before stabilisation is a commonly observed phenomenon. The principal hypothesis put forward within the scientific community to explain this is that there is a competition effect between the kinetics of sorption and desorption. It is assumed that the desorption kinetic begins with a time lag after the sorption kinetic. The moment when the curve starts to decline – and therefore, the hydrogen concentration begins to drop – would be when the desorption mechanisms start to activate and compete with those of sorption. The subsequent plateau observed after the curve inflexion would correspond to the attainment of equilibrium between these two kinetics operating simultaneously. Their "natural" hydrogen content was also measured using two samples per microstructure (no hydrogen charging). It was $0,05 \pm 0,04$ wppm for both microstructures.

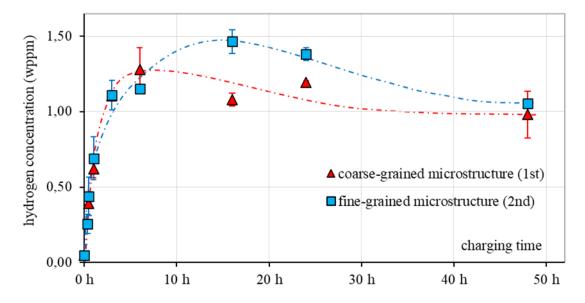


Diagram VI-c: hydrogen charging domain in the coarse- and fine-grained microstructures (1^{st} and 2^{nd})

Diagram VI-d compares the charging duration to the maximum hydrogen content with the previous investigations undertaken during the previous project of Qianqiang at the LaSIE [47], [166]. The hydrogen concentration in the 3rd, tempered, microstructure after charging for the period associated with the maximum level in the 2nd microstructure is also included.

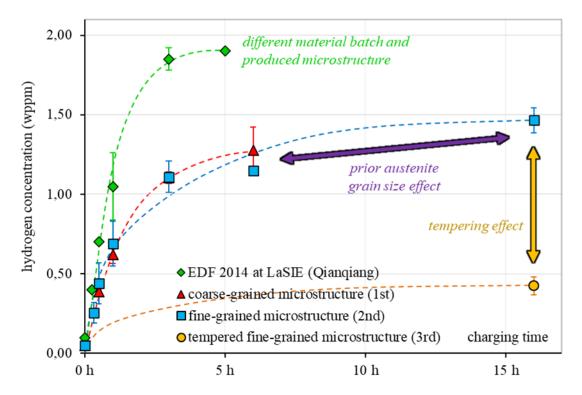


Diagram VI-d: hydrogen solubility comparison with the tempered fine-grained microstructure (3rd), as well as with the previous microstructure investigated at the LaSIE during the research project of Qianqiang [47], [166]

The gap between the coarse- and fine-grained microstructure (1st and 2nd) curves is small. Nevertheless, it is observed that a little bit more hydrogen can be introduced in the fine-grained microstructure (2nd) with a longer charging time. On the other hand, tempering the microstructure seems to reduce hydrogen solubility significantly. The wide gap with the previous research project may be explained by the differences in the used material batch and the produced microstructure investigated at that time. Finally, the low scatter in results indicates good experimental reproducibility.

VI.4.C Hydrogen content distribution

The distribution of hydrogen between the three categories (diffusible, reversibly trapped, and irreversibly trapped) was investigated for the coarse- and fine-grained microstructures only (1st and 2nd). It is of interest to know this since the degree of noxiousness of these different categories is not the same [112]. Consequently, a given concentration of hydrogen can have an impact of variable magnitude depending on its distribution.

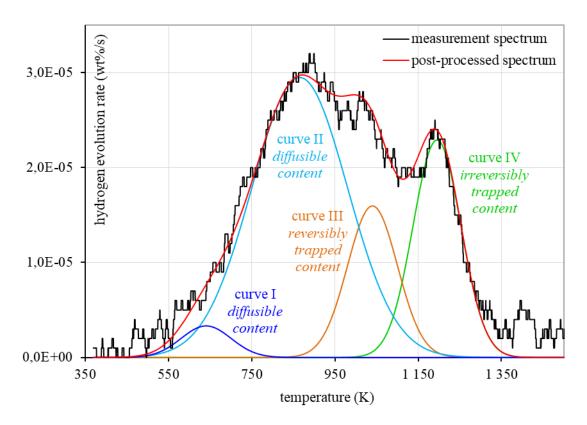


Diagram VI-e: hydrogen desorption profile obtained during thermal desorption spectroscopy analysis at a heating rate of 230 K/min of the content distribution in the fine-grained microstructure (2nd) charged at the maximum concentration

To that end, additional samples were charged to their maximum hydrogen level and placed into the hydrogen analyser chamber following the procedure described above (again, two samples per microstructure). However, instead of rapidly heating up to 2 000 °C, a controlled heating rate was applied to allow the different hydrogen contents to be distinguished. It was established by [112] that 230 K/min is the most relevant rate for low-alloy martensitic steels. The thermal desorption spectra obtained were post-processed by decomposing them into the sum of four Gaussian distributions. One of those obtained for the fine-grained microstructure (2nd) is given as an example in **Diagram VI-e**. Since the difference in peak temperatures of the gaussian curves correspond to a gap in binding forces between hydrogen and the trapping sites [147], it is therefore possible to identify the different contents:

- Curves I & II: correspond to diffusible hydrogen
- Curve III: corresponds to reversibly trapped hydrogen
- Curve IV: corresponds to irreversibly trapped hydrogen

Each test condition was repeated once to assess the repeatability. The results showing distributions of the hydrogen content are given in **Diagram VI-f**.

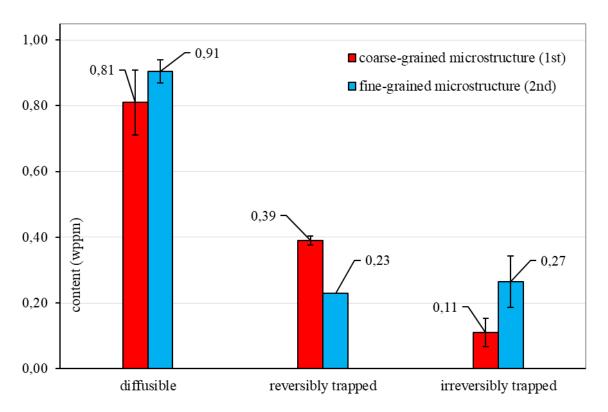


Diagram VI-f: hydrogen content distributions in the coarse- and fine-grained microstructures (1^{st} and 2^{nd}) charged at the maximum concentrations

VI.5 MECHANICAL TESTING

Then, tensile test specimens were produced. To that end, during the first campaign investigating the coarse-grained microstructure (1st), rods were first extracted from the block of the considered steel batch by electrical discharge machining, then specimens were machined by turning, and finally quenched. Both smooth and V-notched specimens were produced for this microstructure. This manufacturing sequence order was chosen for preventing any machining residual stress.

However, the fine-grained microstructure (2^{nd}) specimen rods were finally quenched before the machining steps because it was considered that their thermal treatment generated a higher level of quenching residual stress (a few hundred megapascals, approximated by computing simulation and by X-ray diffraction analysis of some samples post-processed following the method defined by [281], [282]) plus a decarburisation in the sub-surface ($\approx 200~\mu m$, assessed by nano-indentation analysis). These phenomena could thus lead to misinterpretations, since material at the notch root could be decarburised. Only V-notched specimens were produced for the 2^{nd} microstructure. Some of them were then tempered to produce 3^{rd} microstructure specimens.

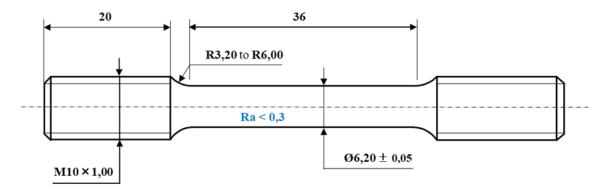


Figure VI-b: layout of the smooth tensile test specimens

The layouts of the smooth and the V-notched tensile test specimens are given in **Figure VI-b** and **Figure VI-c**. The dimensions of each specimen were individually measured before testing by optical microscopy using a stereo microscope Leica M205 A. The stress concentration factor, K_t , generated by the V-notch geometry as defined by the implant test standard [240] is 4,08. However, because of fluctuations in machining accuracy, the final K_t coefficients of the notches produced were about 2,98 \pm 0,06 and 3,68 \pm 0,01 for the coarse- and fine-grained microstructure specimens, respectively.

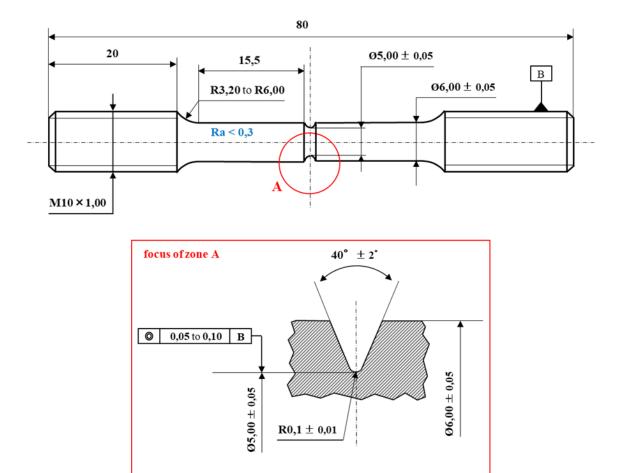


Figure VI-c: layout of the V-notched tensile test specimens (designed according to the implant test standard [240])

All tests were performed at ambient temperature (20 ± 5 °C) and following a strain rate of 10^{-5} s⁻¹, the optimum speed commonly used throughout the scientific community for studying the impact of hydrogen on the material tensile behaviour. Consequently, the strain measurement sensitivity is of the order of 10^{-5} [112]. Tensile tests were realised using a fatigue testing machine Instron 8862 and an extensometer MTS 632.13F-20 (gauge length of 10 mm) to measure specimen extension directly. **Picture VI-i** shows the specimen positioning on the testing machine. In addition, most of the tested conditions were repeated once for the coarse-grained microstructure (1^{st}) specimens to assess the reproducibility of the results. Then, they were repeated twice for the fine-grained and tempered fine-grained microstructure (2^{nd} & 3^{rd}) specimens. Engineering stress-strain curves were used to plot the results. Concerning V-notched specimens, the stress is calculated at the net section at the root of the notch.



Picture VI-i: positioning of a notched specimen on the testing machine

VI.5.A As-quenched

Baseline behaviour was first established by testing specimens not exposed to hydrogen. These results are presented in **Diagram VI-g**. Variations in stiffness and ultimate elongation are observed between the smooth and the V-notched specimens ($\approx 186 \text{ MPa}$ and $\approx 9 \%$ versus $\approx 242 \text{ MPa}$ and $\approx 4.5 \%$, respectively). On the other hand,

the microstructure condition did not seem to influence behaviour. However, concerning its impact on the ultimate tensile strength value, it was difficult to propose a relevant comparison because of the difference in the K_t coefficients and the difference between the specimen manufacturing sequences.

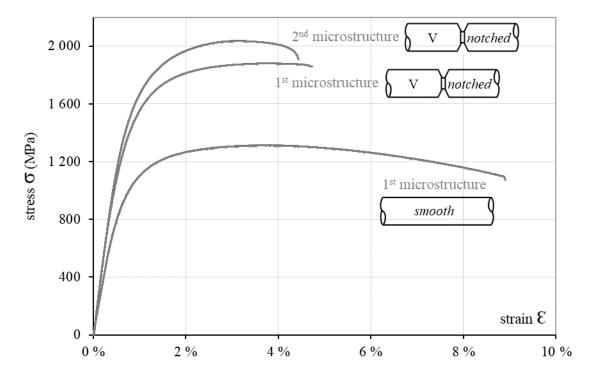


Diagram VI-g: engineering stress-strain curves comparing specimens not exposed to hydrogen

VI.5.B Hydrogen-exposed material

The remaining tensile specimens were then charged in hydrogen at various concentrations before being tested to evaluate the impact of hydrogen on the mechanical properties. The charging curves presented in **Diagram VI-c** were used to establish an appropriate test matrix, as follows in **Table VI-D**.

Table VI-D: summary of the hydrogen concentration levels selected for the tensile testing

charging time	hydrogen concentration	standard deviation
	coarse-grained microstructure (1st)	
30 min	0,39 wppm	0,01 wppm
2 h	0,75 wppm	0,06 wppm
4 h	1,00 wppm	0,04 wppm
6 h	1,28 wppm	0,14 wppm
	fine-grained microstructure (2 nd)	
20 min	0,26 wppm	0,06 wppm
30 min	0,44 wppm	0,13 wppm
16 h	1,47 wppm	0,08 wppm
1	tempered fine-grained microstructure (3 ¹	rd)
16 h	0,42 wppm	0,06 wppm

Prior to immersion into the chemical charging cells, the threaded ends and fillets of the tensile specimens were protected from hydrogen with two layers of acrylic coating varnish plus a "bandage" of Teflon tape. These zones contain local stress concentration, and it is important to prevent failure outside the gauge section. The predicted stress concentration within the fillet region is illustrated in **Figure VI-d**. In parallel, the "functional" surfaces, including the notches, were wet ground down to P2400 grade, ethanol-cleaned, and dried using dry air (exactly as the previous parallelepiped samples in section **VI.4.A**). The specimens were then plunged into the charging solution baths (diluted NH4SCN, 50 °C), as shown in **Picture VI-j**, for the desired period.

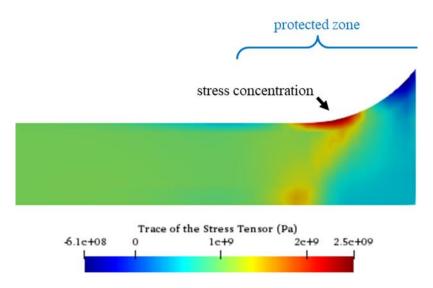
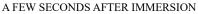


Figure VI-d: Code_Aster simulation of the local stress distribution (trace of the tensor) in the fillet region of a smooth tensile test specimen loaded to an average stress σ_{avg} of 1 495 MPa (calculated in the gauge section)

After that, the hydrogen-charged specimens were water-rinsed twice, their Teflon tape protections removed, mechanically wet ground again with grade P2400 SiC paper (to discard any possible residual corrosion product), and the protective varnish using acetone in an ultrasonic cleaner. They were then mounted in the testing machine and the tensile test was performed. Consequently, the minimum achievable transfer delay from the charging chemical cell to the test start was about 15 minutes.







AFTER SEVERAL CHARGING HOURS (SURFACE OXIDATION)

Picture VI-j: tensile test specimens immersed into jacketed reaction beakers used as chemical charging cells

The engineering stress-strain curves are presented in **Diagram VI-h**, **Diagram VI-i**, **Diagram VI-j**, and **Diagram VI-k**. It must be noted that the ordinate axis scale (elongation *A*) has been adjusted for the notched specimen curves in order to improve readability (**Diagram VI-i** and **Diagram VI-j**). Significant and progressive reductions in elongation to failure as the hydrogen content increased were observed for both coarseand fine-grained microstructures (1st and 2nd). The shape of the stress-strain responses suggests that the primary effect of hydrogen is a loss in ductility.

In the tempered fine-grained microstructure (3rd) specimens, the ultimate elongation after introducing the maximum hydrogen content was about twice that observed prior to tempering with no exposure hydrogen. It is evident that the tempered microstructures seem to be much less sensitive to the effects of hydrogen.

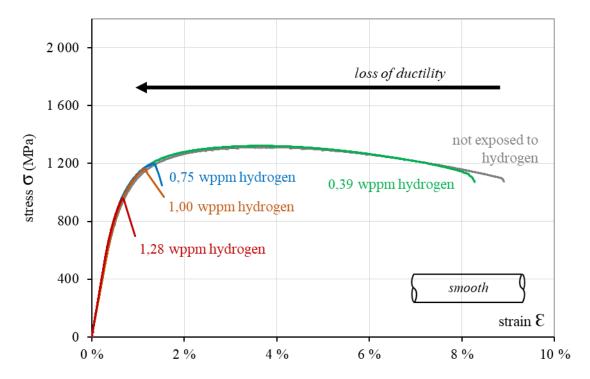


Diagram VI-h: engineering stress-strain curves obtained with the coarse-grained microstructure (1st) smooth tensile test specimens exposed to hydrogen

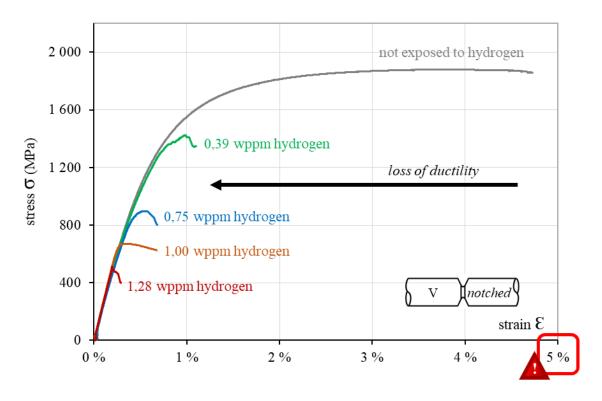


Diagram VI-i: engineering stress-strain curves obtained with the coarse-grained microstructure (1st) notched tensile test specimens exposed to hydrogen

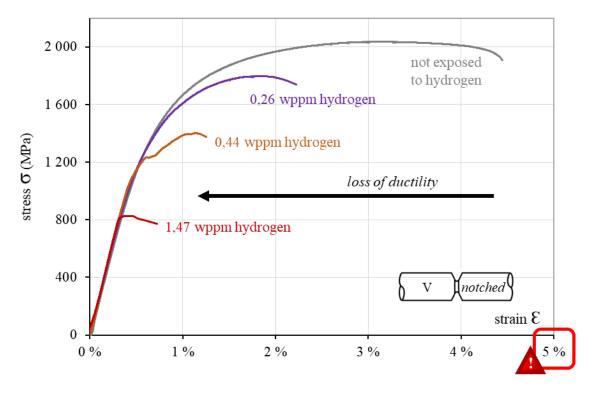


Diagram VI-j: engineering stress-strain curves obtained with the fine-grained microstructure (2nd) notched tensile test specimens exposed to hydrogen

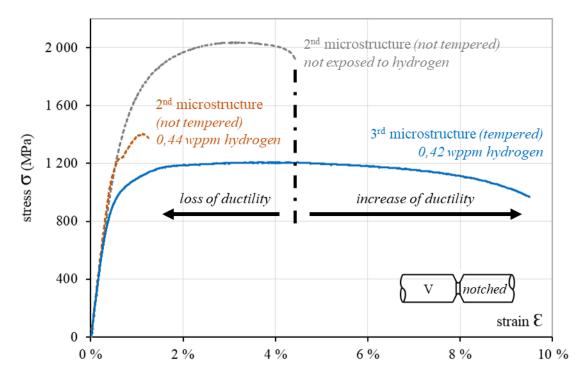


Diagram VI-k: engineering stress-strain curves obtained with the tempered fine-grained microstructure (3rd) notched tensile test specimens exposed to hydrogen

VI.5.C Effect of time since hydrogen charging

A further series of tests were performed to investigate the impact of time delays after charging. Previous observations indicate that when most of the diffusible hydrogen escapes from the material, the initial loss of ductility can be either amplified or recovered [112]. To examine this phenomenon, one coarse- and two fine-grained microstructure (1st and 2nd) specimens were first charged to their respective maximum hydrogen level, and then cleaned, wet ground, and left to stand for 24 hours at ambient condition before testing. The engineering stress-strain curves are presented in **Diagram VI-I** and **Diagram VI-m** (once again, the ordinate axis scale has been adjusted to improve readability). In both cases, nearly half of the initial loss of ductility was restored. Therefore, a time-dependent recovery phenomenon appears to be operating. However, further extending the period between hydrogen charging and testing was not explored, so it is impossible to judge when, or whether, the recovery effect saturates.

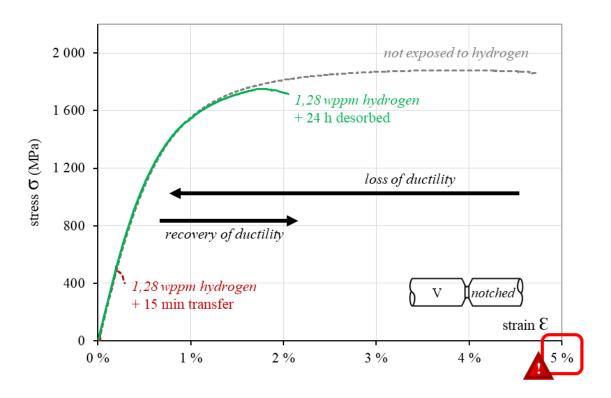


Diagram VI-1: engineering stress-strain curves obtained with the coarse-grained microstructure (1st) notched tensile test specimens left to stand for 24 h after exposure to hydrogen

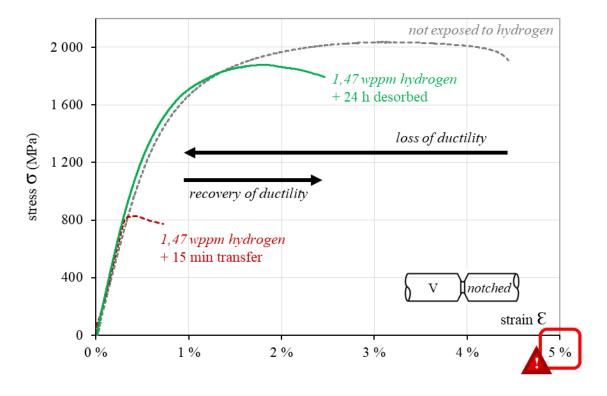


Diagram VI-m: engineering stress-strain curves obtained with the coarse-grained microstructure (2nd) notched tensile test specimens left to stand for 24 h after exposure to hydrogen

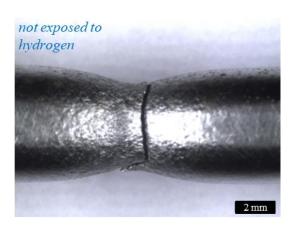
VI.6 RESULT ANALYSES & DISCUSSION

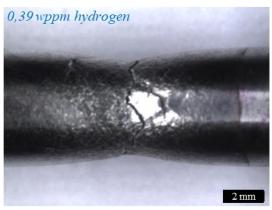
Following the mechanical tests, the fracture surfaces were examined, and the tensile test data were post-processed to characterise and quantify the changes in ductility.

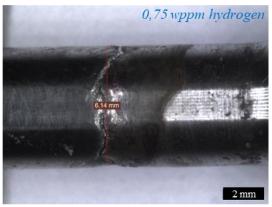
VI.6.A Fractography

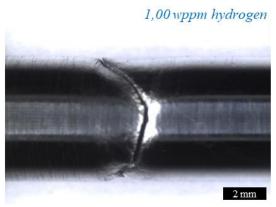
VI.6.A.1 Optical microscopy

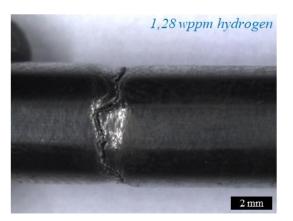
The cross-sections of each specimen were re-measured at different locations after breakage using the stereo microscope (section crossing the V-notch centre for the case of the notched specimens). These data were then used in the quantification of the ductility loss (next sections). Only the necking of smooth specimens is shown here (refer to **Picture VI-k**) because its evolution is significantly less evident in the case of notched specimens. As with the reduction in ultimate elongation, the necking of the specimens decreases as the hydrogen concentration goes up.











Picture VI-k: Micrographs showing the effect of hydrogen concentration on the development of necking in smooth tensile test specimens

VI.6.A.2 Electron microscopy

Fracture surfaces were then observed with a scanning electron microscope to investigate the fracture mode and verify the transition from ductile to brittle fracture following the introduction of hydrogen. This was done using either a Philips FEI Quanta 200 FEG/ESEM, a Thermo Fisher Scientific Axia ChemiSEM, or a Hitachi S-3400N. These observations to track the emergence of brittle zones were focused on the areas having experienced the highest stress levels, as these are likely to be where the failures were initiated. This is the centre for smooth specimens [283] and the area under the notch

root for notched specimens. Furthermore, these observations have also provided insight into the reasons for any unexpected tensile test results, often caused by the presence of inclusion(s) – nearly always revealed by the resulting "fish-eye" phenomenon. These tests were then removed from further data analysis. A selection of the observations is illustrated in the following pictures. The main conclusions drawn from these investigations are:

• Coarse-grained microstructure (1st) smooth specimens: Picture VI-l Transition from the ductile transgranular regime (presence of "dimples") to the brittle transgranular type (quasi-cleavage topography) and finally to the brittle intergranular mode (decohesion).

- Coarse-grained microstructure (1st) V-notched specimens: Picture VI-m

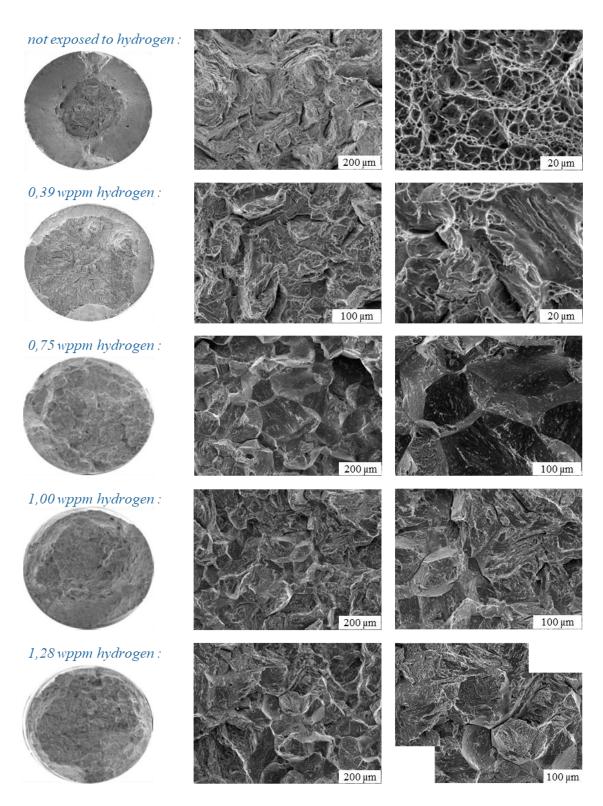
 Transition from the brittle transgranular regime (quasi-cleavage topography) to

 brittle intergranular type (decohesion).
- Fine-grained microstructure (2nd) V-notched specimens: Picture VI-n

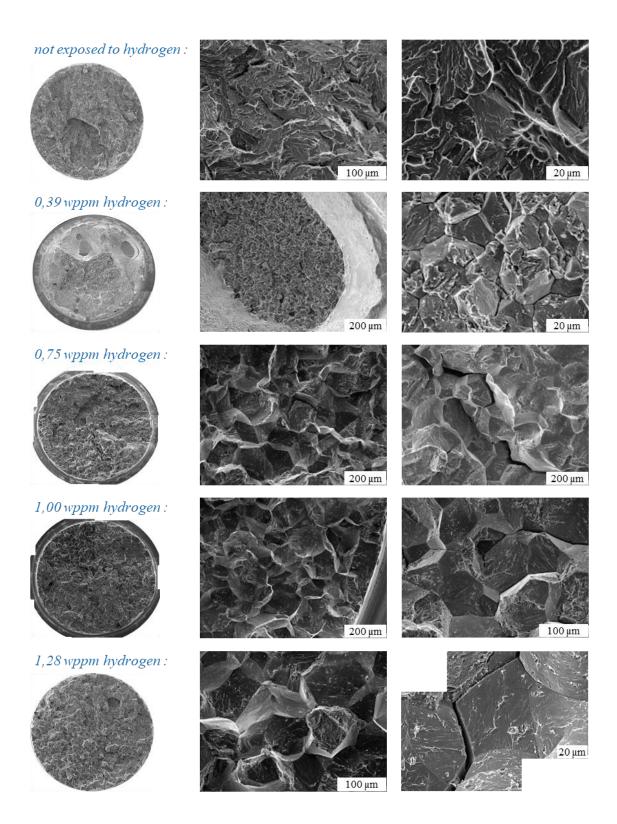
 Transition from the ductile transgranular regime (presence of dimples) to the brittle transgranular regime (quasi-cleavage topography) mixed more and more with the brittle intergranular mode (decohesion); after 24 hours delay before testing, the brittle transgranular regime has returned to predominate.
- Tempered fine-grained microstructure (3rd) V-notched specimens : Picture VI-o

Mix of the brittle transgranular (quasi-cleavage topography) and the brittle intergranular (decohesion) regimes.

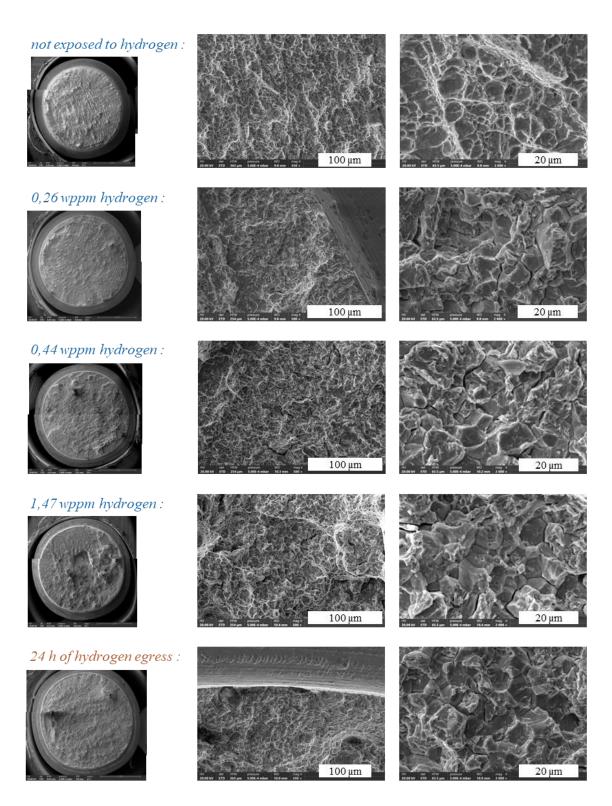
For every case, the observation of the breakage surface has thus confirmed a change into brittle fracture mechanisms following exposure to hydrogen, consistent with the trend in ductility loss.



Picture VI-1: breakage profiles of the coarse-grained microstructure (1^{st}) smooth tensile test specimens

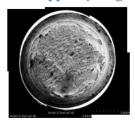


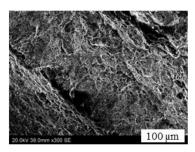
Picture VI-m: breakage profiles of the coarse-grained microstructure (1st) V-notched tensile test specimens

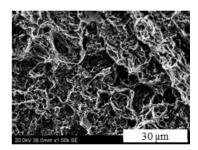


Picture VI-n: breakage profiles of the fine-grained microstructure (2nd) V-notched tensile test specimens (including a case having experienced hydrogen egress)

0,42 wppm hydrogen:







Picture VI-o: breakage profiles of the tempered fine-grained microstructure (3rd) V-notched tensile test specimen

VI.6.B Evolution of the mechanical properties

In agreement with other work on this theme, it was found that the elastic modulus of this steel does not vary much following exposure to hydrogen. The impact is mainly on the plastic domain, and then, once this has become insignificant, the extent of the elastic domain. These are successively reduced with an increase in the hydrogen concentration, decreasing the elongation to failure.

Three criteria were used to characterise the effects of hydrogen and to compare the different configurations investigated. The engineering description of the stress-strain curves allowed determination of the ultimate tensile strength (refer to **Diagram VI-n**) and the corresponding elongation before necking (refer to **Diagram VI-o**). Then, using the fractographic observations, the reduction in area was also calculated (refer to **Diagram VI-p**). In addition, **Table VI-E** summarise the number of tests considered valid to establish these analyses.

Table VI-E: summary of tests considered valid for subsequent analysis

charging time	hydrogen concentration	number of valid tests	
coarse-grained microstructure (1st)			
_	0,05 wppm	$2 \times smooth$	2 × V-notched
30 min	0,39 wppm	$1 \times \text{smooth}$	1 × V-notched
2 h	0,75 wppm	$2 \times smooth$	2 × V-notched
4 h	1,00 wppm	$2 \times smooth$	2 × V-notched
6 h	1,28 wppm	$2 \times smooth$	1 × V-notched
6 h + 24 h	1,28 wppm	$1 \times \text{smooth}$	1 × V-notched
	fine-grained microstructure	(2 nd)	
_	0,05 wppm	2 × V-notched	
20 min	0,26 wppm	3 × V-notched	
30 min	0,44 wppm	$3 \times V$ -notched	
16 h	1,47 wppm	2 × V-notched	
16 h + 24 h	1,47 wppm	2 × V-notched	
	tempered fine-grained microstru	cture (3 rd)	
16 h	0,42 wppm	2 × V-notched	

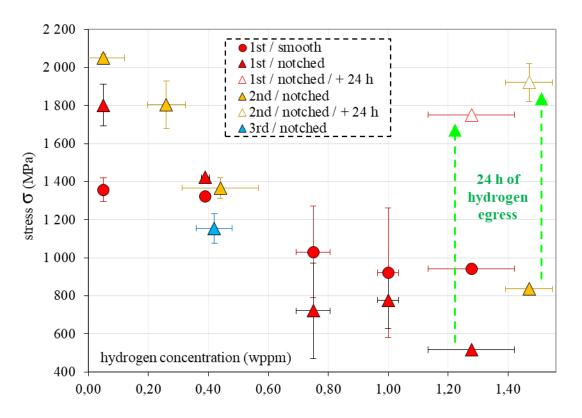


Diagram VI-n: showing the effect of introduced hydrogen content on ultimate tensile strength

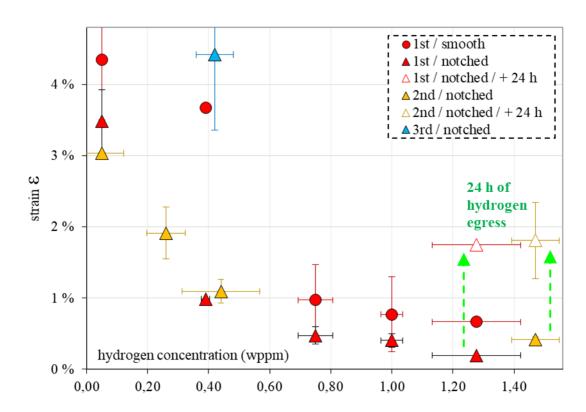


Diagram VI-o: showing the effect of introduced hydrogen content on elongation prior to neck formation

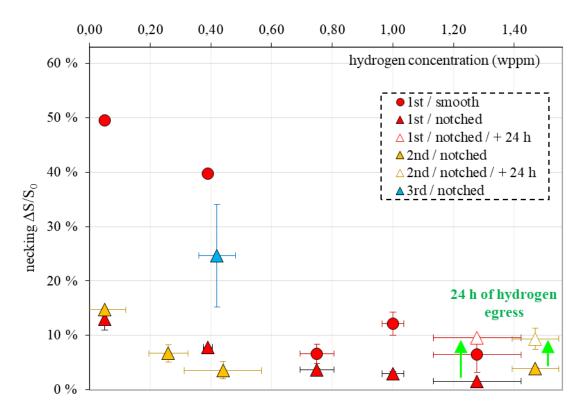


Diagram VI-p: showing the effect of introduced hydrogen content on reduction in area

The elongation before necking was the parameter selected to both quantify the loss of ductility and compare different test conditions and microstructures, because it appeared to be the most consistent criterion. It also allowed to discard the effects of prior austenite grain size differences. In addition, a strain value would also be relevant for further use in any cold crack susceptibility criterion. Indeed, these criteria would then be easy to implement in large-scale computational simulations as the calculated deformation is generally a reliable and easily accessible parameter.

VI.6.C Quantification of the ductility loss

Loss of ductility – or embrittlement – indexes were derived from the evolution of the elongation before necking using formula (VI-1). The configurations with the tensile specimens not exposed to hydrogen (noted "w/o H") were considered as the baselines (initial ductility). However, since this was not tested for the tempered fine-grained microstructure (3^{rd}), the fine-grained microstructure (2^{nd}) specimens without hydrogen were kept as the baselines.

ductility
$$loss_{\Delta S/S_0}(\mathbf{H}) = 1 - \frac{\Delta S/S_0(\mathbf{H})}{\Delta S/S_0(w/o \text{ H})}$$
 (VI-1)

The results obtained from smooth and notched specimens were first compared (refer to **Diagram VI-q**). They both showed similar trends of ductility loss, although the notched specimen curve is more severe than the smooth specimen one. Nevertheless, this may ensure margins regarding the final application. Therefore, notched specimens were then preferred for the rest of the investigation because their geometry is consistent with implant welding test specimens, making any further comparison more relevant.

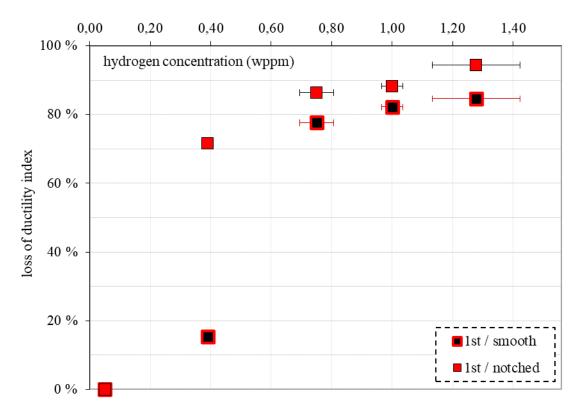


Diagram VI-q: diagram comparing the indices of ductility loss between the smooth and notched specimens made of the coarse-grained microstructure (1st) proportionally to the increase in hydrogen content

Then, as expected, the indexes calculated using this criterion for the coarse- and fine-grained microstructures (1st and 2nd) were quite similar, minimising the impact of the prior austenite grain size (refer to **Diagram VI-r**). Furthermore, the effect of time with the specimens left to stand for 24 hours was clearly outlined. According to this strain criterion, half – or even more – of the ductility loss was recovered in both cases.

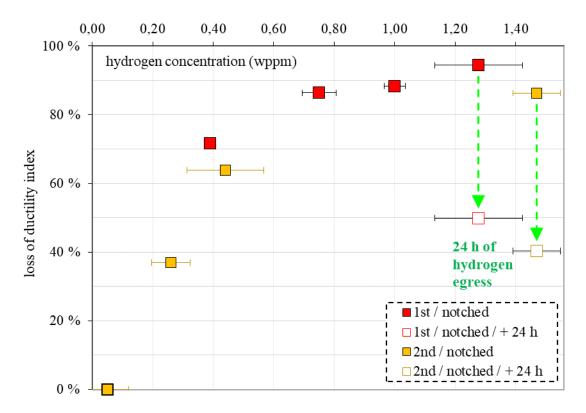


Diagram VI-r: diagram showing the indices of ductility loss of the coarse- and fine-grained microstructure (1st and 2nd) specimens proportionally to the increase in hydrogen content

Finally, the impact of hydrogen on ductility loss with the tempered fine-grained microstructure (3rd) was compared in **Diagram VI-s** to the non-tempered specimens made of the 2nd microstructure and equivalent in hydrogen content (0,42 wppm versus 0,44 wppm, respectively). It can be concluded here that in addition to substantially reducing the hydrogen solubility, tempering produced a microstructure significantly less susceptible to hydrogen-induced loss of ductility.

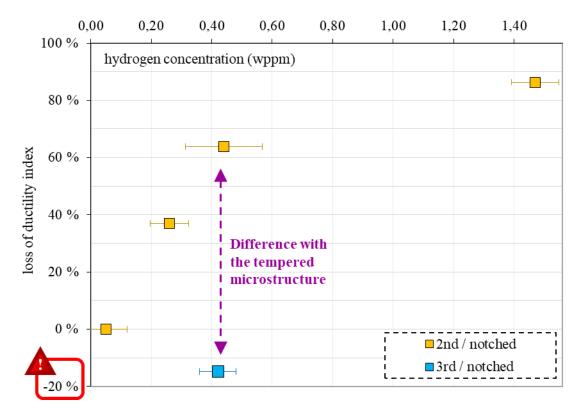


Diagram VI-s: diagram comparing the ductility loss indices obtained with tempered and non-tempered (2nd and 3rd) fine-grained microstructure specimens under equivalent hydrogen concentration (the non-hydrogen exposed specimens of the 2nd microstructure is used as the baseline for both)

VI.6.D Limits of this work

Before moving on to the conclusion of this chapter, a few weaknesses of this work are summarised below. Also, comparisons of these results with those from a previous study using specimens made of the same type of steel and with a similar geometry are undertaken.

First, the precision of the comparisons between the results obtained from the studied microstructures can be questioned as a second and different manufacturing sequence order was required to solve quenching residual stress and decarburisation problems experienced during the second campaign. In addition, inconsistencies in the geometry of the samples between the two different campaigns were detected, caused by the variability in the precision of the turning operations. This has mainly affected the machining of the V-notches, modifying the stress concentration coefficients (first campaign *(coarse-grained microstructure)* $\approx 2,98$ versus second campaign *(fine-grained microstructures)* $\approx 3,68$). However, it was assumed that the general tendencies were not sufficiently affected to lead to misinterpretations.

Second, this study did not focus on the evolution of embrittlement during the hours following hydrogen exposure. Therefore, the loss of ductility could be more important after a critical delay of a few hours, as has sometimes been observed with other metals [112]. This would then significantly influence the kinetics of the cold cracking phenomenon.

Nevertheless, using pure martensitic samples has provided margins that should absorb the impact of uncertainties due to the above. Furthermore, comparisons with the results of the previous study conducted by Rhode [110] demonstrated a rather good degree of consistency despite the geometric differences of the specimens used, especially concerning the V-notches (refer to **Diagram VI-t** and **Diagram VI-u**). It can therefore be assumed that the hydrogen degradation mechanisms are such that they may outweigh the effects of the uncertainties.

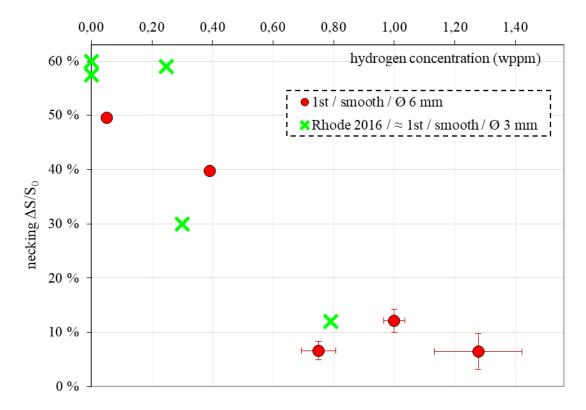


Diagram VI-t: comparison of the results obtained using the smooth tensile specimens with those established by [110]

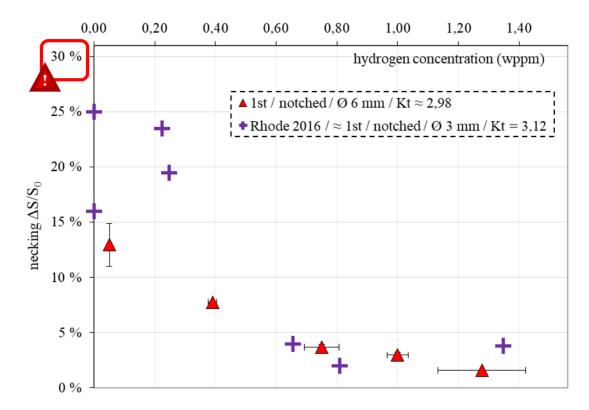


Diagram VI-u: comparison of the results obtained using the notched tensile specimens with those established by [110]

VI.7 CONCLUSIONS

The behaviour of the heat-affected zone exposed to hydrogen has been investigated to enhance the understanding of the role of this factor in the cold cracking phenomenon. The following conclusions can be drawn:

- Hydrogen-induced ductility loss in typical arc-weld heat-affected zones has been quantified as a function of hydrogen concentration, from low levels to the solubility limit. This has demonstrated a significant impact of hydrogen on mechanical properties. This was reflected in a reduction in the ultimate elongation before breakage, rapidly supplemented by a decrease in the ultimate tensile strength value as the hydrogen content was increased. It therefore demonstrates the loss of ductility (or "embrittlement"). This was confirmed by the changes in the fracture modes, from ductile to brittle regimes. Fine- and coarse-grained microstructures have finally shown similar trends and degrees of hydrogen embrittlement.
- It has also been found that after a 24 h delay, some of the lost ductility has been recovered. This is encouraging for the weld integrity in the mid- to long-term. Nonetheless, during the first minutes/hours after a weld bead deposit, which

includes – in the case of multi-pass welds – the inter-pass delay to be observed, the effect of the hydrogen egress is not known. This remains thus to be investigated to determine whether it is only positive, or whether it could lead to a higher peak of embrittlement before recovery kinetics are initiated.

• It has been demonstrated with a few tests that a tempered microstructure is significantly more resistant to hydrogen embrittlement. This highlights one of the positive effects of bead tempering methods. Nevertheless, more accurate quantifications of this would be of interest to optimise best the welding parameters and take full advantage of this behaviour. However, it should be remembered that the so-called "temper layer" passes, including their corresponding heat-affected zones, can be left in the as-welded state for several minutes/hours – and thereby exposed to the risk of cold cracking – prior to re-heating and achieving these positive tempering effects, if the inter-pass duration is extended for any reason. This is why single-bead cold cracking testing is essential to gauge the degree of this risk.

VII.1 SUMMARY

This current project aimed to contribute to the discussion of three conservatisms (presented in section I.1.F). As a reminder, the first one is related to assessment of the viability of multi-pass welding repair techniques optimised by so-called "bead tempering" methods, and more precisely, the temper bead welding, to treat defective areas of the nickel-based alloy 182 patches attaching the bottom-mounted instrumentation nozzles with the shell of the pressurised reactor vessel of certain French nuclear power plants. The second relates to the historical, and still dominant, usage in France of deterministic failure criteria to the detriment of probabilistic criteria. This is the case for the latest computational risk prediction model for cold cracking developed previously at EDF [47]. The third conservatism concerns the historical and still current prescription by French regulatory codes [33], [46] of solely the cold cracking test method known as the "implant test" procedure, which is considered to be excessively severe and does not validate the multi-pass welding procedure needed to deal with these repairs.

Therefore, at the conclusion of the literature review, two first areas of research were identified. First, the historical cold cracking implant testing method should be consistently compared with other proposed standardised testing methods. The so-called "Tekken test" method was selected. Second, further progress was needed in the "materials science" of the extent to which hydrogen impacts the mechanical properties of the low-alloy ferritic steel used in the vessel, in a microstructural configuration relevant to the heat-affected zone of the weld. These two lines of research were conducted mainly experimentally.

However, to carry out the first area of research, a third one appeared to be a prerequisite: to address the need for more knowledge of the residual stress levels generated by the self-restraint phenomenon in the Tekken test mock-up. Thus, a computational modelling and simulation study was conducted. This was accompanied by several small-scale testing programmes to provide data for and qualify the material models used.

Hence, below is proposed a summary of the main conclusions of each of the three research axes covered during this current project.

VII.2 RECAPITULATION OF THE MAIN RESULTS AND OBSERVATIONS

VII.2.A Outcomes of the Tekken test investigation

First, concerning the **study of the Tekken mock-ups** using 2D modelling, the following are the main findings:

- Although the standard Tekken design allows thicknesses up to 150 mm, the residual stress saturates above a thickness of 50 mm using these materials and welding parameters.
- Moreover, this saturation stress is rapidly reached at such thicknesses because of fast heat dissipation into the material remote from the weld.
- This martensitic microstructure has a very high yield strength, suggesting that residual stress levels will be controlled by the softer Alloy 52 weld metal and parent material surrounding it. Thus, the mechanical behaviour of the weld metal is important here. Its material model was extensively developed and validated during parallel programmes, so our model is considered qualified to meet the objectives of a comparative study. Nevertheless, it must be noted that the stress state values given are relative and not absolute.

VII.2.B Outcomes of the welding test benchmarking

Second, regarding the **experimental benchmarking between the two cold cracking testing methods**, the following findings can be highlighted:

- A divergence in the conclusions drawn from these two methods was found. The
 Tekken campaign led to a positive assessment of the proposed repair welding
 procedure. In contrast, the implant campaign led to a negative appraisal for a
 condition based on tensile stresses higher than the base metal 0,2 proof stress.
- Detecting cold cracking using acoustic emission, as conducted during these tests, was not always accurate. Indeed, small defects were often not detected. In addition, many parasitic emissions were experienced, presumably associated with the stress

state evolution and probably with other phenomena such as, for instance, the diffusion of hydrogen and phase transformations. Nevertheless, acoustic emission can likely be optimised to meet this objective better.

VII.2.C Outcomes of the material study

Third, the following conclusions were drawn from the experimental material study:

- The results demonstrated a net loss of ductility directly attributable to the presence of hydrogen in microstructures of the same type as those produced in the arc-weld heat-affected zone.
- It was found that the coarse- and fine-grained microstructures have similar embrittlement rates in presence of hydrogen.
- Almost total embrittlement of both microstructures was observed when hydrogen concentration at the solubility limit was imposed.
- However, it was found that a delay of 24 hours after hydrogen exposure, during which the amount of hydrogen falls, allows recovery of nearly half of the lost ductility.
- Finally, it was also found that the so-called "tempered" microstructures seem to tolerate the presence of hydrogen much better.

VII.3 Answers to the Ambitions of this Project

VII.3.A Deterministic versus probabilistic criteria

Regarding this conservatism (the second), in view of the uncertainties governing the outcome of a cold cracking test (for instance, unfortunate presence of an inclusion – refer to the **welding test benchmarking**) and the gradual fall in ductility observed as a function of the increase in the level of hydrogen (as seen in the **behaviour study of the heat-affected zone exposed to hydrogen**), a probabilistic failure criterion would make sense. Indeed, instead of imposing additional safety margins, it would allow a complete understanding of the magnitude of risk.

VII.3.B Tekken versus historical implant test

As highlighted in VII.2.B, the study of the Tekken welding test demonstrated that, as in the implant method, the mechanical loading peaks quickly after weld completion with thick specimens (from ≈ 50 mm) using this welding configuration (presented in III). Thus, this happens when the hydrogen level is at its peak, which is thereby the moment when the risk of cold cracking occurrence is the highest. In addition, the heat-affected zone generated using a 40 mm thick specimen is composed of a quasi-fully martensitic microstructure. Considering that brittle microstructures such as this are one of the three factors driving the cold cracking phenomenon, it is suggested that this heat-affected zone is propitious for this type of defect occurrence. Hence, these observations contribute considerably to the discussion of this third conservatism as they confirm that the Tekken test method achieves a configuration similar to the implant test method where severe conditions that can lead to cold cracking are generated.

However, although they are issued from the same ISO 17642 standard [87], [191], [240] and are supposed to meet the same needs, these two testing methods led to dissimilar conclusions (refer to **welding test benchmarking**). Nevertheless, the heat-affected zones produced in the Tekken and implant test specimens were similar in both extent and microstructure. There was little doubt about the similarity of their hydrogen content. Thus, only the mechanical loading factor differs between the two test methods. However, this aspect has not been sufficiently finely covered in this research project to conclude which of them is the most appropriate and thus to advance further the discussion of the third conservatism on this topic.

VII.3.C Viability of bead tempering methods

Despite the negative assessment resulting from the implant test method conducted during the **welding test benchmarking**, in view of the overly severe welding conditions imposed, the positive evaluation by at least one of the two methods employed represents a significant and major contribution towards demonstrating the viability of this repair welding procedure (discussion of the first conservatism).

In addition, certain findings from the **experimental material study** are also suggesting its viability:

- Tempered microstructures appear to be relatively not very sensitive to hydrogen embrittlement: This is a major positive aspect in this discussion since it tends to demonstrate the benefits of bead tempering techniques.
- Recovery of nearly half of the lost ductility after 24 hours: This is again a positive observation because it demonstrates that hydrogen embrittlement will not affect a repair beyond the short-term.

VII.4 RECOMMENDATIONS FOR FURTHER WORK

- To refine the discussion of the first conservatism, it would now be important to establish what is the actual concentration of hydrogen in the heat-affected zone below a weld bead, particularly the first bead in a multi-pass weld, under conditions as close as possible to the repair application. A Pressouyre's setup [220] developed in another EDF parallel program would undoubtedly be of interest in addressing this. In addition, it would also be of interest to extend the study of the hydrogen embrittlement of the 16MND5 steel by investigating other heat-affected zone microstructure types, in particular, a more extensive examination of those that have been tempered.
- Before proposing a new failure criterion more appropriate to the case of the studied repair (second conservatism), the Code_Aster module modelling hydrogen diffusion and trapping previously implemented by [47] should be re-calibrated using newer experimental data for the base and filler metals used. Once again, the Pressouyre's setup [220] will be crucial to achieving this. Nevertheless, additional small-scale testing will also be necessary. It must also be the accuracy of both microstructure predictions in the heat-affected zone (micro-constituent and prior austenite grain size) and stress predictions must be established and if necessary improved in order to underwrite hydrogen diffusion and trapping predictions.
- To refine the discussion of the third conservatism, the local stresses experienced in the areas where stress concentrations occur should be confirmed by a combination of simulation and measurements.

BIBLIOGRAPHY

- [1] **ISO 80000-1**, *ISO (International Organization for Standardization)*, Dec-2022, Document URL: https://www.iso.org/fr/standard/76921.html (consulted on 26/04/2023)
- [2] H. Granjon, Les bases metallurgiques du soudage, IIW (International Institute of Welding), 1989, Document identifier = ISBN : 2-85701-159-8
- [3] **AWS A3.0M/A3.0:2010**, *AWS (American Welding Society)*, 2010, Document identifier = ISBN: 978-0-87171-763-4
- [4] **Electricity information: Overview**, *IEA (International Energy Agency)*, 2021, Document URL: https://www.iea.org/reports/electricity-information-overview (consulted on 05/10/2022)
- [5] Le nucléaire dans le monde, SFEN (Société Française d'Energie Nucléaire), 2019 [webpage], Document URL: http://www.sfen.org/energie-nucleaire/panorama-nucleaire/nucleaire-monde (consulted on 09/08/2019)
- [6] J.-N. Geist, L'énergie nucléaire se développe-t-elle dans le monde? Et pourquoi?, *The Shift Project*, 21-Jun-2022 [webpage], Document URL: https://theshiftproject.org/article/electricite-nucleaire-developpement-monde/ (consulted on 05/10/2022)
- [7] G. Le Gros, **Le nucléaire dans le monde**, SFEN (Société Française d'Energie Nucléaire), 22-Apr-2021 [webpage], Document URL: https://www.sfen.org/dossiers/le-nucleaire-dans-le-monde/ (consulted on 05/10/2022)
- [8] B. Mougel, **EDF**, *I2EN* (Institut International de l'Energie Nucléaire), 2021, Document URL: https://www.i2en.fr/fiche-universite/edf/?download=pdf&post=697 (consulted on 05/10/2022)
- [9] **Nuclear Power Reactors in the World**, Vienna: *IAEA (International Atomic Energy Agency)*, 2018, Document identifier = ISBN: 978-92-0-101418-4
- [10] **EDF group**, *Électricité De France* [webpage], Document URL : https://www.edf.fr/groupe-edf (consulted on 09/08/2019)
- [11] R. Davies, **A canter around the nuclear jumps**, presented at the *Cambridge lecture*: *Areva*, University of Cambrige, 08-Feb-2012, Document URL: https://www.slideshare.net/AbdelrhmanUossef/cambridge-lecture-areva-robert-davies (consulted on 09/08/2019)
- [12] S. K. Sharma, Chapter 7 National technical capability development in nuclear power programmes, in *Infrastructure and Methodologies for the Justification of Nuclear Power Programmes*, A. Alonso, Ed. *Woodhead Publishing*, 2012, pp. 189–219, Document identifier = DOI: 10.1533/9780857093776.1.189
- [13] **Nuclear power plant illustration**, *EDF* (Électricité De France), Document URL : https://www.sindri-partnership.ac.uk/about/ (consulted on 01/11/2021)

- [14] A. H. Cottrell, **Effects of neutron irradiation on metals and alloys**, *Metallurgical Reviews*, vol. 1, no. 1, pp. 479–522, Jan. 1956, Document identifier = DOI: 10.1179/mtlr.1956.1.1.479
- [15] L. M. Davies, A comparison of Western and Eastern nuclear reactor pressure vessel steels, International Journal of Pressure Vessels and Piping, vol. 76, no. 3, pp. 163–208, Mar. 1999, Document identifier = DOI : 10.1016/S0308-0161(97)00075-6
- [16] W. A. Pavinich, T. J. Griesbach, and W. L. Server, An overview of radiation embrittlement modeling for reactor vessel steels, in Radiation Embrittlement of Nuclear Reactor Pressure Vessel Steels: An International Review (Fourth Volume), vol. 4th, L. E. Steele, Ed. Balatonfüred: ASTM International (American Society for Testing and Materials), 1993, pp. 99–117, Document identifier = DOI: 10.1520/STP24767S
- [17] J.-H. Schmitt, **Matériaux à hautes performances pour l'énergie**, presented at the *ECP (Ecole Centrale Paris / CentraleSupelec)*, 2014, Document URL: https://perso.crans.org/epalle/M2/MHP/5_Tenue_cuve_REP.pdf
- [18] M. Consonni, A review of the machine GTAW ambient temperature temper bead repair technique for nuclear power plant components, Members Technical Literature Review TWI Ltd (The Welding Institute), 2013, Document identifier = TWI ref.: 22952
- [19] Rapport de l'ASN sur l'état de la sûreté nucléaire et de la radioprotection en France en 2020, 2020th ed., Montrouge : ASN (Autorité de Sûreté Nucléaire), 2021, Document identifier = ISSN 1967 5127
- [20] C. Lemaignan, Comportement sous irradiation des aciers de structure, in *Matériaux fonctionnels Matériaux biosourcés, Techniques de l'Ingenieur*, 2010, Document identifier = DOI: 10.51257/a-v1-n1280
- [21] M. Yu, Y. J. Chao, and Z. Luo, **An assessment of mechanical properties of A508-3 steel used in chinese nuclear reactor pressure vessels**, *J. Pressure Vessel Technol*, vol. 137, no. 3, pp. 031402-031402-7, Jun. 2015, Document identifier = DOI: 10.1115/1.4029434
- [22] J. Gorman, S. Hunt, P. Riccardella, and G. A. White, Chapter 44 PWR reactor vessel alloy 600 issues, in *Companion guide to the ASME boiler and pressure vessel code*, Third Edition, vol. Volume 3, K. R. Rao, Ed. *ASME (American Society of Mechanical Engineering)*, 2009, Document identifier = DOI: 10.1115/1.802717
- [23] Réparation de défauts détectés dans la cuve du réacteur n°1 de Gravelines, ASN (Autorité de Sûreté Nucléaire), 20-Dec-2011 [webpage], Document URL: https://www.asn.fr/l-asn-informe/actualites/reparation-de-defauts-detectes-dans-la-cuve-du-reacteur-n-1-de-gravelines (consulted on 08/11/2022)
- [24] N. Paul, M. Foata, and P. Kassis, **Traitement numérique des controles ultrasonores de composants présentant un bruit de structure fort et hétérogène**, presented at the *Les journées COFREND 2017*, Strasbourg, 2017, Document URL: https://www.ndt.net/search/docs.php3?id=21321 (consulted on 08/11/2022)

- [25] A. S. Aloraier, A. Al-Mazrouee, J. W. H. Price, and T. Shehata, Weld repair practices without post weld heat treatment for ferritic alloys and their consequences on residual stresses: A review, *International Journal of Pressure Vessels and Piping*, vol. 87, no. 4, pp. 127–133, Apr. 2010, Document identifier = DOI: 10.1016/j.ijpvp.2010.02.001
- [26] **ISO 6520-1**, *ISO (International Organization for Standardization)*, Jul-2007, Document URL: https://www.iso.org/standard/40229.html
- [27] **Défauts des soudures**, *Rocd@cier*, 14-Aug-2017 [webpage], Document URL : https://www.rocdacier.com/defauts-des-soudures/ (consulted on 13/09/2019)
- [28] B. K. Srivastava, A review on effect of preheating and/or post weld heat treatment (PWHT) on mechanical behaviour of ferrous metals, International Journal of Engineering Science and Technology, vol. 2, p. 7, 2010, Document identifier = ISSN: 0975-5462
- [29] A. S. Aloraier, R. N. Ibrahim, and J. Ghojel, Eliminating post-weld heat treatment in repair welding by temper bead technique: role bead sequence in metallurgical changes, Journal of Materials Processing Technology, vol. 153–154, pp. 392–400, Nov. 2004, Document identifier = DOI: 10.1016/j.jmatprotec.2004.04.383
- [30] **Boiler & Pressure Vessel Code (BPVC)**, New-York : *ASME (American Society of Mechanical Engineering)*, 2017, Document URL : go.asme.org/BPVC17
- [31] G. K. Padhy, V. Ramasubbu, N. Murugesan, C. Remash, and S. K. Albert, **Effect of preheat and post-heating on diffusible hydrogen content of welds**, *Science and Technology of Welding and Joining*, vol. 17, no. 5, pp. 408–413, Jul. 2012, Document identifier = DOI: 10.1179/1362171812Y.0000000023
- [32] A. C. Davies, **Science Practice Welding**, *CUP Archive*, 1941, Document identifier = ISBN: 978-0-521-08443-7
- [33] Règles de Conception et de Construction des matériels Mécaniques des ilôts nucléaires REP (RCC-M), Courbevoie : AFCEN (Association française pour les règles de conception, de construction et de surveillance en exploitation des matériels des chaudières électro-nucléaires), 2020, Document URL : https://www.afcen.com/fr/104-rcc-m (consulted on 31/10/2022)
- [34] M. Consonni and C. Verdon, Machine GTAW ambient temperature temper bead technique for Ni-based weld overlay repairs of nuclear components: assessment of hydrogen cracking by implant test, in Volume 1: Operations and Maintenance, Engineering, Modifications, Life Extension, Life Cycle and Balance of Plant; I&C, Digital Controls, and Influence of Human Factors, Shanghai, China, 2017, p. V001T01A031, Document identifier = DOI: 10.1115/ICONE25-67160
- [35] P. Brziak, M. Łomozik, R. Mizuno, and F. Matsuda, **Repair Welding of SQV2A Pressure Vessel Steel by Temper Bead Techniques Without Post Welding Heat Treatment**, *Archives of Metallurgy and Materials*, vol. 56, no. 2, Jan. 2011,

 Document identifier = DOI: 10.2478/v10172-011-0024-x
- [36] J.-M. Carpreau, S. Fabrice, C. Gilles, and D. Bastien, **Soudage Temperbead** applique aux materiaux nucleaire, presented at the *Journées Nationales du*

- [37] S. J. Brett, Repair of Cr-Mo-V components using Inconel 182 electrodes without heat treatment, Repair and reclamation TWI Ltd (The Welding Institute), 1986
- [38] P. Nevasmaa, **Prevention of Weld Metal Hydrogen Cracking in High-Strength Multipass Welds**, *Weld World*, vol. 48, no. 5, pp. 2–18, May 2004, Document identifier = DOI: 10.1007/BF03266427
- [39] T. W. Lau, M. L. Lau, and G. C. Poon, **Development of controlled deposition** repair welding procedures at Ontario Hydro, *Welding Research Council Bulletin*, pp. 35–42, 1996, Document identifier = ISSN: 0043-2326
- [40] V. Robin, Chapter 1 Industrial challenges where computational welding mechanics becomes an engineering tool, in *Thermomechanical industrial processes*, J.-M. Bergheau, Ed. *ISTE Ltd & John Wiley & Sons*, 2013, pp. 1–74, Document identifier = ISBN: 978-1-84821-358-6
- [41] **National Board Inspection Code (NBIC)**, 4 vols, Columbus: *NBBI (The National Board of Boiler and Pressure Vessel Inspectors)*, 2019, Document URL: https://www.nationalboard.org/
- [42] M. Pitrun, D. Nolan, and D. Dunne, **Diffusible Hydrogen Content in Rutile Flux-Cored Arc Welds as a Function of the Welding Parameters**, *Weld World*, vol. 48, no. 1, pp. 2–13, Jan. 2004, Document identifier = DOI: 10.1007/BF03266408
- [43] N. Yurioka and H. Suzuki, **Hydrogen assisted cracking in C-Mn and low alloy steel weldments**, *International Materials Reviews*, vol. 35, no. 1, pp. 217–249, Jan. 1990, Document identifier = DOI: 10.1179/imr.1990.35.1.217
- [44] N. Alam, D. Dunne, I. Squires, F. Barbaro, and B. Feng, Weldment cold cracking the effect of hydrogen and other factors, in *Hydrogen management* in steel weldments, J. L. Davidson and D. L. Olson, Eds. Melbourne: The Organising Committee of the Joint Seminar on behalf of Defence Science and Technology Association and Welding Technology Institute of Australia, 1996, pp. 49–60, Document identifier = ISBN: 978-0-7311-0809-1
- [45] G. L. Hopkin, A suggested cause and a general theory to the cracking of alloy steels on welding, Welding Journal, no. 11, pp. 605–608, 1944
- [46] Règles de Surveillance en Exploitation des matériels Mécaniques des ilôts nucléaires REP (RSE-M), Courbevoie: AFCEN (Association française pour les règles de conception, de construction et de surveillance en exploitation des matériels des chaudières électro-nucléaires), 2020, Document URL: https://www.afcen.com/fr/105-rse-m (consulted on 31/10/2022)
- [47] C. Qianqiang, Modelisation de la fissuration a froid dans un acier ferritique de type 16MND5, PhD thesis, ENSTA (École Nationale Supérieure de Techniques Avancées / ParisTech), Paris, 2015, Document URL: https://pastel.archivesouvertes.fr/tel-01144540/document
- [48] V. Robin and P. Gilles, **Prevention des risques d'apparition de defaut par la simulation numerique des procedes de fabrication**, in 10ème colloque national

- en calcul des structures, Giens, France, 2011, Document URL : https://hal.archives-ouvertes.fr/hal-00592704 (consulted on 10/03/2019)
- [49] S. Debiez and P. Gerard, **Pratique et signification de l'essai de fissuration a froid sur implant**, *Soudage et Techniques Connexes*, 1980
- [50] What is an arc and how does arc welding work?, Fronius International, 29-Oct-2020, Document URL: https://blog.perfectwelding.fronius.com/en/what-is-arc-welding/ (consulted on 11/11/2022)
- [51] What is tungsten inert gas (GTAW or TIG) welding?, TWI Ltd (The Welding Institute) [webpage], Document URL: https://www.twi-global.com/technical-knowledge/job-knowledge/tungsten-inert-gas-tig-or-gta-welding-006.aspx (consulted on 11/11/2022)
- [52] Manual metal arc welding (MMA, SMAW or stick welding), TWI Ltd (The Welding Institute) [webpage], Document URL: https://www.twi-global.com/technical-knowledge/job-knowledge/the-manual-metal-arc-process-mma-welding-002.aspx (consulted on 11/11/2022)
- [53] What is electrode welding?, Fronius International, Document URL: https://www.fronius.com/en/welding-technology/world-of-welding/electrode-welding (consulted on 12/11/2022)
- [54] J. M. Antonini, **8.04 Health Effects Associated with Welding**, in *Comprehensive Materials Processing*, S. Hashmi, G. F. Batalha, C. J. Van Tyne, and B. Yilbas, Eds. Oxford: *Elsevier*, 2014, pp. 49–70, Document identifier = DOI: 10.1016/B978-0-08-096532-1.00807-4
- [55] In Pocket Welding Guide, Troy, OH: Hobart Brothers Company, 1997
- [56] **ISO 25901-1**, *ISO (International Organization for Standardization)*, 2016, Document URL: https://www.iso.org/standard/55758.html
- [57] Welding defects types, causes, prevention, Fractory, 10-Oct-2022, Document URL: http://https%253A%252F%252Ffractory.com%252Fwelding-defects-types-causes-prevention%252F (consulted on 23/12/2022)
- [58] J. Angles, Modélisation et Simulation de la Fissuration à Froid: Etude numérique d'une maquette pour la préparation d'essais, EDF (Électricité De France), EDF R&D A.M.A., EDF internal publication H-T59-2011-02090-FR, 2011
- [59] What is the heat affected zone (HAZ)?, TWI Ltd (The Welding Institute) [webpage], Document URL: https://www.twi-global.com/technical-knowledge/faqs/what-is-the-heat-affected-zone.aspx (consulted on 15/11/2022)
- [60] M. Sokolov, A. Salminen, E. I. Khlusova, M. M. Pronin, M. Golubeva, and M. Kuznetsov, **Testing of new materials and computer aided optimization of laser beam welding of high-strength steels**, *Physics Procedia*, vol. 78, pp. 255–264, Jan. 2015, Document identifier = DOI: 10.1016/j.phpro.2015.11.036
- [61] M. Lomozik, Effect of the welding thermal cycles on the structural changes in the heat affected zone and on its properties in joints welded in low-alloy steels,

- *Welding International*, vol. 14, no. 11, pp. 845–850, 2000, Document identifier = DOI: 10.1080/09507110009549281
- [62] M. Wang and B. Duan, **Materials and their biomedical applications**, in *Encyclopedia of biomedical engineering*, R. Narayan, Ed. Oxford: *Elsevier*, 2019, pp. 135–152, Document identifier = DOI: 10.1016/B978-0-12-801238-3.99860-X
- [63] A. Pundt, **Hydrogen in nano-sized Metals**, *Advanced Engineering Materials*, vol. 6, no. 1–2, pp. 11–21, 2004, Document identifier = DOI : 10.1002/adem.200300557
- [64] What is the difference between FCC and BCC? (crystal structure, properties, interstitial sites, and examples), Materials Science & Engineering Student [webpage], Document URL: https://msestudent.com/what-is-the-difference-between-fcc-and-bcc-crystal-structure-properties-interstitial-sites-and-examples/ (consulted on 22/01/2023)
- [65] P. Hairy, **La solidification des alliages métalliques**, *CTIF MetalBlog (Centre Technique des Industries de la Fonderie)*, 10-Sep-2018, Document URL: https://metalblog.ctif.com/2018/09/10/la-solidification-des-alliages-metalliques/ (consulted on 16/01/2023)
- [66] J. L. Dossett and H. E. Boyer, Chapter 2 fundamentals of the heat treating of steel, in *Practical Heat Treating*, 2nd ed., *ASM International (American Society for Metals)*, 2006, Document identifier = ISBN: 978-0-87170-829-8
- [67] S. B. Hendricks, **The crystal structure of cementite**, *Zeitschrift für Kristallographie Crystalline Materials*, vol. 74, no. 1–6, pp. 534–545, Dec. 1930, Document identifier = DOI: 10.1524/zkri.1930.74.1.534
- [68] H. K. D. H. Bhadeshia, **Cementite**, *International Materials Reviews*, vol. 65, no. 1, pp. 1–27, Jan. 2020, Document identifier = DOI : 10.1080/09506608.2018.1560984
- [69] I. G. Wood *et al.*, **Thermal expansion and crystal structure of cementite, Fe3C,** between 4 and 600 K determined by time-of-flight neutron powder diffraction, *Journal of Applied Crystallography*, vol. 37, no. 1, pp. 82–90, 2004, Document identifier = DOI: 10.1107/S0021889803024695
- [70] W. D. Jr. Callister, **Materials Science and Engineering: An Introduction**, 7th ed., *John Wiley & Sons*, 2007, Document identifier = ISBN: 978-0-471-73696-7
- [71] T. B. Massalski, H. Okamoto, P. R. Subramanian, and L. Kacprzak, Eds., **Binary Alloy Phase Diagrams**, 2nd ed., 3 vols, *ASM International (American Society for Metals)*, 1990, Document identifier = ISBN: 978-0-87170-403-0
- [72] M. Benti, **Dossier métallurgie du soudage**, Montluçon : *CNRSM (Centre National de Ressources Structures Métalliques)*, Document URL : https://eduscol.education.fr/sti/sites/eduscol.education.fr.sti/files/ressources/pedag ogiques/5241/5241-metallurgie-du-soudage-dossier-professeur.pdf (consulted on 30/12/2022)
- [73] J.-P. Brog, C.-L. Chanez, A. Crochet, and K. Fromm, **Polymorphism, what it is and how to identify it: A systematic review**, *RSC Advances*, Jun. 2013,

- Document identifier = DOI: 10.1039/c3ra41559g
- [74] P. G. Caceres, **M.Eng. class lecture MSE8-2: Martensite**, presented at the *University of Puerto Rico at Mayagüez*, Puerto Rico, 25-Mar-2010, Document URL: https://academic.uprm.edu/pcaceres/Courses/MatEng/ (consulted on 23/08/2019)
- [75] J. Ruste, **IX Les traitements thermiques des aciers**, in *Cours de métallurgie*, Marne la Vallée : *Université de Marne la Vallée*, Document URL : http://micro.icaunais.free.fr/05_trait_therm.pdf (consulted on 09/01/2023)
- [76] Z. Nasiri, S. Ghaemifar, M. Naghizadeh, and H. Mirzadeh, **Thermal mechanisms of grain refinement in steels: a review**, *Met. Mater. Int.*, vol. 27, no. 7, pp. 2078–2094, Jul. 2021, Document identifier = DOI: 10.1007/s12540-020-00700-1
- [77] H. K. D. H. Bhadeshia, **Carbon–carbon interactions in iron**, *Journal of Materials Science*, vol. 39, no. 12, pp. 3949–3955, Jun. 2004, Document identifier = DOI: 10.1023/B:JMSC.0000031476.21217.fa
- [78] N. T. Trinh, Sur la modélisation du comportement thermomécanique et métallurgique des aciers. Application au procédé de soudage et de traitements thermiques, PhD thesis, ENSTA (École Nationale Supérieure de Techniques Avancées / ParisTech), Paris, 2008, Document URL: https://pastel.archivesouvertes.fr/pastel-00004738 (consulted on 09/10/2019)
- [79] **Crystal structure of cementite**, *University of Cambridge*, 2019, Document URL: https://www.phase-trans.msm.cam.ac.uk/2019/cementite.html (consulted on 26/01/2023)
- [80] V. B. Ginzburg, R. Ballas, and R. Ballas, **Flat Rolling Fundamentals**, Kingston : *CRC Press*, 2000, Document identifier = DOI : 10.1201/9781482277357
- [81] T. Kasuya and N. Yurioka, Carbon Equivalent and Multiplying Factor for Hardenability of Steel, in *Welding Research Supplement*, Detroit, 1991, pp. 263–268, Document URL: https://app.aws.org/wj/supplement/WJ_1993_06_s263.pdf (consulted on 22/08/2019)
- [82] R. Kurji and N. Coniglio, **Towards Establishment of Weldability Test Standards for Hydrogen Assisted Cold Cracking**, *International Journal of Advanced Manufacturing Technology*, vol. 77, pp. 1581–1597, 2015, Document identifier = DOI: 10.1007/s00170-014-6555-3
- [83] J. Dearden and H. O'Neill, A guide to the selection and welding of low alloy structural steels, *Institute of Welding Transactions*, vol. 3, pp. 203–214, 1940
- [84] L. Bill, G. Mathers, and D. Abson, **Defects / hydrogen cracks in steels identification**, *TWI Ltd (The Welding Institute)* [webpage], Document URL: https://www.twi-global.com/technical-knowledge/job-knowledge/defects-hydrogen-cracks-in-steels-identification-045.aspx (consulted on 22/12/2022)
- [85] What is the difference between heat input and arc energy?, TWI Ltd (The Welding Institute) [webpage], Document URL: https://www.twi-global.com/technical-knowledge/faqs/faq-what-is-the-difference-between-heat-input-and-arc-energy.aspx (consulted on 25/02/2023)

- [86] **NF EN 1011-2**, *AFNOR*, Jul-2002, Document URL https://www.boutique.afnor.org/fr-fr/norme/nf-en-10112/soudage-recommandations-pour-le-soudage-des-materiaux-metalliques-partie-2-/fa102142/20043 (consulted on 09/04/2023)
- [87] **ISO 17642-1**, *ISO (International Organization for Standardization)*, 2005, Document identifier = ISSN: 0335-3931
- [88] Carbon equivalent formulae in relation to hydrogen cracking, TWI Ltd (The Welding Institute) [webpage], Document URL: https://www.twi-global.com/technical-knowledge/faqs/faq-what-is-the-difference-between-the-various-carbon-equivalent-formulae-used-in-relation-to-hydrogen-cracking (consulted on 20/09/2019)
- [89] T. Schaupp, W. Ernst, H. Spindler, and T. Kannengiesser, **Hydrogen-assisted cracking of GMA welded 960 MPa grade high-strength steels**, *International Journal of Hydrogen Energy*, vol. 45, no. 38, pp. 20080–20093, Jul. 2020, Document identifier = DOI: 10.1016/j.ijhydene.2020.05.077
- [90] B. A. Graville, Cold cracking in welds in HSLA steels, in *International conference on welding of HSLA (microalloyed) structural steels*, A. B. Rothwell and J. Malcolm Gray, Eds. Rome: *ASM International (American Society for Metals)*, 1976, pp. 85–101
- [91] G. K. Padhy and Y. Komizo, **Diffusible hydrogen in steel weldments: a status review**, *Transactions of JWRI (Joining and Welding Research Institute of Osaka University)*, vol. 42, no. 1, pp. 39–62, Jun. 2013, Document identifier = ISSN: 03874508
- [92] K. Badri, **Fissuration à froid des soudures**, *Sodel Ltée*, Document URL : https://www.sodel.com/medias/iw/fissuration-a-froid-des-soudures-sodel.pdf (consulted on 11/11/2022)
- [93] H. W. Lee, **Weld metal hydrogen-assisted cracking in thick steel plate weldments**, *Materials Science and Engineering*: A, vol. 445–446, pp. 328–335, Feb. 2007, Document identifier = DOI: 10.1016/j.msea.2006.09.046
- [94] I. K. Pokhodnya and V. I. Shvachko, **Cold cracks in welded joints of structural steels**, *Mater Sci*, vol. 32, no. 1, pp. 45–55, Jan. 1996, Document identifier = DOI: 10.1007/BF02538924
- [95] F. Baillon and P. Lours, **Les faciès de rupture**, in *Au cœur des matériaux cristallins*, Albi : *École des Mines d'Albi-Carmaux*, Document URL : https://nte.mines-albi.fr/SciMat/fr/co/SM6uc1-4.html (consulted on 07/02/2022)
- [96] J. Grill, **Welding cracks & how to prevent them**, *Weld Guru*, 01-Aug-2022 [webpage], Document URL: https://weldguru.com/welding-cracks/ (consulted on 24/12/2022)
- [97] T. Kannengiesser and T. Boellinghaus, Cold cracking tests an overview of present technologies and applications, Weld World, vol. 57, no. 1, pp. 3–37, Feb. 2013, Document identifier = DOI: 10.1007/s40194-012-0001-7
- [98] N. Bailey, F. R. Coe, T. G. Gooch, P. H. M. Hart, N. Jenkins, and R. J. Pargeter,

- Welding Steels Without Hydrogen Cracking, 2nd ed., Woodhead Publishing, 1993, Document identifier = ISBN: 978-1-85573-014-4
- [99] E. Dabah, **Hydrogen interaction with supermartensitic stainless steel studied by energy dispersive X-ray diffraction**, PhD thesis, *Universität Magdeburg*, 2015, Document URL: https://core.ac.uk/download/pdf/51449102.pdf (consulted on 26/08/2019)
- [100] S. A. Gedeon, **Hydrogen Assisted Cracking of High Strength Steel Welds**, PhD thesis, *MIT (Massachusetts Institute of Technology)*, Watertown, 1988, Document identifier = DOI: 10.21236/ADA196738
- [101] T. Boellinghaus, T. Mente, P. Wongpanya, E. Viyanit, and E. Steppan, **Numerical Modelling of Hydrogen Assisted Cracking in Steel Welds**, in *Cracking Phenomena in Welds IV*, T. Boellinghaus, J. C. Lippold, and C. E. Cross, Eds. Cham: *Springer International Publishing*, 2016, pp. 383–439, Document identifier = DOI: 10.1007/978-3-319-28434-7 18
- [102] T. Inoue and Z. Wang, Coupling between stress, temperature, and metallic structures during processes involving phase transformations, *Materials Science and Technology*, vol. 1, no. 10, pp. 845–850, Oct. 1985, Document identifier = DOI: 10.1179/mst.1985.1.10.845
- [103] V. N. Bugaev, V. G. Gavriljuk, Yu. N. Petrov, and A. V. Tarasenko, Mechanism of hydrogen-induced phase transformations in metals and alloys, *International Journal of Hydrogen Energy*, vol. 22, no. 2, pp. 213–218, Feb. 1997, Document identifier = DOI: 10.1016/S0360-3199(96)00154-1
- [104] M. Coret, S. Calloch, and A. Combescure, **Experimental study of the phase transformation plasticity of 16MND5 low carbon steel under multiaxial loading**, *International Journal of Plasticity*, vol. 18, no. 12, pp. 1707–1727, Dec. 2002, Document identifier = DOI: 10.1016/S0749-6419(01)00067-5
- [105] C. D. Beachem, **A new model for hydrogen-assisted cracking (hydrogen "embrittlement")**, *MT*, vol. 3, no. 2, pp. 441–455, Feb. 1972, Document identifier = DOI: 10.1007/BF02642048
- [106] H. G. Nelson, **Hydrogen Embrittlement**, in *Treatise on Materials Science & Technology*, vol. 25, C. L. Briant and S. K. Banerji, Eds. *Elsevier*, 1983, pp. 275–359, Document identifier = DOI: 10.1016/B978-0-12-341825-8.50014-3
- [107] J.-B. Leblond and D. Dubois, A general mathematical description of hydrogen diffusion in steels—I. Derivation of diffusion equations from boltzmann-type transport equations, *Acta Metallurgica*, vol. 31, no. 10, pp. 1459–1469, Oct. 1983, Document identifier = DOI: 10.1016/0001-6160(83)90142-6
- [108] J.-B. Leblond and D. Dubois, A general mathematical description of hydrogen diffusion in steels—II. Numerical study of permeation and determination of trapping parameters, *Acta Metallurgica*, vol. 31, no. 10, pp. 1471–1478, Oct. 1983, Document identifier = DOI: 10.1016/0001-6160(83)90143-8
- [109] F. Matsuda, H. Nakagawa, K. Shinozaki, H. Morimoto, and Y. Sanematsu, Criterion of alternative initiation of cold cracking in HAZ or weld metal for root pass welds of high strength steels, *Transactions of JWRI (Joining and*

- Welding Research Institute of Osaka University), vol. 12, no. 2, pp. 235–245, Dec. 1983, Document identifier = DOI: 10.18910/11298
- [110] M. Rhode, **Hydrogen diffusion and effect on degradation in welded microstructures of creep-resistant low-alloyed steels**, PhD thesis, *Universität Magdeburg*, Berlin, 2016, Document identifier = ISBN: 978-3-9817853-3-3
- [111] P. Nevasmaa, Predictive model for the prevention of weld metal hydrogen cracking in high-strength multipass welds, PhD thesis, *University of Oulu*, Oulu, 2003, Document identifier = ISBN: 951-42-7181-5
- [112] A. Oudriss *et al.*, Consequence of the diffusive hydrogen contents on tensile properties of martensitic steel during the desorption at room temperature, *Materials Science and Engineering: A*, vol. 598, pp. 420–428, Mar. 2014, Document identifier = DOI: 10.1016/j.msea.2014.01.039
- [113] S. P. Lynch, **Hydrogen embrittlement phenomena and mechanisms**, *corrrev*, vol. 30, no. 3–4, pp. 105–123, 2012, Document identifier = DOI: 10.1515/corrrev-2012-0502
- [114] A. R. Troiano, **The role of hydrogen and other interstitials in the mechanical behavior of metals**, *Transactions of American Society for Metals*, vol. 52, pp. 58–60, 1960, Document identifier = DOI: 10.1007/s13632-016-0319-4
- [115] W. H. Johnson, **On some remarkable changes produced in iron and steel by the action of hydrogen and acids**, *Nature*, no. 11, p. 393, Mar. 1875, Document identifier = DOI: 10.1038/011393a0
- [116] T. Boellinghaus, H. Hoffmeister, and A. Dangeleit, A scatterband for hydrogen diffusion coefficients in microalloyed and low carbon structural steels, *Welding in the World*, vol. 2, no. 35, p. 149, 1995, Document identifier = ISSN: 0043-2288
- [117] J. du Plessis, Control of diffusible weld metal hydrogen through arc chemistry modifications, MSc thesis, *University of Pretoria*, Pretoria, 2007, Document URL: https://www.semanticscholar.org/paper/CONTROL-OF-DIFFUSIBLE-WELD-METAL-HYDROGEN-THROUGH-Plessis/20e29416186879fbd5b82906937080445bf426d1 (consulted on 30/12/2022)
- [118] F. Matsuda, H. Nakagawa, K. Shinozaki, and H. Kihara, **Evaluation of transformation expansion and its beneficial effect on cold crack susceptibility using Y-slit crack test instrumend with strain gauge**, *Transactions of JWRI (Joining and Welding Research Institute of Osaka University)*, vol. 13, no. 1, pp. 47–55, Jul. 1984, Document identifier = DOI: 10.18910/6144
- [119] S. Debiez, **Determination des conditions de soudage des aciers faiblement allies pour prevenir le risque de fissuration a froid**, *Soudage et Techniques Connexes*, vol. 38, no. 5, pp. 188–205, 1984
- [120] J. L. Davidson, S. P. Lynch, and A. Majumdar, The relationship between hydrogen-induced cracking resistance, microstructure and toughness in high strength weld metal, in *Hydrogen management in steel weldments*, J. L. Davidson and D. L. Olson, Eds. Melbourne: *The Organising Committee of the Joint Seminar on behalf of Defence Science and Technology Association and Welding Technology*

- *Institute of Australia*, 1996, pp. 21–34, Document identifier = ISBN: 978-0-7311-0809-1
- [121] F. Faure, R. Palengat, F. Roux, P. Bocquet, and M. Delafin, Modified implant test for studying cold cracking sensitivity of interface between stainless steel and ferritic steel, in *International Conference on Welding in Nuclear Engineering*, Aachen, 1982, vol. 75, pp. 56–54, Document identifier = ISBN: 3-87155-380-8
- [122] R. Vasudevan, R. D. Stout, and A. W. Pense, **Hydrogen-assisted cracking in HSLA pipeline steels**, *Welding Journal Welding Research Supplement*, vol. 60, no. 9, pp. 155s–168s, Sep. 1981, Document URL: https://app.aws.org/wj/supplement/WJ 1981 09 s155.pdf
- [123] M. Pitrun, **The effect of welding parameters on levels of diffusible hydrogen in weld metal deposited using gas shielded rutile flux cored wires**, PhD thesis, *University of Wollongong*, Wollongong, 2004, Document URL: https://ro.uow.edu.au/theses/361 (consulted on 09/09/2019)
- [124] G. Miyamoto, Y. Karube, and T. Furuhara, **Formation of grain boundary ferrite** in eutectoid and hypereutectoid pearlitic steels, *Acta Materialia*, vol. 103, pp. 370–381, Jan. 2016, Document identifier = DOI: 10.1016/j.actamat.2015.10.032
- [125] B. A. Graville, **A survey review of weld metal hydrogen cracking**, *Welding in the World*, vol. 9/10, no. 24, pp. 190–199, 1986, Document identifier = ISSN: 0043-2288
- [126] A. S. Keh and W. C. Leslie, Recent observations on quench-aging and strainaging of iron and steel, in *Materials Science Research*, H. H. Stadelmaier and W. W. Austin, Eds. Boston, MA: *Springer US*, 1963, pp. 208–250, Document identifier = DOI: 10.1007/978-1-4899-5537-1
- [127] W. F. Hosford, **Iron and Steel**, University of Michigan: *Cambridge University Press*, 2012, Document identifier = DOI: 10.1017/CBO9781139086233
- [128] V. K. Euser, D. L. Williamson, K. O. Findley, A. J. Clarke, and J. G. Speer, **The role of retained austenite in tempered martensite embrittlement of 4340 and 300-M steels investigated through rapid tempering**, *Metals*, vol. 11, no. 9, p. 1349, Sep. 2021, Document identifier = DOI: 10.3390/met11091349
- [129] What is temper embrittlement, and how can it be controlled?, TWI Ltd (The Welding Institute) [webpage], Document URL: https://www.twi-global.com/technical-knowledge/faqs/faq-what-is-temper-embrittlement-and-how-can-it-be-controlled.aspx (consulted on 09/09/2023)
- [130] W. M. Garrison and N. R. Moody, Hydrogen embrittlement of high strength steels, in *Gaseous Hydrogen Embrittlement of Materials in Energy Technologies*, vol. 2, R. P. Gangloff and B. P. Somerday, Eds. *Woodhead Publishing*, 2012, pp. 421–492, Document identifier = DOI: 10.1533/9780857093899.3.421
- [131] H. K. D. H. Bhadeshia and D. V. Edmonds, **Tempered martensite embrittlement: role of retained austenite and cementite**, *Metal Science*, vol. 13, pp. 325–334, Jun. 1979, Document URL: https://www.phasetrans.msm.cam.ac.uk/abstracts/tme.html (consulted on 09/09/2023)

- [132] R. M. Horn and R. O. Ritchie, **Mechanisms of tempered martensite embrittlement in low-alloy steels**, *Metall Trans A*, vol. 9, no. 8, pp. 1039–1053, Aug. 1978, Document identifier = DOI: 10.1007/BF02652208
- [133] W. C. Leslie, **The quench-ageing of low-carbon iron and iron-manganese alloys** an electron transmission study, *Acta Metallurgica*, vol. 9, no. 11, pp. 1004–1022, Nov. 1961, Document identifier = DOI: 10.1016/0001-6160(61)90244-9
- [134] J. D. Fast, **Le vieillissement du fer et de l'acier**, *Rev. Met. Paris*, vol. 47, no. 10, pp. 779–786, Oct. 1950, Document identifier = DOI : 10.1051/metal/195047100779
- [135] C. J. (Colin J. Smithells, **Smithells Metals Reference Book**, 7th ed., *Butterworth-Heinemann*, 1992, Document identifier = DOI: 10.1016/C2009-0-25363-3
- [136] H. J. Grabke and E. Riecke, **Absorption and diffusion of hydrogen in steels**, *Materiali in Tehnologije*, vol. 34, no. 6, pp. 331–342, Dec. 2000, Document identifier = ISSN: 1580-2949
- [137] G. M. Pressouyre, A classification of hydrogen traps in steel, *Metall Mater Trans A*, vol. 10, no. 10, pp. 1571–1573, Oct. 1979, Document identifier = DOI: 10.1007/BF02812023
- [138] G. M. Pressouyre and I. M. Bernstein, **A quantitative analysis of hydrogen trapping**, *Metall Mater Trans A*, vol. 9, no. 11, pp. 1571–1580, Nov. 1978, Document identifier = DOI: 10.1007/BF02661939
- [139] E. T. Turkdogan, **Fundamentals of Steelmaking**, London: *The Institute of Materials*, 1996, Document identifier = ISBN: 978-1-906540-97-5
- [140] Xie Z., Ikeda T., Okuda Y., and Nakajima H., **Characteristic of absorbing sound** in lotus-type porous magnesium, *J.Japan Inst.Metals*, vol. 67, no. 12, pp. 708–713, 2003, Document identifier = DOI: 10.2320/jinstmet1952.67.12 708
- [141] J.-B. Leblond, D. Nejem, D. Dubois, and S. Talbot-besnard, **Experimental and numerical study of diffusion and trapping of hydrogen in plastically deformed A508.Cl.3 steel at room temperature**, *Acta Metallurgica*, vol. 35, no. 7, pp. 1703–1714, Jul. 1987, Document identifier = DOI: 10.1016/0001-6160(87)90116-7
- [142] D. Nolan and M. Pitrun, **Diffusible Hydrogen Testing in Australia**, *Weld World*, vol. 48, no. 1, pp. 14–20, Jan. 2004, Document identifier = DOI: 10.1007/BF03266409
- [143] J. Crank and E. P. J. Crank, **The Mathematics of Diffusion**, *Clarendon Press*, 1979, Document identifier = ISBN: 978-0-19-853411-2
- [144] Y. Fukai, **The Metal-Hydrogen System: Basic Bulk Properties**, Springer Science & Business Media, 2006, Document identifier = ISBN: 978-3-540-28883-1
- [145] **ISO 3690**, *ISO (International Organization for Standardization)*, 2018, Document identifier = ISSN: 0335-3931
- [146] A. Pundt and R. Kirchheim, Hydrogen in metals: microstructural aspects,

- Annual Review of Materials Research, vol. 36, no. 1, pp. 555–608, 2006, Document identifier = DOI: 10.1146/annurev.matsci.36.090804.094451
- [147] S. Frappart *et al.*, **Hydrogen trapping in martensitic steel investigated using electrochemical permeation and thermal desorption spectroscopy**, *Scripta Materialia*, vol. 65, no. 10, pp. 859–862, Nov. 2011, Document identifier = DOI: 10.1016/j.scriptamat.2011.07.042
- [148] D. Pérez Escobar, K. Verbeken, L. Duprez, and M. Verhaege, **Evaluation of hydrogen trapping in high strength steels by thermal desorption spectroscopy**, *Materials Science and Engineering: A*, vol. 551, pp. 50–58, Aug. 2012, Document identifier = DOI: 10.1016/j.msea.2012.04.078
- [149] M. L. Martin and P. Sofronis, **Hydrogen-induced cracking and blistering in steels: a review**, *Journal of Natural Gas Science and Engineering*, vol. 101, p. 104547, May 2022, Document identifier = DOI: 10.1016/j.jngse.2022.104547
- [150] P. F. Timmins, **Failure Control in Process Operations**, in *Fatigue and Fracture*, vol. 19, *ASM International (American Society for Metals)*, 1996, pp. 468–482, Document identifier = DOI: 10.31399/asm.hb.v19.a0002387
- [151] M. L. Martin, M. J. Connolly, F. W. DelRio, and A. J. Slifka, **Hydrogen embrittlement in ferritic steels**, *Applied Physics Reviews*, vol. 7, no. 4, p. 041301, Dec. 2020, Document identifier = DOI: 10.1063/5.0012851
- [152] J. P. Hirth, **Effects of hydrogen on the properties of iron and steel**, *Metall Mater Trans A*, vol. 11, no. 6, pp. 861–890, Jun. 1980, Document identifier = DOI: 10.1007/BF02654700
- [153] C. St. John and W. W. Gerberich, **The effect of loading mode on hydrogen embrittlement**, *Metall Mater Trans B*, vol. 4, no. 2, pp. 589–594, Feb. 1973, Document identifier = DOI: 10.1007/BF02648714
- [154] M. L. Martin, M. Dadfarnia, A. Nagao, S. Wang, and P. Sofronis, **Enumeration of the hydrogen-enhanced localized plasticity mechanism for hydrogen embrittlement in structural materials**, *Acta Materialia*, vol. 165, pp. 734–750, Feb. 2019, Document identifier = DOI: 10.1016/j.actamat.2018.12.014
- [155] I. M. Robertson *et al.*, **Hydrogen embrittlement understood**, *Metall Mater Trans A*, vol. 46, no. 6, pp. 2323–2341, Jun. 2015, Document identifier = DOI: 10.1007/s11661-015-2836-1
- [156] D. G. Westlake, A generalized model for hydrogen embrittlement, ASM International (American Society for Metals), vol. 62, pp. 1000–1006, Dec. 1969
- [157] R. A. Oriani, A mechanistic theory of hydrogen embrittlement of steels, Berichte der Bunsengesellschaft für physikalische Chemie, vol. 76, no. 8, pp. 848–857, 1972, Document identifier = DOI: 10.1002/bbpc.19720760864
- [158] J. D. Hobson and J. Hewitt, **The effect of hydrogen on the tensile properties of steel**, *Journal of the Iron and Steel Institute*, vol. 173, no. 2, pp. 131–140, 1953
- [159] H. K. Birnbaum and P. Sofronis, **Hydrogen-enhanced localized plasticity a** mechanism for hydrogen-related fracture, *Materials Science and Engineering:*

- A, vol. 176, no. 1, pp. 191–202, Mar. 1994, Document identifier = DOI : 10.1016/0921-5093(94)90975-X
- [160] C. A. Zapffe and C. E. Sims, **Hydrogen embrittlement, internal stress and defects in steel**, *Transactions of the AIME (American Institute of Mining Engineers)*, vol. 145, pp. 225–271, 1941
- [161] S. P. Lynch, Environmentally assisted cracking: Overview of evidence for an adsorption-induced localised-slip process, *Acta Metallurgica*, vol. 36, no. 10, pp. 2639–2661, Oct. 1988, Document identifier = DOI : 10.1016/0001-6160(88)90113-7
- [162] O. Sobol, **Hydrogen assisted cracking and transport studied by ToF-SIMS and data fusion with HR-SEM**, PhD thesis, *Universität Magdeburg*, Berlin, 2018, Document identifier = ISSN: 1613-4249
- [163] Au cœur des matériaux cristallins: les faciès de rupture, École des Mines d'Albi-Carmaux [webpage], Document URL: https://nte.mines-albi.fr/SciMat/co/SM6uc1-4.html (consulted on 28/08/2019)
- [164] M. L. Martin, J. A. Fenske, G. S. Liu, P. Sofronis, and I. M. Robertson, **On the formation and nature of quasi-cleavage fracture surfaces in hydrogen embrittled steels**, *Acta Materialia*, vol. 59, no. 4, pp. 1601–1606, Feb. 2011, Document identifier = DOI: 10.1016/j.actamat.2010.11.024
- [165] M. Rhode, J. Steger, E. Steppan, and T. Kannengiesser, Effect of hydrogen on mechanical properties of heat affected zone of a reactor pressure vessel steel grade, *Weld World*, vol. 60, no. 4, pp. 623–638, Jul. 2016, Document identifier = DOI: 10.1007/s40194-016-0325-9
- [166] A. Oudriss, X. Feaugas, J. Creus, and R. Milet, **Influence de l'hydrogène sur les propriétés mécanique du 16MND5**, *LaSIE (University of La Rochelle)*, LaSIE (University of La Rochelle), LaSIE technical report Etude FPH du 16MND5, Jun. 2014
- [167] J. du Plessis and M. du Toit, **Reducing diffusible hydrogen contents of shielded metal arc welds through addition of flux-oxidizing ingredients**, *J. of Materi Eng and Perform*, vol. 17, no. 1, pp. 50–56, Feb. 2008, Document identifier = DOI: 10.1007/s11665-007-9133-0
- [168] M. Suban, J. Tušek, and M. Uran, **Use of hydrogen in welding engineering in former times and today**, *Journal of Materials Processing Technology*, vol. 119, no. 1, pp. 193–198, Dec. 2001, Document identifier = DOI: 10.1016/S0924-0136(01)00956-6
- [169] O. Schwedler, M. Zinke, and S. Jüttner, **Determination of hydrogen input in welded joints of press-hardened 22MnB5 steel**, *Weld World*, vol. 58, no. 3, pp. 339–346, May 2014, Document identifier = DOI: 10.1007/s40194-014-0119-x
- [170] S. A. Gedeon and T. W. Eagar, **Thermochemical analysis of hydrogen absorption in welding**, *Welding Journal*, vol. 69, no. 7, pp. s264–s271, 1990, Document URL: http://files.aws.org/wj/supplement/WJ 1990 07 s264.pdf
- [171] E. Viyanit, Numerical Simulation of Hydrogen Assisted Cracking in

- **Supermartensitic Stainless Steel Welds**, PhD thesis, *Universität der Bundeswehr Hamburg*, Hamburg, 2005, Document identifier = ISBN: 3-86509-270-5
- [172] S. Kou, Welding Metallurgy, Hoboken: John Wiley & Sons, 2002, Document identifier = ISBN: 0-471-43491-4
- [173] K. Satoh, Y. Ueda, and H. Kihara, **Recent trend of researches on restraint stresses and strains for weld cracking**, *Journal of the Japan Welding Society*, vol. 42, no. 1, pp. 57–72, 1973, Document identifier = DOI: 10.2207/qjjws1943.42.57
- [174] N. O'Meara, **Developing material models for use in finite element predictions of residual stresses in ferritic steel welds**, PhD thesis, *University of Manchester*, Manchester, 2015, Document URL: https://search.proquest.com/openview/6ff15d4ec8af4af3e6d8b4a20c7a6864/1?pq-origsite=gscholar&cbl=51922&diss=y (consulted on 03/11/2020)
- [175] D. C. Dunand and P. Zwigl, **Hydrogen-induced internal-stress plasticity in titanium**, *Metall Mater Trans A*, vol. 32, no. 3, pp. 841–843, Mar. 2001, Document identifier = DOI: 10.1007/s11661-001-0100-3
- [176] K. Satoh, **Transient thermal stresses of weld heat-affected zone by both-ends-fixed bar analogy**, *Transactions of the JWS (Japan Welding Society)*, vol. 3, no. 1, pp. 125–134, Apr. 1972, Document URL: https://cir.nii.ac.jp/crid/1543387470125111808 (consulted on 08/02/2023)
- [177] J. K. Rai, A. Mishra, and U. R. K. Rao, Residual stresses due to quenching process, International Journal of Machine Tool Design and Research, vol. 20, no. 1, pp. 1–8, Jan. 1980, Document identifier = DOI: 10.1016/0020-7357(80)90013-X
- [178] A. C. Roberts and A. H. Cottrell, Creep of alpha uranium during irradiation with neutrons, *The Philosophical Magazine*, vol. 1, no. 8, pp. 711–717, Aug. 1956, Document identifier = DOI: 10.1080/14786435608238145
- [179] C.-Y. Huang and G. S. Daehn, **Densification of composite powder compacts in pressure cycling**, *Acta Materialia*, vol. 44, no. 3, pp. 1035–1045, Mar. 1996, Document identifier = DOI: 10.1016/1359-6454(95)00230-8
- [180] L. Taleb, **Transformation-Induced Plasticity (TRIP)**, in *Encyclopedia of Thermal Stresses*, R. B. Hetnarski, Ed. *Springer Dordrecht*, 2013, pp. 6153–6163, Document identifier = DOI: 10.1007/978-94-007-2739-7 858
- [181] L. Taleb, N. Cavallo, and F. Waeckel, **Experimental analysis of transformation plasticity**, *International Journal of Plasticity*, vol. 17, no. 1, pp. 1–20, Jan. 2001, Document identifier = DOI: 10.1016/S0749-6419(99)00090-X
- [182] P. J. Withers, **Residual stress: definition**, in *Encyclopedia of Materials: Science and Technology*, K. H. J. Buschow, R. W. Cahn, M. C. Flemings, B. Ilschner, E. J. Kramer, S. Mahajan, and P. Veyssière, Eds. Oxford: *Elsevier*, 2001, pp. 8110–8112, Document identifier = DOI: 10.1016/B0-08-043152-6/01455-8
- [183] P. J. Withers and H. K. D. H. Bhadeshia, **Residual stress. Part 1 Measurement techniques**, *Materials Science and Technology*, vol. 17, no. 4, pp. 355–365, Apr. 2001, Document identifier = DOI: 10.1179/026708301101509980

- [184] P. J. Withers and H. K. D. H. Bhadeshia, **Residual stress. Part 2 Nature and origins**, *Materials Science and Technology*, vol. 17, no. 4, pp. 366–375, Apr. 2001, Document identifier = DOI: 10.1179/026708301101510087
- [185] T. G. Nieh, J. Wadsworth, and O. D. Sherby, **Superplasticity in Metals and Ceramics**, Cambridge: *Cambridge University*, 1997, Document identifier = DOI: 10.1017/CBO9780511525230
- [186] M. Coret and A. Combescure, **Experiments and simulation of transformation induced plasticity under multiaxial loading for a 16MND5 ferritic steel**, presented at the *16th international conference on structural mechanics in reactor technology (SMiRT 16)*, Washington DC, 2001, Document identifier = Paper #2054
- [187] S. P. Lynch, **Mechanisms of hydrogen assisted cracking a review**, in *Metals & Materials Society*, 2003, pp. 449–466, Document identifier = ISBN : 978-0-87339-501-4
- [188] W. D. Pilkey, **Peterson's Stress Concentration Factors**, 2nd ed., *John Wiley & Sons*, 1997, Document identifier = ISBN: 0-471-53849-3
- [189] G. Fréchette, Étude du comportement au fluage de l'alliage 13Cr-4Ni en vue de simuler la redistribution des contraintes résiduelles lors du traitement thermique post-soudage, MSc thesis, ETS (École de Technologie Supérieure), Montréal, 2018, Document URL: https://espace.etsmtl.ca/id/eprint/2079/(consulted on 06/01/2023)
- [190] A. A. Griffith and G. I. Taylor, **The phenomena of rupture and flow in solids**, *Philosophical Transactions of the Royal Society of London*, vol. 221, no. 582–593, pp. 163–198, Jan. 1921, Document identifier = DOI: 10.1098/rsta.1921.0006
- [191] **ISO 17642-2**, *ISO (International Organization for Standardization)*, 2005, Document identifier = ISSN: 0335-3931
- [192] J. L. González-Velázquez, **A Practical Approach to Fracture Mechanics**, *Elsevier*, 2021, Document identifier = DOI: 10.1016/C2019-0-05011-X
- [193] G. R. Irwin, **Analysis of stresses and strains near the end of a crack traversing a plate**, *Journal of Applied Mechanics*, vol. 24, no. 3, pp. 361–364, Sep. 1957, Document identifier = DOI: 10.1115/1.4011547
- [194] F. Erdogan, **Fracture mechanics**, *International Journal of Solids and Structures*, vol. 37, no. 1, pp. 171–183, 2000, Document identifier = DOI: 10.1016/S0020-7683(99)00086-4
- [195] F. Baillon and P. Lours, **Facteur d'intensité de contrainte**, in *Au cœur des matériaux cristallins*, Albi : *École des Mines d'Albi-Carmaux*, Document URL : https://nte.mines-albi.fr/SciMat/fr/co/SM6uc2-1.html (consulted on 09/01/2023)
- [196] J. Besson, **Chapitre XXIII: endommagement et rupture**, in *Mécanique*, *Matériaux*, *et Structures*, *essentiellement pour les milieux solides*, Paris: *ENSMP* (École Nationale Supérieure des Mines de Paris), Document URL: http://mms2.ensmp.fr/mat_paris/duree/polycop/Ch_23_Endommagement.pdf (consulted on 09/01/2023)

- [197] M. Medraj, **Modes of crack displacement**, presented at the *Concordia University*, Montréal, 2019, Document URL: http://users.encs.concordia.ca/~mmedraj/mech321/lecture_9_fracture_2.pdf (consulted on 08/01/2023)
- [198] B. Tomkins and M. F. Hamza, **Structural integrity issues in the nuclear industry**, in *Reference Module in Materials Science and Materials Engineering*, *Elsevier*, 2017, Document identifier = DOI: 10.1016/B978-0-12-803581-8.00852-3
- [199] F. Matsuda, H. Nakagawa, K. Shinozaki, Y. Nishio, and H. Kihara, Effect of transformation expansion on restraint stress of weldment in relation to cold cracking of high strength steels, *Transactions of JWRI (Joining and Welding Research Institute of Osaka University)*, vol. 11, no. 2, pp. 57–65, Dec. 1982, Document identifier = DOI: 10.18910/9554
- [200] K. Satoh, Reaction stress and weld cracking under hindered condition, Technological reports of the Osaka University, vol. 17, no. 783, pp. 353–375, 1967, Document URL: https://cir.nii.ac.jp/crid/1570854175244200704 (consulted on 10/01/2023)
- [201] J. R. Cho, B. Y. Lee, Y. H. Moon, and C. J. Van Tyne, Investigation of residual stress and post weld heat treatment of multi-pass welds by finite element method and experiments, *Journal of Materials Processing Technology*, vol. 155–156, pp. 1690–1695, Nov. 2004, Document identifier = DOI: 10.1016/j.jmatprotec.2004.04.325
- [202] N. Yurioka, M. Okumura, T. Kasuya, and H. J. U. Cotton, **Prediction of haz hardness of transformable steels**, *Metals Construction*, vol. 4, no. 19, pp. 217R-223R, 1987, Document identifier = ISSN: 0307-7896
- [203] G. Bernard, Les études poursuivies à l'IRSID sur la soudabilité des aciers de construction, Rev. Met. Paris, vol. 76, no. 10, pp. 637–648, Oct. 1979, Document identifier = DOI: 10.1051/metal/197976100637
- [204] D. Fydrych, A. Świerczyńska, and J. Tomków, **Diffusible Hydrogen Control in Flux Cored Arc Welding Process**, *Key Engineering Materials*, 2014, Document identifier = DOI: 10.4028/www.scientific.net/KEM.597.171
- [205] T. Kannengiesser and T. Lausch, **Diffusible Hydrogen Content Depending on Welding and Cooling Parameters**, *Weld World*, vol. 56, no. 11, pp. 26–33, Nov. 2012, Document identifier = DOI: 10.1007/BF03321392
- [206] R. Kuebler, M. Pitrun, and I. Pitrun, **The effect of welding parameters and hydrogen levels on the weldability of high strength Q & T steel welded with FCAW consumables**, *Australasian Welding Journal*, vol. 45, pp. 38–47, 2000
- [207] Satoh K. and Terasaki T., **Effect of joint geometry on stress concentration factor at the root of weld**, *Journal of the JWS (Japan Welding Society)*, vol. 48, no. 5, pp. 298–303, 1979, Document identifier = DOI: 10.2207/qjjws1943.48.298
- [208] L. M. Friedman, **EWI/TWI controlled deposition repair welding procedure for** 1{1/4}Cr-{1/2}Mo and 2{1/4}Cr-1Mo steels, *Bulletin Welding Research Council*, no. 412, Jun. 1996, Document URL: https://www.osti.gov/biblio/471160 (consulted on 11/09/2019)

- [209] W. D. Doty, **History and need behind the new NBIC rules on weld repair without PWHT**, *Bulletin Welding Research Council*, no. 412, Jun. 1996, Document URL: https://www.osti.gov/biblio/471157 (consulted on 11/09/2019)
- [210] R. L. Jones, Development of two-layer deposition techniques for the manual metal arc repair welding of thick C-Mn steel plate without postweld heat treatment, TWI Ltd (The Welding Institute), p. 31, 1987
- [211] S. Issler, A. Klenk, A. A. Shibli, and J. A. Williams, **Weld repair of ferritic welded materials for high temperature application**, *International Materials Reviews*, vol. 49, no. 5, pp. 299–324, Oct. 2004, Document identifier = DOI: 10.1179/095066004225021936
- [212] Cold welding: The science and art of quality weld repairs, Combined Cycle Journal, 2014 [webpage], Document URL: http://www.ccj-online.com/2q-2013/cold-welding-the-science-and-art-of-quality-weld-repairs/ (consulted on 11/09/2019)
- [213] C. Yang, H. Zhang, J. Zhong, Y. Chen, and S. Chen, **The effect of DSAW on preheating temperature in welding thick plate of high-strength low-alloy steel**, *Int J Adv Manuf Technol*, vol. 71, no. 1, pp. 421–428, Mar. 2014, Document identifier = DOI: 10.1007/s00170-013-5287-0
- [214] V. D. Poznyakov *et al.*, **Cold cracking resistance of butt joints in high-strength steels with different welding techniques**, *Strength Mater*, vol. 51, no. 6, pp. 843–851, Nov. 2019, Document identifier = DOI: 10.1007/s11223-020-00132-7
- [215] H. Granjon, **Informations sur les essais de fissuration**, *Soudage et Techniques Connexes*, pp. 7–8, 1963
- [216] W. Campbell, Experiences with HAZ cold cracking tests on a C-Mn structural steel, Welding Journal, vol. 55, no. 5, 1976
- [217] H. Hoffmeister, Concept and procedure of the IRC test for assessing hydrogen assisted weld cracking, Steel Research, vol. 57, no. 7, pp. 344–347, 1986, Document identifier = DOI: 10.1002/srin.198600779
- [218] A. Ferrari and F. Scandella, **Estimation de la sensibilité à la fissuration à froid des aciers : revue des différents essais de soudabilité**, presented at the *IS groupe* (*Institut de Soudure*), 05-Nov-2019
- [219] V. Akrivos *et al.*, **Neutron diffraction measurements of weld residual stresses in three-pass slot weld (Alloy 600/82) and assessment of the measurement uncertainty**, *J Appl Cryst*, vol. 53, no. 5, pp. 1181–1194, Oct. 2020, Document identifier = DOI: 10.1107/S1600576720009140
- [220] G. Pressouyre, V. Lemoine, D. Dubois, J.-B. Leblond, P. Saillard, and F. Faure, In situ measurement of hydrogen in weld heat affected zones thru mass spectrometry and computer analysis, *Hydrogen Embrittlement: Prevention and Control*, pp. 219–237, Jan. 1988, Document identifier = DOI: 10.1520/STP45304S
- [221] W. E. Jominy, **Standardization of hardenability tests**, *Metal Progress*, vol. 40, pp. 911–914, 1941

- [222] W. E. Jominy and A. L. Boegehold, **A hardenability test for carburizing steel**, *Transactions of American Society for Metals*, vol. 26, pp. 574–606, 1938
- [223] V. Cano, Simulation complète des expériences de chauffage laser du disque N4 et comparaison avec l'expérience, *EDF* (Électricité De France), EDF R&D Clamart, EDF internal publication H-I70-1999-00893-FR, Mar. 1999
- [224] P. Sofronis and R. M. McMeeking, **Numerical analysis of hydrogen transport near a blunting crack tip**, *Journal of the Mechanics and Physics of Solids*, vol. 37, no. 3, pp. 317–350, Jan. 1989, Document identifier = DOI: 10.1016/0022-5096(89)90002-1
- [225] G. Obasi *et al.*, **Measurement and prediction of phase transformation kinetics in a nuclear steel during rapid thermal cycles**, *Metall and Mat Trans A*, vol. 50, no. 4, pp. 1715–1731, Apr. 2019, Document identifier = DOI: 10.1007/s11661-018-05102-y
- [226] Y. L. Sun *et al.*, **Effects of dilution on alloy content and microstructure in multipass steel welds**, *Journal of Materials Processing Technology*, vol. 265, pp. 71–86, Mar. 2019, Document identifier = DOI: 10.1016/j.jmatprotec.2018.09.037
- [227] G. Murry, **Soudage et soudabilité métallurgique des métaux**, in *Mise en forme des métaux et fonderie*, *Techniques de l'Ingenieur*, 1994, Document identifier = DOI: 10.51257/a-v1-m715
- [228] V. Robin et al., Net Project Task Group 8 an international benchmark on residual stress assessment for welding repair, presented at the PVP2022 ASME 2022 Pressure Vessels and Piping Conference, Las Vegas, Nevada, 2022, vol. Volume 4B: Materials and Fabrication, Document identifier = DOI: 10.1115/PVP2022-85083
- [229] M. C. Smith, A. N. Vasileiou, D. W. Rathod, J. Francis, N. M. Irvine, and Y. Sun, A review of welding research within the new nuclear manufacturing (NNUMAN) programme, presented at the *PVP2017 ASME 2017 Pressure Vessels and Piping Conference*, Waikoloa, Hawaii, 2017, vol. Volume 6B: Materials and Fabrication, Document identifier = DOI: 10.1115/PVP2017-66180
- [230] X. Yue, Investigation on heat-affected zone hydrogen-induced cracking of high-strength naval steels using the Granjon implant test, *Weld World*, vol. 59, no. 1, pp. 77–89, Jan. 2015, Document identifier = DOI: 10.1007/s40194-014-0181-4
- [231] X. Yue and J. C. Lippold, **Evaluation of heat-affected zone hydrogen-induced cracking in navy steels**, *Welding Journal*, vol. 92, no. 1, pp. 20–28, 2013, Document URL: http://files.aws.org/wj/supplement/WJ 2013 01 s20.pdf
- [232] V. Robin, F. Gommez, C. Primault, and J. Devaux, **Implant test modeling for risk of cold cracking assessment during welding operations**, presented at the *PVP2012 ASME 2012 Pressure Vessels and Piping Conference*, Toronto, 2012, pp. 557–565, Document identifier = DOI: 10.1115/PVP2012-78376
- [233] A. Talebi Hanzaei, S. P. H. Marashi, and E. Ranjbarnodeh, The effect of hydrogen content and welding conditions on the hydrogen induced cracking of the API X70 steel weld, *International Journal of Hydrogen Energy*, vol. 43, no. 19, pp.

- 9399–9407, May 2018, Document identifier = DOI : 10.1016/j.ijhydene.2018.03.216
- [234] X. Yue, Evaluation of heat-affected zone hydrogen-induced cracking in high-strength steels, PhD thesis, *The Ohio State University*, Columbus, 2013, Document URL : https://etd.ohiolink.edu/apexprod/rws_etd/send_file/send?accession=osu1374109 768&disposition=inline
- [235] S. Sekfali, **Influence de la microstructure sur le comportement local dans les aciers 16MND5**, PhD thesis, *ECP (École Centrale Paris)*, Châtenay Malabry, 2004, Document URL: https://tel.archives-ouvertes.fr/tel-00419622 (consulted on 08/09/2019)
- [236] Y. Vincent, Simulation numérique des conséquences métallurgiques et mécaniques induites par une opération de soudage: acier 16MND5, PhD thesis, INSA Lyon (Institut National des Sciences Appliquées de Lyon), Lyon, 2002, Document URL: https://www.theses.fr/2002ISAL0024 (consulted on 03/11/2020)
- [237] V. Da Silva and J. Haouas, **Réalisation d'essais d'implants modifiés sur acier 16MND5**, *IS groupe (Institut de Soudure)*, IS technical report RT 01 rév. 1, Dec. 2011, Document identifier = IS ref. : RT 01 rév. 1
- [238] J.-B. Leblond, J. Devaux, and J. Devaux, **Simulation numerique de l'essai** d'implant, *Soudage et Techniques Connexes*, pp. 312–324, 1988
- [239] C. Primault, G. Tirand, F. Gommez, and V. Robin, **Etablissement d'un critère numérique de fissuration à froid**, *Matériaux & Techniques*, vol. 102, no. 4, p. 408, 2014, Document identifier = DOI: 10.1051/mattech/2014041
- [240] **ISO 17642-3**, *ISO (International Organization for Standardization)*, 2005, Document identifier = ISSN: 0335-3931
- [241] N. Cavallo, Contribution à la validation expérimentale de modèles décrivant la Z.A.T. lors d'une opération de soudage, PhD thesis, INSA Lyon (Institut National des Sciences Appliquées de Lyon), Lyon, 1998, Document URL: https://www.theses.fr/1998ISAL0024 (consulted on 25/02/2023)
- [242] J.-B. Leblond, Etude théorique et numérique de la diffusion de l'hydrogène dans les aciers, PhD thesis, *Université Pierre et Marie Curie*, Paris VI, 1984
- [243] X. S. Qingrong, NeT TG8 dissimilar metal welding between 18MND5 and alloy 52 final technical report, EDF UoM MaSC, University of Manchester, Post-Doctoral technical report, Jun. 2019
- [244] **Relations de comportement élasto-visco-plastique de Chaboche**, *Code_Aster*, 25-Sep-2013, Document identifier = R5.03.04
- [245] M. V. Li, D. V. Niebuhr, L. L. Meekisho, and D. G. Atteridge, **A computational model for the prediction of steel hardenability**, *Metall Mater Trans B*, vol. 29, no. 3, pp. 661–672, Jun. 1998, Document identifier = DOI: 10.1007/s11663-998-0101-3
- [246] C. J. Hamelin et al., Validation of a numerical model used to predict phase

- **distribution and residual stress in ferritic steel weldments**, *Acta Materialia*, vol. 75, pp. 1–19, Aug. 2014, Document identifier = DOI : 10.1016/j.actamat.2014.04.045
- [247] J. Draup, **Python based Continuous-Cooling-Transformation (CCT) digitizer tool**, *EDF Energy R&D (UK Center MaSC)*, University of Manchester, EDF internal publication UKC-R-2018-0xx (provisional), Dec. 2019
- [248] G. Miroslav, J. Petržela, V. Lázló, T. Cechel, and M. Juhas, **Development of technology for forging of bottoms of pressure vessels for nuclear power plants**, *Hutnicke Listy Metallurgical Journal*, vol. 63, no. 4, p. 41, 2010, Document URL: http://konsys-t.tanger.cz/files/proceedings/metal_11/lists/papers/947.pdf (consulted on 19/10/2022)
- [249] R. D. Stout, S. S. Tor, L. G. McGeady, and G. E. Doan, **Quantitative** measurement of the cracking tendency in welds, *Welding Journal*, vol. 25, no. 9, pp. 522s-532s, 1946
- [250] R. D. Stout, R. Vasudevan, and A. W. Pense, **A field weldability test for pipeline steels**, *Welding Journal Welding Research Supplement*, vol. 55, no. 4, pp. 89s–94s, Apr. 1976, Document URL: http://files.aws.org/wj/supplement/WJ 1976 04 s89.pdf
- [251] R. Vasudevan, R. D. Stout, and A. W. Pense, **A field weldability test for pipeline steels part II**, *Welding Journal Welding Research Supplement*, vol. 59, no. 3, pp. 76s–84s, Mar. 1980, Document URL: http://files.aws.org/wj/supplement/WJ 1980 03 s76.pdf
- [252] P. Le-Masson, **201006** Le-Masson P. TG4 equivalent heat source calibration, presented at the *Net-TG4*, Garching, Jun-2010
- [253] V. Cano and J. Angles, **Recueil bibliographique de caractéristiques thermiques, métallurgiques et mécaniques de l'acier 16MND5**, *EDF (Électricité De France)*, EDF R&D Clamart, EDF internal publication H-T64-2008-03224-FR, Mar. 2010
- [254] A. Ferrari, Dosages d'hydrogène réalisés avec le procédé TIG automatique et l'emploi d'un fil Inconel 52M sur substrat en acier faiblement allié 18MnNiMo5, IS groupe (Institut de Soudure), IS technical report 4325-5G465Y-V1, Feb. 2021, Document identifier = IS ref.: 4325-5G465Y-V1
- [255] A. A. M. Paget et al., Numerical study of the TEKKEN welding test, in Mathematical modelling of weld phenomena 13, C. Sommitsch, N. Enzinger, and P. Mayr, Eds. Graz - Schloss Seggau - Austria: Technischen Universität Graz, 2023, pp. 449–469, Document identifier = DOI: 10.3217/978-3-85125-968-1-25
- [256] MTLP102 Calcul métallurgique pour un acier avec prise en compte de la taille de grain, Code Aster, 12-Dec-2011, Document identifier = V4.61.102
- [257] MTLP103 Trempe d'un barreau cylindrique en acier 16MND5, Code_Aster, 20-Dec-2017, Document identifier = V4.61.103
- [258] Comportements non linéaires, Code_Aster, 05-Jan-2018, Document identifier = U4.51.11

- [259] Notice d'utilisation pour des calculs thermo-métallo-mécaniques sur des aciers, Code Aster, 24-Jun-2016, Document identifier = U2.03.04
- [260] Modélisation élasto-visco-plastique prenant en compte des transformations métallurgiques, Code Aster, 20-Jul-2017, Document identifier = R4.04.02
- [261] **Opérateur DEFI_MATERIAU**, *Code_Aster*, 02-Jul-2019, Document identifier = U4.43.01
- [262] **ISO 642**, *ISO (International Organization for Standardization)*, 1999, Document identifier = ISSN: 0335-3931
- [263] Coefficient de transfert thermique par convection, SolidWorks help centre, 2012 [webpage], Document URL: https://help.solidworks.com/2012/french/solidworks/cworks/Convection_Heat_C oefficient.htm (consulted on 05/04/2023)
- [264] Echanges convectifs, UTC (Université de Technologie de Compiègne), 2003 [webpage], Document URL : https://www.utc.fr/mecagom4/MECAWEB/EXEMPLE/FICHES/CVCAF1.htm (consulted on 31/07/2022)
- [265] **Tableau émissivités en thermographie**, *The Thermograpic Library*, 16-Aug-2015 [webpage], Document URL: http://www.thethermograpiclibrary.org/index.php?title=Tableau_%C3%A9missivit%C3%A9s en thermographie (consulted on 31/07/2022)
- [266] D. Landek, B. Liščić, T. Filetin, and T. Lübben, End quench hardenability test for gas quenched steels, *Strojarstvo: časopis za teoriju i praksu u strojarstvu*, vol. 53, no. 1, pp. 33–37, Feb. 2011, Document identifier = ISSN: 0562-1887
- [267] J.-K. Hwang, Effects of water jet height and end dipping on the cooling rate and hardenability in the Jominy end quench test, *Processes*, vol. 9, no. 4, p. 607, Apr. 2021, Document identifier = DOI: 10.3390/pr9040607
- [268] **Mesh user's guide:** aspect ratio 2D, Salome_Meca [webpage], Document URL: https://docs.salome-platform.org/7/gui/SMESH/aspect_ratio_page.html (consulted on 24/09/2020)
- [269] **Modélisations AXIS, D_PLAN, C_PLAN,** *Code_Aster*, 26-Sep-2013, Document identifier = U3.13.01
- [270] **Opérateur CALC_CHAMP**, *Code_Aster*, 04-Apr-2013, Document identifier = U4.81.04
- [271] A. L. Wingrove, **An appraisal of the Tekken test**, PhD thesis, *University of Wollongong*, Wollongong, 1986, Document URL: https://ro.uow.edu.au/cgi/viewcontent.cgi?referer=https://scholar.google.com/&httpsredir=1&article=2606&context=theses (consulted on 10/05/2021)
- [272] A. Traverson, Essais d'implant réalisés avec le procédé TIG mécanisé et l'emploi d'un fil Inconel 52M sur substrat en acier faiblement allié 18MND5, IS groupe (Institut de Soudure), IS technical report 5958-6FUA6L-V1, Sep. 2022, Document identifier = IS ref.: 5958-6FUA6L-V1

- [273] **ASTM E976**, ASTM International (American Society for Testing and Materials), 2021, Document identifier = DOI:10.1520/E0976-15R21
- [274] M. R. Horne, **Rayleigh Wave Acoustic Emission during Crack Propagation in Steel**, PhD thesis, *Virginia Polytechnic Institute and State University*, Blacksburg, 2003, Document URL: https://www.proquest.com/openview/de471a165a35c9ec47689a024b80c924/1?pq-origsite=gscholar&cbl=18750&diss=y (consulted on 23/12/2021)
- [275] Calibration: Signal Source, ATG (Acoustic Technology Group) [webpage], Document URL: https://atgndt.com/ae-calibration-and-simulators/calibration-signal-source/ (consulted on 15/04/2023)
- [276] A. Beyer, **Fissuration à froid et essais de soudabilité**, *CTICM (Centre Technique Industriel de la Construction Métallique)*, Aout-2020, Document URL: https://metaletech.com/wp-content/uploads/2020/08/Essais-de-soudabilite.pdf (consulted on 10/04/2023)
- [277] H. Granjon and S. Debiez, **Note on acoustic emission in relation to cold cracking in the welding of steel**, presented at the *Eighth world conference on non-destructive testing*, Cannes, 1976, Document identifier = No. FRNC-CONF--171
- [278] Y. Javadi *et al.*, **Investigating the effect of residual stress on hydrogen cracking in multi-pass robotic welding through process compatible non-destructive testing**, *Journal of Manufacturing Processes*, Apr. 2020, Document identifier = DOI: 10.1016/j.jmapro.2020.03.043
- [279] P. D. Hodgson, K. M. Browne, R. K. Gibbs, T. T. Pham, and D. C. Collinson, **The mathematical modeling of temperature and microstructure during spray cooling**, presented at the *First international conference on quenching and control of distortion*, Chicago, 1992, pp. 41–49, Document identifier = ISBN: 978-0-87170-455-9
- [280] A. Oudriss *et al.*, Consequence of hydrogen desorption on local mechanical properties and the fracture mechanisms of a martensitic steel, presented at the *TMS2017*, San Diego, 27-Mar-2017, Document URL: http://www.programmaster.org/PM/PM.nsf/ApprovedAbstracts/714EEAA6BAF5 6ECD85257FF100692D1B?OpenDocument (consulted on 27/06/2019)
- [281] K. Pearson, **IX. Mathematical contributions to the theory of evolution.—XIX. Second supplement to a memoir on skew variation**, *Philosophical Transactions of the Royal Society of London*, vol. 216, no. 538–548, pp. 429–457, Jan. 1916, Document identifier = DOI: 10.1098/rsta.1916.0009
- [282] G. K. Williamson and W. H. Hall, **X-ray line broadening from filed aluminium and wolfram**, *Acta Metallurgica*, vol. 1, no. 1, pp. 22–31, Jan. 1953, Document identifier = DOI: 10.1016/0001-6160(53)90006-6
- [283] H. Ford, **I. the Tensile Properties of Metals**, *Journal of the Royal Society of Arts*, vol. 103, no. 4953, pp. 471–486, 1955, Document identifier = ISSN: 0035-9114